Numerical modelling of chill cooling of levitated steel melts solidified in the International Space Station

Ayoub Aalilija

To cite this version:

Ayoub Aalilija. Numerical modelling of chill cooling of levitated steel melts solidified in the International Space Station. Mechanics of materials [physics.class-ph]. Université Paris sciences et lettres, 2020. English. ⟨NNT : 2020UPSLM064⟩. ⟨tel-03245908⟩

HAL Id: tel-03245908

https://pastel.hal.science/tel-03245908v1

Submitted on 2 Jun 2021

THÈSE DE DOCTORAT
DE L'UNIVERSITÉ PSL

Préparée à MINES ParisTech

Modélisation numérique de la solidification des aciers fondus en lévitation dans la Station Spatiale Internationale

Numerical modelling of chill cooling of levitated steel melts solidified in the International Space Station

Soutenue par
Ayoub AALILIJA
Le 21 décembre 2020

École doctorale n°364
Sciences Fondamentales et Appliquées

Spécialité
Mécanique Numérique et Matériaux

Composition du jury :

Pr. Catherine COLIN Professeur INP Toulouse , France	Présidente
Pr. Emmanuelle ABISSET-CHAVANNE Professeur Arts et Métiers, France	Rapportrice
Pr. Douglas MATSON Professeur Université Tufts, USA	Rapporteur
Dr. Charles-André GANDIN Directeur de recherche CNRS, France	Directeur de thèse
Pr. Elie HACHEM Professeur MINES ParisTech, France	Directeur de thèse

Acknowledgements

Upon concluding this doctoral thesis, I am convinced that a PhD work is far from being a one-person effort. The achievement of this thesis could never have been successful without the support of a large number of people who, through their devotion to my work, their scientific contributions and their encouragement, have enabled me to progress in this challenging step of my professional career.

The first people to whom I would like to address my acknowledgements and gratitude are my two PhD supervisors Dr. Charles-André GANDIN and Prof. Elie HACHEM. I thank them for the trust they have placed in me, their scientific supervision and their continuous encouragement. Many obstacles have been overcome in this adventure thanks to their expertise and wisdom. The discussions we had were enriching both professionally and personally.

I also would like to thank the members of the jury: Prof. Catherine COLIN, Prof. Emmanuelle ABISSET-CHAVANNE and Prof. Douglas MATSON for agreeing to read and review this manuscript.

My thanks also go to those at CEMEF who contributed in one way or another to the preparation of this thesis. Thank you Hanadi, Ichraq, Chahrazade, Ghalia, Mehdi, Qiang, Carlos, Vincent, Shaojie, Julien and Shitij for the friendly atmosphere and spirit of mutual support that forged our relationship inside and outside CEMEF. Thank you Florence MORCAMP, Marie-Françoise GUENEGAN and Patrick COELS for helping me with the administrative procedures. Thank you Carole TORRIN, Hallen BEN AISSA and Sélim KRARIA for having helped me to solve the technical IT problems.

Special thanks are sent to Thomas VOLKMANN from the German Aerospace centre (DLR) in Cologne for answering all my questions concerning the experimental aspects of the CCEMLCC project.

My sincere thanks go to my splendid band of lifelong friends who, even if they do not fully understand what I am doing in my thesis, have understood very well how to support me and keep me in good company. Thank you Selma, Zineb, Youness, Mohammed, Otman, Abdelhamid and Amine.

Finally, my deepest gratitude goes to my sweet family who, despite the long distance that separates us, have showered and still shower me with unconditional love and emotional support. Heartfelt thanks to my mother, father, sisters and brother.

Contents

Contents iii

Glossary vii

List of Figures ix

List of Tables xv

1 General Introduction 1
- 1.1 Context 4
- 1.2 Physical phenomena during solidification of a levitated steel droplet 5
  - 1.2.1 Heat transfer 6
  - 1.2.2 Solidification 7
  - 1.2.3 Chemical segregation 8
  - 1.2.4 Fluid flow 8
- 1.3 Previous contributions 10
- 1.4 Objectives and outline 12

2 Chill cooling experiments in microgravity 15
- 2.1 Introduction 18
  - 2.1.1 The experimental set-up 18
  - 2.1.2 Steel samples processed 19
- 2.2 Microgravity experiments: from precursor tests to experiment on board the International Space Station 20
  - 2.2.1 Parabolic flights experiments 20
  - 2.2.2 Sounding rocket experiments 25
  - 2.2.3 International Space Station experiment 27
- 2.3 Conclusion 35

3 Numerical modelling of multiphase flows including surface tension 37
- 3.1 Introduction 40
- 3.2 Interface modelling 40
  - 3.2.1 Level-Set function 41
  - 3.2.2 Level-Set transport 41
  - 3.2.3 Mass correction 42
- 3.3 Flow modelling 43
  - 3.3.1 Governing equations 43

3.3.2 Two-fluid flow formulation . . . 44
3.3.3 Diffuse interface approach and mixing laws . . . 45
3.3.4 Surface tension modelling . . . 46
3.3.5 Semi-implicit BDF time discretisation of Navier-Stokes equations . . . 50
3.3.6 Stabilised Variational MultiScale method . . . 50
3.4 Partial conclusion . . . 52
3.5 The oscillating drop method : analytical solution . . . 53
3.5.1 State of the art . . . 53
3.5.2 The free-oscillating viscous drop problem . . . 55
3.5.3 Analytical solutions in the framework of the linear theory . . . 57
3.6 Numerical simulations . . . 62
3.6.1 2D preliminary numerical tests . . . 62
3.6.2 2D simulation of single oscillation modes . . . 69
3.6.3 2D simulation of an arbitrary initial form . . . 73
3.6.4 3D simulation of the oscillation of a liquid iron drop . . . 76
3.7 Conclusion . . . 77

4 Numerical modelling of heat transfer with solidification and thermal contact resistance 79
4.1 Introduction . . . 82
4.2 Thermal contact resistance . . . 82
4.2.1 State of the art . . . 82
4.2.2 Governing equations and modelling . . . 84
4.2.3 Results and discussion . . . 89
4.3 Heat conduction with solidification . . . 97
4.3.1 Introduction . . . 97
4.3.2 Volume averaging method . . . 97
4.3.3 Averaged energy conservation equation . . . 99
4.3.4 Monolithic formulation of the energy conservation in a multi-domain system 100
4.4 Application to chill cooling and solidification experiment on board the ISS . . . 101
4.5 Conclusion . . . 105

5 Numerical simulation of chill cooling and solidification of a levitated steel sample in microgravity 107
5.1 Introduction . . . 110
5.2 Governing equations for conjugate heat transfer including solidification, chemical segregation and capillary forces . . . 110
5.2.1 Mass conservation . . . 110
5.2.2 Momentum conservation . . . 112
5.2.3 Energy conservation equation . . . 117
5.2.4 Chemical species conservation equation . . . 120
5.2.5 Modelling of interfaces . . . 123
5.3 Coupling resolution strategy . . . 126
5.4 Application to chill cooling and solidification experiment on board the ISS . . . 128
5.4.1 Preliminary results and numerical investigations . . . 128
5.4.2 3D simulation . . . 143

5.5 Conclusion 147

6 Conclusions and Perspectives **149**

Glossary

Notation	Description
BDF	Backward Differentiation Formulas
CA	Cellular Automata
CAFE	Cellular Automata Finite Element
CCEMLCC	Chill Cooling for the Electromagnetic Levitator in relation with Continuous Casting of steel
CEMEF	Centre for Material Forming
CFD	Computational Fluid Dynamics
CSF	Continuum Surface Force
EML	Electromagnetic Levitation
ESA	European Space Agency
FE	Finite Element
ISS	International Space Station
LHS	Right-Hand-Side
MAP	Microgravity Applications Promotion
MHD	Magneto-HydroDynamic
NEQUISOL	Non EQUIlibrium SOLidification
ODE	Ordinary Differential Equation
REV	Representative Elementary Volume
RHS	Right-Hand-Side
SUPG	Streamline Upwind Petrov–Galerkin
VMS	Variational MultiScale
XFEM	Extended Finite Element Method

List of Figures

1.1 A liquid metallic drop of Ni-Cu alloy with a diameter of 7 mm, freely suspended within an electromagnetic levitation coil [3] . . . 4

1.2 Illustration of heat transfer modes involved in chill cooling experiments in the context of the CCEMLCC project . . . 6

1.3 (a) In situ observation of columnar microstructures for transparent alloy of succinonitrile–acetone (SCN–2wt% Ace) [4]. (b) A typical image of a settling equiaxed dendrite [5] . . . 8

1.4 (a) Numerical simulation showing the velocity field of the solid phase (black arrows) and the liquid phase (orange arrows) at t = 1.5 s during the solidification of a 3.3mm radius steel droplet. (b) Droplet shape predicted by numerical simulation with macrosegregation (grey) and without macrosegregation (blue) in comparison with TEXUS experimental profile (red) at t = 4.5 s [12]. The top of the experimental shape was not visible in the experiment. . . . 11

1.5 (a) Numerical simulation of the fluid flow in the liquid metal and the surrounding gas during solidification of a steel droplet. (b) Comparison of experimental (blue) and numerical (red) final droplet profiles, compared to its initial shape (green) [6] . 12

2.1 (a) Schematics of the experimental set-up used in a TEXUS sounding rocket where a cage was used to limit the sample displacement. (b) Schematics of the cup holder used for chill cooling of EML samples on board the ISS [16]. . . . 19

2.2 (a) A parabolic flight profile [18]. (b) View inside the Zero-G Airbus aircraft during the 46^{th} ESA flight campaign [19]. . . . 21

2.3 Time evolutions for a Fe-0.9C-0.2Si sample during a chill cooling cycle in TEMPUS parabolic flight: (blue) temperature, (red) heater control voltage and (green) microgravity level. The time interval between contact with the chill plate and completion of solidification is marked by the vertical dashed lines. . . . 22

2.4 Image sequence given by a high-speed camera showing the solidification progress between 0 s (when contact with the chill is initiated) to 3.75 s in a Fe-0.9C-0.2Si steel droplet. The progress of the solidification front is marked by the green dashed line. In some frames, the droplet is partially hidden by the narrow opening of the sample holder facing the camera [6]. . . . 22

2.5 The final shape of the solidified sample [6]. . . . 22

2.6 Time evolutions for a Fe-0.1C-0.2Si sample during a chill cooling cycle in TEMPUS parabolic flight: (blue) temperature, (red) heater control voltage and (green) micro-gravity level. The time interval between contact with the chill plate and completion of solidification is marked by the vertical dashed lines. 23

2.7 Sequence of video images for the Fe-0.1C-0.2Si experiment showing the sample shape time evolution (from left to right). The time increment between images is 0.5 s starting at the time of contact with the chill plate at 25.9 s. The chill plate (not visible) was located at the top and moved downwards. The red line marks the position of the growth front. From the video taken at 500 fps growth velocity is determined to approximately 1mm.s^{-1} [20]. 24

2.8 Time evolutions for a Fe-0.05C-0.2Si sample during a chill cooling cycle in TEMPUS parabolic flight: (blue) temperature, (red) heater control voltage and (green) micro-gravity level. 24

2.9 Sequence of video images for the Fe-0.05C-0.2Si experiment showing the sample shape time evolution (from left to right). The time increment between images is 0.5 s starting at the time of contact with the chill plate at 40.1 s. The chill plate moved downwards. The interface chill plate-metal is represented by the dashed blue line. The position of the growth front is marked by the red line. From the video taken at 500 fps growth velocity is determined to approximately 1mm.s^{-1}. 24

2.10 (a) A parabolic flight profile [21]. (b) Successful launch of TEXUS-42 sounding rocket [22]. 25

2.11 Time evolutions during 5 cycles of processing Fe-0.1C-0.2Si sample on board TEXUS-46 sounding rocket: (blue) temperature measured by the lateral pyrometer and (orange) temperature measured by the axial pyrometer [23]. 26

2.12 Sequence of video images for the Fe-0.9C-0.2Si TEXUS experiment showing the sample shape time evolution (from left to right). The time increment between images is 1 s starting at time of contact with the chill plate. The position of the growth front is marked by the red line [12] 26

2.13 The International Space Station [24]. 27

2.14 Temperature-time profile (blue) and heater control voltage (red) for Fe-0.9C-0.2Si during a chill cooling cycle in ISS-EML (batch #2.3). The time interval between contact with the chill plate and completion of solidification is marked by the vertical dashed lines. 28

2.15 Sequence of snapshots from the high-speed camera that recorded the Fe-0.9C-0.2Si experiment onboard the ISS is showing the time evolution of the sample's shape. The chill plate was moving downwards during the first 2 seconds from the contact. The blue line represents the interface of the contact with the chill plate. The red line marks the position of the growth front. 29

2.16 The final shape of the sample *d1* after completion of solidification on board the ISS. 29

2.17 Time-evolution of the front position. 30

2.18 Snapshots showing the shape of the droplet during solidification. The red lines mark the front position. The contour of the final shape, marked by the blue dashed lines, is superimposed to the solidifying droplet shape at different times. 31

2.19 Snapshots showing some light spots (encircled in red and yellow) located at the solid phase at different times. The invisible part of the droplet is hidden by the holder. The red lines mark the front position. 31
2.20 Snapshots showing differences in solid and liquid angles at the solidification front position. The liquid angle θ_l is marked in red and the solid angle θ_s is marked in blue. 32
2.21 Time-evolution of the solid and liquid angles at the front position. 32
2.22 Temperature-time profile (red) and heater control voltage (blue) for Fe-0.9C-0.2Si during properties measurement cycle in ISS-EML (batch #2.3). The two peaks in the heater signal represent the electromagnetic pulses to make the droplet oscillate [25]. 33
2.23 The time evolution of the oscillation of the radius of the droplet [25]. 34
2.24 Surface tension as function of temperature [25]. 34

3.1 Illustration of the Level-Set function 41
3.2 The diffuse interface approach illustrated via the density profile across the interface 46
3.3 Illustration of the centred Dirac function and the density-scaled Dirac function . . . 47
3.4 Illustration of the simulated velocity field (depicted by black arrows) of a circular drop with (a) the standard CSF method and (b) the density-scaled CSF method . . . 48
3.5 Schematics of the framework of 3D and 2D oscillations 57
3.6 Mesh grid for the parametric study 64
3.7 (a) Comparison of the time-evolutions of the radius of the drop without mass correction (black line), the radius with mass correction (blue line) and the theoretical solution (red line) (b) The temporal variation of the surface of the 2D drop without and with mass correction method 65
3.8 Comparison of the frequency spectrum of the radius of the drop without mass correction (black dashed line) and the spectrum with mass correction (blue line). The theoretical position of the peak is marked by the red dashed line 65
3.9 Comparison of the temporal variation of the surface of the 2D drop between the *Conv+DRT* method and *Leveler* method 66
3.10 Comparison of the oscillation radius simulated with the *Conv+DRT* method (green line) and the radius simulated with the *Leveler* method (blue line) 66
3.11 Comparison of the oscillation radius simulated with the explicit surface tension and the radius simulated with the semi-implicit surface tension with different time steps 67
3.12 Comparison of the oscillation radius simulated with the 1^{st} order of discretisation of Navier-Stokes and the radius simulated with 2^{nd} order with different time steps . . . 68
3.13 Time-evolutions of the normalized radius $R(\theta = 0, t)/R_0 - 1$ obtained from simulations with different mesh resolutions 69
3.14 The time-evolution of the droplet shape over the first oscillation period for modes from $n = 2$ (upper row) to $n = 7$ (lower row). From the left column to the right, time corresponds to t=0, $\frac{T_n}{4}$, $\frac{T_n}{2}$, $\frac{3T_n}{4}$ and T_n respectively 71
3.15 The temporal signals of the droplet's radius in direction $\theta = 0$ for modes $n \in [\![2, 7]\!]$ . . 72
3.16 The variation of (a) the oscillation frequency and (b) the damping rate with respect to the oscillation mode 72
3.17 Snapshots of the droplet shape and velocity field at various times 74
3.18 Comparison of simulation results and the analytical solution 75

3.19 The time evolution of the displacement of the upper point of intersection of the interface with the z-axis . . . 76

4.1 Scanning Electron Microscopy imaging of the contact area of the solidified sample processed during a parabolic flight on board a zero-g airplane [1] . . . 82
4.2 Schematic of two materials in contact, Ω_1 and Ω_2, forming a thermally resistant interface Γ_{12} due to the presence of a gap layer, Ω_G, with thickness e. . . . 87
4.3 Setup for numerical simulations using a 1D heat flow configuration between the two materials in contacts, as defined in figure 4.2. . . . 89
4.4 Conductivity profile for different thermal contact resistance values. . . . 90
4.5 Steady temperature showing the jump at the interface for different thermal contact resistance values . . . 90
4.6 Setup of the numerical simulation for a 3D heat flow configuration. . . . 91
4.7 Temperature field in YZ plane through the centre of the simulation domain. . . . 93
4.8 Mesh . . . 93
4.9 Steady temperature profiles showing the jump at the interface for different thermal contact resistance values. . . . 93
4.10 Setup for the unsteady conduction validation test. The reference case is referred to as "Explicit" and the evaluated case is referred to as "Implicit". . . . 94
4.11 Mesh size and distribution of the heat conductivity for the (a) explicit and (b) implicit gap configurations. . . . 95
4.12 Time-evolution of the temperature jump across the interface for $\mathrm{C}_{p,\mathrm{G}} \ll \overline{\mathrm{C}_p}$ . . . 95
4.13 Time-evolution of the temperature jump across the interface for $\mathrm{C}_{p,\mathrm{G}} = \mathcal{O}(\overline{\mathrm{C}_p})$ . . . 96
4.14 Time-evolution of the temperature jump across the interface for $\mathrm{C}_{p,\mathrm{G}} \gg \overline{\mathrm{C}_p}$ . . . 96
4.15 Schematic representation of the REV . . . 98
4.16 Tabulated thermodynamic properties for the Fe-0.9wt.%C-0.26wt.%Si alloy at nominal composition. . . . 102
4.17 The setup of the simulation for chill cooling and solidification of a deformed steel droplet showing (a) the geometries of the droplet and chill plate inside the computational domain and (b) a cross section through the 3D finite element mesh . . . 103
4.18 The time-evolutions of the front position for different thermal contact resistance compared to the experiment (the yellow square is extrapolated) . . . 104

5.1 Schematic of a multidomain system involving a solidifying metallic subdomain . . . 115
5.2 The order of the resolution of conservation equations during a time increment . . . 127
5.3 The setup of the 2D simulation for chill cooling and solidification of a steel droplet showing: (a) the geometries of the droplet, chill plate and the computational domain, (b) the 2D mesh used for calculations. . . . 129
5.4 Snapshots of the solidifying droplet showing temperature field superimposed to the velocity in the metal at different times. . . . 134
5.5 (a) Temporal signals of the front position for 2D simulation with only heat conduction (dashed black line), 2D simulation with both conduction and convection (black continuous line) and for the experiment on board the ISS (red squares: measured; yellow square: extrapolated). (b) The comparison of the initial shape and the final shape predicted by the 2D simulation showing a slightly-elongated droplet. . . . 135

5.6 Snapshots of the solidifying droplet showing the composition field within the metal domain at different times. 135
5.7 Time-evolution of the mass of the droplet and the mass of Carbon 136
5.8 Simulation of solidification of a ternary alloy showing the final composition in (a) Carbon and (b) Silicon. 137
5.9 Comparison of the solid fraction field at the time $t = 2s$ for (a) a binary alloy with a constant and uniform Carbon composition, (b) a binary alloy with Carbon transport and (c) a ternary alloy with Carbon and Silicon transport. The red and blue lines mark the position of the iso-values $g^s = 1\%$ and $g^s = 99\%$ respectively 137
5.10 Comparison of the final shape of solidified droplet resulting from simulations with a binary alloy Fe-0.9wt.%C, with and without segregation, and a ternary alloy Fe-0.9wt.%C-0.26wt.%Si. 138
5.11 Comparison of time-evolution of the position of solidification front for simulations with a binary alloy Fe-0.9wt.%C, with and without segregation, and a ternary alloy Fe-0.9wt.%C-0.26wt.%Si. 138
5.12 Comparison of the flow pattern in the liquid metal for (left) a positive Marangoni and (right) a negative Marangoni. The velocity vectors are superimposed to temperature field at different times. The red and blue lines mark the position of the iso-values $g^s = 1\%$ and $g^s = 99\%$ respectively 140
5.13 Comparison of the final shape predicted by a positive Marangoni coefficient (red) and a negative coefficient (blue). The initial shape is plotted in dashed black line. . . 141
5.14 Parametric study in 2D pure conduction in which the thermal contact resistance is varying from 0 to $3.\,10^{-4}$ $\mathrm{W}^{-1}.\mathrm{m}^2.\mathrm{K}$. The numerical results are plotted in dashed lines. The measured front position is marked by red squares. The yellow square is the final front position extrapolated form measurements. 142
5.15 Comparison of 2D simulations with R_{th}=0 $\mathrm{W}^{-1}.\mathrm{m}^2.\mathrm{K}$, $\mathrm{R}_{th} = 10^{-4}$ $\mathrm{W}^{-1}.\mathrm{m}^2.\mathrm{K}$ and R_{th} =$2.\,10^{-4}$ $\mathrm{W}^{-1}.\mathrm{m}^2.\mathrm{K}$ for (a) time evolution of the solidification front position and (b) the final droplet shapes 142
5.16 Snapshots of the solidifying droplet showing temperature field superimposed to the velocity of the metal at different times. The red and blue lines mark the position of $g^s = 1\%$ and $g^s = 99\%$ respectively 143
5.17 The static 3D mesh in a cross section of the computational domain showing the characteristics of the mesh size in each subdomain. 144
5.18 Snapshots of the solidifying 3D droplet in perfect contact with the chill. The images show the velocity of the liquid metal and the temperature of the whole domain. The red and the blue lines mark the position of $g^s = 1\%$ and $g^s = 99\%$ respectively. 145
5.19 Comparison of a 3D simulation with perfect contact with the ISS experiment for (a) the time-evolution of the front position (b) the final shape of the solidified droplet. . 145
5.20 A clip of the 3D mesh showing mesh adaptation around the interfaces of the steel droplet and the chill plate. Calculations failed with this mesh. 146

List of Tables

1.1 Some dimensionless numbers involving surface tension 12

2.1 Composition in wt.% of the steel samples investigated in the CCEMLCC project . . . 20
2.2 The references of TEMPUS successful experiments 21

3.1 The values of λ_n^2, $\omega_{n,0}^2$ and Δ'_n for each oscillation mode 70
3.2 Random values of $\varepsilon_{n,0}$ and ψ_n for each normal mode 73

4.1 Values of the simulation parameters for results presented in figures 4.8 and 4.9. . . . 92

5.1 Physical properties of materials 131

Chapter 1

General Introduction

Résumé

Cette thèse de doctorat s'inscrit dans le cadre des projets CCEMLCC et NEQUISOL de l'Agence spatiale européenne (ESA) en collaboration avec plusieurs partenaires académiques et industriels. L'objectif commun de ces deux projets est d'étudier la solidification d'alliages métalliques en lévitation en microgravité. Deux approches sont adoptées pour répondre à cet objectif : une approche expérimentale et une approche numérique. Cette thèse se focalise sur les aspects de modélisation numérique. L'objectif étant de simuler numériquement les expériences de solidification en microgravité, il est essentiel d'identifier les phénomènes à modéliser qui régissent les échanges de masse et de chaleur ainsi que la solidification et la ségrégation chimique. Dans ce chapitre, nous présentons les principaux phénomènes physiques présents dans ces expériences. Nous résumons les contributions précédentes du CEMEF à ces projets. Nous mettons l'accent sur la tension de surface qui est absente dans les précédentes contributions et qui est l'un des phénomènes clés régissant les expériences de solidification de gouttelettes d'alliage fondu. Enfin, nous présentons les objectifs détaillés de ce travail et la structure de ce manuscrit.

Contents

1.1 Context **4**
1.2 Physical phenomena during solidification of a levitated steel droplet **5**
  1.2.1 Heat transfer 6
    1.2.1.1 Conduction 6
    1.2.1.2 Convection 6
    1.2.1.3 Radiation 7
  1.2.2 Solidification 7
  1.2.3 Chemical segregation 8
  1.2.4 Fluid flow 8
    1.2.4.1 Solidification shrinkage 8
    1.2.4.2 Microgravity 9
    1.2.4.3 Electromagnetic stirring 9
    1.2.4.4 Surface tension 9
    1.2.4.5 Marangoni effect 10
1.3 Previous contributions **10**
1.4 Objectives and outline **12**

1.1 Context

Since its creation in 1975, the European Space Agency (ESA) has actively participated in scientific research in various fields such as materials science. In addition to its financial support of projects, ESA provides its scientific partners with facilities to carry out their microgravity experiments. Microgravity allows researchers to decouple gravity-dependent phenomena from non-gravity-dependent ones in order to better understand specific mechanisms such as solidification. This can lead to the improvement of processes on Earth and the design of innovative materials with particular properties to meet industrial needs. Despite the growing number of scientific projects that express an interest in investigating under microgravity conditions, opportunities to benefit from microgravity facilities such as parabolic flights with aircrafts, sounding rockets and the International Space Station (ISS) are limited. In addition, few projects have been able to benefit from a flight ticket to the ISS. Centre for Material Forming (CEMEF) is one of the French research centres that participate in ESA research projects and have the privilege of operating their experiments in the ISS. CEMEF contributes to these projects through several doctoral theses. The present work is one of them. It is part of two ESA projects in the framework of the Microgravity Applications Promotion (MAP) programme. The first project is entitled Non EQUIlibrium SOLidification (NEQUISOL) and the second is entitled Chill Cooling for the Electromagnetic Levitator in relation with Continuous Casting of steel (CCEMLCC). The main common objective of these projects is to investigate the containerless solidification of levitated metallic alloys in microgravity [1; 2] using an electromagnetic field. This latter provides a Lorentz force to keep the sample in a stable position (Figure 1.1). The electromagnetic field is also used to heat the sample and melt it.

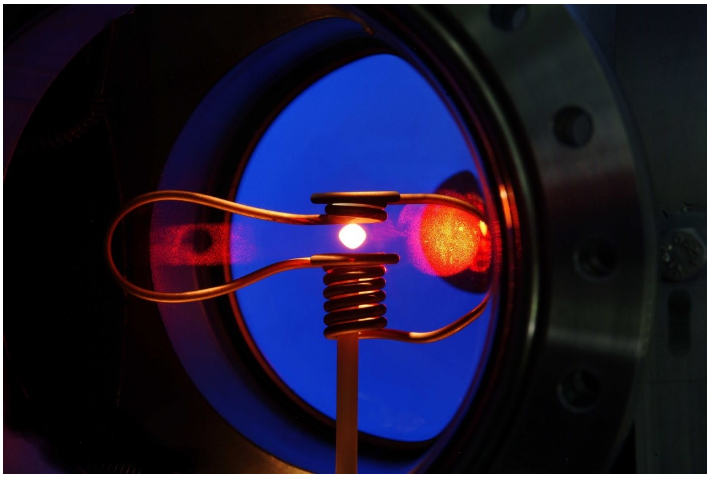

Figure 1.1: A liquid metallic drop of Ni-Cu alloy with a diameter of 7 mm, freely suspended within an electromagnetic levitation coil [3]

The NEQUISOL project focuses mainly on the dynamics of crystal growth in non-equilibrium solidification of aluminium-based alloys. In this project, nucleation is naturally triggered from an undercooled state.

In the CCEMLCC project, investigation focuses on "surface defects formed during the treatment of steels in the liquid state". Solidification is triggered by contact with a ceramic substrate (Si_3N_4) which extracts heat from the sample.

The academic and industrial partners working in collaboration with CEMEF in the context of NEQUISOL and CCEMLCC project are given in the following list:

Academic partners

- MINES ParisTech, PSL Research University, Center for Material Forming (CEMEF) UMR CNRS 7635, Sophia Antipolis, France (**CCEMLCC & NEQUISOL projects**)
- Deutsches Zentrum für Luft-und Raumfahrt e.V. (DLR), Institut für Materialphysik im Weltraum, Köln, Germany (**CCEMLCC & NEQUISOL projects**)
- University of Alberta, Department of Chemical and Materials Engineering, Advanced Materials and Processing Laboratory, Edmonton (**CCEMLCC & NEQUISOL projects**)
- Université de Lorraine, Institut Jean Lamour (IJL) UMR CNRS 7198, Nancy, France (**CCEMLCC project**)
- National Center for Metallurgical Research CENIM-CSIC, Dept. Metalurgia Física, Madrid, Spain (**NEQUISOL project**)
- Institute of Materials Research, University Leeds, Leeds, UK (**NEQUISOL project**)
- Otto-Schott-Institut für Materialforschung, Friedrich Schiller University, Jena, Germany (**NEQUISOL project**)

Industrial partners

- ARCELORMITTAL Maizières Research, Maizières-lès-Metz, France (**CCEMLCC project**)
- TRANSVALOR, Biot, France (**CCEMLCC project**)
- INDUSTEEL FRANCE, Le Creusot, France (**CCEMLCC project**)
- ASCO INDUSTRIES, Hagondange, France (**CCEMLCC project**)
- APERAM ALLOYS IMPHY, Imphy, France (**CCEMLCC project**)
- EVRAZ, Regina, Canada (**CCEMLCC project**)
- HYDRO Aluminium Deutschland AG, Bonn, Germany (**NEQUISOL project**)
- RGS Development, Broek op Langedijk, The Netherlands (**NEQUISOL project**)
- Equispheres Inc., Ottawa, Canada (**NEQUISOL project**)

In these projects, both experimental and numerical approaches are used for investigation. Various facilities are provided for carrying out microgravity experiments: parabolic flights, sounding rockets and the ISS. CEMEF contributes to research work by numerical modelling with the aim of proposing a numerical tool capable of reproducing the experiments and helping to interpret their results.

1.2 Physical phenomena during solidification of a levitated steel droplet

Before addressing numerical modelling aspects dealt with in this work, it is essential to identify relevant physical phenomena involved in the solidification of a levitated droplet in microgravity. Note that, hereafter, attention goes to solidification triggered by chill cooling.

1.2.1 Heat transfer

Thermal or heat transfer is a fundamental concept in thermodynamics. Together with work, it represents the modes of internal energy exchange between two systems. There are three types of heat transfer which can operate simultaneously: conduction, convection and radiation. All these heat transfer modes are involved in the chill cooling experiment as illustrated in Figure 1.2.

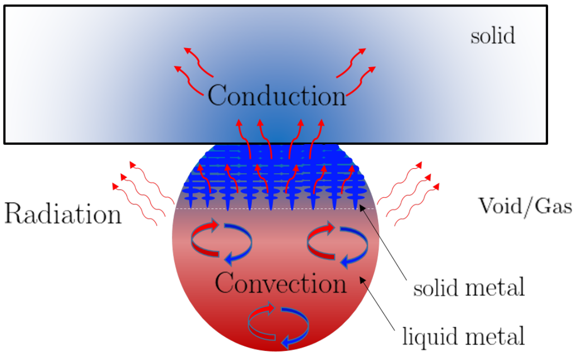

Figure 1.2: Illustration of heat transfer modes involved in chill cooling experiments in the context of the CCEMLCC project

1.2.1.1 Conduction

Conduction is a mode of energy transfer that occurs on a macroscopic scale by the displacement of heat from hot regions to cold regions of the same body or several bodies in contact. Conduction is due to particle collisions at the microscopic scale. An atom (or molecule) in vibration releases part of its kinetic energy to the neighbouring atoms. The transport of heat by conduction occurs within and through the body itself without displacement of matter. Conduction is more important in solids because the relatively dense crystal lattice helps to transfer energy between atoms by vibration. It is heat conduction that is at the origin of triggering solidification in the CCEMLCC project experiment.

1.2.1.2 Convection

Convection is the movement of particles within a fluid (gas or liquid) leading to the transport of heat from one point to another. The movement of the fluid can be natural (natural convection) or forced (forced convection). Natural convection occurs when a gradient induces movement in the fluid. The gradient can concern different quantities such as temperature ("thermal convection"), the concentration of a solute ("solutal convection") or surface tension ("thermo-capillary convection"). A temperature or concentration gradient leads to differences in density within the fluid. Gravity drives the denser particles downwards and the less dense particles upwards, producing a vertical flow. In the absence of gravity, convection due to the difference in density is no longer possible because the driving force behind the movement of particles with different densities is the gravitational force. However, thermo-capillary convection can still exist in microgravity. Indeed, a surface tension gradient caused by a temperature or concentration gradient at the interface between two fluids induces a movement of particles along the interface towards regions of high surface tension. This effect, which is independent of the gravitational force, is called the "Marangoni effect". For forced convection, the movement of the fluid is artificially caused by an external mechanism such as a pump or turbine or by electromagnetic induction forced by a coil.

1.2.1.3 Radiation

Thermal radiation is the transfer of energy by emission of electromagnetic waves from any material whose temperature is above absolute zero. Thermal radiation is the direct result of the microscopic agitation of atoms and molecules in matter. Since these atoms and molecules are composed of charged particles (protons and electrons), their agitation causes the emission of electromagnetic waves, which carry the energy away from the body's surface. The radiation can propagate in a vacuum and does not require a physical medium.

1.2.2 Solidification

Solidification is the transformation of matter from a liquid-state to a solid-state. In the liquid phase, the atoms are in permanent agitation and without a specific ordered structure. On the contrary, in the solid phase, the atoms are "at rest" - or at least very slightly agitated - and above all are organised in an ordered crystalline structure (compact hexagonal, face-centred cubic...). This rearrangement of the matter is accompanied by the release of heat, known as latent heat of fusion, which compensates for the heat lost by cooling. Thus, for a pure metal under thermodynamic equilibrium, the phase transformation takes place at a constant temperature. In the case of a multicomponent alloy, the temperature generally drops during solidification.

Solidification begins with the appearance of a solid germ in the liquid. This solid germ can be created spontaneously (homogeneous nucleation) or from impurities in the liquid or by contact with a substrate (heterogeneous nucleation). Once nucleated, the solid structure develops in a particular form called dendrite. It can be columnar (Figure 1.3a) or equiaxed (Figure 1.3b). The evolution of the solid germ into an equiaxed or a columnar dendrite depends on the local temperature gradient. For columnar dendrite, the temperature gradient has a locally preferred direction, whereas for equiaxed dendrite the gradient is negligible. The growth of these structures during solidification gives rise to a zone where solid and liquid phases coexist. This is called the mushy zone. The size of this zone depends on the alloy, the process and the cooling conditions and can be several metres long, especially in continuous casting of steels. The dendritic microstructure is characterised by the primary, λ_1, and secondary, λ_2, interdendritic spacing.

Solidification is a crucial step in steel production. It is one of the factors that determine the future properties of the material. Defects occurring during this stage affect the quality of the solidified metal. These defects are only reversible to a certain extent through mechanical deformation and heat treatment. For this reason, it is important to better understand solidification in order to avoid the defects produced during this stage and to achieve the expected properties.

On an industrial level, three main processes are used to solidify liquid steel: continuous casting, ingot casting and foundry casting.

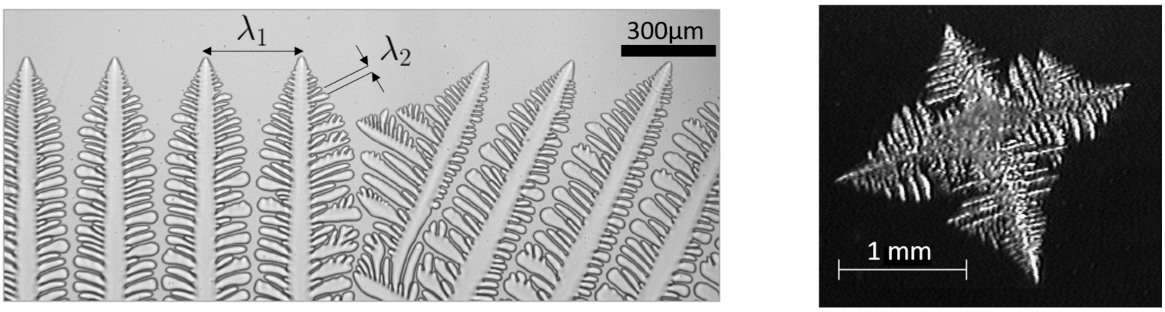

(a)

(b)

Figure 1.3: (a) In situ observation of columnar microstructures for transparent alloy of succinonitrile–acetone (SCN–2wt% Ace) [4]. (b) A typical image of a settling equiaxed dendrite [5]

1.2.3 Chemical segregation

Segregation is the non-uniform distribution of chemical species within a material. When it takes place at a microscopic scale (usually 10^{-6}m-10^{-4}m), it is called microsegregation. When segregation takes place on a macroscopic scale (usually 10^{-4}m-1m), it is called macrosegregation. Micro-segregation results from the redistribution of chemical species between the solid and the liquid phases. The formation of this heterogeneity is related to solubility. It often happens that the chemical solute species are difficult to incorporate into one of the two phases (the solid phase in general). Thus, during solidification, the solid "rejects" solute in front of the solidification front, resulting in an increase in concentration of the liquid phase. This difference extends to the macroscopic scale due to mass transfer caused by the relative movements of the phases in relation to the others.

It is easy to understand that segregation, as an intrinsic phenomenon of the solidification of alloys, is a source of heterogeneities in composition. It leads to non-homogeneous properties of the product, which can be disastrous for its lifetime or for its further processing. Usually, segregation cannot be corrected due to low diffusion in the solid metal. Limiting segregation as soon as it occurs would save time and money for the steel industry. The study of segregation is, therefore, of major interest.

1.2.4 Fluid flow

Convective fluid flow is an important factor in the solidification of alloys as it contributes to macrosegregation by impacting heat transfer and distribution of species. In the context of containerless solidification during Electromagnetic Levitation (EML), the convective flow in the liquid phase can be driven by solidification shrinkage, residual gravitational force, electromagnetic stirring, capillary forces at the liquid metal/gas interface (surface tension and Marangoni).

1.2.4.1 Solidification shrinkage

The transition from the liquid to the solid-state involves rearrangement of matter. This rearrangement leads to a variation in density, independently of thermal contraction. In steels, this volume change induces a convective motion of the liquid towards the denser solid phases to compensate for the volume difference. As solidification is at the origin of this volume difference, we talk about solidification shrinkage.

1.2.4.2 Microgravity

The effect of gravity on an object can be completely cancelled out when it is in a "free fall". This state is called weightlessness. The term "microgravity" refers to a condition in which weightlessness is not entirely achieved due to small residual forces. Microgravity is expressed as a fraction of g, where g is the gravitational acceleration at the Earth's surface, equal to 9.81 m.s^{-2}.

Practically speaking, the best way to achieve microgravity is to place an object in orbit, such as the ISS. This is because orbiting objects are theoretically subject only to the gravitational force, allowing them to experience a constant free fall.

Simulations of Saad [6] showed that microgravity can significantly drive the flow of the liquid in the absence of capillary forces.

1.2.4.3 Electromagnetic stirring

The particularity of the solidification experiments conducted in the context of these projects is the use of an electromagnetic levitator. This levitation device is used both to melt the metal by Joule effect and to maintain a stable position of the droplet by Lorentz force which counterbalances the external forces to which the droplet is subjected. Furthermore, the electromagnetic field used causes forced convection within the liquid with a velocity of up to 0.5 m.s^{-1} under terrestrial (1g) conditions [7]. In microgravity, the electromagnetic field needed is 1000 times less intense than on Earth. However, forced convection by the electromagnetic field is not completely eliminated. Magneto-HydroDynamic (MHD) simulations carried out by Hyers [8] estimate a fluid flow speed of around 0.05 m.s^{-1}.

1.2.4.4 Surface tension

In two-fluid flows, the interface is defined as the transition zone, which separates two fluids of different properties. The thickness of this zone is of the order of a few diameters of the molecule. A molecule of the bulk is surrounded by molecules of the same type in all directions, and therefore the net inter-molecular force is zero. A molecule at the interface has not the same neighbouring molecules in all sides of it. It is consequently attracted more strongly in one side than the other. The net inter-molecular force of the molecules at the interface is not zero. This implies that they have higher free energy than bulk molecules. The natural tendency of the system to reach the minimal free energy gives rise to the concept of surface tension. Surface tension is then that force per unit length which makes a fluid minimise the area of its interface with the other fluid. The surface tension is an important physical parameter that dominates deformable surfaces in many industrial processes in metallurgy like casting, welding and quenching. For liquid metals, surface tension is very high. For instance, for a pure liquid iron, it reaches 1.87 N.m^{-1} [9], i.e. more than 20 times surface tension of liquid water which is about 0.075 N.m^{-1}.

1.2.4.5 Marangoni effect

The surface tension can vary depending on the temperature and/or the composition of the fluid. When a temperature or concentration gradient exists at the interface, this creates a gradient in surface tension. This causes the fluid to move along the interface from areas of low surface tension to areas of high surface tension. This movement of the liquid is known as Marangoni convection. Marangoni convection can play an important role in heat and mass transport and can contribute considerably to segregation during the solidification process by altering the distribution of species.

1.3 Previous contributions

The contribution of CEMEF in the NEQUISOL project was initiated by the PhD work of Salem Mosbah [10]. In his work, a 2D axisymmetric Cellular Automata Finite Element (CAFE) numerical model was proposed for the prediction of the segregation maps and the influence of non-equilibrium solidification for samples with spontaneous and triggered nucleation. The numerical model is based on coupling between the Finite Element (FE) method and Cellular Automata (CA) method. The FE is used to solve the diffusive transport of energy and solute mass using the method of volume averaging. The CA is used for modelling the grains structures accounting for the primary and the secondary dendrite arm spacing together with nucleation and growth undercooling via the coupling with a microsegregation model. The CAFE model was applied for simulation of solidification experiments of Al-Cu droplets processed by the EML technique in terrestrial conditions [11]. Although the model allows coherent explanation of the measured temperature profiles, it presents some limitations such as the absence of the convective transport of heat and mass.

As for the contribution of CEMEF in the first phase of the CCEMLCC project, modelling was initiated by the PhD work of Benjamin Rivaux [12]. His work was based on a Lagrangian approach to consider both the steel sample and the ceramic chill using separate meshes for each domain. The conservation equations of energy, mass of chemical species, momentum and total mass were solved in the steel domain. In contrast, energy conservation was the only equation solved in the chill domain. The thermal contact between the chill and the droplet was taken into account by a Fourier boundary condition using a transfer coefficient calibrated on the experiments. The conservation equations for the steel domain were solved by coupling two calculation platforms: CimLib® for Navier-Stokes, energy and chemical species equations and TherCast® for solid mechanics equations. Shrinkage was considered as part of solid mechanics where an average density is tabulated with temperature. The interface between the solid and liquid phases of the metallic domain was implicitly represented by the volume average theory. The ALE (Arbitrary Lagrangian-Eulerian) method was used to update the position of the deformable surface of the droplet. However, the comparison (figure 1.4) with the experiments carried out on the sounding rocket (TEXUS) shows that the simulation does not make it possible to predict the deformed shape of the steel sample. In the simulation, the orientation of the gravity vector was arbitrarily set from the droplet to the chill with a magnitude of 10^{-7} m.s^{-2}.

In the second phase of the CCEMLCC project, modelling was improved by the PhD work of

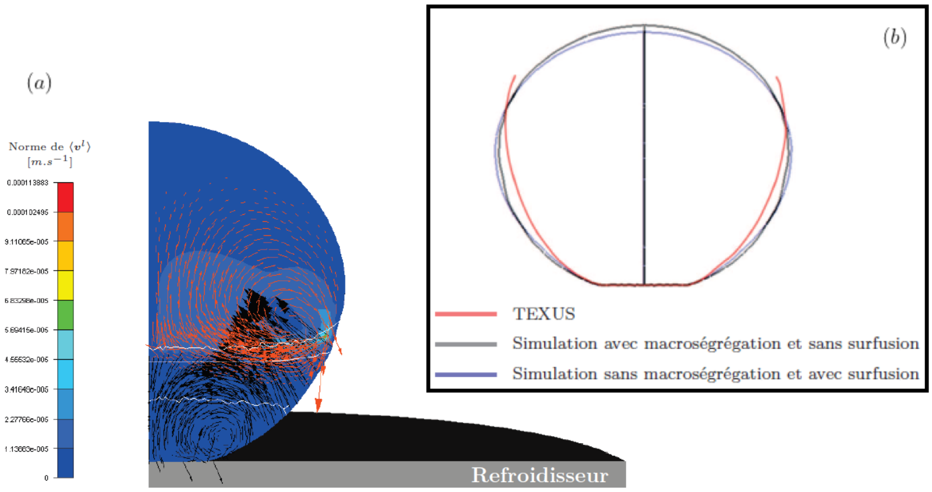

Figure 1.4: (a) Numerical simulation showing the velocity field of the solid phase (black arrows) and the liquid phase (orange arrows) at t = 1.5 s during the solidification of a 3.3mm radius steel droplet. (b) Droplet shape predicted by numerical simulation with macrosegregation (grey) and without macrosegregation (blue) in comparison with TEXUS experimental profile (red) at t = 4.5 s [12]. The top of the experimental shape was not visible in the experiment.

Ali Saad [6]. In his work, he adopted an Eulerian approach. A single mesh was considered for both metal and surrounding gas. The chill was not included in the computational domain, but the thermal contact between the sample and the chill was implicitly taken into account via a Fourier boundary condition. The volume average method was retained to represent the solid-liquid interface within the metal. The energy solver was improved by achieving full coupling with thermodynamic tabulations for multicomponent alloys. The Level-Set method was used to track the droplet interface with the surrounding gas. A monolithic formulation of the conservation equations for energy, chemical species, momentum and total mass allowed the resolution of a single system of equations for the entire computational domain. The solid metal was assumed to be rigid and fixed. A condition of liquid compressibility was introduced into the Navier-Stokes equations to represent solidification shrinkage. Gravity was directed from the chill to the droplet. A parametric study of the amplitude of the residual gravity and the heat transfer coefficient at the contact surface between the sample and the substrate was carried out to find optimal values that approximate the experimental shape of the droplet (figure 1.5). Simulations showed that the droplet could be deformed by the liquid flow caused by residual gravity of the order of 10^{-5} m.s^{-2}.

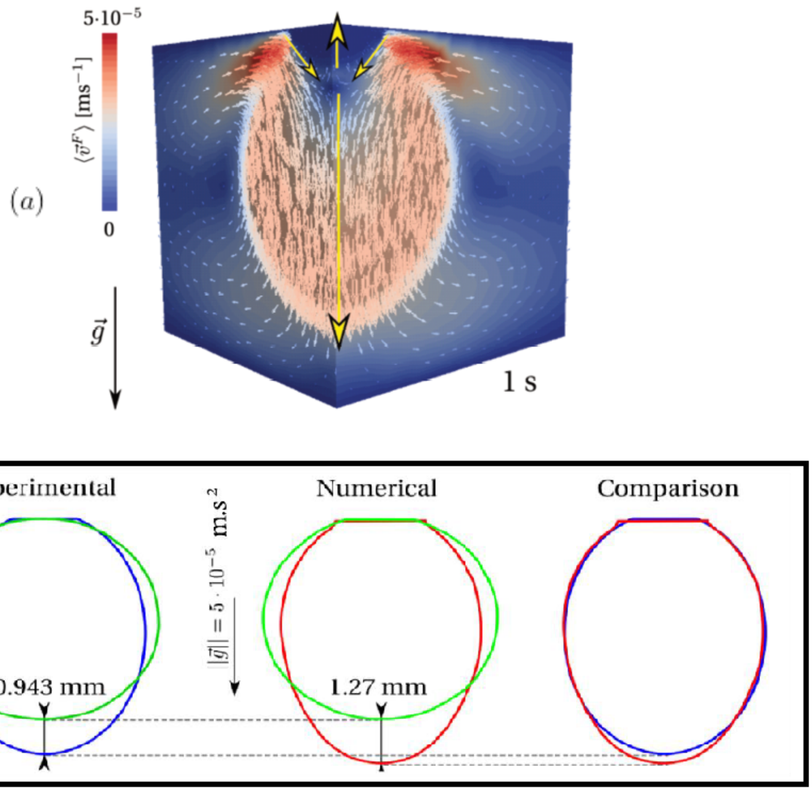

Figure 1.5: (a) Numerical simulation of the fluid flow in the liquid metal and the surrounding gas during solidification of a steel droplet. (b) Comparison of experimental (blue) and numerical (red) final droplet profiles, compared to its initial shape (green) [6]

1.4 Objectives and outline

Despite the variety of applications made possible by the the previous contributions, there are nevertheless some limitations to their model. The main limitation is the lack of a model for surface tension, which is a very important physical phenomenon given the very high value of the surface tension coefficient for liquid metals. In order to show the relevance of surface tension in comparison to other phenomena that influence the fluid flow, we present in the following table the main dimensionless numbers that express the ratios of forces involving surface tension. The values are calculated for an iron droplet with radius $R_0 = 3$ mm, dynamic viscosity $\mu = 10^{-3}$ Pa.s, density $\rho = 7000$ kg.m^{-3}, thermal diffusivity $\alpha = 8.6 \times 10^{-6}$ m.s^{-2} and surface tension $\gamma = 1.46$ N.m^{-1}, placed in a residual gravity of $g = 10^{-5}$ m.s^{-2} with a characteristic velocity of $u_0 = 0.05$ m.s^{-1}.

Table 1.1: Some dimensionless numbers involving surface tension

Dimensionless number	**Symbol**	**Formula**	**Forces ratio**	**Value**
Goucher	Go	$R_0\left(\frac{\rho g}{2\gamma}\right)^{0.5}$	$\left(\frac{\text{Gravity force}}{\text{Surface tension}}\right)^{0.5}$	$4.64 \times 10^{-4} \ll 1$
Ohnesorge	Oh	$\frac{\mu}{\sqrt{\rho\gamma R_0}}$	$\frac{\text{viscous forces}}{\sqrt{\text{Inertia . Surface tension}}}$	$1.81 \times 10^{-4} \ll 1$
Weber	Go	$\frac{\rho u_0^2 R_0}{\gamma}$	$\frac{\text{Inertia}}{\text{Surface tension}}$	$3.60 \times 10^{-2} \ll 1$
Marangoni	Ma	$\frac{\partial\gamma}{\partial T}\cdot\frac{R_0\Delta T}{\mu\alpha}$	$\frac{\text{Marangoni convection}}{\text{Heat diffusion}}$	$1.90 \times 10^{5} \gg 1$

As can be seen from the values of dimensionless numbers, surface tension is a force that predominates over inertia, viscous forces and gravity. Therefore, it is a parameter that cannot be excluded from the study of the solidification of a levitated metal droplet. In addition to the surface tension, the Marangoni force caused by the temperature gradient is an important factor for this study as expressed by the Marangoni number calculated for a coefficient $\frac{\partial \gamma}{\partial T} = 5.44 \times 10^{-4}$ N.m^{-1}.K^{-1} and a temperature gradient of $\Delta T = 1000$ K.

Taking capillary effects into account may clearly impact on the results of the numerical simulations performed in the PhD theses described earlier. The first objective of this PhD thesis is, therefore, to enrich the previous simulations by modelling of the capillary forces (surface tension and Marangoni) that govern the dynamics of the droplet free surface. Implementation of surface tension has been initiated within CEMEF by Khalloufi [13] for water bubbles in the quenching process and Chen [14] for ceramics in additive manufacturing. However, there are several numerical difficulties related to surface tension, which are more pronounced and critical for high surface tension values, in particular calculation stability, mass loss and spurious currents. In this work, we propose some improvements in the modelling of surface tension in the context of the Level-Set method. These improvements deal with the numerical problems of mass loss, parasitic currents, stability and accuracy of the calculation. To evaluate the new contributions related to surface tension, we propose an analytical solution in both 2D and 3D of a benchmark based on the oscillating drop method used in ESA projects to measure surface tension and viscosity of the studied alloys. Note that this objective oriented towards the improvement of Fluid Mechanics modelling, brings a new contribution for both CCEMLCC and NEQUISOL projects.

After the Fluid Mechanics aspect addressed in the first objective of the thesis, the second objective consists in improving the modelling of heat transfer in the presence of solidification. As previously mentioned, the NEQUISOL project focuses on the investigation of microstructure development in non-equilibrium solidification of Al-based alloys. Solidification is triggered spontaneously from an undercooling state which allows several modes of solidification, a wide range of metastable microstructures and structurally different phases [15]. The CCEMLCC project focuses on the study of surface defects formed during continuous casting of steels. The two solidification conditions are different. Therefore, in the context of the CCEMLCC project, the volume averaging method in FE framework is adequate to predict the formation of surface defects at the macroscopic scale. As for the NEQUISOL project, a CAFE model is required to account for the grains structures. In this PhD, we confine our attention in solidification during chill cooling investigated in the CCEMLCC project.

In the previous contributions of the CCEMLCC project, the condition of thermal contact between the droplet and the chill was approximated by a Fourier condition. This approximation assumes that the temperature of the chill away from the contact surface is constant. This is equivalent to considering the chill as an infinite heat source whose temperature does not vary. However, the ceramic plate in contact with the sample has a finite volume and is heated by contact with the molten metal and its thermal radiation. Therefore, we propose to incorporate the chill in the calculation domain using the level-set method. Attention will be focused on the heat exchange between two bodies in contact. For this purpose, a contact thermal resistance model will be proposed and validated by analytical test cases and then applied to the chill cooling and solidification of the droplet. Thermal radiation will not be the subject of this work. However, this numerical framework will be suitable for possible consideration of the radiative exchanges studied within CEMEF by other work in progress.

The final objective will, therefore, be to couple these new models with previous contributions, in particular those of Saad [6], in order to propose a simulation of a steel droplet solidification experiment in microgravity. The comparisons will be based on the experiment recently carried out on board the ISS. Before coming to this point, we first present in the next chapter the state of the art of the solidification experiments performed in the framework of the CCEMLCC project, with particular attention to the most recent of the experiments and the first one performed on board the ISS.

Therefore, after the present introduction of the PhD thesis, the manuscript will be structured as follows:

- **Chapter 2** entitled "*Chill cooling experiments in microgravity*" is dedicated to the experimental results of the CCEMLCC project.
- **Chapter 3** entitled "*Numerical modelling of multiphase flows including surface tension*" is devoted to surface tension implementation and validation via the oscillating drop method.
- **Chapter 4** entitled "*Numerical modelling of heat transfer with solidification and thermal contact resistance*" suggests a model for thermal contact resistance in the context of diffusive interfaces with level-set method
- **Chapter 5** entitled "*Numerical simulation of chill cooling and solidification of a levitated steel sample in microgravity*" is dedicated to modelling and simulation of the coupling of fluid mechanics including surface tension and Marangoni with heat transfer, solidification and chemical segregation.
- **Chapter 6** for general conclusions and perspectives

Chapter 2

Chill cooling experiments in microgravity

Résumé

Dans ce chapitre, nous nous penchons sur les expériences réalisées dans le cadre du projet CCEMLCC. Nous présentons le dispositif expérimental et les échantillons métalliques étudiés. Puis nous présentons les résultats des expériences de solidification avec différentes plateformes d'expérimentation en condition de microgravité: vols paraboliques, fusées sondes et Station Spatiale Internationale (ISS). Une attention particulière sera accordée à la première expérience de ce projet réalisée avec succès à bord de l'ISS. L'objectif est de tirer profit de ces expériences pour extraire des données qui serviront de référence pour l'évaluation de notre outil de simulation numérique.

Contents

2.1 Introduction . . . 18
2.1.1 The experimental set-up . . . 18
2.1.2 Steel samples processed . . . 19
2.2 Microgravity experiments: from precursor tests to experiment on board the International Space Station . . . 20
2.2.1 Parabolic flights experiments . . . 20
2.2.2 Sounding rocket experiments . . . 25
2.2.3 International Space Station experiment . . . 27
2.3 Conclusion . . . 35

2.1 Introduction

The main objective of the CCEMLCC project is to enhance our understanding of solidification of steel products, in particular, the defects formed during casting processes of steels [1]. For this purpose, the solidification of an initially freely suspended steel droplet in microgravity conditions is investigated. The mould, in a real continuous casting process, is modelled by the use of a ceramic chill plate which extracts the heat from the sample and thus triggers nucleation. The motivation for conducting experiments in microgravity is to reduce the effects of gravity-related sources of mass and heat transfers and to determine how gravity-independent phenomena can influence the solidification process of steels. The ISS provides a platform for such research projects to carry out experiments in ideal microgravity conditions. Despite the increasing number of scientific research projects investigating microgravity conditions, the opportunities to send the experiments into a spaceflight to the ISS are limited. Relatively few projects in material science have benefited from a flight ticket to the ISS.

Two complementary approaches are used in the CCEMLCC project: experiments and numerical modelling. It is well known that numerical simulations provide a rich insight into what happens in the experiments, and thus help to interpret the experimental results. With reliable numerical models, numerical simulations allow exploring other situations not investigated by the experiments. But before reaching this point of exploration, the numerical models must be validated. Experimental data serve as a benchmark for numerical simulation to compare and validate.

The project being currently in its third phase, several campaigns of experiments have been performed since 2007. In this chapter, we present the experiments and their findings with a focus on the first successful experiment of this project recently performed on board the ISS. The objective is to take advantage of these experiments to extract data that will serve as a reference for the evaluation of our numerical modelling.

2.1.1 The experimental set-up

The main idea of the experiments is to contact a levitated molten steel sample with a ceramic Si_3N_4 chill plate which extracts heat from the sample and thus triggers solidification. The sample is heated and positioned using an electromagnetic system consisting of two coils. One coil is used for heating, the so-called heater coil. The second coil, called the positioner, is designed to use Lorentz forces to counterbalance the external forces applied to the sample and hold it in a stable position. A cage, called the sample holder, surrounds the droplet to force it to stay within a certain area. A high-speed camera records the experiments from the side of the sample and monitors the solidification of the droplet. Through a tiny hole in the plate, an axial pyrometer measures the temperature of the metal at the contact interface with the chill plate (see Figure 2.1).

The experimental setup was designed by a team at the Institute for Materials Physics in Space in the German Aerospace Centre, Cologne. It was first tested on Earth, where the electromagnetic field required to levitate the drop against gravity is so large that it generates strong convection in the bulk liquid and thus adds more complexity to the process. Under microgravity conditions, the electromagnetic stirring vanishes because the intensity of the electromagnetic field is 1000 times lower [9]. The experimental device was then tested and validated in microgravity conditions by parabolic flights and sounding rockets before being sent to a long-time microgravity environment on the ISS.

In an ideal experiment cycle, the metallic droplet is heated and maintained in a stable floating position. After the temperature of the metal is well above the liquidus temperature, the heater is turned off. The sample holder moves towards the droplet so that the chill plate attached to the holder touches it. As the sample is still liquid, a flat contact interface is formed, allowing heat exchange between the metal and the chill plate. Chill cooling and complete solidification must ideally occur during microgravity. Note that these ideal experimental conditions are not easily respected when short-duration facilities are used (parabolic flight, sounding rocket). Several experimental cycles failed either because the chill-cooling had started before the heater was turned off, or because the microgravity period had ended before a complete solidification was achieved, or because other incidents like the sample stuck on the cage before chill cooling.

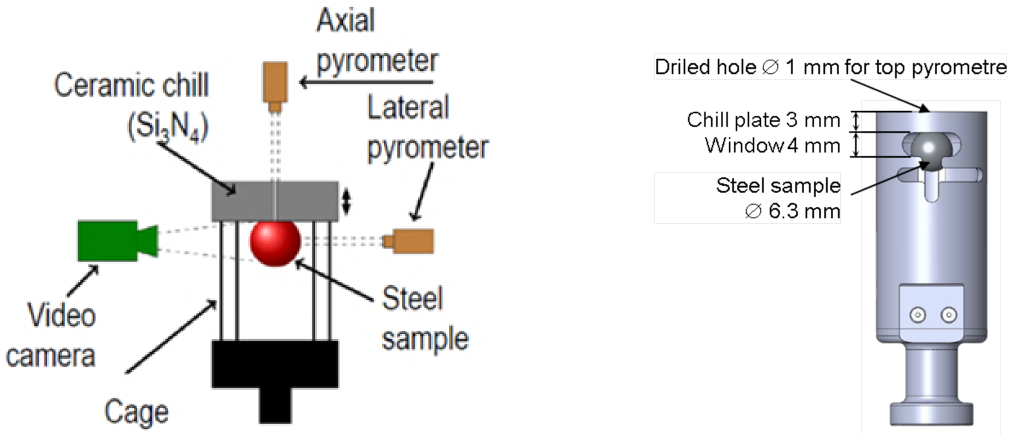

(a) (b)

Figure 2.1: (a) Schematics of the experimental set-up used in a TEXUS sounding rocket where a cage was used to limit the sample displacement. (b) Schematics of the cup holder used for chill cooling of EML samples on board the ISS [16].

2.1.2 Steel samples processed

In the CCEMLCC project, a variety of steel alloys are processed in microgravity using the EML facility. The choice of the steel alloys compositions was motivated by the applications of the industrial partners joining the project. The list of steel samples and their compositions are given in the following table 2.1. Note that, in this work, all the compositions are given in wt.%.

The steel alloys can be divided into 3 categories:

- Fe-C-Si steels (*a1* , *b1* and *d1*) which contain the same chemical elements but different concentrations in Carbon including austenitic steels *b1* and *d1* , and a ferritic steel *a1* . Theses samples were provided by ArcelorMittal.

- Fe-Cr-Ni steel which is a tool steel of type D2. It was provided by INDUSTEEL.

Table 2.1: Composition in wt.% of the steel samples investigated in the CCEMLCC project

Sample No.	Composition in wt.%					
	C	Si	S	Al	Mn	P
a1	0.05	0.26	0.009	0.002	0.6	0.018
b1	0.105	0.26	0.009	0.006	0.6	0.018
d1	0.9	0.26	0.009	0.11	0.54	0.011

Group 1: Fe-C-Si steels

Sample No.	Composition in wt.%					
	Cr	Ni	Mo	N	Cu	Si
D2	19.70	17.92	6.246	0.204	0.685	0.203

Group 2: Fe-Cr-Ni steels

Sample No.	Composition in wt.%							
	C	B	Si	Cr	Cu	Al	Ti	Mn
Steel A	0.0067	0.0003	0.0267	0.0191	0.0114	0.093	0.0439	0.0994
Steel B	0.0076	0.0007	0.027	0.0186	0.016	0.073	0.044	0.0986
Steel C	0.0076	0.0037	0.0331	0.0187	0.016	0.07	0.047	0.0973

Group 3: Fe-C-B steels

- Fe-C-B steels (A, B and C) which contain a small quantity of Boron (< ppm B) with a Carbon concentration lower than 0.01 wt.%. They were also provided by ArcelorMittal.

Each of these samples was subjected to precursor chill cooling tests mostly during parabolic flights with one test in a sounding rocket trip for *b1* sample. However, only *a1* and *d1* samples have been processed in the ISS so far, but processing of *a1* failed as the sample stuck on the holder and the activation of the high speed camera did not work. Therefore, our attention is confined only in the Fe-C-Si category. It should be noted here that all microgravity tests are performed by the DLR partner.

2.2 Microgravity experiments: from precursor tests to experiment on board the International Space Station

Three microgravity facilities are provided by ESA to perform experiments: parabolic flights, sounding rockets and the ISS. Before sending the experiment to the ISS, precursor tests must be performed in parabolic flights or sounding rockets to validate the experimental instruments and the processing of the samples. In the following, we give an overview of the chill cooling experiments performed in each of these microgravity facilities. As it was stated previously, only the experiments concerning the Fe-C-Si alloys are shown.

2.2.1 Parabolic flights experiments

During a parabolic flight, a dedicated Airbus aircraft, called Zero-G, executes a series of around 30 parabolas. Around the apogee of each parabola, the aircraft and its contents experience a sensation of weightlessness period (10^{-2} g) that lasts about 25 seconds [17]. Despite the short duration of microgravity periods offered by parabolic flights, they are often used to prepare and validate the experimental setups before sending them on a sounding rocket trip or further to the ISS. The reasons why parabolic flights are useful for precursor research in preparation for long-duration missions are their relatively low cost and the short waiting time between submission of a proposal and flight execution. Besides, in a parabolic flight, researchers can join the trip to follow and control the experiments as they float. TEMPUS is the name given to the parabolic flight mission for the containerless solidification using the EML device.

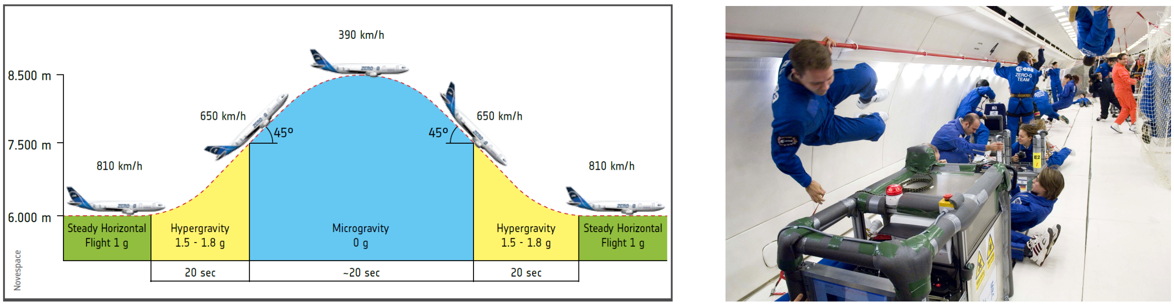

(a)

(b)

Figure 2.2: (a) A parabolic flight profile [18]. (b) View inside the Zero-G Airbus aircraft during the 46^{th} ESA flight campaign [19].

Several TEMPUS parabolic flights campaigns have been conducted. Each campaign lasts 4 days. During each day, about 30 parabolas, named cycles, were performed. Some of these cycles were dedicated to chill cooling experiments. The most recurrent problem is the fact that the droplet stuck on the sample holder during melting. In the following table, we give only the references to some experiments that could be considered successful.

Table 2.2: The references of TEMPUS successful experiments

	Sample	TEMPUS experiment		
No.	Composition [wt.%]	Campaign	Day	Parabola
a1	Fe-0.05C-0.26Si	September 2017	4	7
b1	Fe-0.105C-0.26Si	September 2016	1	14
d1	Fe-0.9C-0.26Si	October 2014	1	14

A temperature-time profile together with the heater control voltage and microgravity level of a chill-cooling experiment on Fe-0.9C-0.2Si is shown in figure 2.3. Just before microgravity starts, the sample was preheated to a temperature around 1000^{o}C. Once the microgravity started, the sample was quickly heated and melted until it reached a temperature of 1650^{o}C, well above the liquidus temperature $T_L = 1461^{o}$C of Fe-0.9C-0.2Si. The heater is then turned off. The contact with the chill plate occurred a few seconds later. The steep drop in temperature profile reveals the time of contact. Chill cooling started and solidification was triggered. The time evolution of the front position as well as the sample shape are monitored by a side camera. As displayed in figure 2.4, only a part of the sample is visible. The invisible part was hidden by the sample holder. The final and the whole sample after complete solidification can yet be monitored as reveales by Figure 2.5. It worth noting that the microgravity period in the parabolic flight ended about 4 s before the solidification process was completed (see Figure 2.3).

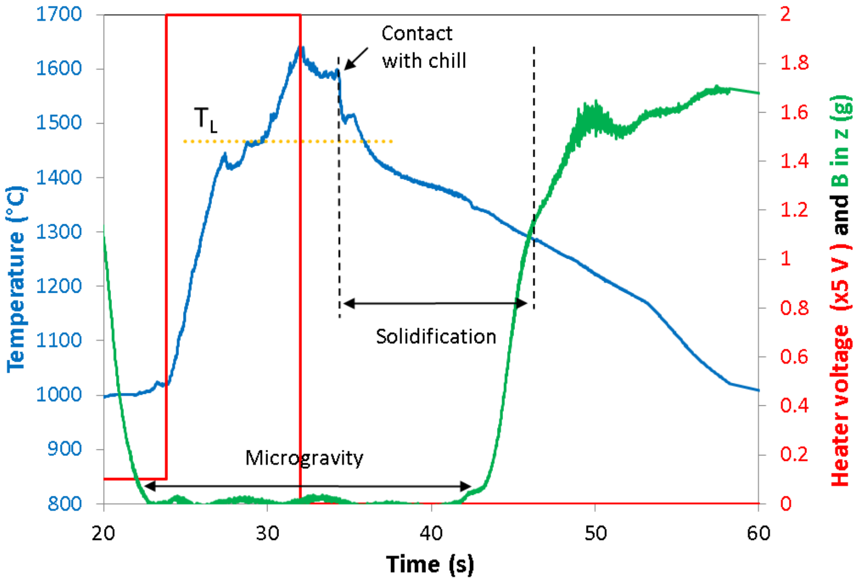

Figure 2.3: Time evolutions for a Fe-0.9C-0.2Si sample during a chill cooling cycle in TEMPUS parabolic flight: (blue) temperature, (red) heater control voltage and (green) microgravity level. The time interval between contact with the chill plate and completion of solidification is marked by the vertical dashed lines.

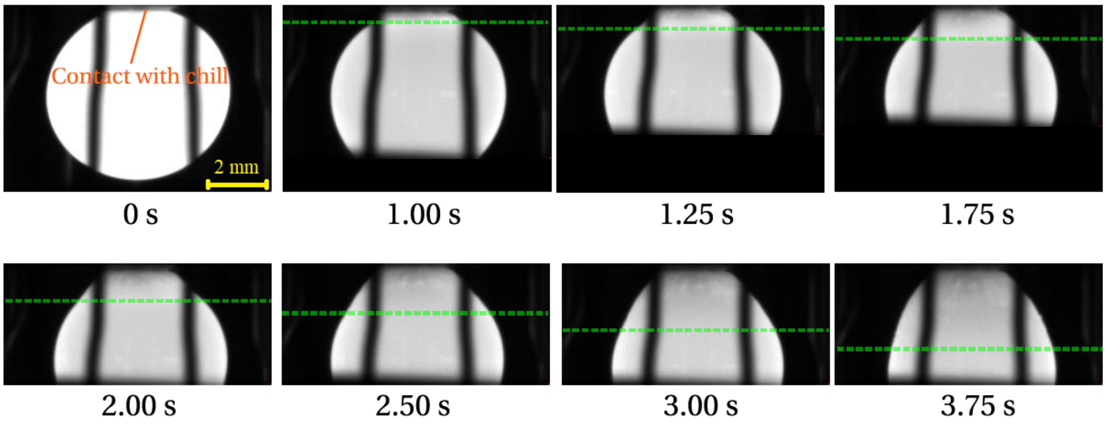

Figure 2.4: Image sequence given by a high-speed camera showing the solidification progress between 0 s (when contact with the chill is initiated) to 3.75 s in a Fe-0.9C-0.2Si steel droplet. The progress of the solidification front is marked by the green dashed line. In some frames, the droplet is partially hidden by the narrow opening of the sample holder facing the camera [6].

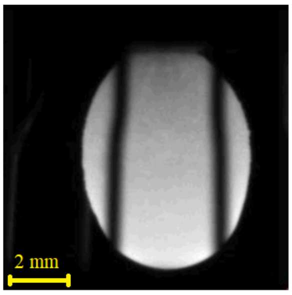

Figure 2.5: The final shape of the solidified sample [6].

For the chill-cooling experiment on Fe-0.1C-0.2Si, the time evolutions of the temperature, the heater control voltage and microgravity level are displayed in figure 2.6. The disturbances and spikes on the temperature curve are due to translation motions of the sample, which changes the pyrometer signal if the sample is not well-positioned in the centre of the levitation coil. Unstable positioning often occurs when starting the levitation process and cannot be damped during the short microgravity period of 20 s in most cases. At a temperature of about 50°C above the liquidus temperature T_L = 1493°C, the sample touched the chill plate and the cooling process sets in, revealed by the steep drop of temperature with an initial cooling rate of about 500 $K.s^{-1}$. We can observe that the contact with the chill plate occurred slightly before the heater is turned off. Solidification proceeds with a velocity of about 1 $mm.s^{-1}$ and deformation of the droplet is monitored by the radial video camera at rate of 500 fps enabling to analyse the evolution of the droplet shape during solidification as illustrated in Figure 2.7. Once again, the microgravity period in the parabolic flight ended before the completion of solidification process was achieved (see Figure 2.6).

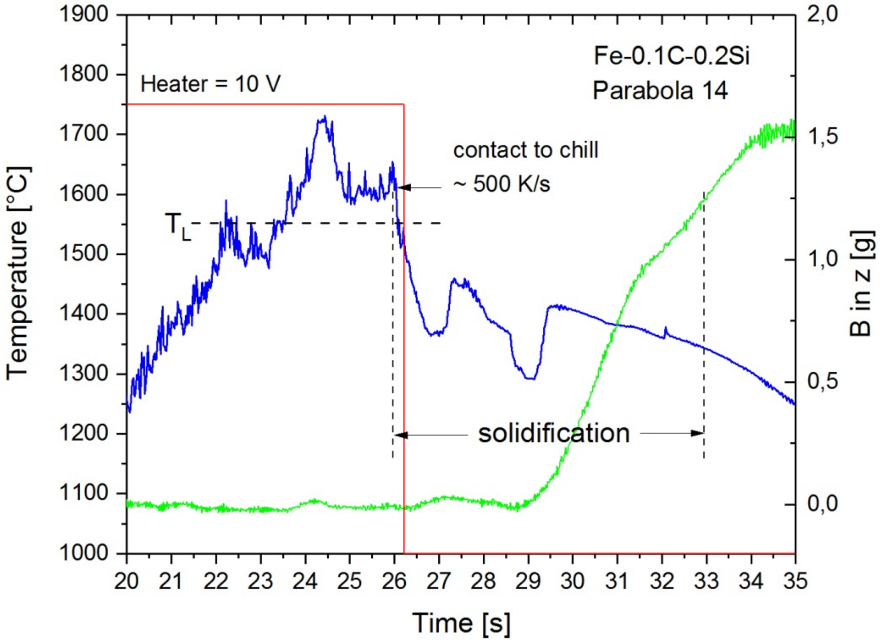

Figure 2.6: Time evolutions for a Fe-0.1C-0.2Si sample during a chill cooling cycle in TEMPUS parabolic flight: (blue) temperature, (red) heater control voltage and (green) microgravity level. The time interval between contact with the chill plate and completion of solidification is marked by the vertical dashed lines.

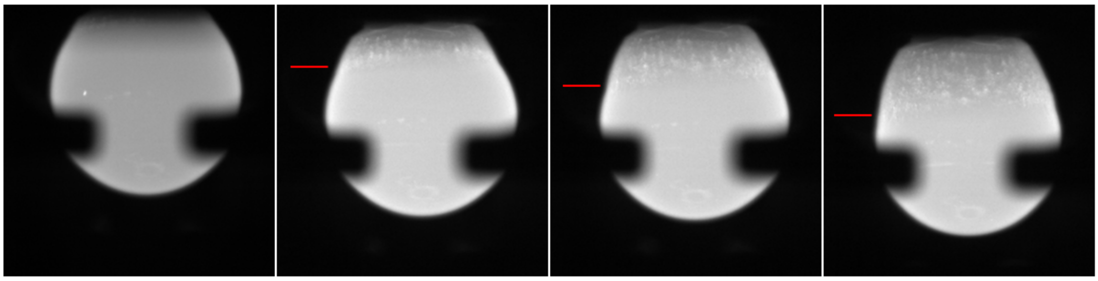

Figure 2.7: Sequence of video images for the Fe-0.1C-0.2Si experiment showing the sample shape time evolution (from left to right). The time increment between images is 0.5 s starting at the time of contact with the chill plate at 25.9 s. The chill plate (not visible) was located at the top and moved downwards. The red line marks the position of the growth front. From the video taken at 500 fps growth velocity is determined to approximately 1mm.s^{-1} [20].

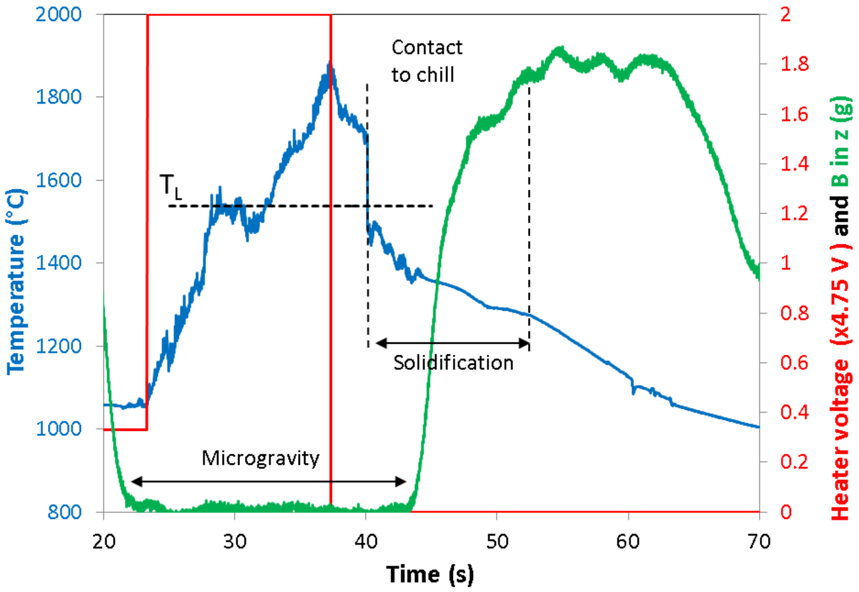

Figure 2.8: Time evolutions for a Fe-0.05C-0.2Si sample during a chill cooling cycle in TEMPUS parabolic flight: (blue) temperature, (red) heater control voltage and (green) microgravity level.

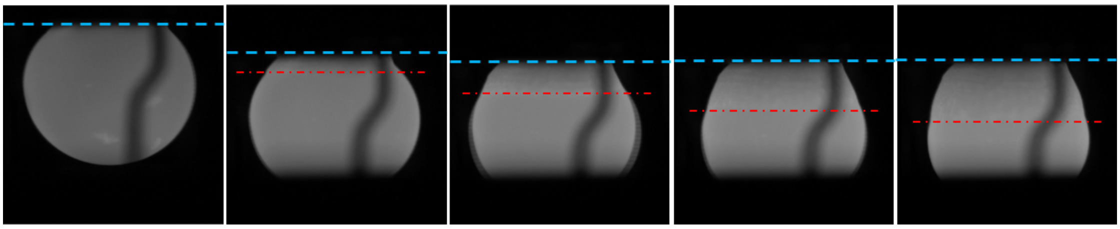

Figure 2.9: Sequence of video images for the Fe-0.05C-0.2Si experiment showing the sample shape time evolution (from left to right). The time increment between images is 0.5 s starting at the time of contact with the chill plate at 40.1 s. The chill plate moved downwards. The interface chill plate-metal is represented by the dashed blue line. The position of the growth front is marked by the red line. From the video taken at 500 fps growth velocity is determined to approximately 1mm.s^{-1}.

2.2.2 Sounding rocket experiments

A sounding rocket (also called research rocket) carries experimental instruments in a parabolic path, like a parabolic aircraft, but goes above the atmosphere of the Earth up to 750 km high. A sounding rocket is divided into two parts: a solid-fuel rocket motor and a payload. The typical trip profile of a sounding rocket trip, as shown in Figure 2.10a, starts from the launch of the rocket (see Figure 2.10b). The rocket motor consumes its fuel for propulsion then separates from the payload leaving it in a free-fall. After the separation, the payload continues upwards into space where the experiments begin. After reaching the apogee of the parabolic arc, the payload goes down, re-renters the atmosphere and returns gently back to Earth under a parachute. The payload is then retrieved. During these flights, researchers can monitor the experiments and even modify parameters as data from experiments are sent to control stations on the ground during the flights. The sounding rocket flight facility offers a higher-quality microgravity condition that lasts for a longer period than a parabolic flight. The residual gravity reaches around 10^{-5} g and lasts for about 13 minutes. TEXUS-46 is the name of the sounding rocket mission that carried the experimental setup for CCEMLCC project. Note that the rocket used in TEXUS-46 mission reaches a height of 250 km above the Earth. For the sake of simplicity, we refer to the experiments conducted in this mission as being the TEXUS experiments.

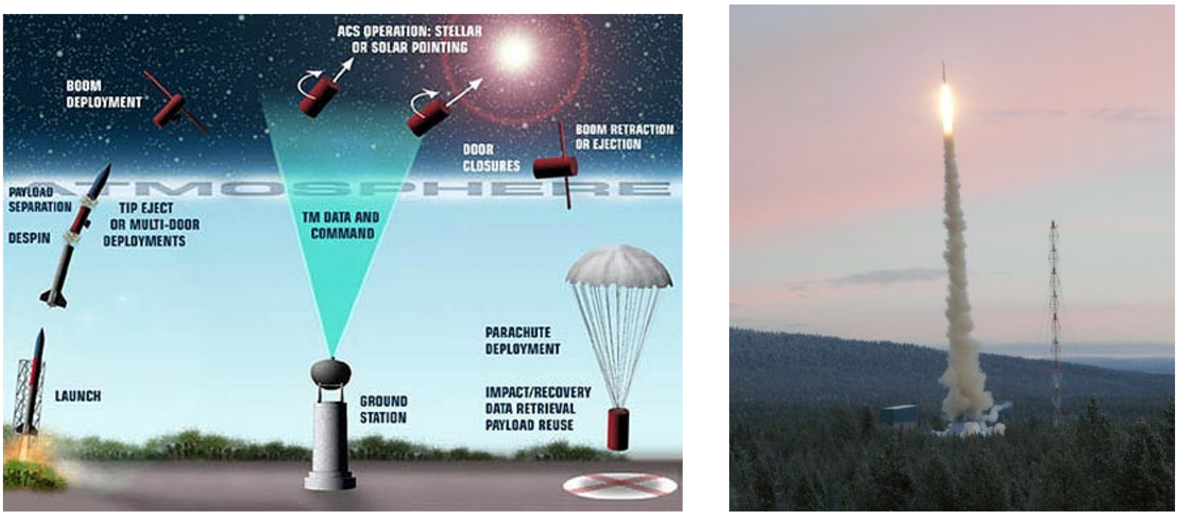

(a)

(b)

Figure 2.10: (a) A parabolic flight profile [21]. (b) Successful launch of TEXUS-42 sounding rocket [22].

The TEXUS experiment, carried out during the flight of a sounding rocket for alloy *b1* , allows five heating-cooling cycles to be performed during the 180 seconds of microgravity. Of these five cycles, the first three were reserved for another ESA project: the Thermolab project, aiming to measure surface tension and viscosity of the sample by the oscillating drop technique. These data are crucial for numerical simulation of the chill cooling experiments. The last two cycles were devoted to the CCEMLCC project. The time evolution of the temperature measured by the pyrometers during the experiment is shown in Figure 2.11. Four temperature rises and falls corresponding to the first four cycles are easily identifiable. At the beginning of the fifth cycle, the temperatures change unexpectedly. This is because the drop has stuck to the chill plate. Due to this malfunction, the lateral pyrometer no longer pointed to the drop: the temperature dropped. In addition, the chill was abnormally heated. The axial pyrometer pointed to the drop, and the chill was calibrated with the emissivity of the metal. Since the emissivity of the ceramic is greater than that of the steel, the measured temperature is much higher than the real temperature.

Of the last two cycles reserved for the CCEMLCC project, the fifth cycle is not usable, given the problem that has arisen. No analysis of the drop recovered at the end of the experiment was conducted. Therefore, the TEXUS experiment can only be exploited using the time-temperature curve shown in Figure 2.11 and the camera to follow the solidification of the drop during the 4$^{\text{th}}$. Images from this video are shown in Figure 2.12.

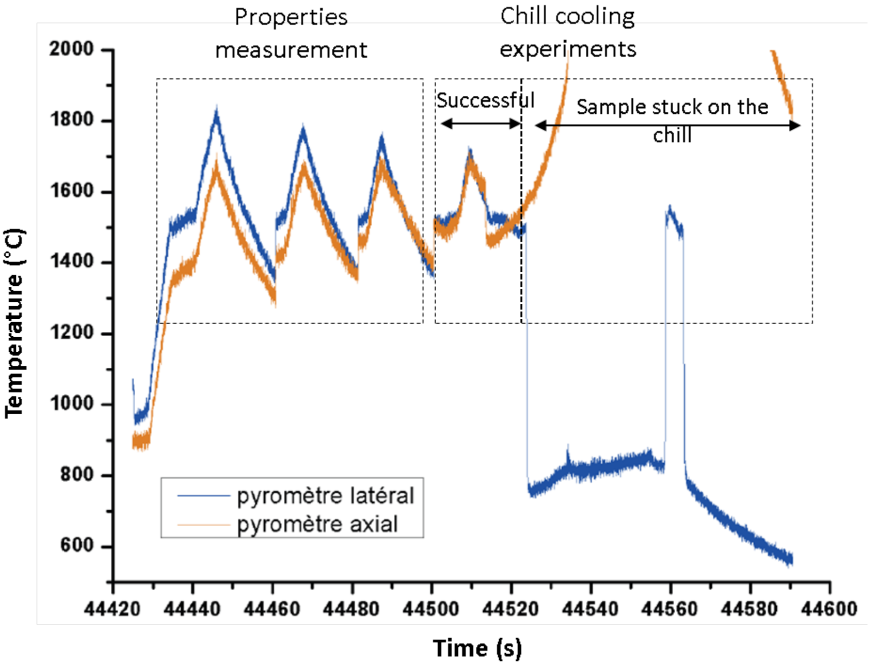

Figure 2.11: Time evolutions during 5 cycles of processing Fe-0.1C-0.2Si sample on board TEXUS-46 sounding rocket: (blue) temperature measured by the lateral pyrometer and (orange) temperature measured by the axial pyrometer [23].

The time-evolutions of the droplet shape as well as the solidification front, are shown in Figure 2.12. As observed in parabolic flights, the sample showed an elongation in the vertical direction that is also the direction of the thermal gradient.

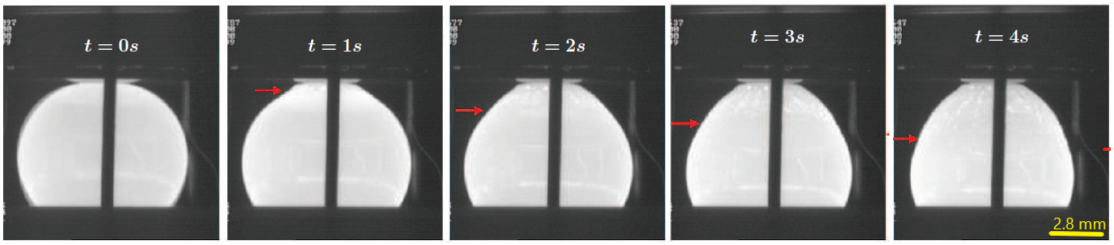

Figure 2.12: Sequence of video images for the Fe-0.9C-0.2Si TEXUS experiment showing the sample shape time evolution (from left to right). The time increment between images is 1 s starting at time of contact with the chill plate. The position of the growth front is marked by the red line [12]

2.2.3 International Space Station experiment

After preparation and validation of the experimental instruments onboard the parabolic flights or sounding rockets, the experimental setup is then sent to the ISS for a long microgravity mission in ESA's Columbus laboratory.

Figure 2.13: The International Space Station [24].

The first chill cooling experiments carried out in the ISS on Fe-C-Si samples were programmed during 2018 in batch #2.2. These experiments did not succeed because the droplet stuck to the sample holder. A second attempt was carried out at the beginning of 2019 during batch #2.3, which also failed due to a technical problem with the recording of the video sequence by the high-speed camera. It was not until April 2019 that the first chill cooling experiment on board the ISS was successful. This experiment, first of its kind, was performed on the austenitic steel *d1* (Fe-0.9C-0.26Si). The average diameter of the sample is $d_0 = 6$mm and its mass is $m = 0.89531$g. The experiment has been controlled and monitored by researchers from the control station at DLR in Cologne. Data concerning the temporal signals of the temperature measured by the pyrometer, the control voltage of the heating and positioning coils were also sent to the control station (Figure 2.14). The high-speed camera transmitted in real-time the video sequence of the process (Figure 2.15). However, at the time of writing this manuscript, the solidified sample has not yet landed and retrieved for micro-analysis of segregation. The analyses of the current experiment are then based on the results extracted from the video sequence and the measured temperature.

The long-duration microgravity environment on board the ISS is a unique opportunity to perform a complete solidification of the entire sample under ideal and controlled conditions without external forces. The experiment proceeded as follows: the sample was initially levitated in the solid-state at low temperatures. The sample started to exhibit some translational and rotational movements, revealed by disturbances on the temperature signal at the beginning of the heating phase. The sample movements were damped out by using the sample holder before further heating and melting. This stabilisation is revealed by a smooth time-evolution of the temperature profile. The phase transformation from solid to liquid started at the liquidus temperature $T_L = 1466\,^{\circ}$C. The energy provided by the heater is deployed to melt the structure of the solid. Liquid state is reached without increasing the temperature of the material. A temperature plateau expresses this isothermal phase transformation as shown in Figure 2.14. After that, the heating continued until reaching a maximal temperature of $T_{max} \approx 1800\,^{o}C$. The sample being completely liquid, the heater is turned off. The sample holder is moved downwards to achieve contact with the sample. The contact with the sample occurred at $T = 1648\,^{o}C$. It is revealed by a steep drop of temperature, expressing the start of chill cooling. During the first 2 seconds of chill cooling, the temperature profile shows a cooling rate around 200 $K.s^{-1}$, then it stabilises around 25 $K.s^{-1}$.

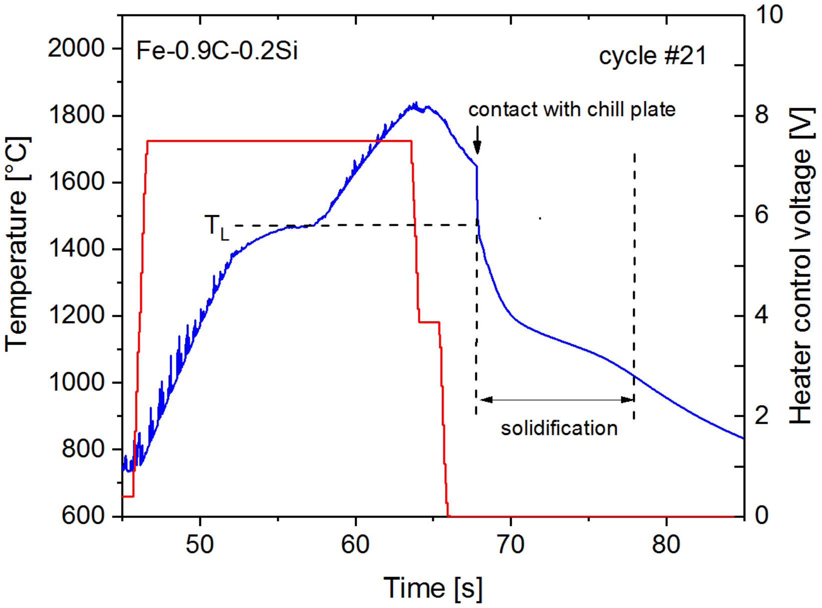

Figure 2.14: Temperature-time profile (blue) and heater control voltage (red) for Fe-0.9C-0.2Si during a chill cooling cycle in ISS-EML (batch #2.3). The time interval between contact with the chill plate and completion of solidification is marked by the vertical dashed lines.

Additional data can be extracted from the sequence of images (Figure 2.15) given by the video recorded by the camera. First, we can observe that the solidifying droplet shows an elongation in the direction of the temperature gradient (downward and perpendicular to the chill plate). The same behaviour was also observed during the parabolic flight (figure 2.5). We can observe that the chill plate (marked by the blue line in figure 2.15) did not stop moving exactly at the time of contact with the sample. It was moved downwards until 2 seconds after the contact. Therefore, the chill involves the droplet in a translational motion of a velocity correlated to the speed of the chill plate. In addition to this downward translation, the sample elongates in the same direction. This makes a part of the droplet go out of the camera's vision area as can be observed from images in the second and third rows of figure 2.15. Therefore, detection of the solidification front position (marked by the red lines) is limited to the visible area.

A while after the end of the test, the chill plate, on which the sample is sticking, was moved upwards to allow the entire solidified droplet to be in the camera's field of vision. The final shape of the droplet after complete solidification is shown in figure 2.16. The final height of the droplet measured from this image is $Z_{final} = 7.32mm$. The time evolution of the front position is reported in figure 2.17. In the latter figure, the red squares mark the position from the chill of the solidification front obtained from image analysis of the snapshots of figure 2.15 up to 8 seconds. The time evolution of the front growth is almost linear with an average speed of $V_{front} = 0.897mm.s^{-1}$

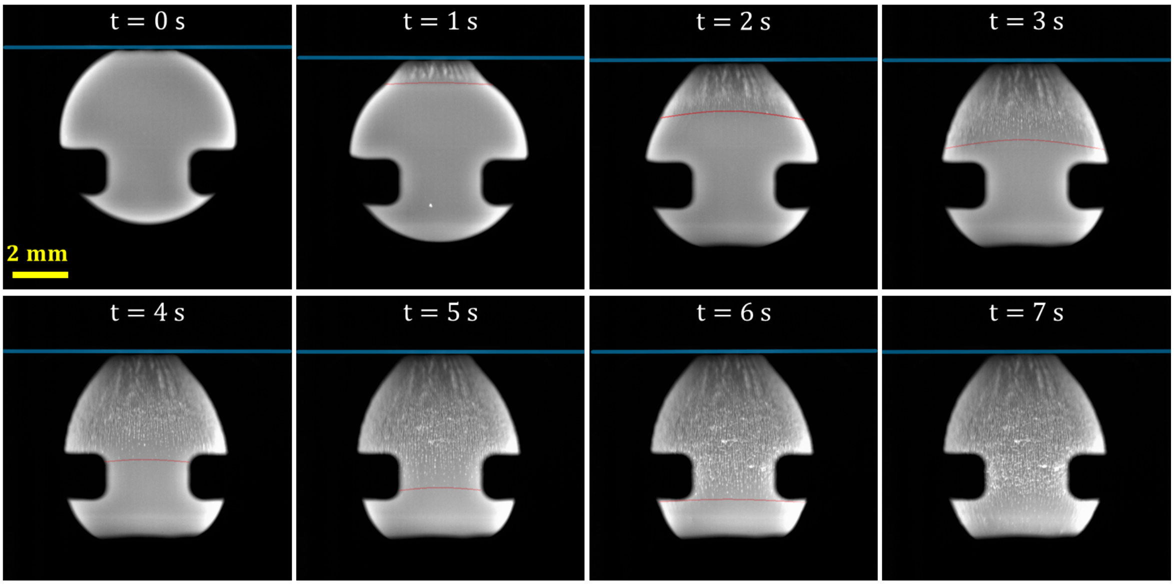

Figure 2.15: Sequence of snapshots from the high-speed camera that recorded the Fe-0.9C-0.2Si experiment onboard the ISS is showing the time evolution of the sample's shape. The chill plate was moving downwards during the first 2 seconds from the contact. The blue line represents the interface of the contact with the chill plate. The red line marks the position of the growth front.

comparable to the growth value observed in parabolic flights. We can extrapolate the time evolution of the front growth by assuming that the front propagated with the average velocity of V_{front}. We obtain this extrapolated point (marked in figure 2.17 in blue) by computing the time t_{final} at which the front reaches the lowest point of the droplet located at Z_{final} from the chill as follows:

$$t_{final} = \frac{Z_{final}}{V_{front}} = 8.16s \tag{2.1}$$

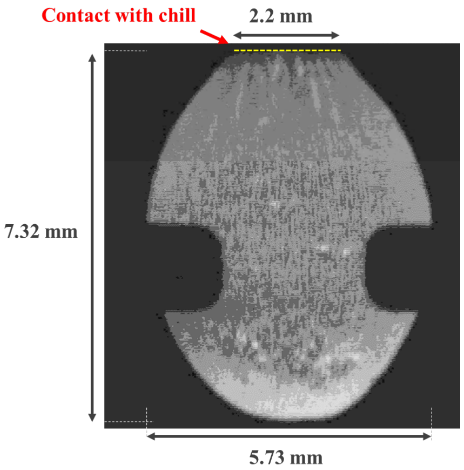

Figure 2.16: The final shape of the sample *d1* after completion of solidification on board the ISS.

In figure 2.18, the contour of the sample after complete solidification (represented by the blue dashed line) is superimposed to the shape of the sample at several times. The key idea is to show that once the interface metal-gas is solidified, i.e. above the red line marking the front position, it remains fixed. This is to say that the assumption of a solid phase that does not deform is correct.

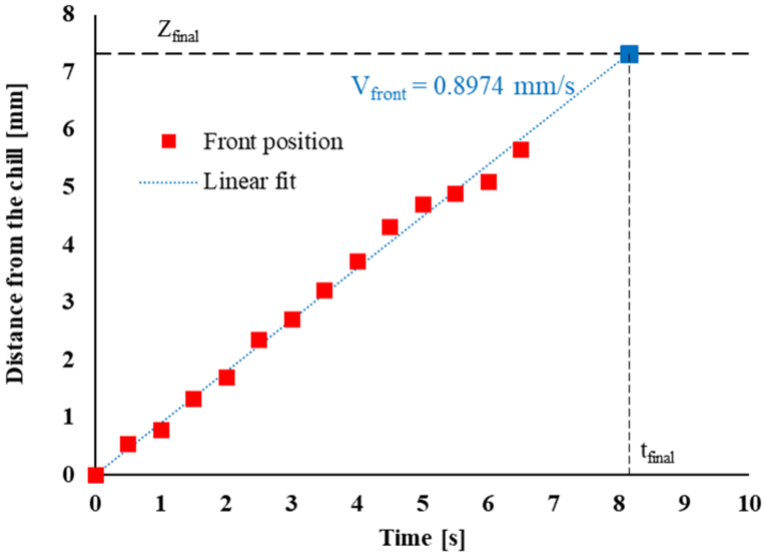

Figure 2.17: Time-evolution of the front position.

Another observation which can confirm this hypothesis is given in figure 2.19. This figure highlights the existence of some light spots in the solid phase that remain fixed and do not deform after solidification.

One additional observation is the appearance of a singular point at the front position where the slope of the sample shape changes from the solid to the liquid phase. This change in slope is very pronounced during the first few seconds after contact with the chill. We can express this change in slope in terms of the difference between the solid angle θ^s and the liquid angle θ^l. These two angles are calculated from the horizontal plane, indicating the position of the front, as shown in Figure 2.20. The time-evolution of θ^s, θ^l and their difference is shown in Figure 2.21. The angle gap is very significant during the first 2 seconds and reaches up to 20° but vanishes within 4 seconds from the contact with the chill.

The present observations with respect to the shape of the droplet, the front growth and the time-temperature profile could be enriched by the chemical segregation profile of the solidified droplet. This will only be possible when the solidified sample is brought back to Earth, which is not the case so far. In the meantime, the present experiment can be supported by additional data concerning the thermophysical properties of the liquid phase of the steel. Knowing the values of the properties of the alloy is crucial for numerical simulation of the solidification process as they serve as input parameters. The lack of values in the literature for the properties of the same alloy created the need for experimental measurements to determine these properties. The properties of interest are surface tension and viscosity of the liquid phase of the alloy. The measurements have been carried out by the teams from ThermoLab/ThermoProp and ELFSTONE projects using the oscillating drop technique. The same experimental device used for the chill cooling experiment on board the ISS is usable for measurements of the surface tension and the viscosity. In addition, the ideal conditions on board the ISS are favourable for the technique to obtain accurate measurements of liquid alloy properties over a wide temperature range, including undercooling.

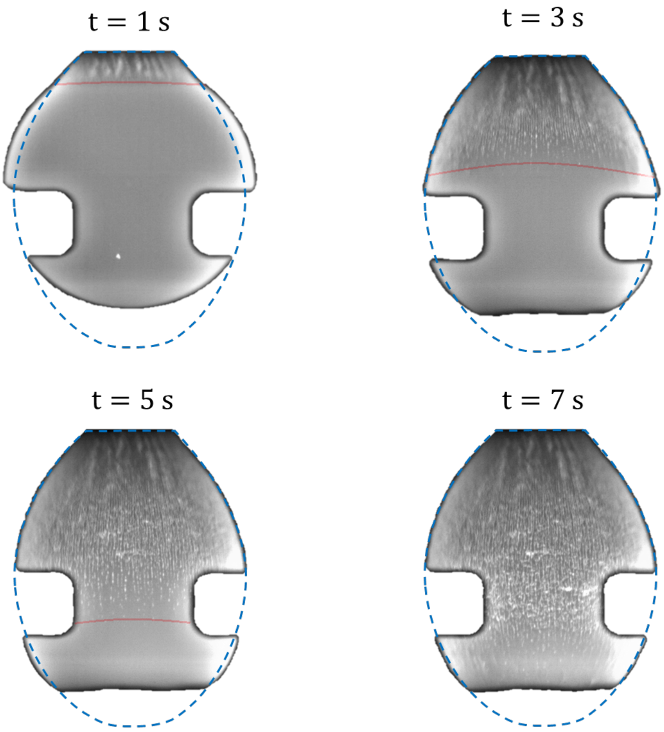

Figure 2.18: Snapshots showing the shape of the droplet during solidification. The red lines mark the front position. The contour of the final shape, marked by the blue dashed lines, is superimposed to the solidifying droplet shape at different times.

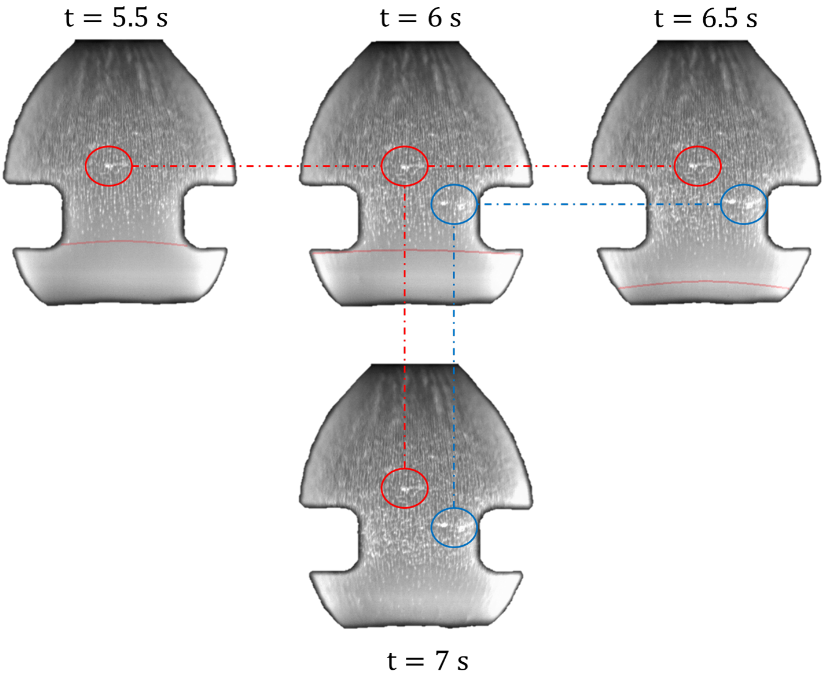

Figure 2.19: Snapshots showing some light spots (encircled in red and yellow) located at the solid phase at different times. The invisible part of the droplet is hidden by the holder. The red lines mark the front position.

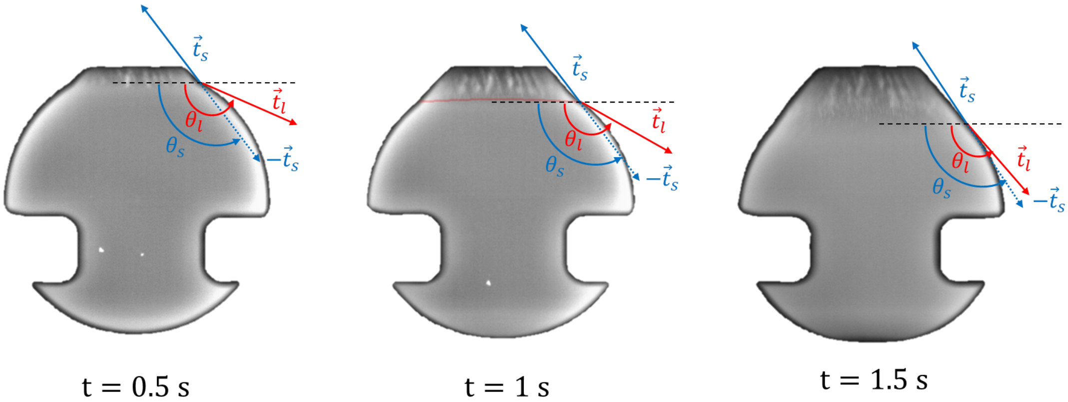

Figure 2.20: Snapshots showing differences in solid and liquid angles at the solidification front position. The liquid angle θ_l is marked in red and the solid angle θ_s is marked in blue.

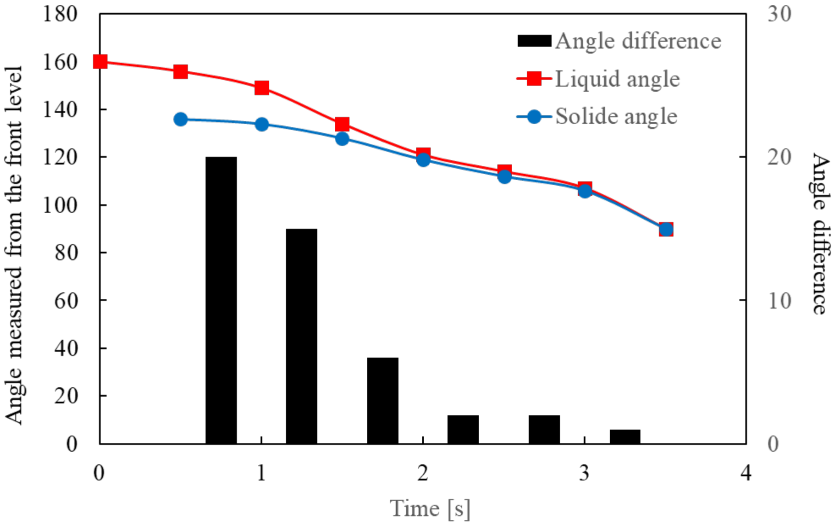

Figure 2.21: Time-evolution of the solid and liquid angles at the front position.

In the logic of deploying the experimental results in the service of numerical modelling, it is relevant to present in this chapter the experiment that had led to the measurement of surface tension and viscosity. In addition, the oscillating drop technique serves as a benchmark for the evaluation of the numerical modelling of surface tension, as it is shown in the next chapter. Like the chill cooling experiment, the oscillating drop technique follows the same steps of levitation, positioning, heating and melting. Once the liquid droplet is put in a stable position, the liquid droplet is excited by an electromagnetic pulse using the heating coil (see the peaks in Figure 2.22). This pulse causes the free surface of the droplet to oscillate as shown in Figure 2.23. More details about the experimental procedure can be found in [25] where Mohr finds that the oscillation frequency is correlated with the value of the surface tension and the damping rate of the oscillation amplitude is related to the viscosity. The formulae used in this technique are presented in details in the following chapter.

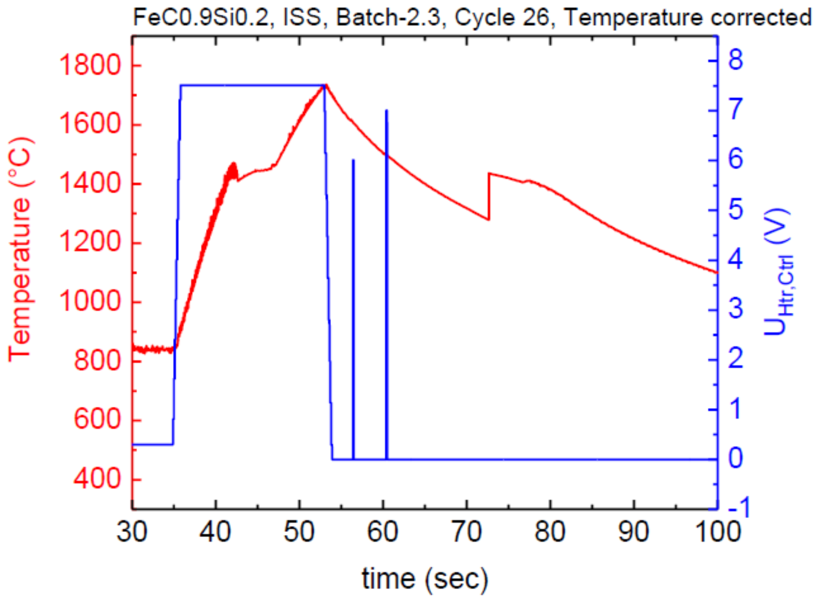

Figure 2.22: Temperature-time profile (red) and heater control voltage (blue) for Fe-0.9C-0.2Si during properties measurement cycle in ISS-EML (batch #2.3). The two peaks in the heater signal represent the electromagnetic pulses to make the droplet oscillate [25].

The video sequence recorded by the high speed camera was analysed by the TEVI software, developed by teams at DLR, in order to extract the radius of the droplet. Figure 2.23 shows the extracted radius in the vertical direction, parallel to the axis of the sample holder. It shows the response of the droplet to the two pulses. The response to the first pulse can not be analysed with respect to the damping rate. The disturbances in the first response can be explained by the strong oscillations that persisted from the heating phase. The response to the second pulse corresponds to the profile of damped oscillation of Rayleigh's mode which is suitable for the measurement of surface tension and viscosity.

Figure 2.24 shows the variation of surface tension with respect to temperature. It can be expressed by a linear function:

$$\gamma = \gamma_0 + \frac{\partial \gamma}{\partial T}(T - T_{ref}) \tag{2.2}$$

where

$$\gamma_0 = 1.439 \pm 0.002 \text{ N.m}^{-1}$$

$$\dot{\gamma} = (5.44 \pm 0.28) \times 10^{-4} \text{ N.m}^{-1}.\text{K}^{-1}$$

$$T_{ref} = 1466\ ^{o}\text{C}$$

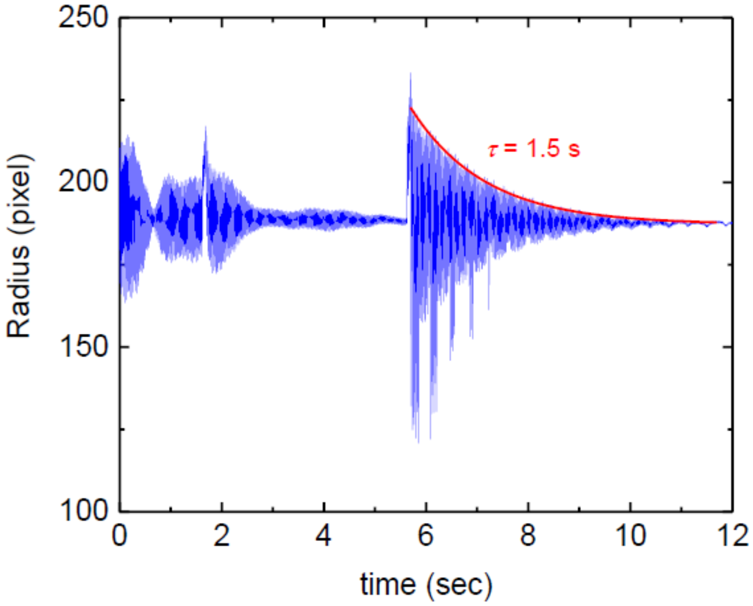

Figure 2.23: The time evolution of the oscillation of the radius of the droplet [25].

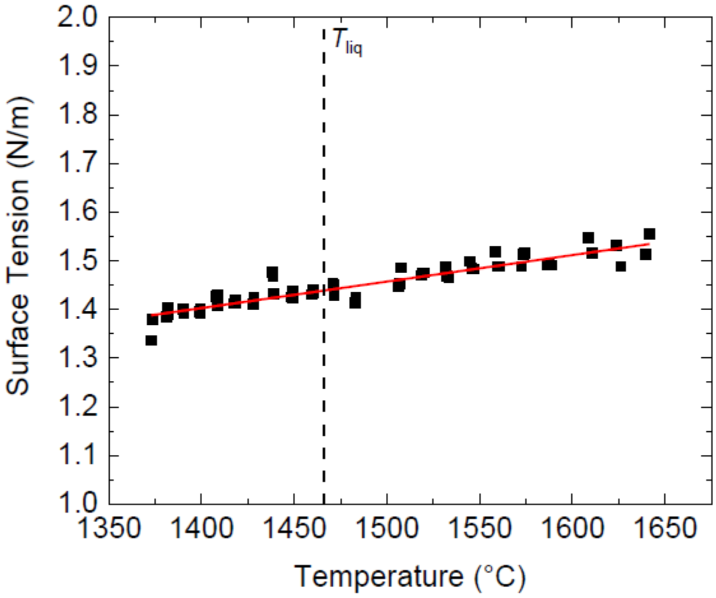

Figure 2.24: Surface tension as function of temperature [25].

The Marangoni coefficient $\frac{\partial \gamma}{\partial T}$ is positive which is not usual for pure liquid metals measured in [9]. A possible explanation to the positive sign is that adsorption or desorption of surface-active species (typically oxygen) or segregated species of surface active elements from the melt might have taken place.

For viscosity, it was only possible to obtain the value at one temperature, namely for the second pulse. The viscosity can hence be given for T = 1460^oC as :

$$\mu = (9.5 \pm 0.2) \times 10^{-3} \text{ Pa.s}$$

2.3 Conclusion

This chapter is devoted to the experimental part of the CCEMLCC project. We first presented the experimental setup with the compositions of the samples under investigation. Then, we presented the results of experiments using three microgravity facilities: parabolic flights, sounding rockets and the ISS. Parabolic flights and sounding rockets are limited by short microgravity duration, as well as the non-negligible residual external forces that disturb the sample. However, they serve as precursor tests to validate the experimental device before sending it to the ISS.

The preliminary results obtained during parabolic flights and sounding rockets were presented for Fe-C-Si samples *a1* , *b1* and *d1* . During these precursor chill cooling tests, the samples showed shape elongation in the growth direction, perpendicular to the chill plate. To confirm or disprove these observations and to draw reliable conclusions about the chill cooling experiments, the experiments must be operated in higher quality conditions where the entire droplet can solidify without external forces. Such ideal conditions were realised onboard the ISS, where the first chill cooling experiment of a steel sample was successfully performed in 2019.

The time-evolution of the temperature measured at the interface of the sample with the chill cooling was analysed. It showed a cooling rate of around 200 K.s^{-1} during the first 2 seconds starting from the contact, then a rate of around 25 K.s^{-1}. The temperature profile enables us also to have a value of temperature for the initialisation of numerical simulations $T_0 = 1648^{\text{o}}$C.

Moreover, we analysed the digital images recordings of the experiment. We observed a final elongation in the vertical direction of around 22% of the sample diameter before processing. The average growth speed of the solidification front was estimated to 0.897 mm.s^{-1}. The observations of the solid phase during solidification allows us to consolidate the fixed-solid assumption, later postulated in numerical modelling. The experimental data were enriched by surface tension and viscosity of the liquid alloy, measured onboard the ISS with the oscillating drop technique.

Further analyses regarding the segregation profile can support the present observations. These analyses could be possible only when the solidified sample is brought back to Earth, which is not the case at the time of writing this manuscript. Accordingly, data are not yet available to compare the chemical segregation predicted by numerical simulations.

Chapter 3

Numerical modelling of multiphase flows including surface tension

Résumé

Ce chapitre est consacré à la modélisation et à la simulation d'écoulements à deux fluides incluant une interface mobile avec tension de surface. Le chapitre est présenté en deux parties. Dans la première partie, nous abordons la modélisation numérique d'une interface mobile avec la méthode level-set. Une formulation bi-fluide de Navier-Stokes est adoptée pour décrire l'écoulement en un seul système d'équations. La méthode de l'interface diffuse est introduite. Dans ce cadre, la variation des propriétés à travers l'interface est lissée par des lois de mélange. La méthode Continuum Surface Force permet d'exprimer la force de tension de surface comme une force de volume. Enfin, une méthode VMS (Variational MultiScale) stabilisée pour le solveur Navier-Stokes est présentée. Dans cette partie, nous présentons quelques améliorations numériques supplémentaires pour mieux maîtriser la conservation de la masse, la stabilité des calculs et la précision du solveur. Dans la deuxième partie, l'objectif est d'évaluer la performance de nos méthodes numériques. Dans ce but, nous présenterons le benchmark de la goutte oscillante. Nous commencerons par dériver la solution analytique en 2D et 3D. Ensuite, nous effectuerons des simulations numériques et montrerons les comparaisons des résultats numériques avec la solution dérivée.

Contents

3.1 Introduction . . . 40
3.2 Interface modelling . . . 40
  3.2.1 Level-Set function . . . 41
  3.2.2 Level-Set transport . . . 41
  3.2.3 Mass correction . . . 42
3.3 Flow modelling . . . 43
  3.3.1 Governing equations . . . 43
  3.3.2 Two-fluid flow formulation . . . 44
  3.3.3 Diffuse interface approach and mixing laws . . . 45
  3.3.4 Surface tension modelling . . . 46
    3.3.4.1 Continuum Surface Force method . . . 46
    3.3.4.2 Semi-implicit surface tension . . . 48
  3.3.5 Semi-implicit BDF time discretisation of Navier-Stokes equations . . . 50
  3.3.6 Stabilised Variational MultiScale method . . . 50
3.4 Partial conclusion . . . 52
3.5 The oscillating drop method : analytical solution . . . 53
  3.5.1 State of the art . . . 53
  3.5.2 The free-oscillating viscous drop problem . . . 55
    3.5.2.1 Governing equations . . . 55
    3.5.2.2 Energy balance . . . 56
  3.5.3 Analytical solutions in the framework of the linear theory . . . 57
    3.5.3.1 Drop shape description . . . 57
    3.5.3.2 Inner flow modelling . . . 59
    3.5.3.3 The energy balance . . . 59
3.6 Numerical simulations . . . 62
  3.6.1 2D preliminary numerical tests . . . 62
    3.6.1.1 Influence of the mass correction method . . . 64
    3.6.1.2 Influence of the Level-Set transport methods . . . 66
    3.6.1.3 Influence of the surface tension formulations . . . 66
    3.6.1.4 Influence of the time-discretisation order . . . 67
    3.6.1.5 Influence of the mesh resolution . . . 68
    3.6.1.6 Conclusion . . . 69
  3.6.2 2D simulation of single oscillation modes . . . 69
  3.6.3 2D simulation of an arbitrary initial form . . . 73
  3.6.4 3D simulation of the oscillation of a liquid iron drop . . . 76
3.7 Conclusion . . . 77

3.1 Introduction

In fluid mechanics, multiphase flows refer to flows involving simultaneously two or several states of matter (liquid, gas, or solid), such as the flow of boiling water including vapour bubbles or the movement of a liquid drop on a solid substrate. This type of flows are characterised by the presence of interfaces through which the thermomechanical properties change. These flows can also involve surface forces at interfaces such as the surface tension and Marangoni forces. Multiphase flows cover a wide range of situations and applications including, for example, energy [26], petroleum engineering [27], nuclear industry [28], biomedicine [29] and environment [30]. A recurring theme throughout the study of multiphase flows is the need to model and predict the behaviour of these flows and the phenomena involved. Adopting a theoretical approach is a very complex and challenging way to predict multiphase flows and may not be feasible when the flow is coupled with other phenomena such as heat transfer or turbulence. The experimental approach is limited to laboratory-scale prototypes. Besides, the experiments still require more sophisticated instruments to provide more detailed flow data. Consequently, predictive capacity relies heavily on numerical modelling. Computational algorithms for solving multiphase flows are widely present in the literature [31]. Despite the maturity of numerical modelling for multiphase flows , many numerical challenges persist, and the magnitude of the challenges depends on the complexity of the phenomena involved. Moreover, further efforts are still needed to meet the growing demand for reliable and accurate numerical tools.

In this chapter, we will present our numerical framework for solving incompressible flows involving two fluids separated by an interface with surface tension force. The chapter is presented in two parts: the first part is dedicated for numerical modelling and the second part is for assessment and validation. In the first part, we will start with interface modelling. We will introduce the level-set method and show how we use it to track the interface over time. A numerical issue related to mass conservation is occurring when using level-method. A mass correction method will be then presented. After that, we will write the governing equations of an incompressible two-fluid flow starting from the strong formulation to the monolithic weak formulation, including surface forces. The diffuse interface method will be introduced. In this framework, the mixing laws of the properties will be given, and the Continuum Surface Force (CSF) method for surface tension will be shown. Finally, the Stabilised Variational MultiScale (VMS) method for Navier-Stokes solver will be presented. Through this part, we will present some additional numerical improvements to deal with the stability and accuracy of the solver. In the second part, the goal is to assess the performance of our numerical tools. For this purpose, we will present the oscillating drop benchmark. We will start by deriving the analytical solution both in 2D and 3D. Then, we will perform numerical tests and show comparisons of the numerical results with the derived solution.

3.2 Interface modelling

In Computational Fluid Dynamics (CFD), one of the questions that arise when dealing with multiphase flows is how to model the interface. There are two main classes of methods to model an interface: Front tracking methods and Front capturing methods. The front tracking methods are based on a Lagrangian description of the interface. These methods are characterised by the use of markers located all over the volume of a chosen phase such as Marker and Cell Method [32], or located only at the interface such as Surface tracking method [33]. As for front capturing methods, the interface is implicitly represented by a phase function that identifies the phase to which a given element of the grid belongs. The interface is, thus, defined by the phase function. The most famous methods of front capturing are the Volume-of-Fluid method [34] and the Level-Set method [35].

In the context of the FE method with fixed Eulerian grids, we use in this work the Level-Set method. It has attractive features as it handles a wide range of complex 3D geometries. In addition, it provides direct access to the geometrical properties of the interface that are necessary for the calculation of surface forces.

3.2.1 Level-Set function

Consider a computational domain Ω containing two sub-domains Ω_1 and Ω_2 separated by an interface Γ. The Level-Set method relies on an implicit representation of Γ via a signed distance function to the interface, defined at each position $\boldsymbol{x}$, at any time t by:

$$\phi(\boldsymbol{x},t) = \begin{cases} d(\boldsymbol{x},\Gamma) & \text{if} \quad \boldsymbol{x} \in \Omega_1 \\ 0 & \text{if} \quad \boldsymbol{x} \in \Gamma \\ -d(\boldsymbol{x},\Gamma) & \text{if} \quad \boldsymbol{x} \in \Omega_2 \end{cases} \tag{3.1}$$

where $d(\boldsymbol{x},\Gamma)$ is the geometrical distance from the point $\boldsymbol{x}$ to the interface Γ. Here the positive values are arbitrarily chosen in Ω_1.

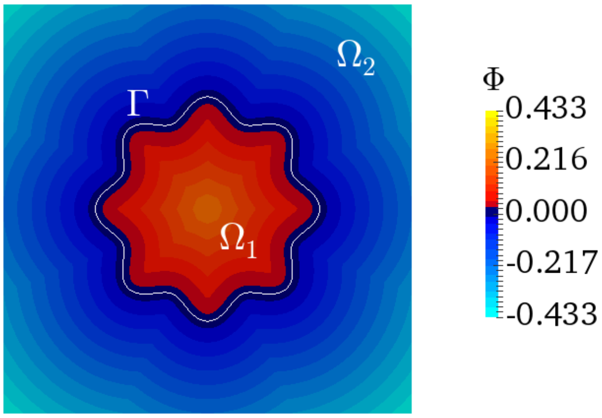

Figure 3.1: Illustration of the Level-Set function

3.2.2 Level-Set transport

To track the time-evolution of the interface position, we solve the following advection equation:

$$\frac{\partial \phi}{\partial t} + \boldsymbol{u}.\nabla\phi = 0 \tag{3.2}$$

where $\boldsymbol{u}$ denotes the flow velocity vector. The zero iso-value resulting from equation (3.2) represents the new position of the interface. However, the non-zero levels can be distorted by the flow velocity, especially when the velocity field $\boldsymbol{u}$ is not uniform. Therefore, they are not guaranteed to represent the geometrical distance to the interface. Consequently, a regularisation or re-initialisation of the Level-Set function is needed in order to recover the intrinsic property of the distance function which writes $\|\nabla\phi\| = 1$. Solving the Hamilton-Jacobi equation (3.3) is a classical way for re-distancing.

$$\frac{\partial\phi}{\partial\tau} + s(\phi)\left(\|\nabla\phi\| - 1\right) = 0 \tag{3.3}$$

where τ is a pseudo-time and $s(\phi)$ is the sign of the Level-Set function ϕ.

There is another way of re-initialisation based on a direct geometrical computation of the distance function [36]. Once the transport equation (3.2) is solved, the interface is obtained from the iso-value $\Phi(\boldsymbol{x}, t) = 0$. Then, the smallest distance from each mesh node to the interface is computed.

To circumvent the need of two different solvers for transport and re-initialisation, the coupled convection-re-initialisation method formulated by equation (3.4) combines both equations (3.2) and (3.3).

$$\frac{\partial\phi}{\partial t} + \mathbf{U}.\nabla\phi = ks(\phi) \tag{3.4}$$

where k is a numerical constant dimensionally homogeneous to a velocity and $\mathbf{U}$ writes:

$$\mathbf{U} = \boldsymbol{u} + ks(\phi)\frac{\nabla\phi}{\|\nabla\phi\|} \tag{3.5}$$

It should be noted that the convection equation (3.2) as well as the auto-reinitialisation transport equation (3.4) are solved in FE by means of Streamline Upwind Petrov–Galerkin (SUPG) method known to mitigate the numerical instabilities. See [37] for more numerical details.

3.2.3 Mass correction

Despite its mathematical simplicity and attractive ability to deal with complex geometries, the classical Level-Set method (distance function) suffers from mass conservation issues. In fact, after the transport of Level-Set function, the volume (consequently the mass, for an incompressible flow) of the object described by the Level-Set (Ω_1) can be lost or gained due to numerical errors within each time iteration. After several time increments, the accumulation of numerical errors can lead to a significant mass gain/loss. In the present work, we use a simple correction method to enforce the volume (thus the mass) to be constant. The principle of this correction method is to shift the zero iso-value of the Level-Set function (distance function) by some signed distance c_ϕ such as:

$$\phi^{corr}(\boldsymbol{x}, t) = \phi(\boldsymbol{x}, t) + c_\phi(t) \tag{3.6}$$

where ϕ^{corr} is the corrected Level-Set function, and ϕ is the transported Level-Set resulting from (3.4). The signed distance $c_\phi(t)$ is computed as the volume difference, taking as a reference the initial volume, over the surface A_Γ such as:

$$c_\phi(t) = \frac{V(t) - V(0)}{A_\Gamma(t)} \tag{3.7}$$

It should be mentioned that this adjustment $|c_\phi|$ should be small enough (not greater than $O(h^2)$ for $\mathbb{P}1$-elements where h is the mesh size according to [38]) to preserve the shape of the interface. This means that the numerical discretisation errors within each time step must be minimised as possible. For this purpose, we use a high order time-discretisation scheme (2^{nd} order is sufficient) for solving the transport equation (3.4). Note also that the correction method given by the equations (3.6) and (3.7) applies only for a single object with invariant volume. This method will be extended in Chapter 5 to a shrinking-volume droplet during solidification.

3.3 Flow modelling

This section is devoted to the mathematical formulation of a flow involving two fluids separated by a moving interface governed by surface tension force. The numerical framework is based on solving the Navier-Stokes equations. The properties jump across the interface is smoothened via the diffuse interface approach. The surface tension force is included into Navier-Stokes equations as a volume force through the CSF method. The resolution strategy is based on stabilised FE VMS method.

3.3.1 Governing equations

Let ρ_1 and ρ_2 be the densities of the fluids in Ω_1 and Ω_2 respectively and μ_1 and μ_2 their respective dynamic viscosity. We consider in this chapter that the flow is incompressible, isothermal and that no phase transformation occurs. The flow in each subdomain, indexed by i, is described by the following Navier-Stokes equations:

$$\begin{cases} \rho_i\left(\frac{\partial \boldsymbol{u}_i}{\partial t} + \boldsymbol{u}_i \cdot \nabla \boldsymbol{u}_i\right) - \nabla \cdot \boldsymbol{\sigma}_i = \boldsymbol{f}_i \\ \nabla \cdot \boldsymbol{u}_i = 0 \end{cases} \tag{3.8}$$

where $\boldsymbol{u}_i$ is the velocity vector of the fluid in the subdomain Ω_i and $\boldsymbol{f}_i$ is its volume external force. $\boldsymbol{\sigma}_i$ is the stress tensor which is linked to the pressure of the fluid p_i and the strain rate tensor $\dot{\boldsymbol{\epsilon}}(\boldsymbol{u}_i)$ by the following Newtonian-fluid constitutive law:

$$\boldsymbol{\sigma}_i = 2\mu_i \dot{\boldsymbol{\epsilon}}(\boldsymbol{u}_i) - p_i \mathbb{I} \tag{3.9}$$

with $\mathbb{I}$ the identity tensor. In order to close the problem, Equations (3.8) are subjected to boundary and initial conditions.

At the interface Γ, the normal stress jump is given by the surface tension force such as:

$$[\![\boldsymbol{\sigma}]\!] \cdot \boldsymbol{n} = (\boldsymbol{\sigma}_2 - \boldsymbol{\sigma}_1) \cdot \boldsymbol{n} = -\gamma\, \kappa\, \boldsymbol{n} = \boldsymbol{f}_{\mathbf{ST}} \tag{3.10}$$

where γ is the surface tension coefficient, κ is the mean curvature and $\boldsymbol{n}$ is a unit normal vector to Γ oriented inwards Ω_1.

These geometrical properties of the interface are directly computed thanks to the Level-Set function using the following expressions:

$$\boldsymbol{n} = \frac{\nabla\phi}{\|\nabla\phi\|} \tag{3.11}$$

$$\kappa = -\nabla.\boldsymbol{n} \tag{3.12}$$

Following these considerations, the surface tension force is calculated from the Level-Set function as:

$$\boldsymbol{f}_{\mathbf{ST}} = \gamma\nabla.\left(\frac{\nabla\phi}{\|\nabla\phi\|}\right)\frac{\nabla\phi}{\|\nabla\phi\|} \tag{3.13}$$

3.3.2 Two-fluid flow formulation

First, we write the weak form of the set of equations (3.8) for each fluid. It can be obtained by multiplication with test functions and integration over each subdomain then integrating by part the term with the stress tensor. In this work, we denote by $(a,b)_{\mathrm{D}}$ the integral of the product $a \cdot b$ over the domain D, i.e. $(a,b)_{\mathrm{D}} = \int_{\mathrm{D}} a \cdot b \, d\mathrm{D}$.

Let consider the interpolation functions $\mathscr{U}_i$ and $\mathscr{P}_i$ defined in the subdomain Ω_i, $i \in \{1,2\}$. The weak formulation of the problem (3.8) with the constitutive law (3.9) reads:

$$\begin{cases} \left(\rho_1 \frac{\partial \boldsymbol{u}_1}{\partial t}, \mathscr{U}_1\right)_{\Omega_1} + \left(\rho_1 \boldsymbol{u}_1 \cdot \nabla \boldsymbol{u}_1, \mathscr{U}_1\right)_{\Omega_1} + \left(2\mu_1 \dot{\boldsymbol{\epsilon}}(\boldsymbol{u}_1) : \dot{\boldsymbol{\epsilon}}(\mathscr{U}_1)\right)_{\Omega_1} - \left(p_1, \nabla \cdot \mathscr{U}_1\right)_{\Omega_1} \\ \qquad\qquad = \left(\boldsymbol{f}_1, \mathscr{U}_1\right)_{\Omega_1} + (\boldsymbol{\sigma}_1 \cdot \boldsymbol{n}_1, \mathscr{U}_1)_{\partial\Omega_1} \\ (\nabla \cdot \boldsymbol{u}_1, \mathscr{P}_1)_{\Omega_1} = 0 \end{cases} \tag{3.14}$$

$$\begin{cases} \left(\rho_2 \frac{\partial \boldsymbol{u}_2}{\partial t}, \mathscr{U}_2\right)_{\Omega_2} + \left(\rho_2 \boldsymbol{u}_2 \cdot \nabla \boldsymbol{u}_2, \mathscr{U}_2\right)_{\Omega_2} + \left(2\mu_2 \dot{\boldsymbol{\epsilon}}(\boldsymbol{u}_2) : \dot{\boldsymbol{\epsilon}}(\mathscr{U}_2)\right)_{\Omega_2} - \left(p_2, \nabla \cdot \mathscr{U}_2\right)_{\Omega_2} \\ \qquad\qquad = \left(\boldsymbol{f}_2, \mathscr{U}_2\right)_{\Omega_2} + (\boldsymbol{\sigma}_2 \cdot \boldsymbol{n}_2, \mathscr{U}_2)_{\partial\Omega_2} \\ (\nabla \cdot \boldsymbol{u}_2, \mathscr{P}_2)_{\Omega_2} = 0 \end{cases} \tag{3.15}$$

where $\boldsymbol{n}_2 = -\boldsymbol{n}_1 = \boldsymbol{n}$.

The monolithic formulation of a two-fluid flow consists in writing one set of equations to be solved in the whole computational domain. This approach involves considering the computational domain filled with a single fluid but with variable properties. For this reason, we define the global velocity vector $\boldsymbol{u}$ and the global pressure p such as:

$$\boldsymbol{u}(\boldsymbol{x}) = \begin{cases} \boldsymbol{u}_1 & \text{if } \ \boldsymbol{x} \in \Omega_1 \\ \boldsymbol{u}_2 & \text{if } \ \boldsymbol{x} \in \Omega_2 \end{cases} \tag{3.16}$$

and

$$p(\boldsymbol{x}) = \begin{cases} p_1 & \text{if} \quad \boldsymbol{x} \in \Omega_1 \\ p_2 & \text{if} \quad \boldsymbol{x} \in \Omega_2 \end{cases} \tag{3.17}$$

In the same way, we define the global variable properties ρ and μ such as:

$$\rho(\boldsymbol{x}) = \begin{cases} \rho_1 & \text{if} \quad \boldsymbol{x} \in \Omega_1 \\ \rho_2 & \text{if} \quad \boldsymbol{x} \in \Omega_2 \end{cases} \tag{3.18}$$

and

$$\mu(\boldsymbol{x}) = \begin{cases} \mu_1 & \text{if} \quad \boldsymbol{x} \in \Omega_1 \\ \mu_2 & \text{if} \quad \boldsymbol{x} \in \Omega_2 \end{cases} \tag{3.19}$$

By summing equations (3.14) and (3.15) and applying the boundary condition (3.10), the formulation of the two-fluid flow with surface tension reads:

$$\begin{cases} \left(\rho \frac{\partial \boldsymbol{u}}{\partial t}, \mathscr{U}\right)_\Omega + \left(\rho \boldsymbol{u} \cdot \boldsymbol{\nabla} \boldsymbol{u}, \mathscr{U}\right)_\Omega + \left(2\mu \dot{\epsilon}(\boldsymbol{u}) : \dot{\epsilon}(\mathscr{U})\right)_\Omega - \left(p, \boldsymbol{\nabla} \cdot \mathscr{U}\right)_\Omega \\ \qquad = \left(\boldsymbol{f}, \mathscr{U}\right)_\Omega + \left(\boldsymbol{f}_{\mathbf{ST}}, \mathscr{U}\right)_\Gamma \\ (\boldsymbol{\nabla} \cdot \boldsymbol{u}, \mathscr{P})_\Omega = 0 \end{cases} \tag{3.20}$$

Note that in equation (3.20), we consider a zero Neumann boundary condition on $\partial_O mega$, i.e.

$$\left(\boldsymbol{\sigma}_i \cdot \boldsymbol{n}_i, \mathscr{U}_i\right)_{\partial\Omega_i \cap \partial\Omega} = 0 \tag{3.21}$$

At this stage, the two-fluid flow formulation (3.20) together with the variable properties as given by (3.18) and (3.19) are the basis of the sharp interface approach which requires appropriate methods able to handle the discontinuity of properties across the interface as well as a surface integral method to compute the surface tension force. To avoid dealing with discontinuities which can be source of calculation instabilities, we use in this work a different numerical approach, called the diffuse interface method.

3.3.3 Diffuse interface approach and mixing laws

Unlike the sharp interface approach, the diffuse interface method considers the interface as a non-zero thickness layer. The interface is then a region of thickness 2ε centred around the zero iso-value of the Level-Set function ($-\varepsilon \leq \Phi \leq +\varepsilon$) in which the transition from one fluid to the other occurs continuously and smoothly (see Figure 3.2). We use for that a smooth Heaviside function $H(\phi)$ which allows computation of the smooth variable properties ρ and μ. There is a variety of smooth Heaviside functions. In this work, we choose a sinusoidal smoothing function such as:

$$H(\phi) = \begin{cases} 1 & \text{if } \phi > \varepsilon \\ 0 & \text{if } \phi < -\varepsilon \\ \frac{1}{2}\left[1 + \frac{\phi}{\varepsilon} + \frac{1}{\pi}\sin\left(\frac{\pi\phi}{\varepsilon}\right)\right] & \text{if } |\phi| \le \varepsilon \end{cases} \tag{3.22}$$

Note that the half-thickness ε should be smaller than the smallest length scale of the problem. On the other hand, the transition zone should contain enough mesh elements to ensure smooth variations across the interface.

The way the transition of fluid properties across the interface is given by mixing laws. For the density and the viscosity, the common way to define the transition across the transition zone is the arithmetic mixing law [39], described as follows:

$$\rho = \rho_1 H + \rho_2 (1 - H) \tag{3.23}$$

$$\mu = \mu_1 H + \mu_2 (1 - H) \tag{3.24}$$

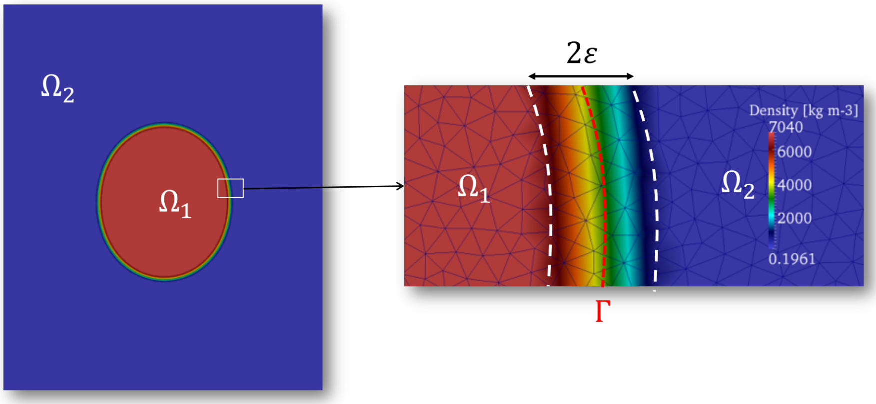

Figure 3.2: The diffuse interface approach illustrated via the density profile across the interface

3.3.4 Surface tension modelling

3.3.4.1 Continuum Surface Force method

In the context of the diffuse interface method, the surface tension force, defined originally as a surface integral, is approached by a volume integral via a smoothed Dirac function $\delta(\phi)$ centred at the interface. This method is called the CSF [40]. Accordingly, the surface tension force term is expressed as follows:

$$(\boldsymbol{f}_{\mathbf{ST}}, \mathcal{U})_\Gamma = (\delta\, \boldsymbol{f}_{\mathbf{ST}}, \mathcal{U})_\Omega \tag{3.25}$$

where the Dirac function δ is derived from the smooth Heaviside function and given as follows:

$$\delta(\phi) = \begin{cases} \dfrac{1}{2\varepsilon}\left[1+\cos\left(\dfrac{\pi\phi}{\varepsilon}\right)\right] & \text{if } \left|\phi\right| \leq \varepsilon \\ 0 & \text{if } \left|\phi\right| > \varepsilon \end{cases} \tag{3.26}$$

For the sake of simplicity, the expression of the surface tension force henceforth will include the Dirac function δ:

$$\boldsymbol{f}_{\mathbf{ST}} = -\delta\,\gamma\,\kappa\,\boldsymbol{n} \tag{3.27}$$

Therefore, the two-fluid formulation (3.20) becomes:

$$\begin{cases} \left(\rho\frac{\partial \boldsymbol{u}}{\partial t}, \mathscr{U}\right)_\Omega + \left(\rho\boldsymbol{u}\cdot\nabla\boldsymbol{u}, \mathscr{U}\right)_\Omega + \left(2\mu\dot{\varepsilon}(\boldsymbol{u}):\dot{\varepsilon}(\mathscr{U})\right)_\Omega - \left(p, \nabla\cdot\mathscr{U}\right)_\Omega \\ \qquad\qquad = \left(\boldsymbol{f}, \mathscr{U}\right)_\Omega + \left(\boldsymbol{f}_{\mathbf{ST}}, \mathscr{U}\right)_\Omega \\ (\nabla\cdot\boldsymbol{u}, \mathscr{P})_\Omega = 0 \end{cases} \tag{3.28}$$

Density-scaled CSF method

The main numerical issue when using the standard CSF method for surface tension is the spurious oscillations around the interface. They are caused by high accelerations in the region of small density due to the symmetrical distribution of the surface tension force around the interface. The use of a centred Dirac function δ gives the same weight to the region of small density as the region of higher density. One way to minimise these spurious oscillations is to use a density-scaled force [41]. The principle of this method is to shift the peak of the Dirac function to give more weight to the higher density region as shown in Figure 3.3. It consists of multiplying the centred Dirac function δ by $\rho/\bar{\rho}$ where $\bar{\rho}$ is the mean density $\frac{\rho_1+\rho_2}{2}$. The density-scaled CSF method writes thus:

$$\boldsymbol{f}_{\mathbf{ST}}^{scaled} = -\frac{\rho}{\bar{\rho}}\,\delta\,\gamma\,\kappa\,\boldsymbol{n} \tag{3.29}$$

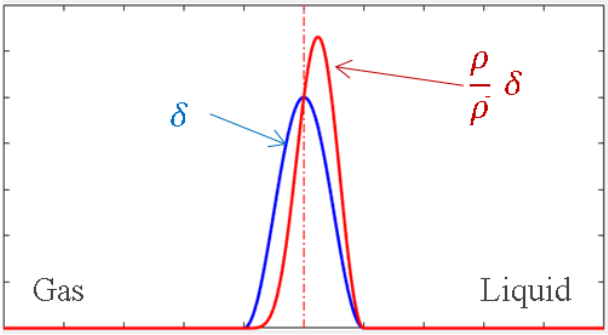

Figure 3.3: Illustration of the centred Dirac function and the density-scaled Dirac function

Another equivalent way to use the Density-scaled force is to substitute the centred Dirac function by the following scaled Dirac:

$$\delta^{scaled} = 2 \times \mathrm{H}(\phi) \times \delta(\phi). \tag{3.30}$$

Hence,

$$\delta^{scaled} = \begin{cases} \frac{1}{2\varepsilon}\left[1+\cos\left(\frac{\pi\phi}{\varepsilon}\right)\right]\left[1+\frac{\phi}{\varepsilon}+\frac{1}{\pi}\sin\left(\frac{\pi\phi}{\varepsilon}\right)\right] & \text{if} \quad |\phi| \le \varepsilon \\ 0 & \text{if} \quad |\phi| > \varepsilon \end{cases} \tag{3.31}$$

To illustrate the issue of the spurious currents, we apply the framework to a simple benchmark called the equilibrium drop problem. In this benchmark a circular water drop of density $\rho_1 = 1000$ kg.m^{-3} and viscosity $\mu_1 = 10^{-3}$ Pa.s surrounded by air of density $\rho_2 = 1$ kg.m^{-3} and viscosity $\mu_2 = 10^{-5}$ Pa.s is released from an equilibrium circular shape. Surface tension is $\gamma = 0.07$ N.m^{-1}. Physically, the velocity field must be zero as the drop is at equilibrium. But numerically, the solution is polluted by the numerical spurious current in the vicinity of the interface. Figure 3.4 shows that the density-scaled method enables a significant reduction of the intensity of these non-physical currents comparing to the standard CSF method with a centred Dirac function.

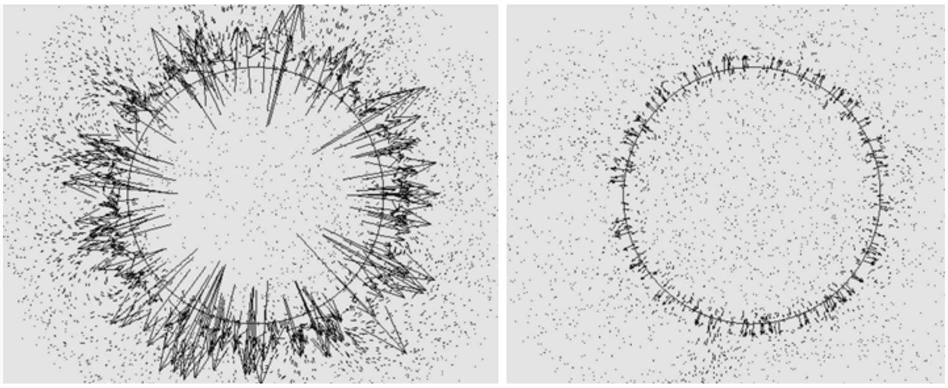
(a) (b)

Figure 3.4: Illustration of the simulated velocity field (depicted by black arrows) of a circular drop with (a) the standard CSF method and (b) the density-scaled CSF method

3.3.4.2 Semi-implicit surface tension

The explicit formulation of the surface tension force evaluates the Right-Hand-Side (RHS) term of the equation (3.28) at the previous time step. The calculation stability with explicit surface tension is limited to time steps Δt up to the maximum value [42]

$$\Delta t_{max} = \sqrt{\frac{\bar{\rho} h^3}{2\pi\gamma}} \tag{3.32}$$

where h is the grid size and $\bar{\rho}$ is the average density at the interface. This stability condition could be very penalising for computational time. For instance, in this thesis, we are dealing with liquid metals with surface tension coefficient of the order of 1.8 N.m^{-1} and density around 7000 kg.m^{-1}. With a minimum mesh size of 10^{-5} m, the maximum time step allowed by the use of explicit surface tension is $\Delta t_{max} = 5.56 \times 10^{-7}$ s. It means that for a simulation of a process that physically lasts 1 s we need about 10^6 time-increments. Using an implicit time scheme for surface tension enables to circumvent this time step restriction. In this work, we adopt a semi-implicit formulation of surface tension. Such formulation has been implemented in Cimlib at CEMEF by Khalloufi [43] and Qiang [44]. In this work, we express the implicit term of surface tension differently so that the implementation in FE is straightforward. For this purpose, we introduce another approach to express the weak form of surface tension, following the work of [45]. First, we rewrite the surface tension force integral such as:

$$\begin{aligned}
\int_\Gamma -\gamma\kappa \boldsymbol{n}\cdot\mathscr{U}\,d\Gamma &= \int_\Gamma (-\gamma\kappa\boldsymbol{n} + \cancel{\boldsymbol{\nabla}_\Gamma \gamma})\cdot\mathscr{U}\,d\Gamma && (3.33)\\
&= \int_\Gamma \boldsymbol{\nabla}\cdot\left[\gamma(\mathbb{I}-\boldsymbol{n}\otimes\boldsymbol{n})\right]\cdot\mathscr{U}\,d\Gamma && (3.34)\\
&= -\int_\Gamma \gamma(\mathbb{I}-\boldsymbol{n}\otimes\boldsymbol{n}):\boldsymbol{\nabla}\mathscr{U}\,d\Gamma && (3.35)
\end{aligned}$$

We denote by $\mathbb{P}$ the projection tensor $\mathbb{I}-\boldsymbol{n}\otimes\boldsymbol{n}$ on the interface Γ. We consider the identity function $\boldsymbol{\chi}$ on Γ. According to [42], we have the following properties:

$$\boldsymbol{\nabla}_\Gamma\boldsymbol{\chi} = \mathbf{I}-\boldsymbol{n}\otimes\boldsymbol{n} = \mathbb{P} \tag{3.36}$$

$$\Delta_\Gamma\boldsymbol{\chi} = \boldsymbol{\nabla}_\Gamma\cdot\boldsymbol{\nabla}_\Gamma\boldsymbol{\chi} = -\kappa\boldsymbol{n} \tag{3.37}$$

where $\boldsymbol{\nabla}_\Gamma$ is the surface gradient on Γ and Δ_Γ is the surface Laplacian, also known as the Laplace-Beltrami operator.

The derivation of the semi-implicit formulation of surface tension arises from the following approximation:

$$\boldsymbol{\chi}^{n+1} \approx \boldsymbol{\chi}^n + \boldsymbol{u}^{n+1}\Delta t \tag{3.38}$$

The exponent $(*)^{n+1}$ denotes the value of the quantity $(*)$ at the current time step and $(*)^n$ its value at the previous time step.

$$\begin{aligned}
\int_\Gamma \gamma\mathbb{P}^{n+1}:\boldsymbol{\nabla}\mathscr{U}\,d\Gamma &= \int_\Gamma \gamma\boldsymbol{\nabla}_\Gamma\boldsymbol{\chi}^{n+1}:\boldsymbol{\nabla}\mathscr{U}\,d\Gamma && (3.39)\\
&\approx \int_\Gamma \gamma\boldsymbol{\nabla}_\Gamma\left(\boldsymbol{\chi}^n+\boldsymbol{u}^{n+1}\Delta t\right):\boldsymbol{\nabla}\mathscr{U}\,d\Gamma && (3.40)\\
&= \int_\Gamma \gamma\mathbb{P}^n:\boldsymbol{\nabla}\mathscr{U}\,d\Gamma + \Delta t\int_\Gamma \gamma\boldsymbol{\nabla}_\Gamma\boldsymbol{u}^{n+1}:\boldsymbol{\nabla}\mathscr{U}\,d\Gamma && (3.41)\\
&= \int_\Gamma \gamma\mathbb{P}^n:\boldsymbol{\nabla}\mathscr{U}\,d\Gamma + \Delta t\int_\Gamma \gamma\left(\boldsymbol{\nabla}\boldsymbol{u}^{n+1}.\mathbb{P}\right):\boldsymbol{\nabla}\mathscr{U}\,d\Gamma && (3.42)
\end{aligned}$$

Note that this latter semi-implicit formulation also accounts for the Marangoni effect, which is accounted for in Chapter 5. In the present chapter, we work in the framework of isothermal flows and constant surface tension coefficient.

Using the CSF method and the equation (3.35), the equation (3.42) becomes:

$$\left(\boldsymbol{f}_{\mathbf{ST}}^{n+1},\mathscr{U}\right)_\Omega = \left(\boldsymbol{f}_{\mathbf{ST}},\mathscr{U}\right)_\Omega - \left(\Delta t\;\gamma\;\delta\;\left(\boldsymbol{\nabla}\boldsymbol{u}^{n+1}.\mathbb{P}\right):\boldsymbol{\nabla}\mathscr{U}\right)_\Omega \tag{3.43}$$

3.3.5 Semi-implicit BDF time discretisation of Navier-Stokes equations

For low discretisation errors, we approximate the time derivative of the transient term in Navier-Stokes equations (3.54) using high order Backward Differentiation Formulas (BDF) schemes [46; 47]

If we denote by $t_n = n\Delta t$ the discrete times and σ the order of the discretisation, the BDF approximation of the time derivative of the velocity field is given by:

$$\frac{\partial \boldsymbol{u}_h}{\partial t} \approx \frac{\alpha_\sigma \boldsymbol{u}_h^{n+1} - \boldsymbol{u}_h^{\mathrm{BDF},\sigma}}{\Delta t} \tag{3.44}$$

where

$$\boldsymbol{u}_h^{\mathrm{BDF},\sigma} = \begin{cases} \boldsymbol{u}_h^n & \text{if } \sigma = 1 \\ 2\boldsymbol{u}_h^n - \dfrac{1}{2}\boldsymbol{u}_h^{n-1} & \text{if } \sigma = 2 \\ 3\boldsymbol{u}_h^n - \dfrac{3}{2}\boldsymbol{u}_h^{n-1} + \dfrac{1}{3}\boldsymbol{u}_h^{n-2} & \text{if } \sigma = 3 \end{cases} \tag{3.45}$$

and

$$\alpha_\sigma = \begin{cases} 1 & \text{if } \sigma = 1 \\ \dfrac{3}{2} & \text{if } \sigma = 2 \\ \dfrac{11}{6} & \text{if } \sigma = 3 \end{cases} \tag{3.46}$$

In this work, the nonlinear convection terms appearing in Navier-Stokes equations are approximated by a high order semi-implicit scheme based on Newton-Gregory backward polynomials:

$$\nabla \boldsymbol{u}_h . \boldsymbol{u}_h \approx \nabla \boldsymbol{u}_h^{n+1} . \boldsymbol{u}_h^{\mathrm{BNG},\sigma} \tag{3.47}$$

where

$$\boldsymbol{u}_h^{\mathrm{BNG},\sigma} = \begin{cases} \boldsymbol{u}_h^n & \text{if } \sigma = 1 \\ 2\boldsymbol{u}_h^n - \boldsymbol{u}_h^{n-1} & \text{if } \sigma = 2 \\ 3\boldsymbol{u}_h^n - 3\boldsymbol{u}_h^{n-1} + \boldsymbol{u}_h^{n-2} & \text{if } \sigma = 3 \end{cases} \tag{3.48}$$

This leads to solve one linear system in each time step in stead of solving a nonlinear system which requires an iterative algorithm within each time step to converge to the solution.

3.3.6 Stabilised Variational MultiScale method

Let discretise the computational domain Ω into a FE mesh grid $\mathcal{T}_h$ made of N_{elt} elements K. We approximate the functional spaces V for the velocity and Q for the pressure by the finite-dimensional spaces V_h and Q_h respectively. In FE method, the stability of resolution of the mixed velocity-pressure formulation is restricted by the Babuska-Brezzi condition [48]. This condition prescribes that the dimension of the functional space for the velocity V_h must be richer than that for the pressure Q_h. The classical Galerkin method with equal order linear interpolation P1/P1 is thus not stable and ends up with spurious oscillations which disturb the solution. There are two main methods to cope with this stability condition: (a) the stable mixed FE (b) the stabilised Variational MultiScale method (VMS). The stable mixed FE [49] is based on the use of P1+/P1 formulation, i.e. the velocity field is discretised with continuous piecewise linear functions enriched by bubble functions, and the pressure by piecewise linear functions. The second method (VMS) is designed to circumvent the stability condition while allowing the use of equal order linear interpolation P1/P1. The key idea of VMS method is to split the velocity and the pressure into two resolution scales, a coarse scale and a fine one. The fine scales are approximated and re-injected in the large-scale problem. The explicit presence of the fine-scale thus disappears, but its effect is accounted for in the resolvable equations. Here we present briefly the outlines of the method. For further details, the readers are referred to [50; 51].

Let us split the velocity and the pressure fields into resolvable coarse-scale $(\boldsymbol{u}_h, p_h)$ and unresolved fine-scale $(\boldsymbol{u}', p')$ such as $\boldsymbol{u} = \boldsymbol{u}_h + \boldsymbol{u}'$ and $p = p_h + p'$. We apply the same decomposition to the interpolation functions such as $\mathscr{U} = \mathscr{U}_h + \mathscr{U}'$ and $\mathscr{P} = \mathscr{P}_h + \mathscr{P}'$. The functional spaces are defined as $\mathrm{V} = \mathrm{V}_h \oplus \mathrm{V}'$, $\mathrm{V}_0 = \mathrm{V}_{h,0} \oplus \mathrm{V}'_0$ and $\mathrm{Q} = \mathrm{Q}_h \oplus \mathrm{Q}'$. The discretised, FE approximation for the time-dependent Navier-Stokes problem therefore reads:

Find$(\boldsymbol{u}, p) \in \mathrm{V} \times \mathrm{Q}$ such that:

$$\begin{cases} \rho\left(\frac{\partial(\boldsymbol{u}_h+\boldsymbol{u}')}{\partial t}, (\mathscr{U}_h + \mathscr{U}')\right)_\Omega + \big(\rho(\boldsymbol{u}_h + \boldsymbol{u}')\cdot\boldsymbol{\nabla}(\boldsymbol{u}_h + \boldsymbol{u}'), (\mathscr{U}_h + \mathscr{U}')\big)_\Omega \\ \qquad + \big(2\mu\dot{\epsilon}(\boldsymbol{u}_h + \boldsymbol{u}') : \dot{\epsilon}(\mathscr{U}_h + \mathscr{U}')\big)_\Omega - \big((p_h + p'), \boldsymbol{\nabla}\cdot(\mathscr{U}_h + \mathscr{U}')\big)_\Omega \\ \qquad + \big(\Delta t\, \gamma\, \delta\, \left(\boldsymbol{\nabla}(\boldsymbol{u}_h + \boldsymbol{u}').\mathbb{P}\right) : \boldsymbol{\nabla}(\mathscr{U}_h + \mathscr{U}')\big)_\Omega = \big(\mathbf{f} + \mathbf{f}_{\mathbf{ST}}, (\mathscr{U}_h + \mathscr{U}')\big)_\Omega, \quad \forall \mathscr{U} \in \mathrm{V}_0 \\ \big(\boldsymbol{\nabla}\cdot(\boldsymbol{u}_h + \boldsymbol{u}'), (\mathscr{P}_h + \mathscr{P}')\big)_\Omega = 0, \quad \forall \mathscr{P} \in \mathrm{Q}. \end{cases} \tag{3.49}$$

In order to derive the stabilised formulation, we split Equation (3.49) into a large-scale and a fine-scale problem. The fine-scale problem is defined on element interiors. Under several assumptions regarding the time-dependency and the non-linearity of the momentum equation of the sub-scale system detailed in [51], the fine-scale solutions $\boldsymbol{u}'$ and p' are written in terms of the time-dependent large-scale variables using consistently derived residual-based terms. Consequently, we can use static condensation, that consists in substituting directly $\boldsymbol{u}'$ and p' into the large-scale problem, which gives rise to additional terms in the FE formulation, tuned by a local stabilising parameter. These terms are responsible for the enhanced stability compared to the standard Galerkin formulation. The large-scale system finally reads:

$$\begin{cases} \left(\rho\frac{\partial \boldsymbol{u}_h}{\partial t}, \mathscr{U}_h\right)_\Omega + \big(\rho\boldsymbol{u}_h\cdot\boldsymbol{\nabla}\boldsymbol{u}_h, \mathscr{U}_h\big)_\Omega + \big(2\mu\dot{\epsilon}(\boldsymbol{u}_h) : \dot{\epsilon}(\mathscr{U}_h)\big)_\Omega \\ \qquad - \big(p_h, \boldsymbol{\nabla}\cdot\mathscr{U}_h\big)_\Omega + \big(\Delta t\, \gamma\, \delta\, (\boldsymbol{\nabla}\boldsymbol{u}_h.\mathbb{P}) : \boldsymbol{\nabla}\mathscr{U}_h\big)_\Omega \\ \qquad - \sum_{\mathrm{K}\in\mathscr{T}_h}\big(\tau_1\mathscr{R}_{\mathrm{M}}, \rho\boldsymbol{u}_h\boldsymbol{\nabla}\mathscr{U}_h\big)_{\mathrm{K}} - \sum_{\mathrm{K}\in\mathscr{T}_h}(\tau_2\mathscr{R}_{\mathrm{C}}, \boldsymbol{\nabla}\cdot\mathscr{U}_h)_{\mathrm{K}} = \big(\boldsymbol{f} + \boldsymbol{f}_{\mathbf{ST}}, \mathscr{U}_h\big)_\Omega, \quad \forall \mathscr{U}_h \in \mathrm{V}_{h,0} \\ (\boldsymbol{\nabla}\cdot\boldsymbol{u}_h, \mathscr{P}_h)_\Omega - \sum_{\mathrm{K}\in\mathscr{T}_h}(\tau_1\mathscr{R}_{\mathrm{M}}, \boldsymbol{\nabla}\mathscr{P}_h)_{\mathrm{K}} = 0, \quad \forall \mathscr{P}_h \in \mathrm{Q}_h \end{cases} \tag{3.50}$$

where $\mathscr{R}_{\mathrm{M}}$ and $\mathscr{R}_{\mathrm{C}}$ are momentum and continuity residual expressed as

$$\begin{aligned} &\mathscr{R}_{\mathrm{M}} = \boldsymbol{f} + \boldsymbol{f}_{\mathbf{ST}} - \rho\partial_t \boldsymbol{u}_h - \rho \boldsymbol{u}_h \cdot \boldsymbol{\nabla} \boldsymbol{u}_h - \boldsymbol{\nabla} p_h \\ &\mathscr{R}_{\mathrm{C}} = -\boldsymbol{\nabla} \cdot \boldsymbol{u}_h \end{aligned} \tag{3.51}$$

and τ_1 and τ_2 are stabilization parameters for which we adopt the definition proposed in [52]:

$$\tau_1 = \left[\left(\frac{2\rho\|\boldsymbol{u}_h\|_{\mathrm{K}}}{h_{\mathrm{K}}}\right)^2 + \left(\frac{4\mu}{h_{\mathrm{K}}^2}\right)^2\right]^{-\frac{1}{2}}, \tag{3.52}$$

$$\tau_2 = \left[\left(\frac{\mu}{\rho}\right)^2 + \left(\frac{c_2\|\boldsymbol{u}_h\|_{\mathrm{K}}}{c_1 h_{\mathrm{K}}}\right)^2\right]^{\frac{1}{2}} \tag{3.53}$$

where h_{K} is the characteristic length of the element and c_1 and c_2 are algorithmic constants. We take them as $c_1 = 4$ and $c_2 = 2$ for linear elements [52]. Compared to the standard Galerkin method, the proposed stabilised formulation involves additional integrals that are evaluated element-wise. These additional terms represent the stabilising effect of the sub-grid scales and are introduced consistently in the Galerkin formulation. They allow avoiding instabilities caused by both dominant convection terms and incompatible approximation spaces.

The final resolvable set of equations of Navier-Stokes including the implicit term of surface tension and the semi-implicit BDF time discretisation reads:

$$\left\{\begin{aligned} &\left(\rho\frac{\alpha_\sigma \boldsymbol{u}_h}{\Delta t}, \mathscr{U}_h^{\mathrm{SUPG}}\right)_{\mathrm{K}} + \left(\rho\boldsymbol{u}_h^{\mathrm{BNG},\sigma}.\boldsymbol{\nabla}\boldsymbol{u}_h, \mathscr{U}_h^{\mathrm{SUPG}}\right)_{\mathrm{K}} + \left(2\mu\dot{\boldsymbol{\epsilon}}(\boldsymbol{u}_h) : \dot{\boldsymbol{\epsilon}}(\mathscr{U}_h)\right)_{\mathrm{K}} + \left(\boldsymbol{\nabla} p_h, \mathscr{U}_h^{\mathrm{SUPG}}\right)_{\mathrm{K}} \\ &\qquad + (\tau_2\boldsymbol{\nabla}.\boldsymbol{u}_h, \boldsymbol{\nabla}.\mathscr{U}_h)_{\mathrm{K}} + \left(\Delta t\ \gamma\ \delta\ (\boldsymbol{\nabla}\boldsymbol{u}_h.\mathbb{P}) : \boldsymbol{\nabla}\mathscr{U}_h\right)_{\mathrm{K}} = \left(\boldsymbol{f} + \boldsymbol{f}_{\mathbf{ST}} + \rho\frac{\boldsymbol{u}_h^{\mathrm{BDF},\sigma}}{\Delta t}, \mathscr{U}_h^{\mathrm{SUPG}}\right)_{\mathrm{K}} \\ &\left(\rho\frac{\alpha_\sigma \boldsymbol{u}_h}{\Delta t}, \tau_1\boldsymbol{\nabla}\mathscr{P}_h\right)_{\mathrm{K}} + \left(\rho\boldsymbol{u}_h^{\mathrm{BNG},\sigma}.\boldsymbol{\nabla}\boldsymbol{u}_h, \tau_1\boldsymbol{\nabla}\mathscr{P}_h\right)_{\mathrm{K}} + (\boldsymbol{\nabla} p_h, \tau_1\boldsymbol{\nabla}\mathscr{P}_h)_{\mathrm{K}} \\ &\qquad + (\boldsymbol{\nabla}.\boldsymbol{u}_h, \mathscr{P}_h)_{\mathrm{K}} = \left(\boldsymbol{f} + \boldsymbol{f}_{\mathbf{ST}} + \rho\frac{\boldsymbol{u}_h^{\mathrm{BDF},\sigma}}{\Delta t}, \tau_1\boldsymbol{\nabla}\mathscr{P}_h\right)_{\mathrm{K}} \end{aligned}\right. \tag{3.54}$$

where

$$\mathscr{U}_h^{\mathrm{SUPG}} = \mathscr{U}_h + \tau_1\rho\boldsymbol{u}_h\boldsymbol{\nabla}\mathscr{U}_h \tag{3.55}$$

The term coloured in red expresses the contribution of semi-implicit surface tension. As for the terms coloured in blue, they are showing the contribution of the semi-implicit BDF time discretisation of the transient and advection terms in Navier Stokes. More details about this methodology are available in [51].

3.4 Partial conclusion

Let us summarise what we have done so far in this chapter. We have presented our numerical framework for modelling a two-fluid incompressible flow, including a moving interface governed by surface tension. The current numerical framework is based on the use of a global computational domain with a single Eulerian mesh for both fluids. The interface is implicitly represented by the Level-Set function. The time-evolution of the interface is monitored by solving a transport equation of the Level-Set function. The flow dynamics is described by conservation equations given by Navier-Stokes. A monolithic formulation of mass conservation and momentum enables the resolution of a single set of equations over the entire computational domain. These equations are enriched by the contribution of surface tension as a volume force via the CSF method. The Navier-Stokes resolution is based on the stabilised FE VMS method. We have also suggested some numerical improvements to address numerical issues such as mass loss, spurious currents, penalising stability condition and numerically-added diffusion. Now we move on to the assessment step of our numerical modelling. For this purpose, our evaluation must be based on the criteria of mass conservation described by the Level-Set function and of mechanical energy conservation given by the flow velocity field governed by surface tension and the mechanical properties of the fluids.

The test case of the oscillating drop is a perfect candidate for the evaluation of current numerical modelling on the previously-mentioned criteria. This test case consists in studying the oscillations of a liquid drop surrounded by gas in weightlessness. The drop is released from a deformed shape. The surface tension at the liquid-gas interface causes the drop to oscillate around its equilibrium shape. The frequency of the oscillations is correlated with the value of the surface tension. The amplitude of the oscillations is damped due to the viscous friction forces of the bulk liquid, thus related to the viscosity. In this test case, the system is considered to be isothermal. The volume of the drop must, therefore, be constant to preserve the mass. Accordingly, the time-evolution of the volume described by the Level-Set function will allow us to evaluate the mass conservation. Knowing the analytical expression of the frequency of the oscillations and their damping rate as a function of the properties of the fluid, we will be able to compare the numerical results with the theory. Before being a numerical test case, the oscillating drop was first an experimental technique used to measure the surface tension and viscosity of liquids. The measurements are based on the use of some existing theories. Rayleigh [53] and Lamb [54] are pioneers in the development of such analytical solutions. Their theories are the most widely used in experiments. However, all these theories are developed in 3D. For the evaluation of our numerical modelling, we have to perform several simulations with different parameters and numerical methods. The execution of several simulations in 3D is obviously time-consuming for such a parametric study. Hence, we suggest in this section to develop the theory of damped oscillations of a viscous liquid drop in 2D.

3.5 The oscillating drop method : analytical solution

3.5.1 State of the art

One of the main physical phenomena behind the oscillation of fluid drops is surface tension. It is well-known that when a liquid drop is sustained in a gas under microgravity, the surface tension makes the drop minimise the area of its interface with the surrounding gas. The equilibrium shape that corresponds to the minimal surface area is a sphere. When the drop is distorted from its equilibrium shape, it displays oscillations with a frequency correlated to surface tension. If the liquid is viscous, the oscillations are damped with a decay rate linked to viscosity. The knowledge of how the observed frequency and the damping rate are related to surface tension and viscosity, yields access to the values of these properties. This is the principle of the oscillating drop technique used for the measurement of surface tension and viscosity [55].

Shape oscillation of drops driven by surface tension has been addressed theoretically by several authors over more than a century. The earliest theoretical investigation started with Rayleigh who derived, under the irrotational flow assumption, the frequency spectrum of small-amplitude axisymmetrical oscillations of non-viscous drops in a vacuum with zero gravity [53]. This analysis was extended by Lamb to inviscid drops immersed in an inviscid medium [56]. Lamb also showed that for weakly viscous liquids, the frequency spectrum is identical to that found by Rayleigh and the assumption of the irrotational flow can be used to determine the damping rate [54]. Valentine et al. used the same approximation to derive the frequency and the damping rate of oscillating drops in liquid-liquid systems [57]. Miller and Scriven established that the irrotational approximation does not account for the dissipation in the boundary layer near the interface which is predominant for liquid-liquid systems even though the viscosities are very low unless the droplet size is very small [58]. They proposed a general solution for the linear oscillations of liquid droplets hosted in another fluid medium for arbitrary viscosities including the interfacial viscoelastic properties. However, their solution is limited to free non-extensible interfaces. Prosperetti derived a more general solution [59] and showed that for the limiting case of low viscosities, the drop behaves as a damped harmonic oscillator [60]. Further studies of this problem analysed the nonlinear oscillations starting from moderate-amplitudes by Tsamopoulos and Brown [61] to large-amplitudes with Lundgreen and Mansour [62], Trinh and Wang [63], and Foote [64]. Correction of the Rayleigh theory that includes the effect of both temperature variations and large-amplitudes was also proposed by Xiao et al. [65].

Many other investigations have been dedicated to the oscillations of a drop sustained against gravity by a levitation technique. The use of a strong levitator field can make the equilibrium shape of the levitated drop aspherical. Thus, the presence of the levitator field affects the dynamics of the drop interface and the theories cited above must be revisited. For this purpose, Cummings and Blackburn proposed an approximated solution for a non-viscous drop in an electromagnetic levitator [66]. Later on, their work was extended by Bratz and Egry to account for the viscous dissipation effect for the same levitation technique [67]. However, their theories cannot take into consideration the electromagnetic stirring, which leads to turbulent flow in the bulk liquid. In the presence of turbulence, the observed damping rate includes the effect of the turbulent viscosity, which is not modelled in the available theories.

For the sake of more accuracy, measurements under microgravity are carried out, preferentially within the limit of maximum 1% small-amplitude axisymmetrical oscillations with mode $n = 2$ [68]. The objective is to approach at best the approximations of the Rayleigh and Lamb theories. Despite these efforts, it does not remain straightforward to tailor experimental conditions. The thorough interpretations of raw data are indeed challenging due to various deleterious effects:

oscillation amplitude, sample rotation and procession, temperature variation, mixture of oscillation modes [61]-[65]. Only very recently and based on careful analyses of selected experimental data conducted in the ISS, Wunderlich and Mohr concluded that non-linear effects are not present even when reaching up to 10% deformation in liquid metallic drops [69].

Most of these theoretical analyses confine the attention to three-dimensional (3D) cases regarding their relevance for experiments and real applications, whereas the two-dimensional (2D) cases have been marginally addressed. The 2D oscillations of a free-surface around a circular shape correspond to the oscillations occurring in a transverse section of a liquid jet injected from a non-circular orifice and showing no longitudinal variations. This configuration has been studied by Rayleigh for an inviscid liquid [53]. For the best of our knowledge, no analytical solution for damped oscillations of this 2D configuration has been explicitly derived. This configuration will be referred to as the "2D drop" case.

The present work is an extension of Rayleigh's theory by adding the viscous effect of the inner flow. Lamb addressed the damped oscillations for small viscosities assuming a priori that the oscillation frequency found by Rayleigh is not altered by viscosity. Unlike Lamb, the solution derived hereafter applies for whatever value of the viscosity, i.e. for finite viscous and potential forces. Furthermore, it will be shown that three possible regimes of an initially-distorted drop can describe its behaviour: aperiodic regime, critically-damped regime and oscillatory regime. In the latter regime, the oscillation frequency results from the interaction between surface tension and viscosity. Although the effect of the non-negligible viscosity has been studied by Prosperetti in more comprehensive and sophisticated cases[59]-[60], the present work re-derives the 3D solution in a rather simple way through the energy balance. The novelty also lies in the 2D solution, which can provide a quantitative benchmark for testing the accuracy and the robustness of numerical modelling of multiphase flows.

3.5.2 The free-oscillating viscous drop problem

Hereafter we first present the set of equations to describe the oscillation of a free-surface around a (2D) circular and (3D) spherical shape while considering possible interactions between finite viscous and potential forces. The analytical solution will be derived for the time-evolution of the radius of the free-surface as well as the spatial-temporal variation of the velocity field in the bulk liquid.

3.5.2.1 Governing equations

Consider the motion of a Newtonian liquid of density ρ^l and viscosity μ^l. Let Ω^l be the time-dependent domain occupied by the liquid and Γ its interface with a surrounding low-density gas phase or, more simply, with a vacuum. The liquid is assumed incompressible with a constant density of ρ^l, isothermal, and no phase transformation is considered. We also neglect all external forces (gravity, magnetic field, forced gas flow, etc.) applied to the liquid. In this framework, the flow is governed by the following Navier-Stokes equations:

$$\begin{cases} \rho^l \left(\dfrac{\partial \boldsymbol{u}^l}{\partial t} + \nabla \boldsymbol{u}^l \cdot \boldsymbol{u}^l \right) - \boldsymbol{\nabla} \cdot \boldsymbol{\sigma}^l = \boldsymbol{0} \\ \boldsymbol{\nabla} \cdot \boldsymbol{u}^l = 0 \end{cases} \tag{3.56}$$

$\boldsymbol{u}^l$ is the liquid velocity vector and $\boldsymbol{\sigma}^l$ is the liquid stress tensor given by the incompressible Newtonian constitutive law:

$$\boldsymbol{\sigma}^l = 2\mu^l \dot{\boldsymbol{\epsilon}}^l - p^l \mathbb{I} \tag{3.57}$$

where $\dot{\boldsymbol{\epsilon}}^l = \frac{1}{2}\left[\boldsymbol{\nabla}\boldsymbol{u}^l + (\boldsymbol{\nabla}\boldsymbol{u}^l)^{\mathrm{T}}\right]$ is the strain-rate tensor, p^l is the pressure field in the liquid and $\mathbb{I}$ is the identity tensor.

At the time $t = 0s$, we assume that we know the initial shape of the liquid domain and its velocity field such as:

$$\Omega^l(0) = \Omega^l_0, \quad \boldsymbol{u}^l(x,0) = \boldsymbol{u}^l_0(x), \quad \boldsymbol{\nabla}.\boldsymbol{u}^l_0 = 0 \tag{3.58}$$

Since no mass exchange occurs through Γ, the local mass flux leaving the liquid domain $\rho^l(\boldsymbol{u}^l.\boldsymbol{n} - v_\Gamma)$ is zero, where $\boldsymbol{n}$ is the unit external normal vector on Γ and v_Γ is its normal velocity. This leads to writing the kinematic interface condition as:

$$\boldsymbol{u}^l \cdot \boldsymbol{n} = v_\Gamma \tag{3.59}$$

The second interface condition, named the dynamic condition, arises from the force balance at the interface Γ:

$$\boldsymbol{\sigma}^l \cdot \boldsymbol{n} = -\gamma\kappa\boldsymbol{n} - p_{ext}\boldsymbol{n} \tag{3.60}$$

where γ is surface tension coefficient, κ is the curvature of the interface and p_{ext} is the pressure in the surrounding gas phase. Further assuming that the liquid is placed in vacuum, Γ is a free surface and $p_{ext} = 0$.

3.5.2.2 Energy balance

To obtain the energy balance of the drop, we integrate the scalar product of the second equation of (3.56) with the velocity vector over Ω^l as follows:

$$\iiint\limits_{\Omega^l} \left[\rho^l \left(\frac{\partial \boldsymbol{u}^l}{\partial t} + \nabla \boldsymbol{u}^l \cdot \boldsymbol{u}^l \right) - \boldsymbol{\nabla} \cdot \boldsymbol{\sigma}^l \right] \cdot \boldsymbol{u}^l \, d\mathrm{V} = 0 \tag{3.61}$$

After integrating by part the stress tensor term, we can write:

$$\iiint\limits_{\Omega^l} \frac{1}{2}\rho^l \left(\frac{\partial \boldsymbol{u}^{l2}}{\partial t} + \boldsymbol{u}^l \cdot \boldsymbol{\nabla}\boldsymbol{u}^{l2} \right) d\mathrm{V} - \iint\limits_{\Gamma} \boldsymbol{\sigma}^l \cdot \boldsymbol{n} \cdot \boldsymbol{u}^l \, d\mathrm{S} + \iiint\limits_{\Omega^l} \boldsymbol{\sigma}^l : \boldsymbol{\nabla}\boldsymbol{u}^l \, d\mathrm{V} = 0 \tag{3.62}$$

The development of this equation (details are given in the appendix) leads to the following equation:

$$\frac{d}{dt}\underbrace{\left(\iiint_{\Omega^l}\frac{1}{2}\rho^l \boldsymbol{u}^{l^2}\,dV\right)}_{E^l_{kin}\text{: kinetic energy}} + \frac{d}{dt}\underbrace{\left(\iint_{\Gamma}\gamma\,dS\right)}_{E^l_{pot}\text{: potential energy}} + \underbrace{\iiint_{\Omega^l} 2\mu^l\,\dot{\boldsymbol{\epsilon}}^l : \dot{\boldsymbol{\epsilon}}^l\,dV}_{\dot{W}^l_{vis}\text{: work of viscous force}} = 0 \tag{3.63}$$

This equation expresses the energy balance:

$$\frac{d}{dt}\left(E^l_{kin} + E^l_{pot}\right) = -\dot{W}^l_{vis} \tag{3.64}$$

3.5.3 Analytical solutions in the framework of the linear theory

3.5.3.1 Drop shape description

The physics of oscillation refers to the time and space evolution of the surface at the liquid-gas interface Γ. As shown in figure 3.5a, we look for the solution of $R(\theta, \phi, t)$ for the interface position of a perturbed spherical droplet in 3D assuming axisymmetric variations with respect to z-axis (no dependence on ϕ). In 2D, the solution $R(\theta, t)$ is the interface position of a perturbed cross section through an infinite cylinder as shown in figure 3.5b. In the latter case, denoting z the longitudinal axis of the cylinder, the analysis is focused on a cross section of infinitely small portion δz defining the liquid domain of surface Ω^l and contour Γ. We consider that the liquid is Newtonian and the flow is incompressible.

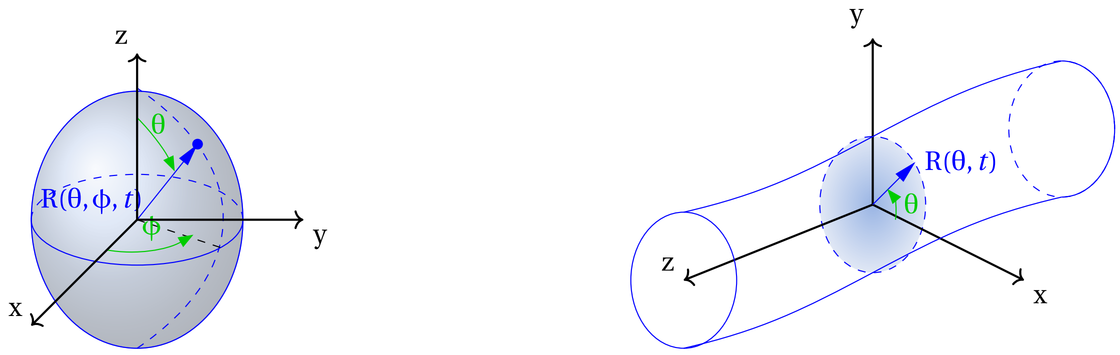

(a) Schematic of 3D axisymetric oscillations occurring in a spherical droplet

(b) Schematic of 2D oscillations occurring in a cross section of an infinite cylinder

Figure 3.5: Schematics of the framework of 3D and 2D oscillations

The radius of the free surface at each section of the cylinder can be expressed as the sum of a constant part represented by the equilibrium radius R_0 and a variable part $f(\theta, t)$ which describes the spatial-temporal variations of the free-surface from its equilibrium shape:

$$R(\theta, t) = R_0 + f(\theta, t) \tag{3.65}$$

As there is no dependency on ϕ angle in 3D axisymmetric configuration, formulation (3.65) is valid also for the 3D case.

In this paper, we work in the context of small-amplitude variations. Therefore, we can write

$f(\theta, t)$ as a linear combination of normal modes denoted by the integer n as follows:

$$f(\theta,t) = \sum_{n=0}^{\infty} \alpha_n(t) cos(n\theta) \quad \text{for 2D} \tag{3.66a}$$

$$f(\theta,t) = \sum_{n=0}^{\infty} \alpha_n(t) P_n(cos(\theta)) \quad \text{for 3D} \tag{3.66b}$$

where

- $\frac{\alpha_n(t)}{R_0} \ll 1$.
- P_n are Legendre polynomials.
- Mode $n = 0$ is related to the volume oscillation. We denote by $b_0(t)$ the sum $R_0 + \alpha_0(t)$. Thus b_0 will be determined hereafter by the condition that the volume must remain constant.
- Mode $n = 1$ describes the translational oscillations of the mass centre. We consider that the mass centre is fix (zero translational velocity). Consequently $\alpha_1(t) = 0$.
- Modes $n \geq 2$ describe the shape oscillations around the equilibrium. In the linear theory we can consider that these modes are independent each other and can be treated separately.

Following these considerations, the radius reads:

$$R(\theta,t) = b_0(t) + \alpha_n(t) cos(n\theta) \quad \text{for 2D} \tag{3.67a}$$

$$R(\theta,t) = b_0(t) + \alpha_n(t) P_n(cos(\theta)) \quad \text{for 3D} \tag{3.67b}$$

Note that in the latter equation and in the following $n \geq 2$.

Assuming that the flow is incompressible, the volume of the oscillating drop is the same as the volume at the equilibrium. Thus:

$$V = \delta z \int_{\theta=0}^{2\pi} \int_{r=0}^{R(\theta,t)} r dr d\theta = \delta z(\pi b_0^2 + \frac{1}{2}\pi\alpha_n^2) = \delta z \pi R_0^2 \quad \text{for 2D} \tag{3.68a}$$

$$V = 2\pi \int_{\theta=0}^{\pi} \int_{r=0}^{R(\theta,t)} r^2 dr sin(\theta) d\theta = \frac{4\pi}{3} b_0^3 \left(1 + \frac{3}{2n+1}\left(\frac{\alpha_n}{b_0}\right)^2\right) = \frac{4\pi}{3} R_0^3 \quad \text{for 3D} \tag{3.68b}$$

Hence,

$$b_0 = R_0 \sqrt{1 - \frac{1}{2}(\frac{\alpha_n}{R_0})^2} \approx R_0 \left(1 - \frac{1}{4}\left(\frac{\alpha_n}{R_0}\right)^2\right) \quad \text{for 2D} \tag{3.69a}$$

$$b_0 = R_0 \left(1 + \frac{3}{2n+1}\left(\frac{\alpha_n}{b_0}\right)^2\right)^{-\frac{1}{3}} \approx R_0 \left(1 - \frac{1}{2n+1}\left(\frac{\alpha_n}{R_0}\right)^2\right) \quad \text{for 3D} \tag{3.69b}$$

Then the radius can be approximated as

$$R(\theta,t) = R_0 \left(1 + \varepsilon_n cos(n\theta) - \frac{1}{4}\varepsilon_n^2\right) \quad \text{for 2D} \tag{3.70a}$$

$$R(\theta,t) = R_0 \left(1 + \varepsilon_n P_n(cos(\theta)) - \frac{1}{2n+1}\varepsilon_n^2\right) \quad \text{for 3D} \tag{3.70b}$$

where $\varepsilon_n = \frac{\alpha_n}{R_0} \ll 1$. It is worth noting that for small-amplitude oscillations, the term ε_n^2 is negligible. However, it will be shown in section 3.5.3.3 that potential energy is of the same order as ε_n^2. Consequently, its presence in equation (3.70) is crucial for the approximation of the potential energy

The objective now is to find the time-variation of ε_n. The outlines of our demonstration are the following: we assume that the flow is irrotational, and we find the velocity potential, then we compute the kinetic and potential energies of the drop. Next, we express the viscous energy dissipation. Finally, we apply the energy balance, which leads to a linear differential equation of the quantity ε_n.

3.5.3.2 Inner flow modelling

Following the discussion in [70], the fluid motion can be approximated by an irrotational flow. The velocity field derives from a potential $\boldsymbol{u}^l = \boldsymbol{\nabla}\varphi$.

The velocity potential of the n^{th} mode can be formulated as:

$$\varphi(r,\theta,t) = \beta_n(t) r^n cos(n\theta) \quad \text{for 2D} \tag{3.71a}$$

$$\varphi(r,\theta,t) = \beta_n(t) r^n P_n(cos(\theta)) \quad \text{for 3D} \tag{3.71b}$$

The coefficient β_n is obtained from the kinematic boundary condition at the free-surface

$$u_r^l(r=R) = \frac{\partial\varphi}{\partial r}(r=R) = \frac{\partial R}{\partial t} \tag{3.72}$$

This condition leads to the following approximation which is the same for both 2D and 3D analyses: $n\beta_n R_0^{n-2} \approx \dot{\varepsilon}_n$ Hence, we can write the velocity potential as follows:

$$\varphi(r,\theta,t) = \frac{1}{n} R_0^2 \left(\frac{r}{R_0}\right)^n cos(n\theta)\dot{\varepsilon}_n(t) \quad \text{for 2D} \tag{3.73a}$$

$$\varphi(r,\theta,t) = \frac{1}{n} R_0^2 \left(\frac{r}{R_0}\right)^n P_n(cos(\theta))\,\dot{\varepsilon}_n(t) \quad \text{for 3D} \tag{3.73b}$$

3.5.3.3 The energy balance

The kinetic energy of the drop is given by

$$E_{kin}^l = \iiint\limits_V \frac{1}{2}\rho^l \left\|\boldsymbol{\nabla}\varphi\right\|^2 dV = \iint\limits_S \frac{1}{2}\rho^l \varphi \boldsymbol{\nabla}\varphi.\boldsymbol{n} dS - \iiint\limits_V \frac{1}{2}\rho^l \varphi \underbrace{\boldsymbol{\nabla}^2\varphi}_{=0} dV \tag{3.74}$$

$$E_{kin}^l = \frac{1}{2}\rho^l \delta z \int_0^{2\pi} \varphi \frac{\partial\varphi}{\partial r} R d\theta \approx \frac{1}{2n}\pi\rho^l R_0^4 \dot{\varepsilon}_n^2 \delta z \quad \text{for 2D} \tag{3.75a}$$

$$E_{kin}^l = \pi\rho^l \int_0^{\pi} \varphi \frac{\partial\varphi}{\partial r} R^2 sin(\theta) d\theta \approx 2\pi\rho^l R_0^5 \frac{1}{n(2n+1)} \dot{\varepsilon}_n^2 \quad \text{for 3D} \tag{3.75b}$$

Following the work of Rayleigh [53], the potential energy is expressed as:

$$E^l_{pot} = \gamma (S - S_0) \tag{3.76}$$

Where S denotes the area of the free-surface and S_0 the area of the equilibrium shape.

For the 2D case, the area $S = \delta z P$ where P is the perimeter of the cross section of the cylinder and $S_0 = 2\pi R_0^2 \delta z$. The perimeter P is calculated through the following integral:

$$P = \int_0^{2\pi} \sqrt{R^2 + \left(\frac{\partial R}{\partial \theta}\right)^2} d\theta \quad \text{for 2D} \tag{3.77}$$

Using the expression of the radius R given by the equation (3.70a) and Taylor expansions we obtain the following approximation

$$P \approx 2\pi R_0 + \frac{1}{2}\pi(n^2 - 1) R_0 \varepsilon_n^2 \tag{3.78}$$

For the 3D case, the area S of the drop is expressed as:

$$S = 2\pi \int_0^{\pi} \sqrt{R^2 + \left(\frac{\partial R}{\partial \theta}\right)^2} R sin(\theta) d\theta \quad \text{for 3D} \tag{3.79}$$

After replacing R by the expression (3.70b), we use Taylor series and some known properties of Legendre polynomials. The area S of the 3D drop is approximated as follows

$$S \approx S_0 + 2\pi R_0^2 \frac{n^2 + n - 2}{2n+1} \varepsilon_n^2 \tag{3.80}$$

where $S_0 = 4\pi R_0^2$

Hence,

$$E^l_{pot} \approx \frac{1}{2}\pi(n^2 - 1)\gamma R_0 \delta z \varepsilon_n^2 \quad \text{for 2D} \tag{3.81a}$$

$$E^l_{pot} \approx 2\pi\gamma R_0^2 \frac{(n+2)(n-1)}{2n+1} \varepsilon_n^2 \quad \text{for 3D} \tag{3.81b}$$

Now we can write the rate of change of the total energy:

$$\frac{dE^l_{tot}}{dt} = \pi \frac{1}{n} \rho^l R_0^4 \delta z \dot{\varepsilon}_n \left[\ddot{\varepsilon}_n + n(n^2 - 1) \frac{\gamma}{\rho^l R_0^3} \varepsilon_n \right] \quad \text{for 2D} \tag{3.82a}$$

$$\frac{dE^l_{tot}}{dt} = 4\pi\rho^l R_0^5 \frac{1}{n(2n+1)} \dot{\varepsilon}_n \left[\ddot{\varepsilon}_n + n(n-1)(n+2) \frac{\gamma}{\rho^l R_0^3} \varepsilon_n \right] \quad \text{for 3D} \tag{3.82b}$$

If the fluid is inviscid ($\mu^l = 0$), the conservation of the total energy $\frac{dE^l_{tot}}{dt} = 0$ leads to the solution of a perpetual oscillator of the form $\varepsilon_n(t) = A\cos(\omega_{n,0}t + B)$ where the angular frequency is

$$\omega_{n,0} = \sqrt{n(n-1)(n+1)\frac{\gamma}{\rho^l R_0^3}} \quad \text{for 2D} \tag{3.83a}$$

$$\omega_{n,0} = \sqrt{n(n-1)(n+2)\frac{\gamma}{\rho^l R_0^3}} \quad \text{for 3D} \tag{3.83b}$$

as it was found by Rayleigh [53].

As an extension of the work of Rayleigh, we take into consideration, the energy dissipation due to the viscous force of the the bulk liquid. For that, we calculate the rate of the viscous dissipation energy:

$$\dot{W}^l_{vis} = \iiint\limits_V 2\mu^l\left(\dot{\boldsymbol{\epsilon}}^l : \dot{\boldsymbol{\epsilon}}^l\right) dV \tag{3.84}$$

Following the work of Lamb in [56] we can write the volume integral as a surface integral:

$$\dot{W}^l_{vis} = \iint\limits_S \mu^l \frac{\partial \boldsymbol{u}^{l^2}}{\partial \boldsymbol{n}} dS \tag{3.85}$$

The integral over the free surface is calculated as follows:

$$\dot{W}^l_{vis} = \mu^l \delta z \int_0^{2\pi} \frac{\partial \|\nabla\varphi\|^2}{\partial r} R d\theta \quad \text{for 2D} \tag{3.86a}$$

$$\dot{W}^l_{vis} = \mu^l 2\pi \int_0^{\pi} \frac{\partial \|\nabla\varphi\|^2}{\partial r} R^2 sin(\theta) d\theta \quad \text{for 3D} \tag{3.86b}$$

Using Taylor expansions, the dissipation rate can be approximated as

$$\dot{W}^l_{vis} \approx 4\pi\mu^l R_0^2 \delta z\,(n-1)\,\dot{\varepsilon}_n^2 \quad \text{for 2D} \tag{3.87a}$$

$$\dot{W}^l_{vis} \approx 8\pi\mu^l R_0^3\,\frac{n-1}{n}\,\dot{\varepsilon}_n^2 \quad \text{for 3D} \tag{3.87b}$$

We can now write the energy balance given in (3.64). This leads to the following linear second order Ordinary Differential Equation (ODE):

$$\ddot{\varepsilon}_n + 2\lambda_n\dot{\varepsilon}_n + \omega_{n,0}^2\varepsilon_n = 0 \tag{3.88}$$

where

$$\lambda_n = 2n(n-1)\frac{\mu^l}{\rho^l R_0^2} \quad \text{for 2D} \tag{3.89a}$$

$$\lambda_n = (2n+1)(n-1)\frac{\mu^l}{\rho^l R_0^2} \quad \text{for 3D} \tag{3.89b}$$

The form of the solution of the ODE (3.88) depends on the sign of its reduced discriminant

$$\Delta'_n = \lambda_n^2 - \omega_{n,0}^2 \tag{3.90}$$

When $\Delta'_n > 0$ the viscosity is dominant over the surface tension. The solution corresponds to decay to the equilibrium shape without oscillations. This behaviour is known as the over-damped regime. When $\Delta'_n < 0$, the surface tension is dominant over viscosity. The solution corresponds to oscillations about the equilibrium shape with a decreasing amplitude and a frequency lower than the frequency of an inviscid fluid. In this case, we talk about the under-damped regime. In the particular case, when $\Delta'_n = 0$, the solution is a rapid relaxation to the equilibrium form without any oscillation. This is known as the critically damped regime.

Without detailing the well-known procedure for solving a linear second-order ODE, we synthesise, in which follows, the 3 different solutions of the ODE (3.88)

- Case $\Delta'_n > 0$: overdamped regime

$$\varepsilon_n(t) = e^{-\lambda_n t}\left[\varepsilon_n(0)\cosh(\sqrt{\Delta'_n}\,t) + \frac{\dot{\varepsilon}_n(0) + \lambda_n \varepsilon_n(0)}{\sqrt{\Delta'_n}}\sinh(\sqrt{\Delta'_n}\,t)\right] \tag{3.91}$$

- Case $\Delta'_n = 0$: Critically damped regime

$$\varepsilon_n(t) = e^{-\lambda_n t}\left[(\dot{\varepsilon}_n(0) + \lambda_n \varepsilon_n(0))\,t + \varepsilon_n(0)\right] \tag{3.92}$$

- Case $\Delta'_n < 0$: underdamped regime

$$\varepsilon_n(t) = e^{-\lambda_n t}\varepsilon_{n,max}\cos(\omega_n t + \zeta_n) \tag{3.93}$$

where

$$\left\{\begin{aligned} \omega_n &= \sqrt{\omega_{n,0}^2 - \lambda_n^2} \\ \varepsilon_{n,max}^2 &= \varepsilon_n^2(0) + \left(\frac{\dot{\varepsilon}_n(0) + \lambda_n \varepsilon_n(0)}{\sqrt{-\Delta'_n}}\right)^2 \\ \tan\zeta_n &= -\frac{\dot{\varepsilon}_n(0) + \lambda_n \varepsilon_n(0)}{\varepsilon_n(0)\sqrt{-\Delta'_n}} \\ &\cos(\zeta_n)\varepsilon_n(0) \geq 0 \end{aligned}\right. \tag{3.94}$$

3.6 Numerical simulations

3.6.1 2D preliminary numerical tests

In the first section of this chapter, we presented two methods for transporting the Level-Set function as well as the VMS method to solve a flow including surface tension with different time discretisation schemes. The objective of this sub-section is to compare all these methods and schemes in order to find the numerical parameters giving the best results with respect to the derived theory. This parametric study is performed through 2D simulations. To do so, we consider a droplet of liquid iron suspended in the air in the absence of gravity. The surface of the droplet is πR_0^2 where $R_0 = 3 \times 10^{-3}$ m is the radius of the equilibrium shape of the droplet. The material properties are taken at a temperature of 1800 K. The density of liquid iron is $\rho^l = 7040 \; kg.m^{-3}$ while the density of air is $\rho^g = 0.19 \; kg.m^{-3}$. The dynamic viscosities are $\mu^l = 5.85 \; 10^{-3} \; Pa.s$ and $\mu^g = 5.82 \; 10^{-5} \; Pa.s$ for liquid iron and air respectively. The density and viscosity ratios are large enough to neglect the effects of air on droplet dynamics. This condition is essential to be in agreement with the previous theoretical analysis, which assumes that the droplet is free of force. The whole system is enclosed in a square cavity of size $9 \times R_0$ (see figure 3.6). The initial droplet shape is slightly deformed according to the 4^{th} mode with a relative deformation of $\varepsilon_{4,0} = 2\%$. The initial radius of the droplet is written:

$$R(\theta, t=0) = R_0 \left(1 + \varepsilon_{4,0} cos(4\theta) - \frac{1}{4}\varepsilon_{4,0}^2\right) \tag{3.95}$$

Following the previous theoretical analysis, $\lambda_4^2 = 4.91 s^{-2}$ and $\omega_{4,0}^2 = 7.08 \times 10^5 rad^2.s^{-2}$. The reduced discriminant is $\Delta_4' = -7.08 \times 10^5 \approx -\omega_{4,0}^2$. This means that the drop displays an underdamped regime. The droplet is released from a zero-velocity initial state. The analytical expression of the radius of oscillation reads:

$$R(\theta, t) = R_0 \left(1 + \varepsilon_4(t) cos(4\theta) - \frac{1}{4}\varepsilon_4^2(t)\right) \tag{3.96}$$

where

$$\varepsilon_4(t) \approx \varepsilon_{4,0} e^{-\lambda_4 t} cos(\omega_{4,0} t) \tag{3.97}$$

Taking this analytical solution as a reference, in this parametric study, we first show the effect of the mass correction method on oscillation physics. Then, we compare two methods of transporting the Level-Set function: (i) solving the convection equation (3.2) + geometrical reinitialisation, here referred to as *Conv+DRT* (ii) solving the auto-reinitialisation convection equation (3.4), denoted by *Leveler*. Next, we will study the influence of the time discretisation scheme for the formulation of the surface tension: (i) explicit surface tension, denoted by *Explicit* and (ii) semi-implicit surface tension, denoted by *Implicit*. Next, we compare the results of temporal discretisation of the Navier-Stokes equations at order 1^{st} and those of a second-order discretisation. For all these latter tests, we use the same unstructured mesh, which consists of a square domain, containing about 59100 of triangular elements and 29559 of nodes. The mesh is refined within a circular band that covers the region likely to contain the interface during motion (see figure 3.6). Inside this region, the characteristic mesh size $h = 3 \times 10^{-5} \; m$. With this mesh resolution, the maximal time step allowed by the use of the explicit formulation of surface tension is $\Delta t_{max} = 2.3 \times 10^{-6} s$. Finally, in the last paragraph, we compare two different mesh resolutions.

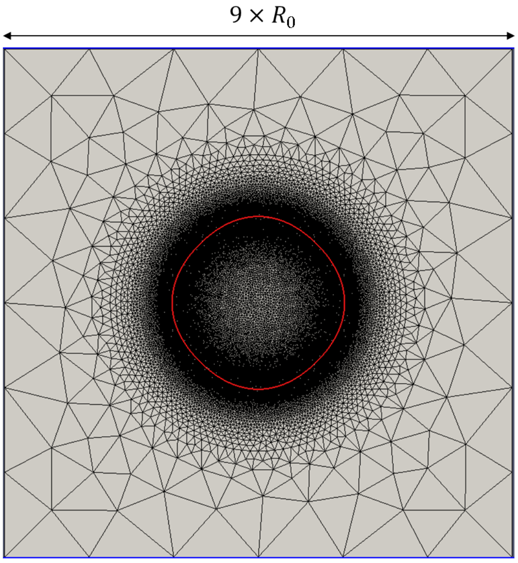

Figure 3.6: Mesh grid for the parametric study

3.6.1.1 Influence of the mass correction method

The goal here is first to evaluate the mass conservation of the standard numerical framework without mass correction, then to see either or not the mass correction method improves the mass conservation without altering the dynamics of the droplet. The classical numerical framework that we test is the standard CSF method introduced explicitly in Navier-Stokes equations with the Level-Set convection solver and the geometrical re-initialisation.

Figure 3.7a shows the time-evolution of the droplet radius in $\theta = 0$ direction for two simulations: without correction (black line) and with correction (blue line). Both signals are compared to the derived analytical solution (red line) given by equations (3.96) and (3.97). One can notice that the temporal signal extracted from the simulation without mass correction is oscillating around a decreasing equilibrium radius. This is nothing else than mass loss. Indeed, the temporal variation of the surface of the 2D drop, displayed in figure 3.7b, is decreasing linearly with a rate of 38% of the initial surface per 100 millisecond. With mass correction, the radius is oscillating around a constant equilibrium radius. We extract the oscillation frequency from the temporal signals via the *fft* (Figure 3.8). The peak of the spectrum indicates the oscillation frequency of the temporal signal. Without mass correction, the spectrum shows a frequency slightly higher than the theoretical one, which is in agreement with the fact that the frequency is inversely related to the equilibrium radius (3.83a). As the mass correction method preserves the equilibrium radius, the frequency spectrum is therefore enhanced and seems to be in perfect agreement with the theory. Therefore, the mass correction improves the mass conservation but does not alter the dynamics of the oscillating drop. However, one can observe from figure 3.7a that the amplitude of oscillations of the simulated signal is more damped than the theoretical one. This over-estimation of the damping rate is probably related to numerical diffusion. In the continuation of the current parametric study, we compare the numerical methods and schemes in terms of oscillation frequency together with the damping rate.

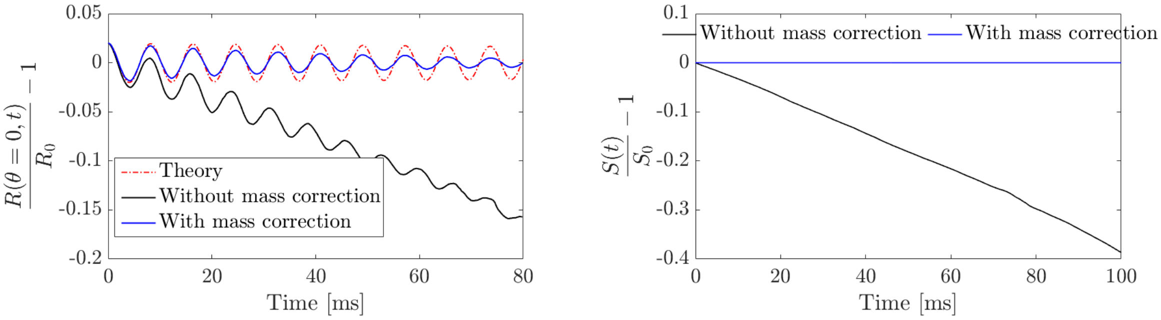

(a) (b)

Figure 3.7: (a) Comparison of the time-evolutions of the radius of the drop without mass correction (black line), the radius with mass correction (blue line) and the theoretical solution (red line)
(b) The temporal variation of the surface of the 2D drop without and with mass correction method

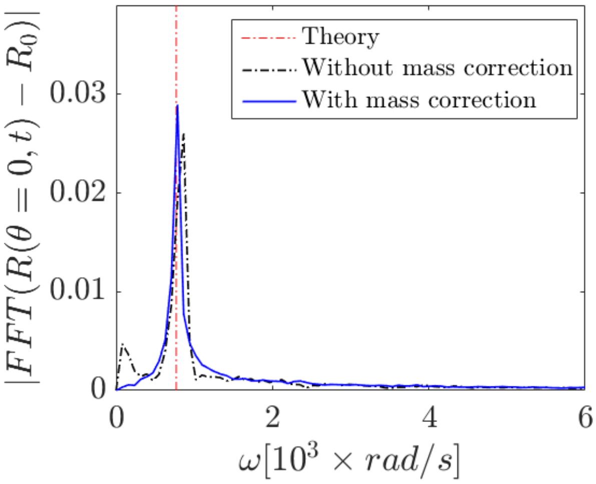

Figure 3.8: Comparison of the frequency spectrum of the radius of the drop without mass correction (black dashed line) and the spectrum with mass correction (blue line). The theoretical position of the peak is marked by the red dashed line

3.6.1.2 Influence of the Level-Set transport methods

In this sub-section, we compare two methodologies of transporting the Level-Set function: the convection and the reinitialisation (*Conv+DRT*) in two separate steps used in the previous test and the auto-reinitialised convected Level-Set method (*Leveler*). We first compare the mass conservation of the two methods. For that, simulations without mass correction are performed for both methods. Figure 3.9 shows the time-evolution of the surface of the 2D drop. We observe that the mass loss is much more reduced with *Leveler* method (only 0.86% per 100ms) than *Conv+DRT* method. When the mass correction method is applied for both methods, one can notice from figure 3.10 that the damping rate simulated with the *Leveler* method is closer to the theory than the *Conv+DRT* method.

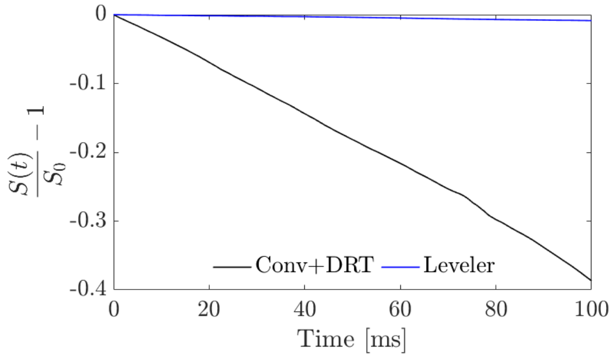

Figure 3.9: Comparison of the temporal variation of the surface of the 2D drop between the *Conv+DRT* method and *Leveler* method

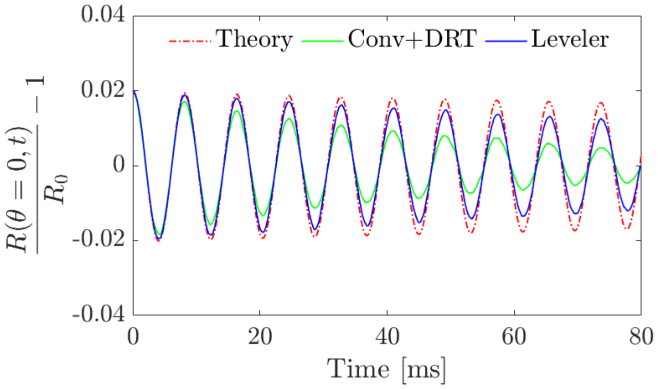

Figure 3.10: Comparison of the oscillation radius simulated with the *Conv+DRT* method (green line) and the radius simulated with the *Leveler* method (blue line)

3.6.1.3 Influence of the surface tension formulations

In the continuation of this parametric study, we keep using only the *Leveler* method as it is more conservative than *Conv+DRT* method. In this sub-section, we compare the semi-implicit formulation of surface tension to the explicit formulation. As the semi-implicit formulation allows time-steps higher than the stability limit Δt_{max}, two simulations for the semi-implicit surface tension are performed, one with Δt_{max} and the second with $10 \times \Delta t_{max}$. The results are shown in figure

3.11. For the same time step Δt_{max} the semi-implicit surface tension is more dissipative than the explicit formulation. For a higher time step, the numerical diffusion is even more important. In fact , the additional term given by the semi-implicit surface tension $\left(\Delta t\, \gamma\, \delta\, \left(\nabla \boldsymbol{u}^{n+1}.\mathbb{P}\right) : \nabla \boldsymbol{w}\right)_{\Omega}$ has the form of the work of a viscous dissipative force which increases when the time-step increases. This additional term is responsible for the stabilisation of the calculation when the time-step condition is broken, but on the other hand, it involves additional numerical dissipation.

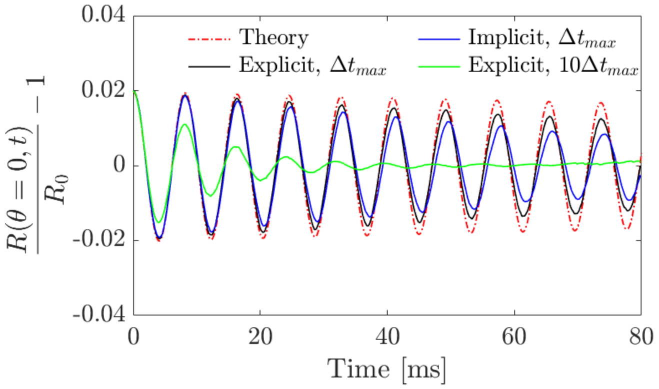

Figure 3.11: Comparison of the oscillation radius simulated with the explicit surface tension and the radius simulated with the semi-implicit surface tension with different time steps

As a conclusion of this test, the semi-implicit surface tension to go beyond the time step limit of stability which can reduce the computational time significantly. However, it adds an artificial diffusion and the higher the time step, the higher the added diffusion. In what follows, we keep using the explicit formulation, although the maximal time step allowed is very small.

3.6.1.4 Influence of the time-discretisation order

In all the latter tests, the transient terms either in the Level-Set convection equation or in Navier-Stokes equations are discretised using a 1^{st} order scheme. Now we test a second-order time scheme both for the Level-Set transport and Navier-Stokes. In figure 3.12, we can see that the second-order improves the prediction of the damping rate, especially when we decrease the time-step. This finding is consistent with the fact that a high discretisation order is known to reduce the discretisation errors and thus the numerical diffusion.

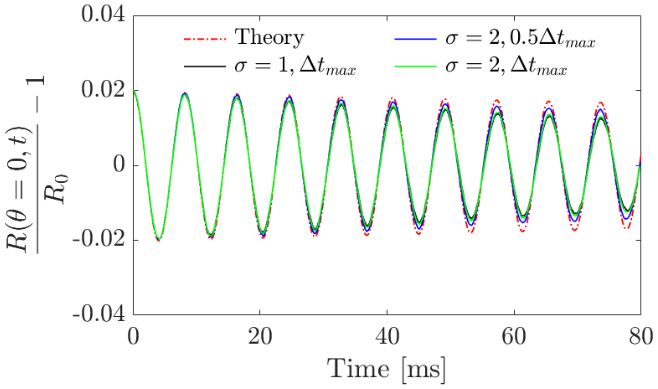

Figure 3.12: Comparison of the oscillation radius simulated with the 1^{st} order of discretisation of Navier-Stokes and the radius simulated with 2^{nd} order with different time steps

3.6.1.5 Influence of the mesh resolution

So far, we use the same mesh grid for all the previous tests. In this sub-section, we compare different mesh resolutions in order to show the influence of the mesh size on the oscillation frequency and the damping rate of the oscillating drop. Meshes differ only in the characteristic mesh size within the region around the interface. We compare three meshes $\mathscr{T}_{h,0}$, $\mathscr{T}_{h,c}$ and $\mathscr{T}_{h,f}$ whose the characteristic sizes are $h_{min,0} = 3.10^{-5}m$, $h_{min,c} = 4.10^{-5}m$ and $h_{min,f} = 2.10^{-5}m$ respectively. The mesh sizes in the bulk liquid and in the air are the same for the three meshes. Changing the mesh size also involves a change in the maximal time-step given by equation (3.32) and in the thickness of the interface taken as $\epsilon = 2.75h_{min}$. The simulations are performed using a second-order time scheme for the *Leveler* method together with Navier-Stokes, including explicit surface tension. The time step for each simulation is half of the maximal time-step given by the condition (3.32). The results of the simulations are shown in figure 3.13. The comparison reveals that for $\mathscr{T}_{h,0}$ and $\mathscr{T}_{h,f}$, the temporal signals are perfectly synchronised with the theoretical signal. $\mathscr{T}_{h,f}$ in a good agreement with the theory in terms of the damping behaviour. The amplitudes of the signal obtained with $\mathscr{T}_{h,0}$ slightly deviate from the theory. As for the coarsest mesh $\mathscr{T}_{h,c}$, the amplitudes are underestimated, and the two last oscillations are slightly shifted in time from the theory.

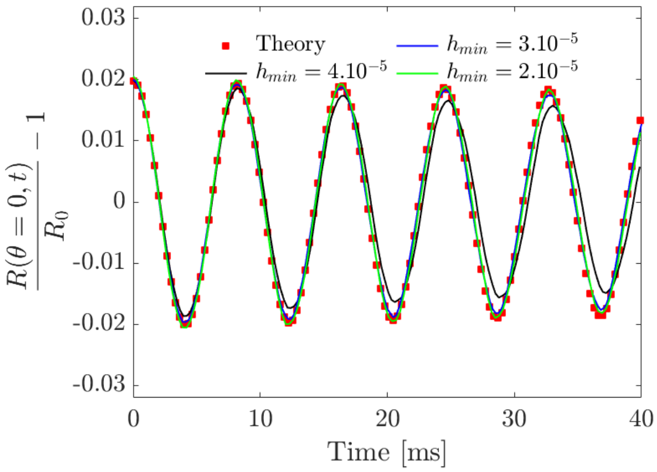

Figure 3.13: Time-evolutions of the normalized radius $R(\theta=0,t)/R_0-1$ obtained from simulations with different mesh resolutions

3.6.1.6 Conclusion

To summarise this parametric study, we found that the mass correction method improves the mass conservation, thus the dynamics of the oscillating drop, in particular, the oscillation frequency. We showed that the *Leveler* method for the transport of the interface is more conservative, in terms of the mass and the mechanical energy than the convection solver with the direct geometrical reinitialisation. Next, we showed that the semi-implicit formulation of surface tension enables the use of time-steps higher than the maximal time-step related to the explicit surface tension. However, the additional implicit term, responsible for stabilising the calculation for higher time-steps, involves more numerical diffusion, thus a poor prediction of the damping rate. The issue of numerical diffusion is enhanced by the use of high order discretisation scheme for the transient terms in the transport of the Level-Set and in the VMS Navier-Stokes equations. Finally, we showed the role of the mesh size around the interface in the prediction of the damping rate and found that the finer is the mesh, the more accurate is the prediction.

We learn from this parametric study that all the numerical methods presented in this chapter allow a correct prediction of the oscillation frequency. However, a good prediction of the damping behaviour requires the use of methods of low numerical diffusion with fine meshes and small time-steps. This makes simulations of high accuracy very time-consuming.

3.6.2 2D simulation of single oscillation modes

In this section, the results of simulations performed with the most accurate numerical framework found in the previous parametric study, are compared with the results of the analytical solution developed in section 3.5.3 for the 2D case. We consider a liquid iron droplet suspended in the air in the absence of gravity. The same physical properties as in the parametric study, are considered here. Calculations are performed with the finer mesh $\mathscr{T}_{h,f}$ with the characteristic size $h_{min,f}=2.10^{-5}m$.

Different modes of deformation (n from 2 to 7) are investigated. The initial shape of each mode is described by:

$$R(\theta, t=0) = R_0 \left(1 + \varepsilon_{n,0} cos(n\theta) - \frac{1}{4}\varepsilon_{n,0}^2\right) \tag{3.98}$$

where $\varepsilon_{n,0} = 0.02$.

Following the previous theoretical analysis of the droplet dynamics, the behaviour of the free-surface depends on the balance of forces between surface tension and viscosity. This balance of forces can be determined from the sign of the reduced discriminant $\Delta'_n = \lambda_n^2 - \omega_{n,0}^2$ which has the same sign as $\frac{4n(n-1)}{n+1} - \frac{\rho^l R_0 \gamma}{\mu^{l2}}$.

Here $\frac{\rho^l R_0 \gamma}{\mu^{l2}}$ is of the order of 10^6. For the range of modes considered here it is obvious that $\frac{4n(n-1)}{n+1}$ is much lower than $\frac{\rho^l R_0 \gamma}{\mu^{l2}}$. So $\Delta'_n < 0$. It means that surface tension is dominant over viscosity; thus, the behaviour of the iron droplet, in the current range of modes, corresponds to the under-damped regime. This qualitative analysis of the balance of forces is confirmed by the following table, which gives the values of λ_n^2, $\omega_{n,0}^2$ and Δ'_n for each mode.

Mode	2	3	4	5	6	7
λ_n^2	0.14	1.23	4.91	13.64	30.69	60.15
$\omega_{n,0}^2$	$7.87\ 10^4$	$2.95\ 10^5$	$7.08\ 10^5$	$1.37\ 10^6$	$2.36\ 10^6$	$3.71\ 10^6$
Δ'_n	$-7.87\ 10^4$	$-2.95\ 10^5$	$-7.08\ 10^5$	$-1.37\ 10^6$	$-2.36\ 10^6$	$-3.71\ 10^6$

Table 3.1: The values of λ_n^2, $\omega_{n,0}^2$ and Δ'_n for each oscillation mode

The droplet is released from a static state which means that $\boldsymbol{u}(r, \theta, t=0) = \mathbf{0}$. This leads to $\dot{\varepsilon}_n(0) = 0$ and $\varepsilon_n(0) = \varepsilon_{n,0}$ Following the values of the table 3.1, the observed oscillation frequency $\sqrt{\Delta'_n}$, in this case, are approximately equal to the frequency of a non-viscous liquid $\omega_{n,0}$. The solution given by the equation (3.93) can be approximated as:

$$\varepsilon_n(t) \approx \varepsilon_{n,0} e^{-\lambda_n t} \cos\left(\omega_{n,0} t\right) \tag{3.99}$$

Figure 3.14 presents the time-evolution of the liquid domain (red region) depicted by positive-Level-Set function ($\phi \geq 0$) for different modes. The black arrows represent the inner velocity field. We can clearly highlight the robustness of the proposed numerical framework to handle different shapes and their oscillations.

To assess the accuracy of these simulations, we extract from the simulation of each mode the time-evolution of the droplet radius in $\theta = 0$ direction. Then, we compare the extracted temporal signals to the derived analytical solution given by equations (3.99), (3.83a), (3.89a) and (3.70a). The numerical signals superimposed to the theoretical ones are shown in figure 3.15. A very good agreement is obtained for different modes, which confirms the accuracy and the robustness of the proposed numerical framework again.

The numerical oscillation frequency of each mode n is extracted from the frequency spectrum of the radius by means of the *fft* whereas the damping coefficient is obtained by fitting the envelope of the temporal signal to $e^{-\lambda_n t}$ using the least-squares algorithm. Figure 3.16 reports the variation of the oscillation frequency and the damping rate with respect to the oscillation mode

n. The numerical results are again in a good quantitative agreement with the analytical formulae (3.89a) and (3.83a).

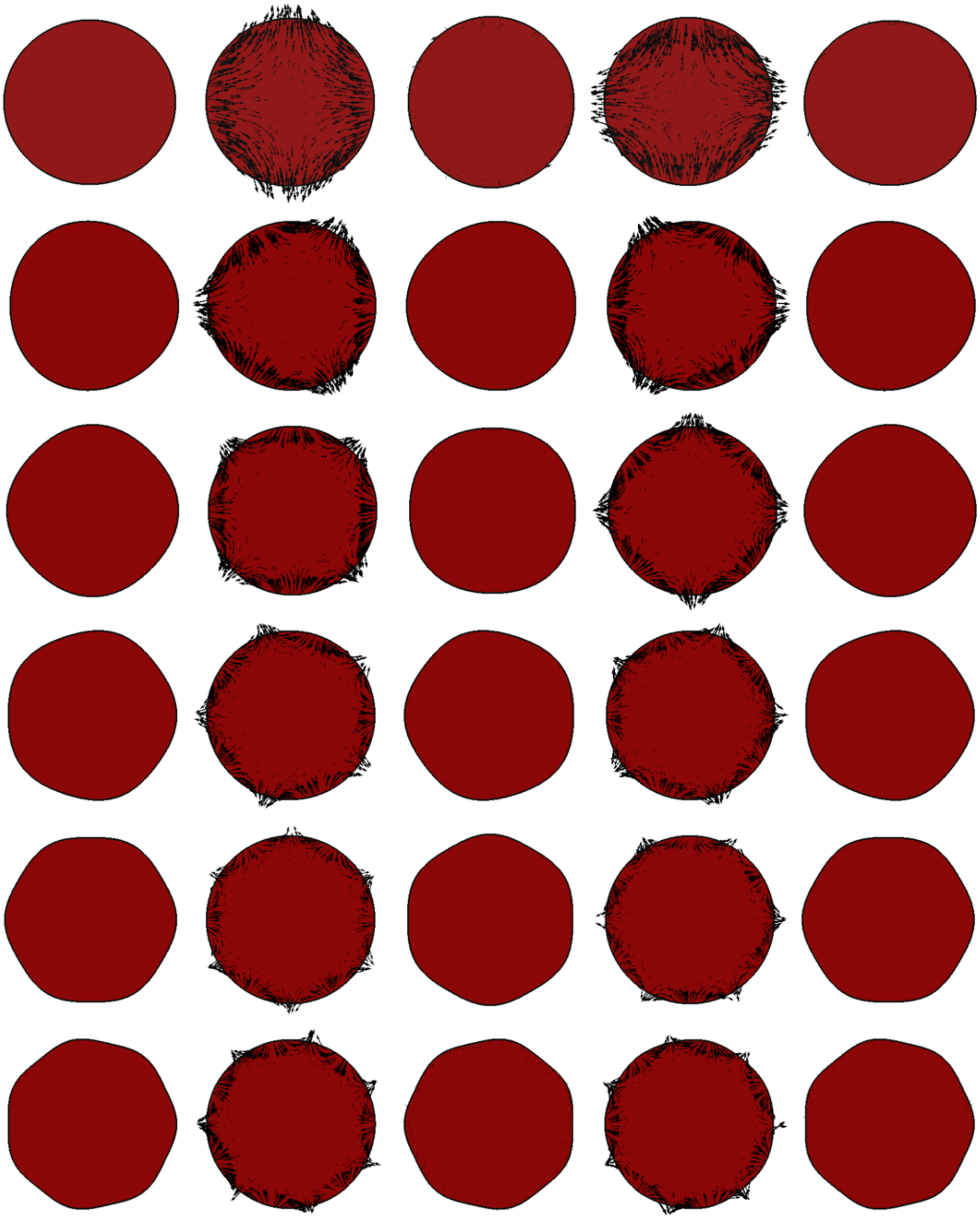

Figure 3.14: The time-evolution of the droplet shape over the first oscillation period for modes from $n = 2$ (upper row) to $n = 7$ (lower row). From the left column to the right, time corresponds to t=0, $\frac{T_n}{4}$, $\frac{T_n}{2}$, $\frac{3T_n}{4}$ and T_n respectively

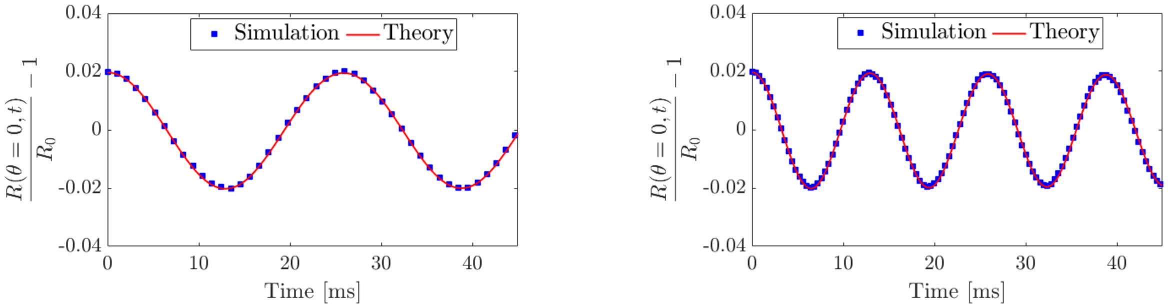

(a) Mode 2

(b) Mode 3

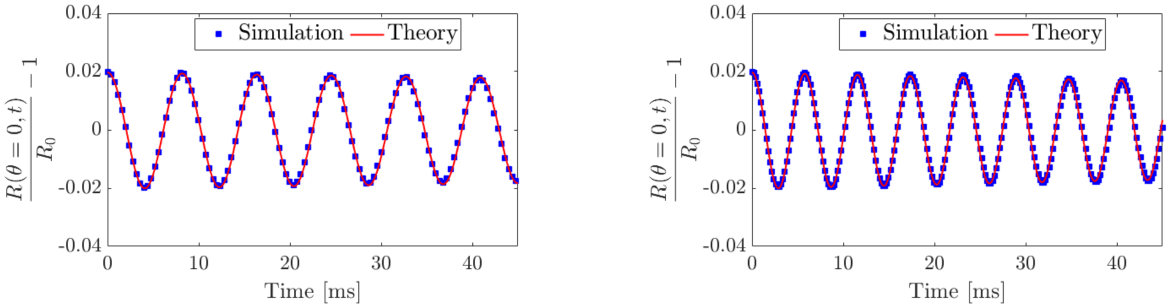

(c) Mode 4

(d) Mode 5

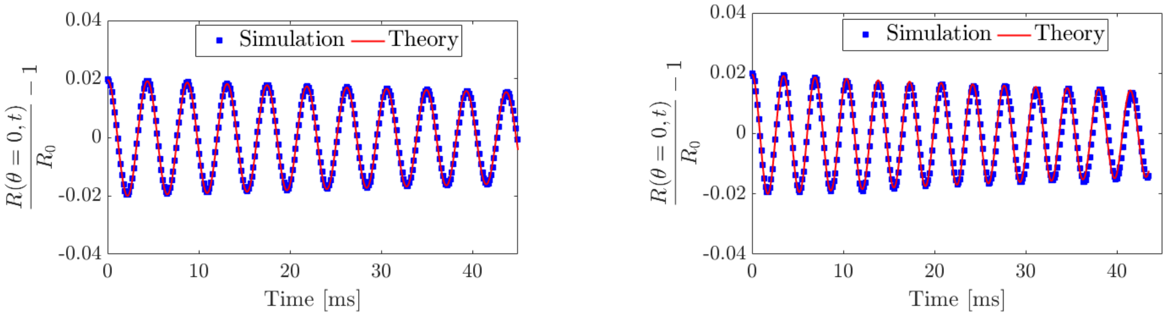

(e) Mode 6

(f) Mode 7

Figure 3.15: The temporal signals of the droplet's radius in direction $\theta = 0$ for modes $n \in [\![2,7]\!]$

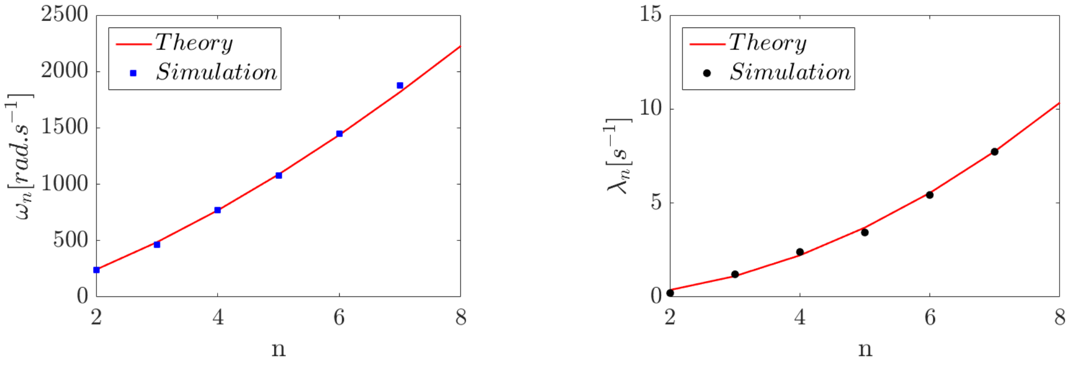

(a)

(b)

Figure 3.16: The variation of (a) the oscillation frequency and (b) the damping rate with respect to the oscillation mode

3.6.3 2D simulation of an arbitrary initial form

In the previous section, the droplet is initially released from a deformed shape describing a specific single mode. Single-mode excitation could be constraining to be set up experimentally. What if the initial shape of the droplet is arbitrary? In this section, we try to investigate this question by proposing an initial shape described by equation (3.100). It describes the combination of several modes. Each mode is rotated from the position given by equation (3.98) with angle ψ_n. Here, we fix the highest order mode to 7, and we generate randomly the values of $\varepsilon_{n,0}$ between 1% and 2% (small amplitudes condition) and ψ_n between 0 and 2π. These values are reported in table 3.2.

$$R(\theta, t=0) = R_0\left[1+\sum_{n=2}^{N}\left(\varepsilon_{n,0}cos(n\theta+\psi_n)-\frac{1}{4}\varepsilon_{n,0}^2\right)\right] \tag{3.100}$$

Mode	2	3	4	5	6	7
$\varepsilon_{n,0}$	1.815%	1.906%	1.127%	1.913%	1.632%	1.098%
$\psi_n[rad]$	1.750	3.436	6.016	6.063	0.990	6.098

Table 3.2: Random values of $\varepsilon_{n,0}$ and ψ_n for each normal mode

In this simulation, material properties are the same as in the previous section. Figure 3.17 displays the velocity field as well as the shape of the interface at different times.

We can show easily from the theoretical analysis detailed in section 3.5.3 that the analytical solution of this problem at each time t is expressed as:

$$R(\theta, t) = R_0\left[1+\sum_{n=2}^{7}\left(\varepsilon_n cos(n\theta+\psi_n)-\frac{1}{4}\varepsilon_n^2\right)\right] \tag{3.101}$$

where

$$\varepsilon_n(t) \approx \varepsilon_{n,0}e^{-\lambda_n t}\cos\left(\omega_{n,0}t+\psi_n\right) \tag{3.102}$$

The blue line in figure 3.18a corresponds to the simulated temporal variation of the radius of the interface in the direction $\theta = 0$. The comparison with the theoretical solution (the red dashed line) shows a good agreement again. We compute the frequency spectrum of the numerical temporal signal via the *fft* . It is clear from figure 3.18b that the spectrum (blue line) displays only the peaks of the modes from 2 to 7 whose the frequencies are represented by the red dashed vertical lines.

The results of this investigation show that if an arbitrary initial shape, slightly deformed from the equilibrium shape, can be written as a combination of normal modes, the linear theory derived in this work can provide the analytical expression of the time-evolution of the radius of the droplet.

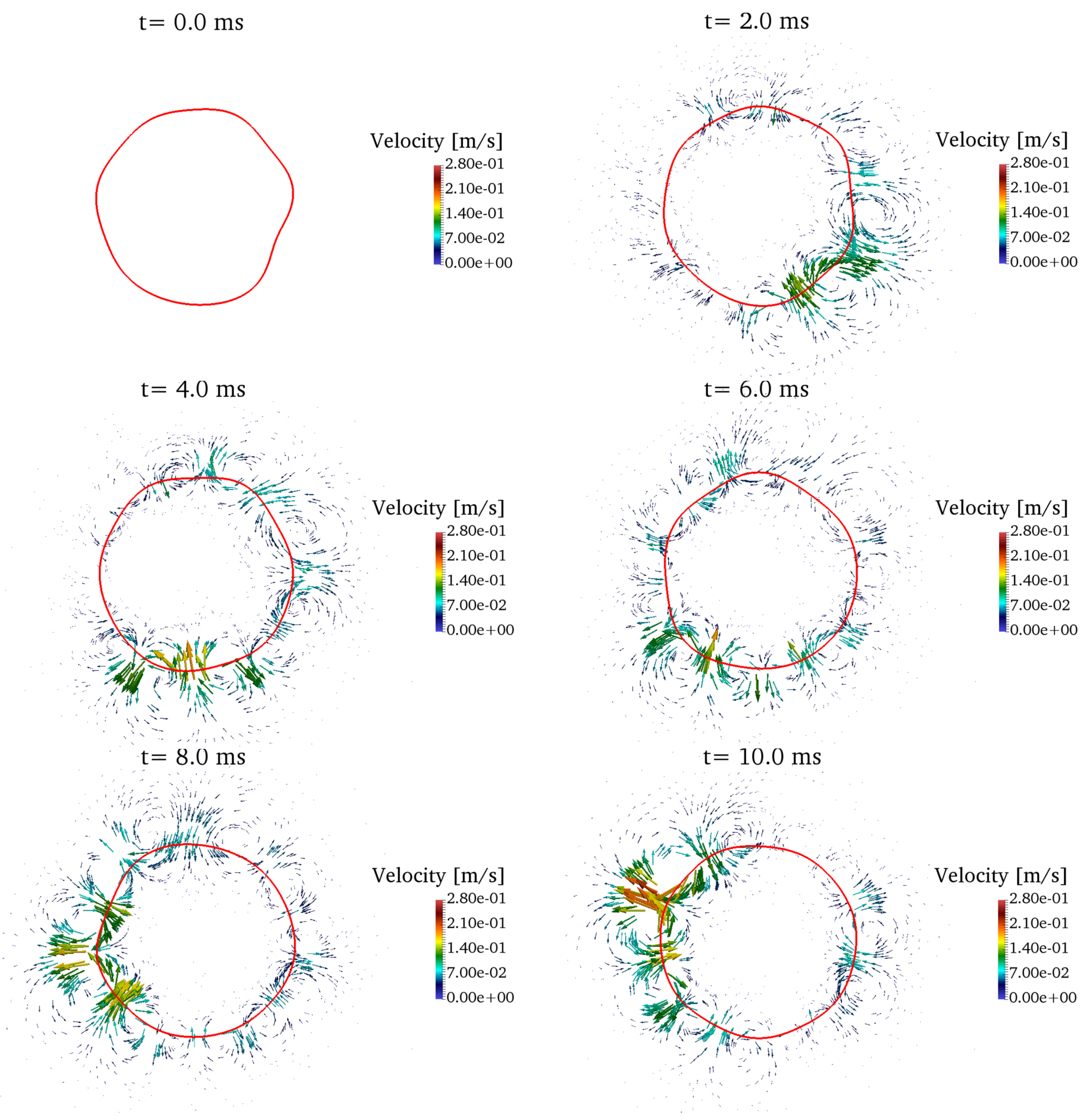

t= 0.0 ms

t= 2.0 ms

t= 4.0 ms

t= 6.0 ms

t= 8.0 ms

t= 10.0 ms

Figure 3.17: Snapshots of the droplet shape and velocity field at various times

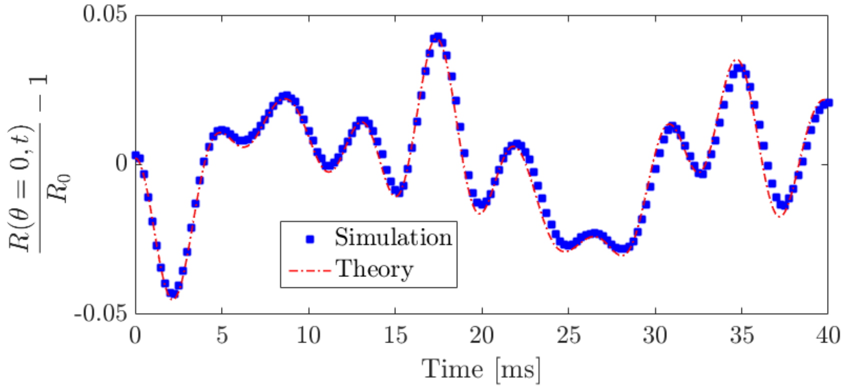

(a) Time evolution of the radius R(θ, *t*)

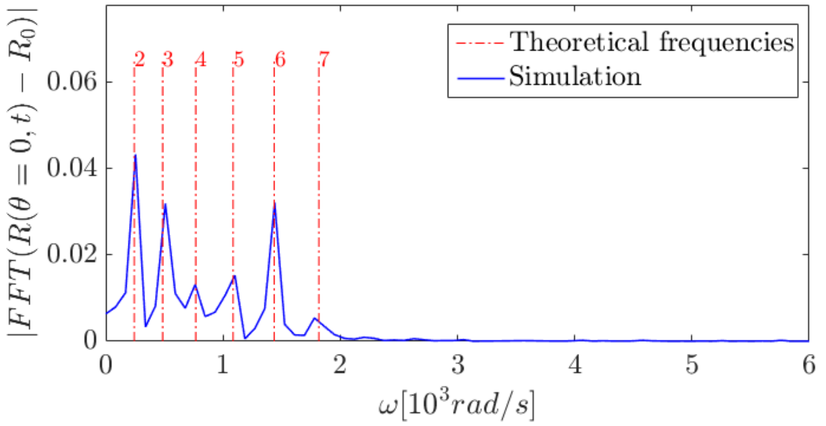

(b) The frequency spectrum of the signal R(θ, *t*) given by the FFT

Figure 3.18: Comparison of simulation results and the analytical solution

3.6.4 3D simulation of the oscillation of a liquid iron drop

In this section, we perform 3D simulation of the oscillation of a liquid iron drop. The liquid iron droplet is suspended in the air in the absence of gravity and enclosed in a cavity of side size $6 \times R_0$. The values of densities and viscosities are the same as in the 2D case as well as surface tension value. The droplet is initially released from Rayleigh's mode $(n = 2)$ described by the following equation:

$$R(\theta, t = 0) = R_0 \left(1 + \varepsilon P_2 \left(cos(\theta)\right) - \frac{1}{5}\varepsilon^2\right) \tag{3.103}$$

where P_2 is the second degree Legendre polynomial and $\varepsilon = 0.08$. The 3D mesh used here is composed of 194981 nodes and 1159517 elements.

Following the theoretical analysis in section 3.5.3, the natural frequency and the damping rate of the 3D iron droplet are :

$$\begin{cases} \omega_{2,0} = \sqrt{\dfrac{8\gamma}{\rho^l R_0^3}} \\ \lambda_2 = \dfrac{5\mu^l}{\rho^l R_0^2} \end{cases} \tag{3.104}$$

$\omega_{2,0} = 280.54\ rad.s^{-1}$ and $\lambda_2 = 0.46\ s^{-1}$. So $\Delta_2' = -78696\ rad^2.s^{-2} \approx -\omega_{2,0}^2$ Therefore, the 3D iron droplet shows an underdamped regime. The analytical solution for this regime is:

$$R(\theta, t) = R_0 \left(1 + \varepsilon_2(t) P_2 \left(cos(\theta)\right) - \frac{1}{5}\varepsilon_2^2(t)\right) \tag{3.105}$$

where

$$\varepsilon_2(t) \approx \varepsilon e^{-\lambda_2 t} \cos\left(\omega_{2,0} t\right) \tag{3.106}$$

As in the previous sections, we assess the accuracy of the numerical solution by comparing it to the derived analytic solution. We extract from the simulation the time-evolution of the displacement of the upper point of intersection of the interface with the z-axis $(\theta = 0)$. The comparison is shown in figure 3.19.

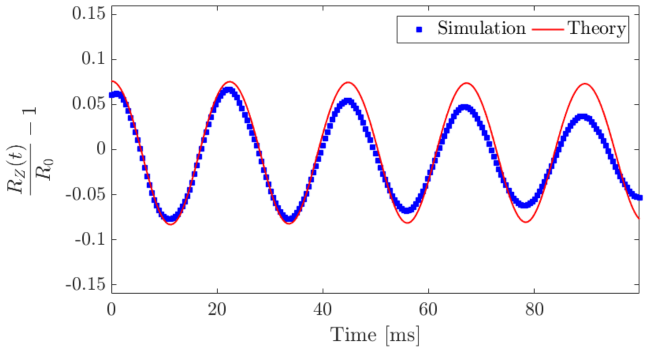

Figure 3.19: The time evolution of the displacement of the upper point of intersection of the interface with the z-axis

One can notice that the numerical signal is synchronised with the theoretical variations. It means that free surface dynamics driven by surface tension is well predicted. However, the amplitudes are more damped in the numerical simulation. The origin of this over-estimation of damping behaviour is attributed to numerical diffusion around the interface due to its thickness. In fact, in this present 3D simulation, the mesh resolution is coarser than the resolution of the 2D mesh, which gave a very good estimation of the damping rate of the oscillations. Consequently, the thickness of the interface, which depends on the mesh size is greater in the present 3D simulation than it must be.

Overall, these results give confidence that the use of a convected Level-Set method combined with a VMS method to solve the unsteady Navier-Stokes equations works well and could play an essential role for modelling the behaviour of drops driven by surface tension. However, this numerical framework requires a high mesh resolution around the interface to reduce the numerical diffusion, which adds artificial damping to the simulated phenomenon. The use of a high-resolution mesh in 3D is very time-consuming. A dynamic conservative mesh adaptation [71] seems a very promising tool to add to the present numerical framework to increase the accuracy with a reasonable computational time.

3.7 Conclusion

In this chapter, we presented the numerical framework of an incompressible flow involving two fluids separated by an interface with surface tension. First, we showed the modelling of the interface by the Level-Set method, which represents the interface using a signed distance function at the interface. We showed two main numerical methodologies to track the dynamics of the interface: convection and reinitialisation in two separate steps and coupled convection-reinitialisation. To address the problem of mass conservation from which the classical Level-Set method suffers, we proposed a simple mass correction method. In the second part, we presented the monolithic formulation of an incompressible two-fluid flow with surface tension. We presented the diffuse interface method, which consists in smoothing the transition from one fluid to the other over a zone of non-zero thickness centred around the interface. Based on the same principle, the CSF method transforms the surface integral of the surface tension force into a volume integral via the smooth Dirac function. Some numerical problems may be encountered when using these methods in a standard way. Spurious currents in the vicinity of the interface is a classical problem that pollutes the solution. The density scaled surface tension method has been proposed to reduce the intensity of these non-physical currents. The explicit use of surface tension imposes a condition of stability on the calculation time step which can considerably increase the computational time. To circumvent this stability restriction, a semi-implicit formulation of the surface tension has been proposed. Finally, a high order temporal discretisation scheme for the Navier-Stokes equations has been presented to reduce discretisation errors, a source of numerical diffusion.

To evaluate the performance of the numerical framework, we propose the quantitative benchmark called the oscillating drop problem for which we derive the analytical solution in both 2D and 3D. The derivation of the theoretical solution for small-amplitude oscillations is detailed. The accuracy and robustness of the proposed Eulerian framework is discussed through 2D and 3D simulations of different oscillation modes for a liquid iron droplet immersed in a very low density gas. The results obtained and comparisons show that the two-fluid flow solver based on the stabilised FE method is capable of exhibiting good stability and accuracy properties.

Chapter 4

Numerical modelling of heat transfer with solidification and thermal contact resistance

Résumé

En raison de la rugosité, de minuscules poches de gaz peuvent être piégées au niveau de la surface de contact entre le refroidisseur et l'échantillon métallique. Ceci peut former une résistance à l'échange thermique entre les deux corps à travers l'interface de contact. Cette dernière observation soulève la question de l'influence de la résistance thermique de contact sur la croissance du front de solidification. Pour répondre à cette question, nous proposons de modéliser la résistance thermique de contact dans un système multi-domaines impliquant un domaine métallique en solidification. Pour introduire la modélisation de la résistance thermique de contact, nous limitons le cadre, dans ce chapitre, à la conduction thermique sans prendre en compte la convection et le rayonnement. Tout d'abord, nous présentons un nouveau modèle pour prendre en compte la résistance thermique de contact entre deux matériaux et nous le validons avec différents cas test, en régime stationnaire et instationnaire. Ensuite, nous présentons le cadre numérique pour la modélisation du transfert de chaleur (par conduction) en présence de solidification. Enfin, nous présentons des simulations de refroidissement et de solidification d'une gouttelette d'acier pour différentes valeurs de résistance thermique de contact.

Contents

4.1 Introduction . . . 82

4.2 Thermal contact resistance . . . 82

- 4.2.1 State of the art . . . 82
- 4.2.2 Governing equations and modelling . . . 84
  - 4.2.2.1 Problem formulation . . . 84
  - 4.2.2.2 Mixing laws for perfect contact . . . 86
  - 4.2.2.3 Mixing laws for thermal contact resistance . . . 86
- 4.2.3 Results and discussion . . . 89
  - 4.2.3.1 Steady conduction . . . 89
  - 4.2.3.2 Unsteady conduction . . . 94

4.3 Heat conduction with solidification . . . 97

- 4.3.1 Introduction . . . 97
- 4.3.2 Volume averaging method . . . 97
- 4.3.3 Averaged energy conservation equation . . . 99
- 4.3.4 Monolithic formulation of the energy conservation in a multi-domain system 100

4.4 Application to chill cooling and solidification experiment on board the ISS . . . 101

4.5 Conclusion . . . 105

4.1 Introduction

Samples processed during parabolic flights and sounding rockets within the CCEMLCC project have shown that the contact surface of the sample with the chill plate is flat but not perfectly smooth as shown in figure 4.1. Due to the roughness of the contact surface, tiny pockets of gas trapped at the boundary between the cooling plate and the metal can form a resistance to heat transfer. This last observation raises the question of the influence of thermal contact resistance on the solidification front growth. To answer this question, we propose to model the thermal contact resistance in a multi-domain system involving a solidifying metal domain.

To introduce the modelling of heat transfer in the presence of solidification in the metallic domain and thermal contact resistance, we limit the modelling, in this chapter, to heat conduction without taking into account convection and radiation. First of all, we present a new model for accounting for the thermal contact resistance between two materials and validate it with different analytical test cases. Next, we present the numerical framework for modelling heat transfer in the presence of solidification. Finally, simulations of chill cooling and solidification of a steel droplet will be presented for different values of thermal contact resistance.

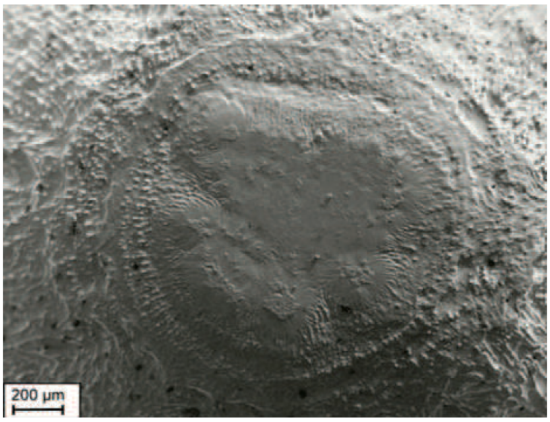

Figure 4.1: Scanning Electron Microscopy imaging of the contact area of the solidified sample processed during a parabolic flight on board a zero-g airplane [1]

.

4.2 Thermal contact resistance

4.2.1 State of the art

An interface between two adjacent bodies is perfect if the real contact occurs in every point of the contacting surfaces. In this ideal case, the temperature and the heat flux are continuous across the interface. In most practical situations, the contacting surfaces are rough and have microscopic asperities. As a result, the mechanical contact occurs only at several microscopic spots interspersed with gaps or gas cavities of poor heat transfer capability. Therefore, the heat flux from the hot body to the cold one is constrained to pass through the real contact spots, which represent only a small fraction of the total interface area. In this case, we say that the interface exhibits a Thermal Contact Resistance, also known as Kapitza resistance [72]. At the macroscopic scale, the existence of a thermal contact resistance appears as a temperature jump across the interface. The Kapitza resistance can occur at solid-solid interfaces [73] but also liquid-solid interfaces [74]. Many physical systems involve a mechanical combination of two or several materials. Therefore, thermal contact resistance can occur in a wide range of applications such as additive manufacturing [75], electronic packaging [76], nuclear reactors [77], hypersonic flights [78], internal combustion engines [79], die casting [80] and injection moulding [81].

The use of numerical simulation to predict different aspects of heat transfer in the industry is becoming a valuable tool to help to improve the performance and the efficiency of industrial processes. Numerical modelling of heat transfer in a multi-material domain, including interfaces, has long been addressed in the literature [39; 82–85]. However, accounting for the thermal contact resistance is still a numerically-challenging task due to the temperature discontinuity that it involves. Consequently, additional numerical efforts are needed to handle the discontinuities at the interfaces. For instance, in the classical FE method, the meshing of the interface is required and has to conform to the adjacent volume parts. Moreover, appropriate surface elements must be constructed. For complex geometries, this is challenging [86; 87]. To circumvent this challenge, some authors built their Kapitza resistance modelling on the Extended Finite Element Method (XFEM) [87–89]. Moreover, numerical models of thermal contact resistance available in the literature focus mostly on the steady state conduction [88; 90–93]. Only a few studies have addressed the Kapitza resistance in transient conduction [86].

In this work, we derive a simple and efficient numerical model from accounting for thermal contact resistance in time-dependent multi-material heat transfer problems for classical FE method. Our numerical framework is based on the diffuse-interface immersed-boundary approach. The interface is implicitly represented by the Level-Set function. The principle of this model is to represent the contact imperfections by a thin intermediate material between the contacting bodies. Consequently, appropriate mixing laws will consistently be derived to mix the properties of the two materials together with the intermediate material. Accordingly, new formulae for mixing heat capacities and thermal conductivities will be derived. The novelty of this work lies in the fact that the proposed model does not require any additional implementation compared to the solver of perfect contact thermal transfer. The change is only made in the mixing laws of thermal properties. Furthermore, no special treatment of temperature discontinuities is needed because the temperature jump is smoothed along the mixing zone.

This section starts from the weak formulation of heat conduction in a two-material domain. The level set method is introduced. The mixing laws for perfect contact are recalled. The modelling of thermal contact resistance is presented. Then, the mixing laws for thermal conductivity and heat capacity are derived. The effectiveness and accuracy of the proposed model are assessed through different benchmarks for both steady-state and transient conduction. The numerical results are compared to analytical solutions and a reference case. Finally, some concluding remarks are drawn.

4.2.2 Governing equations and modelling

This first subsection is devoted to the mathematical formulation of heat conduction involving two materials in contact and the resolution methodology based on the monolithic formulation of the energy conservation equation using the diffuse interface immersed boundary method. The thermal contact resistance modelling is illustrated via a one-dimensional case of two adjacent slabs. A general 3D unsteady heat conduction is formulated by the level-set function.

4.2.2.1 Problem formulation

Consider a computational domain Ω containing two materials indexed by 1 and 2 ($\Omega = \Omega_1 \cup \Omega_2$) separated by an interface Γ_{12}. The heat transfer operated by conduction is described by the following set of equations:

$$C_{p1}\frac{\partial T_1}{\partial t} = \nabla \cdot (k_1 \nabla T_1), \;\; \boldsymbol{x} \in \Omega_1 \tag{4.1a}$$
$$C_{p2}\frac{\partial T_2}{\partial t} = \nabla \cdot (k_2 \nabla T_2), \;\; \boldsymbol{x} \in \Omega_2 \tag{4.1b}$$

where $C_{pi} = \rho_i c_{pi}$ is the specific heat capacity, product of the density, ρ_i, and the heat capacity per unit mass, c_{pi}; k_i is the thermal conductivity and $T_i(x,t)$ is the temperature field, respectively in (i=1) Ω_1 and (i=2) Ω_2. At the interface Γ_{12}, several boundary conditions can be described. At first, the continuity of the normal heat flux across Γ_{12} writes:

$$q_{12} = -k_1 \nabla T_1 \cdot \boldsymbol{n}_{12} = -k_2 \nabla T_2 \cdot \boldsymbol{n}_{12}, \;\; \boldsymbol{x} \in \Gamma_{12} \tag{4.2}$$

where $\boldsymbol{n}_{12}$ is the unit normal vector to Γ_{12} pointing at Ω_2. If the interface is thermally resistive, i.e. a thermal contact resistance $R_{th} \neq 0$ is posing a barrier to heat transfer at the interface Γ_{12}, a macro-scale temperature jump occurs at the interface:

$$[\![T]\!] = -R_{th} q_{12} \;\; \boldsymbol{x} \in \Gamma_{12} \tag{4.3}$$

where $[\![\star]\!] = (\star)_2 - (\star)_1$ means the jump across the interface Γ_{12}.

We consider the Dirichlet and Neumann boundary conditions prescribed on the two complementary and disjoints portions of $\partial\Omega$, denoted by $\partial\Omega_{Dir}$ and $\partial\Omega_{Neu}$ as follows:

$$\begin{cases} \boldsymbol{q}.\boldsymbol{n} = q_B, & \boldsymbol{x} \in \partial\Omega_{Neu} \\ T = T_B, & \boldsymbol{x} \in \partial\Omega_{Dir} \end{cases} \tag{4.4}$$

where $\boldsymbol{n}$ is the outward normal vector to $\partial\Omega_{Neu}$.

Two different resolution strategies could be adopted to deal with this multi-material heat transfer problem. The first, called partitioned resolution, consists of considering two different meshes for each domain and solve two equations with the associated boundary conditions separately. The global solution is then constructed by a suitable assembly method. However, during the assembly, the coordination between the meshes can become complicated or even sometimes infeasible. The second strategy, which we use in this work, is called monolithic resolution. It consists of solving one equation over the whole computational domain in a single global mesh. The principle of the monolithic formulation is to treat the two sub-domains as one with variable properties $k(\boldsymbol{x})$ and $\mathrm{C}_p(\boldsymbol{x})$.

To formulate the problem in a monolithic way, we write the weak formulation of each subdomain. Then, we construct a unified formulation for the global domain by summing the contribution of each subdomain. The weak formulation associated with equations (4.1) and boundary conditions (4.4) is given as follows:

$$\int_{\Omega_1} \mathrm{C}_{p1}\frac{\partial \mathrm{T}_1}{\partial t}\mathscr{T}_1 d\mathrm{V} + \int_{\Omega_1} k_1 \nabla \mathrm{T}_1 \cdot \nabla \mathscr{T}_1 d\mathrm{V} = \int_{\Gamma_{12}} k_1 \nabla \mathrm{T}_1 \cdot \boldsymbol{n}_{12}\mathscr{T}_1 d\mathrm{S} + \int_{\partial\Omega_{Neu}\cap\partial\Omega_1} q_{\mathrm{B}}\mathscr{T}_1 d\mathrm{S} \tag{4.5a}$$

$$\int_{\Omega_2} \mathrm{C}_{p2}\frac{\partial \mathrm{T}_2}{\partial t}\mathscr{T}_2 d\mathrm{V} + \int_{\Omega_2} k_2 \nabla \mathrm{T}_2 \cdot \nabla \mathscr{T}_2 d\mathrm{V} = \int_{\Gamma_{12}} -k_2 \nabla \mathrm{T}_2 \cdot \boldsymbol{n}_{12}\mathscr{T}_2 d\mathrm{S} + \int_{\partial\Omega_{Neu}\cap\partial\Omega_2} q_{\mathrm{B}}\mathscr{T}_2 d\mathrm{S} \tag{4.5b}$$

where $\mathscr{T}_1$ and $\mathscr{T}_2$ are test functions for the subdomains Ω_1 and Ω_2, respectively. Using the flux continuity condition (4.2) and considering the presence of a thermally resistive interface giving rise to a temperature jump at Γ_{12} (equation (4.3)), the general formulation over domain Ω is obtained:

$$\int_{\Omega} \mathrm{C}_p(\boldsymbol{x})\frac{\partial \mathrm{T}}{\partial t}\mathscr{T} d\mathrm{V} + \int_{\Omega} k(\boldsymbol{x})\nabla \mathrm{T}\cdot\nabla\mathscr{T} d\mathrm{V} + \int_{\Gamma_{12}} \frac{[\![\mathrm{T}]\!]}{\mathrm{R}_{th}}[\![\mathscr{T}]\!] d\mathrm{S} = \int_{\partial\Omega_{Neu}} q_{\mathrm{B}}\mathscr{T} d\mathrm{S} \tag{4.6}$$

It is worth noting that for perfect contact at Γ_{12}, the temperature jump $[\![\mathrm{T}]\!]$ vanishes so the monolithic formulation simply becomes:

$$\int_{\Omega} \mathrm{C}_p(\boldsymbol{x})\frac{\partial \mathrm{T}}{\partial t}\mathscr{T} d\mathrm{V} + \int_{\Omega} k(\boldsymbol{x})\nabla \mathrm{T}\cdot\nabla\mathscr{T} d\mathrm{V} = \int_{\partial\Omega_{Neu}} q_{\mathrm{B}}\mathscr{T} d\mathrm{S} \tag{4.7}$$

As we can observe from the latter two equations, the definition of variable properties $\mathrm{C}_p(\boldsymbol{x})$ and $k(\boldsymbol{x})$ as well as the third term in the Right-Hand-Side (LHS) of the equation (4.6) requires a numerical method to localise the boundary between the two sub-domains. In the framework of this PhD, we use the Level-Set method for interface modelling as previously presented in Chapter 3. Hence, we consider the following signed distance function:

$$\phi(\boldsymbol{x},t) = \begin{cases} d(\boldsymbol{x},\Gamma_{12}) \text{ if } \boldsymbol{x}\in\Omega_1 \\ 0 \text{ if } \boldsymbol{x}\in\Gamma_{12} \\ -d(\boldsymbol{x},\Gamma_{12}) \text{ if } \boldsymbol{x}\in\Omega_2 \end{cases} \tag{4.8}$$

where $d(\boldsymbol{x},\Gamma_{12})$ is the geometrical distance between $\boldsymbol{x}$ and Γ_{12}.

Furthermore, the discontinuity of interface properties, as well as the temperature discontinuity resulting from thermal contact resistance, are numerically challenging. It is, therefore, necessary to have a robust numerical method capable of handling high property ratios and capturing the temperature jump across the interface accurately. For this reason, Yvonnet et. al. [88] proposed a numerical procedure for Kapitza resistance at sharp interfaces, based on XFEM and the level set method.

In the present work, we make use of the diffuse-interface approach with the classical FE Method. It is the same approach presented previously in Chapter 3 to model the interface in a two-fluid flow. We recall that the diffuse-interface approach consists in introducing an artificial region around the interface of fixed thickness 2ε comparable to the mesh size in the vicinity of the interface. In this region, the transition of properties from one domain to the other occurs continuously and smoothly. The way the transition occurs is described by the mixing law. The objective of this study is not solving the equation (4.6) for thermal contact resistance. Instead, we look for a simple and efficient solution so as to keep the equation (4.7) for both perfect and imperfect interfaces while finding mixing laws which account for the effect of thermal contact resistance.

4.2.2.2 Mixing laws for perfect contact

For a perfect contact, it is well-known in the literature [94] that a harmonic mixing law for thermal conductivity ensures the conservation of heat flux across the transition zone.

$$k(\phi) = \left(\frac{\mathrm{H}(\phi)}{k_1} + \frac{1-\mathrm{H}(\phi)}{k_2}\right)^{-1} \tag{4.9}$$

where H is a smooth Heaviside function which indicates the presence of domain Ω_1. We choose here a sinusoidal smoothing function of the signed distance function ϕ (equation (4.8)):

$$\mathrm{H}(\phi) = \begin{cases} 1 & \text{if} \;\; \phi > \varepsilon \\ 0 & \text{if} \;\; \phi < -\varepsilon \\ \dfrac{1}{2}\left[1 + \dfrac{\phi}{\varepsilon} + \dfrac{1}{\pi}\sin\left(\dfrac{\pi\phi}{\varepsilon}\right)\right] & \text{if} \;\; |\phi| \leq \varepsilon \end{cases} \tag{4.10}$$

Note that the harmonic mixing law of the thermal conductivity will be retrieved in the section dedicated to the mixing law for thermal contact resistance in the next section.

As for heat capacity, the arithmetic mixing law is used:

$$\mathrm{C}_p(\phi) = \mathrm{C}_{p1}\mathrm{H}(\phi) + \mathrm{C}_{p2}\left(1 - \mathrm{H}(\phi)\right) \tag{4.11}$$

4.2.2.3 Mixing laws for thermal contact resistance

The basic idea of the present modelling of thermal contact resistance is to consider that in a microscale the imperfections of contact can be modelled by a thin layer of thickness e separating Ω_1 and Ω_2. This intermediate domain, denoted by Ω_G (G for Gap), is considered as a third material of properties k_G and $\mathrm{C}_{p,\mathrm{G}}$ as shown in figure 4.2. Following this representation, we intend to find physically-appropriate mixing laws for both k and C_p inside the mixing zone, including the effect of the gap layer. For the sake of clarity, we derive the mixing law in 1D, and then we extend the formulation to higher dimensions using the level-set function.

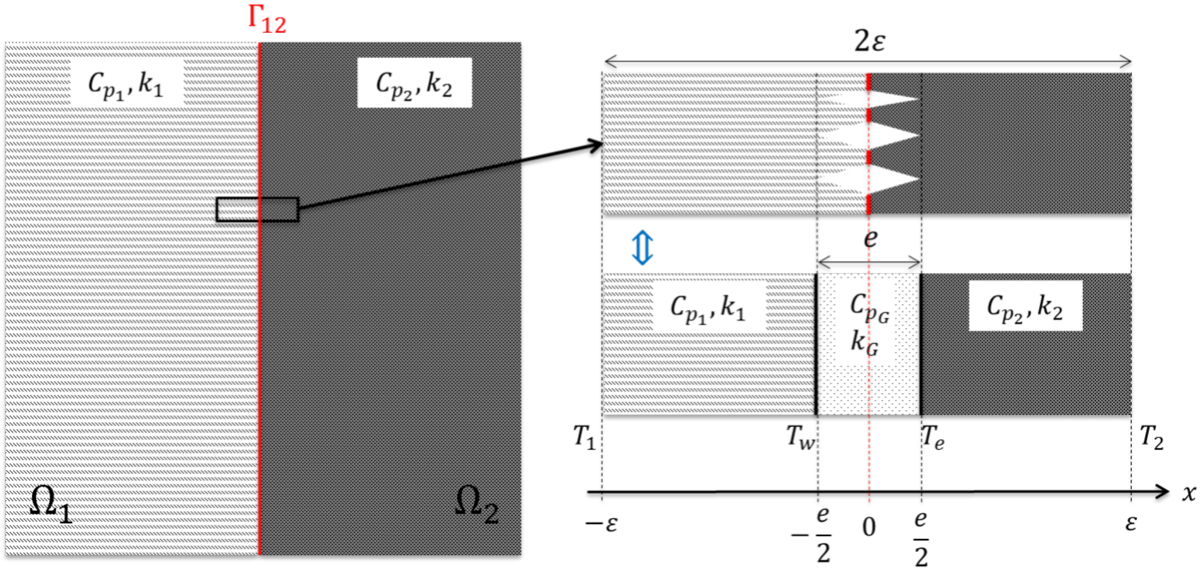

Figure 4.2: Schematic of two materials in contact, Ω_1 and Ω_2, forming a thermally resistant interface Γ_{12} due to the presence of a gap layer, Ω_G, with thickness e.

Thermal conductivity mixing law

For thermal conductivity, we limit our analysis to steady-state conduction in which the heat capacity of the materials does not play a role. Consider the steady-state temperature field $T(x, t \to \infty) = T_s(x)$ in the contact region centred within $x \in [-\varepsilon, \varepsilon]$ shown in figure 4.2. T_s is piecewise linear such as:

$$T_s(x) = \begin{cases} T_1 + a_1(x+\varepsilon) & \text{if} \quad x \in [-\varepsilon, -e/2] \\ T_w + a_G(x+e/2) & \text{if} \quad x \in [-e/2, e/2] \\ T_2 + a_2(x-\varepsilon) & \text{if} \quad x \in [e/2, \varepsilon] \end{cases} \tag{4.12}$$

where $a_1 = \frac{1}{k_1}\left(\frac{T_2 - T_1}{\frac{\varepsilon - e/2}{k_1} + \frac{e}{k_G} + \frac{\varepsilon - e/2}{k_2}}\right)$, $a_G = \frac{k_1}{k_G} a_1$ and $a_2 = \frac{k_1}{k_2} a_1$. We suppose that the mixing zone of thickness 2ε has equivalent properties k_{eq} and $C_{p,eq}$. Therefore, the heat flux across the mixing zone is given by:

$$q_s = k_{eq} \frac{T_2 - T_1}{2\varepsilon}. \tag{4.13}$$

On the other hand, the heat flux in domain Ω_1 is:

$$q_s = k_1 a_1 = \frac{T_2 - T_1}{\frac{\varepsilon - e/2}{k_1} + \frac{e}{k_G} + \frac{\varepsilon - e/2}{k_2}}. \tag{4.14}$$

Consequently, the heat flux conservation yields:

$$\frac{2\varepsilon}{k_{eq}} = \frac{\varepsilon - e/2}{k_1} + \frac{e}{k_G} + \frac{\varepsilon - e/2}{k_2}. \tag{4.15}$$

We assume that the thickness of the gap is much smaller than the one of the mixing zone, $e \ll \varepsilon$, and that the thermal conductivity of the gap is negligible comparing to k_1 and k_2, $k_G \ll k_{i \in \{1,2\}}$.

Hence, the equivalent thermal conductivity reads:

$$\frac{1}{k_{eq}} \approx \frac{1}{2k_1} + \frac{1}{2k_2} + \frac{\mathrm{R}_{th}}{2\varepsilon} \tag{4.16}$$

where $\mathrm{R}_{th} = \frac{e}{k_\mathrm{G}}$ is the thermal contact resistance with unit $\mathrm{K.W}^{-1}.m^2$.

Using the level set function for generalisation, the idea now is to find a formula for the thermal conductivity $k(\phi)$ which links in a continuous way the region $\phi \leq -\varepsilon$ where $k = k_1$ and the region $\phi \geq \varepsilon$ where $k = k_2$ respecting that the harmonic mean of k in the transition zone is:

$$\frac{1}{2\varepsilon}\int_{-\varepsilon}^{\varepsilon} \frac{1}{k(\phi)} d\phi = \frac{1}{k_{eq}} \tag{4.17}$$

These conditions lead to the following mixing low for the thermal conductivity:

$$k(\phi) = \left(\frac{\mathrm{H}(\phi)}{k_1} + \frac{1-\mathrm{H}(\phi)}{k_2} + \delta(\phi)\mathrm{R}_{th} \right)^{-1} \tag{4.18}$$

where δ is the smooth Dirac function derived from equation (4.10):

$$\delta(\phi) = \begin{cases} \frac{1}{2\varepsilon}\left[1+\cos\left(\frac{\pi\phi}{\varepsilon}\right)\right] & \text{if} \quad |\phi| \leq \varepsilon \\ 0 & \text{if} \quad |\phi| > \varepsilon \end{cases} \tag{4.19}$$

For $\mathrm{R}_{th} = 0$, equation (4.18) gives the classical harmonic mixing law for perfect contact.

Heat capacity mixing law

Unlike thermal conductivity, heat capacity is an extensive property. Therefore, the equivalent heat capacity in the mixing zone can be obtained by the volume-average of the heat capacities over the mixing zone. This leads to the following equation:

$$\begin{aligned} \mathrm{C}_{p,eq} &= \frac{\varepsilon - e/2}{2\varepsilon}\mathrm{C}_{p1} + \frac{\varepsilon - e/2}{2\varepsilon}\mathrm{C}_{p2} + \frac{e}{2\varepsilon}\mathrm{C}_{p,\mathrm{G}} \\ &= \overline{\mathrm{C}_p}\left(1 - \frac{e}{2\varepsilon}\right) + \frac{e}{2\varepsilon}\mathrm{C}_{p,\mathrm{G}} \end{aligned} \tag{4.20}$$

where

$$\overline{\mathrm{C}_p} = \frac{\mathrm{C}_{p1} + \mathrm{C}_{p2}}{2}$$

With the assumption that $e \ll 2\varepsilon$

$$\mathrm{C}_{p,eq} \approx \overline{\mathrm{C}_p} + \frac{e}{2\varepsilon}\mathrm{C}_{p,\mathrm{G}}. \tag{4.21}$$

Using a condition equivalent to equation (4.17) for the heat capacity, the mixing law using the level set reads:

$$\mathrm{C}_p(\phi) = \mathrm{C}_{p1}\mathrm{H}(\phi) + \mathrm{C}_{p2}\left(1 - \mathrm{H}(\phi)\right) + e\,\mathrm{C}_{p,\mathrm{G}}\,\delta(\phi) \tag{4.22}$$

Heat capacity mixing law (4.22) requires the knowledge of the values of the thickness and the heat capacity of the gap. In some problems, these values may be unknown. For this reason, we will show, through numerical simulations of unsteady conduction, cases in which the additional term with gap properties is not required. Three different cases exist, $C_{p,G} \ll \overline{C_p}$, $C_{p,G} = \mathcal{O}(\overline{C_p})$ and $C_{p,G} \gg \overline{C_p}$. In each case, equations (4.11) and (4.22) will be tested and compared to a reference case.

4.2.3 Results and discussion

4.2.3.1 Steady conduction

Planar interface benchmark

In this example, we propose a benchmark with a planar and resistive interface. The problem geometry and mesh are illustrated in figure 4.3.

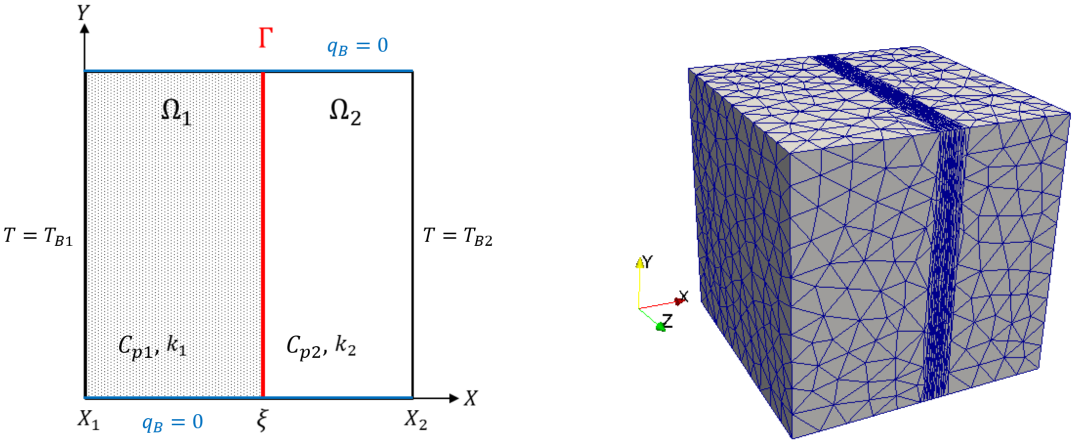

(a) Geometry (b) Mesh

Figure 4.3: Setup for numerical simulations using a 1D heat flow configuration between the two materials in contacts, as defined in figure 4.2.

By considering the steady state in each domain, boundary conditions $T(X = X_1) = T_{B1}$ and $T(X = X_2) = T_{B2}$, the continuity of normal flux q_s across the interface located at $X = \xi$ and the one-dimensional jump condition $[[T(X = \xi)]] = -R_{th} q_s(X = \xi)$, we obtain the following exact solution:

$$T(X) = \begin{cases} \dfrac{q_s}{k_1}(X - X_1) + T_{B1} & \text{if} \quad X \in [X_1, \xi] \\ \dfrac{q_s}{k_2}(X - X_2) + T_{B2} & \text{if} \quad x \in [\xi, X_2] \end{cases} \tag{4.23}$$

where $q_s = (T_{B2} - T_{B1})/(\frac{\xi - X_1}{k_1} + R_{th} + \frac{X_2 - \xi}{k_2})$.

The boundaries are positioned at $X_1 = -1\ m$ and $X_2 = 1\ m$. The temperatures at these two boundaries are $T_{B1} = 0$ K and $T_{B2} = 1$ K. The other boundaries of the computational domain are adiabatic ($q_B = 0$). The interface position is $\xi = 0.09\ m$. The mesh is anisotropic in the mixture zone. The characteristic mesh sizes in this region are $h_\perp = 0.02 m$ in the direction perpendicular to the interface (also the direction of the heat flux) and $h_\parallel = 0.2\ m$ in the direction parallel to the interface. Outside the mixture zone, the mesh is isotropic of characteristic size $h_{max} = 0.2\ m$.

Different computations are performed for different values of the resistance R_{th} ranging from 10^{-5} (nearly perfect interface) to 10^5 K.W^{-1}.m^2 (nearly insulating interface). Thermal conductivity of materials is $k_1 = 0.1$ W.m^{-1}.K^{-1}, $k_2 = 10 \times k_1$. The half-thickness of the mixture zone is taken as $\varepsilon = 0.06$ m. The mixed conductivity profile along the x-axis using equation (4.18) is given in figure 4.4 for different thermal contact resistance values.

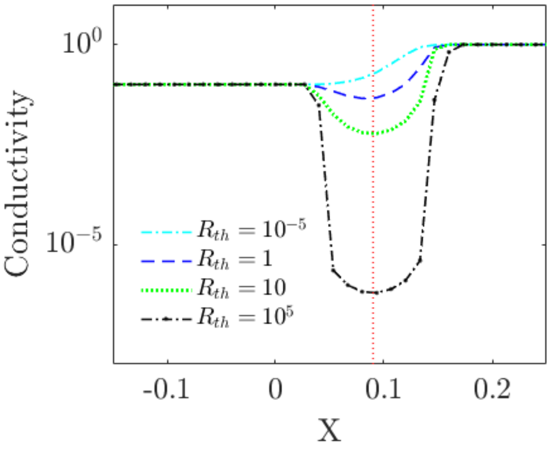

Figure 4.4: Conductivity profile for different thermal contact resistance values.

In figure 4.5, the computed and the exact temperature fields are plotted versus the X coordinate. We can observe that the strong temperature jump occurring at high thermal contact resistance is well captured by the proposed numerical model.

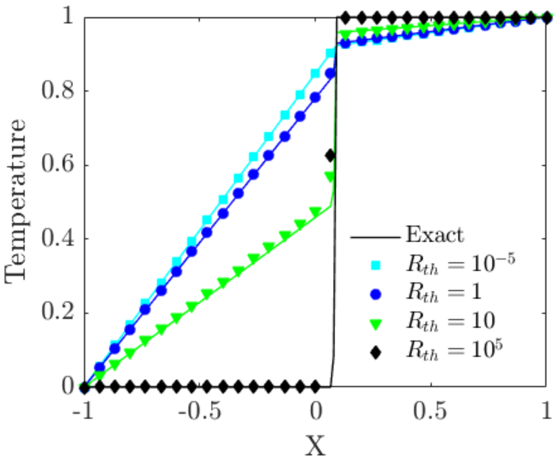

Figure 4.5: Steady temperature showing the jump at the interface for different thermal contact resistance values

Spherical interface benchmark

In the present example schematised in figure 4.6, we consider a composite sphere composed of a coating of outer radius r_2 and a core of radius r_1 separated by an interface with thermal resistance. The surface of the coating is submitted to a fixed temperature field given by a linear evolution along the z-axis, with temperature gradient $\mathbf{G} = (0, 0, e_0)$:

$$\mathrm{T} = \mathbf{G} \cdot \boldsymbol{x} = e_0 \times z \tag{4.24}$$

The steady state solution of this configuration is written in the spherical coordinates system (r, θ, ϕ) as:

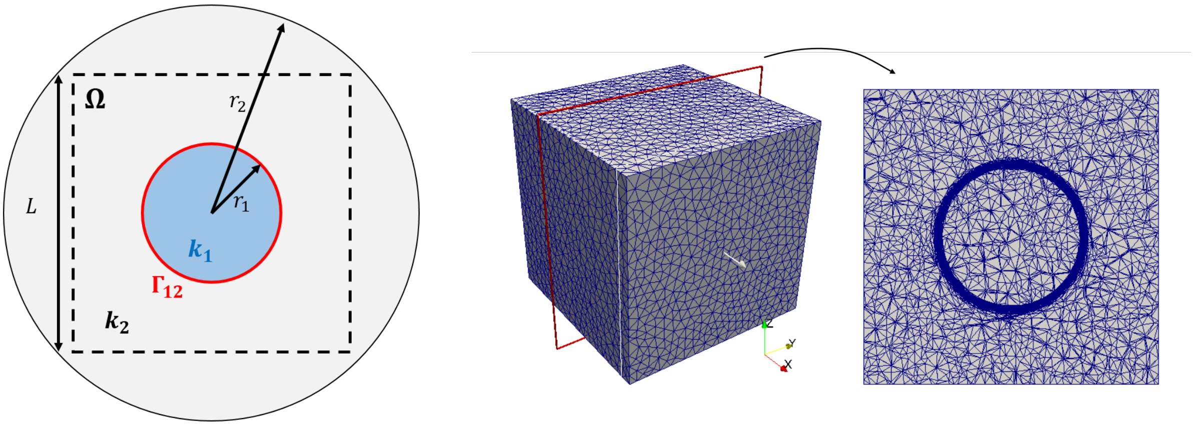

(a) Geometry (b) Mesh

Figure 4.6: Setup of the numerical simulation for a 3D heat flow configuration.

$$\mathrm{T}(r,\theta) = \begin{cases} \left(a_1 r + \dfrac{b_1}{r^2}\right) e_0 \, cos(\theta) & r < r_1 \\ \left(a_2 r + \dfrac{b_2}{r^2}\right) e_0 \, cos(\theta) & r > r_1 \end{cases} \tag{4.25}$$

According to the fact that the temperature at the centre must be finite, we necessarily have:

$$b_1 = 0 \tag{4.26}$$

Similarly as in section 4.2.3.1, the boundary condition (4.24), the continuity of the heat flux across the interface at $r = r_1$ and the temperature jump condition are used to finally find:

$$a_1 = \frac{3k_2 r_1 r_2^3}{\beta + \gamma} \tag{4.27}$$

$$a_2 = \frac{\beta}{\beta + \gamma} \tag{4.28}$$

$$b_2 = \frac{r_2^3 \gamma}{\beta + \gamma} \tag{4.29}$$

where

$$\beta = \left[k_1 r_1 + 2k_2 \left(r_1 + k_1 \mathrm{R}_{th}\right)\right] r_2^3 \tag{4.30}$$

and

$$\gamma = \left[k_1 k_2 \mathrm{R}_{th} + \left(k_2 - k_1\right) r_1\right] r_1^3 \tag{4.31}$$

Equation (4.25) together with (4.27)-(4.29) is the analytical solution which will be compared to the numerical solution given by the present model. For that, we consider a cubic computational domain Ω of a side length size $\mathrm{L} = 4r_1$ centred with the spheres as shown in figure 4.6a. At the boundary of the cube, $\partial\Omega$, we impose the analytical solution as a Dirichlet condition. In the present test, only the material domain corresponding to the coating of outer radius r_2 is concerned by the boundary condition as the core of radius r_1 is fully embedded in the coating.

Calculations are performed with the set of parameters given in Table 1 The simulated temperature field in the YZ-plane centred with the inner spherical domain is given in figure 4.8. Values of the thermal contact resistance are varied from 0 to 10^5 $\mathrm{K.W^{-1}}.m^2$. Figure 4.9 displays the comparison with the analytical solution of temperature profiles along the z-axis, with $z \geq 0$. Note that the solution for $\mathrm{R}_{th} = 0$ $\mathrm{K.W^{-1}}.m^2$ is not shown in figure 4.9 as it superimposes with $\mathrm{R}_{th} = 1$ $\mathrm{K.W^{-1}}.m^2$. For such low values of the heat resistance, the temperature jump at the interface vanishes. This is also shown when comparing figures 4.7a with figures 4.7b. Another observation is that for large values of the heat resistance, the temperature in the spherical core is almost uniform. When increasing R_{th} from 10^3 to 10^5 $\mathrm{K.W^{-1}}.m^2$, the temperature variation at the interface does not vary much. Finally, one can observe that the temperature fields only differ in the inner spherical core due to the high ratio k_2/k_1, low ratio r_2/r_1 and the Dirichlet boundary condition applied at the boundaries of the coating domain. The temperature profile in the core remains linear, which is also expected under a steady diffusion regime. Once again, the thermal contact resistance model presented in this work shows a good comparison with the analytical solution, demonstrating its use in a 3D heat flow configuration with an immersed boundary between domains with different thermal conductivity.

Parameter	e_0	r_1	r_2	k_1	k_2	R_{th}
Value	-1	1	3	0.01	1	$[0, 10^5]$
Unit	$\mathrm{K.m^{-1}}$	m	m	$\mathrm{W.m^{-1}.K^{-1}}$	$\mathrm{W.m^{-1}.K^{-1}}$	$\mathrm{K.W^{-1}.m^2}$

Table 4.1: Values of the simulation parameters for results presented in figures 4.8 and 4.9.

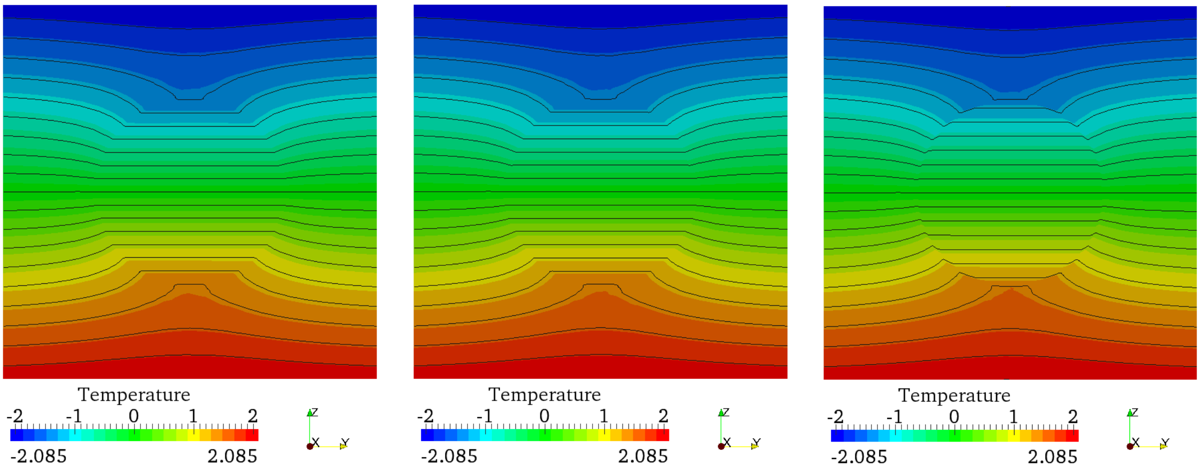

(a) $R_{th} = 0$ K.W^{-1}.m^2 (b) $R_{th} = 1$ K.W^{-1}.m^2 (c) $R_{th} = 10$ K.W^{-1}.m^2

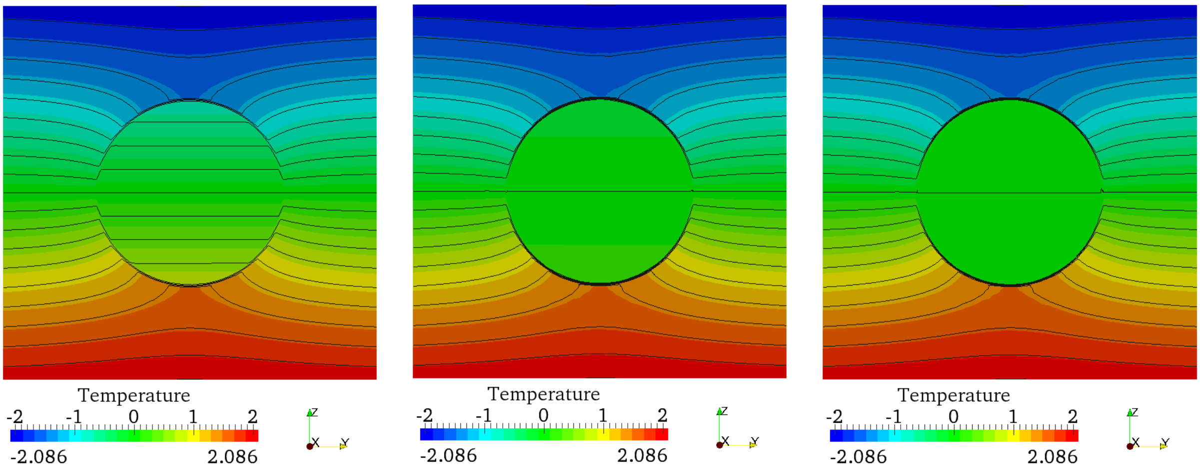

(d) $R_{th} = 10^2$ K.W^{-1}.m^2 (e) $R_{th} = 10^3$ K.W^{-1}.m^2 (f) $R_{th} = 10^5$ K.W^{-1}.m^2

Figure 4.7: Temperature field in YZ plane through the centre of the simulation domain.

Figure 4.8: Mesh

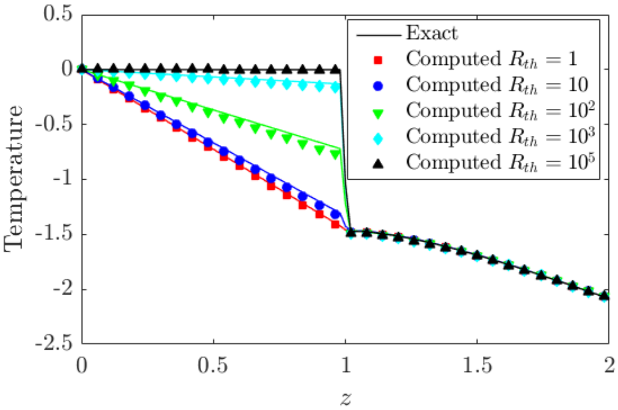

Figure 4.9: Steady temperature profiles showing the jump at the interface for different thermal contact resistance values.

4.2.3.2 Unsteady conduction

In order to evaluate the ability of the new model to handle unsteady heat transfer between two materials including a thermal contact resistance at the interface, we compare the results of the new model (referred to as implicit gap) to the results of a direct numerical simulation of an explicit gap between the two materials (referred to as explicit gap). The geometry of these two cases are shown in figure 4.10.

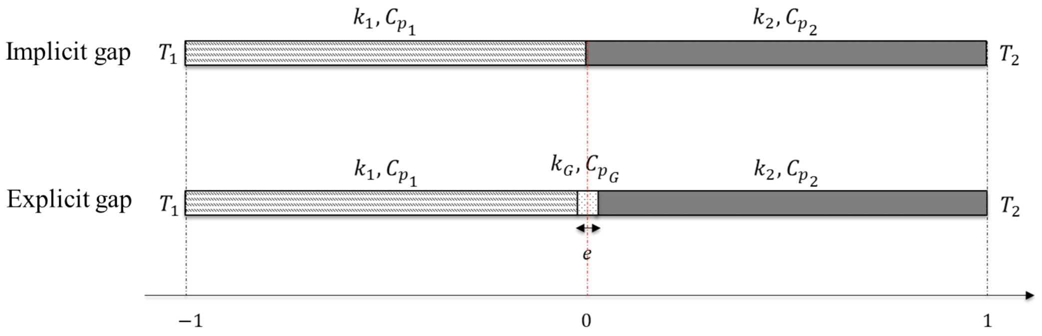

Figure 4.10: Setup for the unsteady conduction validation test. The reference case is referred to as "Explicit" and the evaluated case is referred to as "Implicit".

The temperature at $x = -1$ and $x = 1$ are fixed to $\mathrm{T}_1 = 1\mathrm{K}$ and $\mathrm{T}_2 = -1\mathrm{K}$ respectively. The top and the bottom boundaries are adiabatic ($q_\mathrm{B} = 0$) so heat flux is only one-dimensional. The thermal conductivity of each material are $k_1 = 1\,\mathrm{W}.m^{-1}.\mathrm{K}^{-1}$, $k_2 = 0.1\,\mathrm{W}.m^{-1}.\mathrm{K}^{-1}$ and $k_\mathrm{G} = 0.001\,\mathrm{W}.m^{-1}.\mathrm{K}^{-1}$. The thickness of the gap is $e = 0.002\ m$. So the thermal contact resistance value is $\mathrm{R}_{th} = e/k_\mathrm{G} = 2\,\mathrm{K.W}^{-1}.m^2$.

The meshes of each case are shown in the vicinity of the interface in figure 4.11a and 4.11b. The mesh for the description of the explicit gap is much finer than that for the implicit gap. Inside the region of fine mesh, which covers the gap layer, the mesh size is $10^{-4}\ m$ in the direction perpendicular to the interface. This is required to ensure enough mesh elements within the gap domain. On the other hand, the thickness of the mixing zone for the implicit case is $2\varepsilon = 0.06\ m$ so that ratio $2\varepsilon/e \gg 1$. The mesh size inside the mixing zone is $0.003\ m$ in the direction perpendicular to the interface. The heat capacity of each material are $\mathrm{C}_{p_1} = 1\,\mathrm{J.K}^{-1}.m^{-3}$ and $\mathrm{C}_{p_2} = 0.5\,\mathrm{J.K}^{-1}.m^{-3}$. Three values of $\mathrm{C}_{p_\mathrm{G}}$ are considered: $\mathrm{C}_{p_\mathrm{G}} = 0.001\,\mathrm{J}.m^{-3}.\mathrm{K}^{-1}$, $\mathrm{C}_{p_\mathrm{G}} = 1.3\,\mathrm{J}.m^{-3}.\mathrm{K}^{-1}$ and $\mathrm{C}_{p,\mathrm{G}} = 50\,\mathrm{J}.m^{-3}.\mathrm{K}^{-1}$, corresponding to $\mathrm{C}_{p_\mathrm{G}} \ll \overline{\mathrm{C}_p}$, $\mathrm{C}_{p_\mathrm{G}} = \mathcal{O}(\overline{\mathrm{C}_p})$ and $\mathrm{C}_{p_\mathrm{G}} \gg \overline{\mathrm{C}_p}$, respectively. For each value of $\mathrm{C}_{p_\mathrm{G}}$ two formulae of the heat capacity mixing law are tested, referred to as Formula 1 given by equation (4.22) and Formula 2 given by equation (4.11). Results are shown in figures 4.12, 4.13 and 4.14 as temperature profiles along the x-axis for both the (a) explicit and (b) implicit gap.

In figure 4.12, when $\mathrm{C}_{p_\mathrm{G}} \ll \overline{\mathrm{C}_p}$, the heat capacity mixing law for perfect contact, i.e. using Formula 1 with equation (4.11), is sufficient to describe the transient heat conduction, i.e. to retrieve the more exact numerical solution given by (plain curves) the explicit gap formulation. The same can be observed in figure 4.13 when $\mathrm{C}_{p_\mathrm{G}} = \mathcal{O}(\overline{\mathrm{C}_p})$. No or very little difference is revealed between symbols and curves. However, when $\mathrm{C}_{p,\mathrm{G}} \gg \overline{\mathrm{C}_p}$, figure 4.14 reveals differences between Formula 1 and the more precise Formula 2. This does not concern the steady behaviours when the time is large enough, and two linear temperature evolution have settled in the domains (time $t = 7.9\ s$),

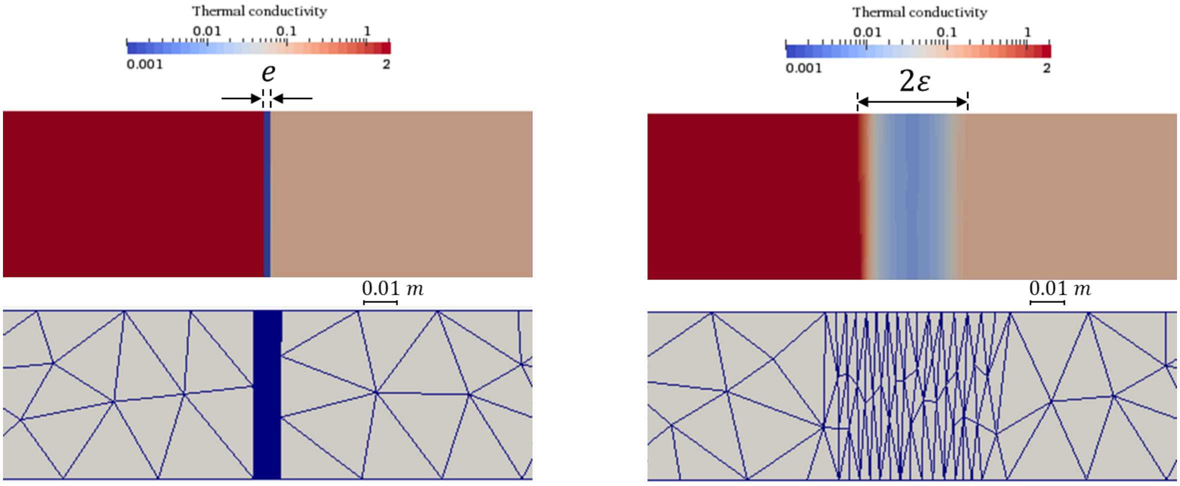

(a) Explicit gap

(b) Implicit gap

Figure 4.11: Mesh size and distribution of the heat conductivity for the (a) explicit and (b) implicit gap configurations.

but intermediate times for unsteady heat flows. For instance, at time $t = 0.6\ s$, a clear difference appears in figure 4.14a between the explicit gap configuration, that corresponds to the reference situation, and the implicit configuration using Formula 1 with equation (4.11). While the deviation is not large, a gap with a high value of the heat capacity compared to the surrounding materials is thus better described with Formula 2 using the mixing law given by equation (4.22). Despite this observation that reveals the consequences of using the heat capacity mixing law for perfect contact, it is clear that using equation (4.22) does not require big additional efforts while reaching excellent agreement when dealing with the prediction of non-stationary heat conduction.

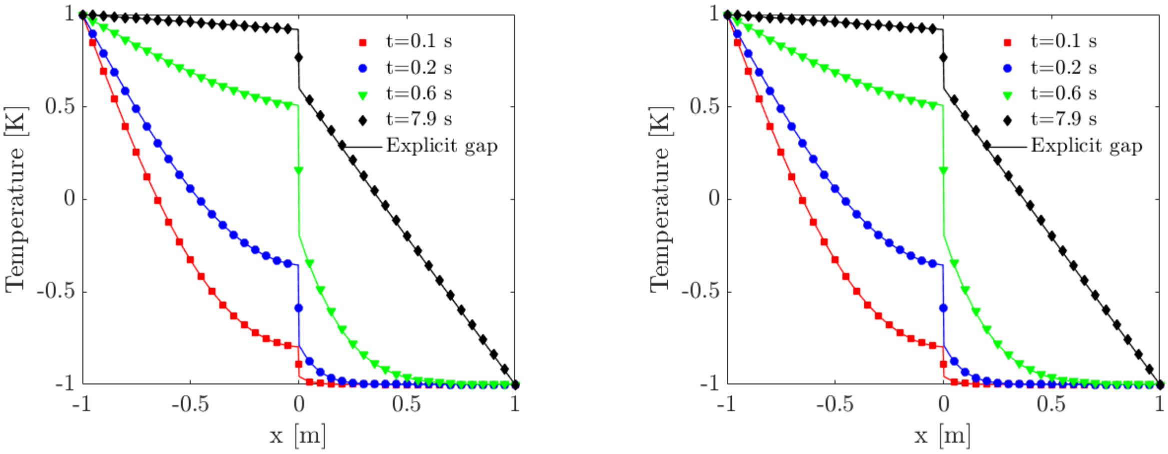

(a) Formula 1: equation (4.11)

(b) Formula 2: equation (4.22)

Figure 4.12: Time-evolution of the temperature jump across the interface for $\mathrm{C}_{p,\mathrm{G}} \ll \overline{\mathrm{C}_p}$

.

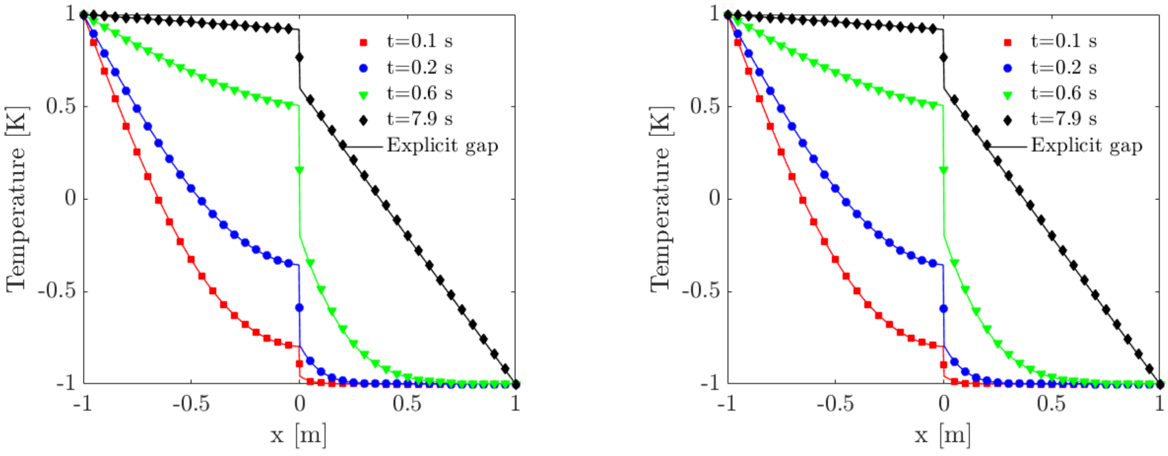

(a) Formula 1: equation (4.11)

(b) Formula 2: equation (4.22)

Figure 4.13: Time-evolution of the temperature jump across the interface for $C_{p,G} = \mathcal{O}(\overline{C_p})$

.

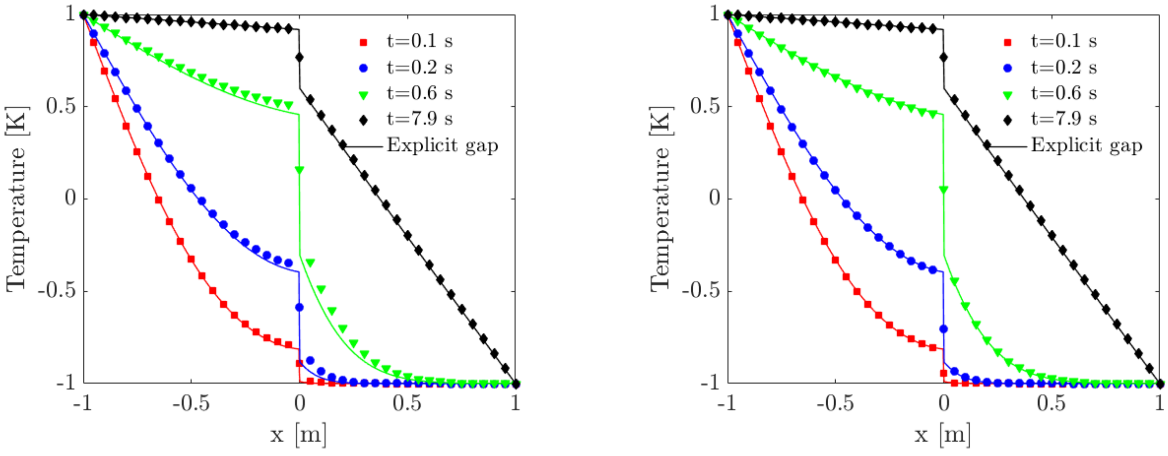

(a) Formula 1: equation (4.11)

(b) Formula 2: equation (4.22)

Figure 4.14: Time-evolution of the temperature jump across the interface for $C_{p,G} \gg \overline{C_p}$

.

4.3 Heat conduction with solidification

4.3.1 Introduction

In solidification of metals, a multi-phase system refers to a metal domain that undergoes phase transformations involving the liquid phase and the different solid phases that may exist depending on the temperature and the chemical composition. The distribution of phases in a metal as a function of temperature and chemical composition is described by the phase diagram. For example, for FeC steel several phases may exist simultaneously during solidification: liquid phase and solid phases with different crystalline structures α-Fe (ferrite), γ-Fe (austenite), δ-Fe, Cementite... We denote by φ a phase involved during solidification and solid-state transformations of a metal (M). For the sake of simplicity, φ is either (l) for the liquid phase or (s) for all possible individual solid phases. In the microscopic scale, the energy conservation equation governed by heat conduction is written in each phase as follows:

$$\frac{\partial\left(\rho^{\varphi} h^{\varphi}\right)}{\partial t} = \boldsymbol{\nabla}\cdot\left(k^{\varphi}\boldsymbol{\nabla}\mathrm{T}^{\varphi}\right),\ \ \boldsymbol{x}\in\varphi \tag{4.32}$$

In order to predict solidification while explicitly solving the boundaries of each phase, it is necessary to adopt a microscopic approach capable of solving dendritic microstructures. For a metric-sized sample, it is not realistic to solve the equations at the microscopic scale. Instead, macroscopic models are used, which can be derived by averaging the microscopic equations over a finite volume that contains both solid and liquid phases. The liquid-solid interface is thus implicitly represented via the volume averaging method. The principle of this method as well as the steps for obtaining the averaged energy conservation equation are presented hereafter.

4.3.2 Volume averaging method

To obtain the macroscopic or averaged energy equation, we first need to define a finite-sized averaging volume. This volume is called Representative Elementary Volume (REV). As its name reveals, the REV must be representative of the phenomenon that we are trying to model. In the case of solidification-related phenomena, the size of the REV must be larger than the characteristic dimension of the microstructure [10^{-6} m, 10^{-4} m] and smaller than that of the system [10^{-3} m, 10^{0} m]. The size of the REV can vary between 10^{-4} m and 10^{-3} m. It thus includes some columnar and/or equiaxed dendrites, as shown in figure 4.15. Two assumptions are also made for this REV:

$\mathscr{H}_1$. Although porosities may form during solidification, the study of porosities is out of the scope of our present study. Therefore, the metal is supposed to be saturated by both liquid and solid phases.

$\mathscr{H}_2$. It is assumed that in the REV the temperature is uniform. This is justified by the fact that the thermal properties of the two phases are not too different, and that the thermal contact resistances between phases are negligible.

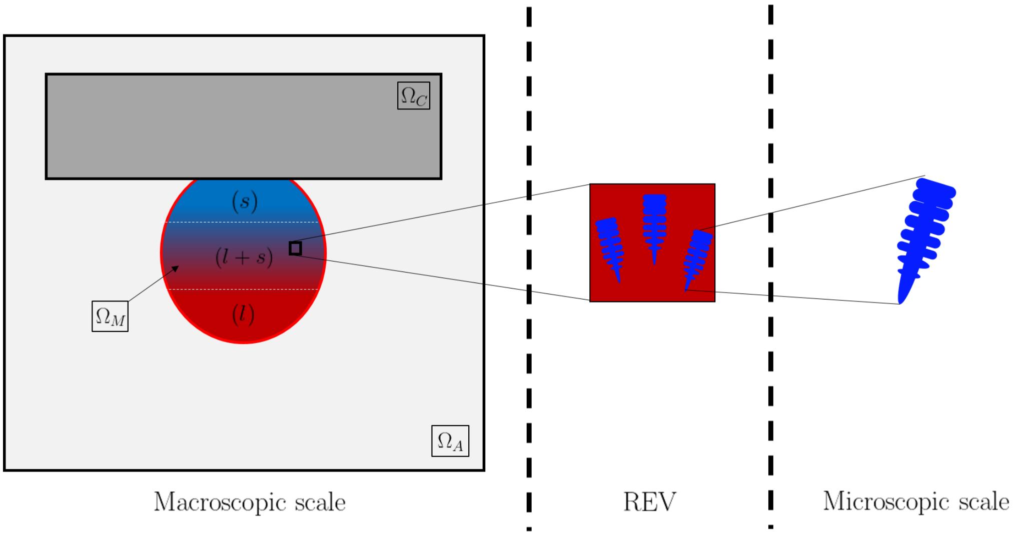

Figure 4.15: Schematic representation of the REV

Considering a REV, the volume averaging method introduces a phase indicator function:

$$\chi^{\varphi} = \begin{cases} 1 & \boldsymbol{x} \in \varphi \\ 0 & \boldsymbol{x} \notin \varphi \end{cases} \tag{4.33}$$

Let consider V_E the volume of the REV and V_φ the volume of the phase φ. For every physical quantity ψ, we define the following averaging operators:

Operator 1: The phase average $\langle \psi^{\varphi} \rangle$:

$$\langle \psi^{\varphi} \rangle = \frac{1}{V_E} \int_{V_E} \psi \, \chi^{\varphi} \, dV \tag{4.34}$$

Operator 2: The phase intrinsic average $\langle \psi \rangle^{\varphi}$

$$\langle \psi \rangle^{\varphi} = \frac{1}{V_\varphi} \int_{V_\varphi} \psi \, dV \tag{4.35}$$

Operator 3: The fluctuation $\widetilde{\psi}^{\varphi}$ of ψ with respect to $\langle \psi \rangle^{\varphi}$

$$\widetilde{\psi}^{\varphi} = \left(\psi - \langle \psi \rangle^{\varphi} \right) \chi^{\varphi} \tag{4.36}$$

For $\psi = 1$, we obtain from equation (4.34) the volume fraction of the phase φ

$$\frac{1}{V_E} \int_{V_E} \chi^{\varphi} \, dV = \frac{V_\varphi}{V_E} = g^{\varphi} \tag{4.37}$$

We deduce from equations (4.34) and (4.37) that:

$$\begin{aligned} \langle \psi^{\varphi} \rangle &= \frac{\mathrm{V}_{\varphi}}{\mathrm{V}_{\mathrm{E}}} \left(\frac{1}{\mathrm{V}_{\varphi}} \int_{\mathrm{V}_{\mathrm{E}}} \psi \, \chi^{\varphi} \, d\mathrm{V} \right) \\ &= \frac{\mathrm{V}_{\varphi}}{\mathrm{V}_{\mathrm{E}}} \left(\frac{1}{\mathrm{V}_{\varphi}} \int_{\mathrm{V}_{\varphi}} \psi \, d\mathrm{V} \right) \\ &= g^{\varphi} \langle \psi \rangle^{\varphi} \end{aligned} \tag{4.38}$$

Following the assumption $\mathscr{H}_1$, the sum of all phase fractions is equal to 1.

$$\sum_{\varphi \in \mathrm{M}} g^{\varphi} = 1 \tag{4.39}$$

Therefore, for a quantity ψ, the global volume average denoted by $\langle \psi \rangle$ writes:

$$\langle \psi \rangle = \sum_{\varphi \in \mathrm{M}} \langle \psi^{\varphi} \rangle = \sum_{\varphi \in \mathrm{M}} g^{\varphi} \langle \psi \rangle^{\varphi} \tag{4.40}$$

Following these definitions, we give hereafter some theorems and refer the reader to the work of [95] for detailed demonstrations:

$$\left\langle \left(\frac{\partial \psi}{\partial t} \right)^{\varphi} \right\rangle = \frac{\partial \langle \psi^{\varphi} \rangle}{\partial t} - \frac{1}{\mathrm{V}_{\mathrm{E}}} \int_{\Gamma_{\varphi\beta}} \psi^{\varphi} \boldsymbol{u}_{\Gamma_{\varphi\beta}} \cdot \boldsymbol{n}^{\varphi} \, d\mathrm{S} \tag{4.41}$$

$$\langle (\nabla \psi)^{\varphi} \rangle = \nabla \langle \psi^{\varphi} \rangle + \frac{1}{\mathrm{V}_{\mathrm{E}}} \int_{\Gamma_{\varphi\beta}} \psi^{\varphi} \boldsymbol{n}^{\varphi} \, d\mathrm{S} \tag{4.42}$$

$$\langle (\nabla \cdot \boldsymbol{v})^{\varphi} \rangle = \nabla \cdot \langle \boldsymbol{v}^{\varphi} \rangle + \frac{1}{\mathrm{V}_{\mathrm{E}}} \int_{\Gamma_{\varphi\beta}} \boldsymbol{v}^{\varphi} \cdot \boldsymbol{n}^{\varphi} \, d\mathrm{S} \tag{4.43}$$

where $\boldsymbol{u}_{\Gamma_{\varphi\beta}}$ is the velocity vector of the boundary $\Gamma_{\varphi\beta}$ separating the two phases φ and β, and $\boldsymbol{n}^{\varphi}$ is the normal to $\Gamma_{\varphi\beta}$ directed outwards to the phase φ. $\boldsymbol{v}$ is an arbitrary vector.

Considering two variables ψ and ξ, the phase intrinsic average of their product is:

$$\langle \psi \xi \rangle^{\varphi} = \langle \psi \rangle^{\varphi} \ \langle \xi \rangle^{\varphi} \ + \ \langle \widetilde{\psi}^{\varphi} \, \widetilde{\xi}^{\varphi} \rangle^{\varphi} \tag{4.44}$$

Following the work of [96], we neglect the fluctuation terms of the density with any mass quantity ψ. Hence, we write:

$$\langle (\rho \psi) \rangle^{\varphi} = \langle \rho \rangle^{\varphi} \langle \psi \rangle^{\varphi} \tag{4.45}$$

4.3.3 Averaged energy conservation equation

For simplicity, the intrinsic phase average $\langle \psi \rangle^{\varphi}$ is denoted by ψ^{φ}. By integrating the microscopic equation for each phase (4.32) over the volume of the REV and making use of the previous formulae, we obtain the macroscopic energy conservation for each phase:

$$\frac{\partial\left(g^l\rho^l h^l\right)}{\partial t} = \nabla\cdot\langle k^l\nabla \mathrm{T}^l\rangle + \mathrm{Q}^{l/s} \tag{4.46}$$

$$\frac{\partial\left(g^s\rho^s h^s\right)}{\partial t} = \nabla\cdot\langle k^s\nabla \mathrm{T}^s\rangle + \mathrm{Q}^{s/l} \tag{4.47}$$

where $\mathrm{Q}^{l/s}$ and $\mathrm{Q}^{s/l}$ are the interfacial heat exchange terms at the liquid/solid interface for which we give the expressions hereinafter:

$$\mathrm{Q}^{l/s} = \frac{1}{\mathrm{V_E}}\int_{\Gamma_{ls}} (\rho h)^l \boldsymbol{u}_{\Gamma_{ls}}\cdot\boldsymbol{n}^l\, d\mathrm{S} + \frac{1}{\mathrm{V_E}}\int_{\Gamma_{ls}} k^l\nabla\mathrm{T}^l\cdot\boldsymbol{n}^l\, d\mathrm{S} \tag{4.48}$$

$$\mathrm{Q}^{s/l} = \frac{1}{\mathrm{V_E}}\int_{\Gamma_{ls}} (\rho h)^s \boldsymbol{u}_{\Gamma_{ls}}\cdot\boldsymbol{n}^s\, d\mathrm{S} + \frac{1}{\mathrm{V_E}}\int_{\Gamma_{ls}} k^s\nabla\mathrm{T}^s\cdot\boldsymbol{n}^s\, d\mathrm{S} \tag{4.49}$$

Considering the hypothesis $\mathscr{H}_2$, we can write $\mathrm{T}^l = \mathrm{T}^s = \mathrm{T}$. Hence, the phase averaged energy conservation equations read:

$$\frac{\partial\left(g^l\rho^l h^l\right)}{\partial t} = \nabla\cdot\left(g^l k^l\nabla\mathrm{T}\right) + \mathrm{Q}^{l/s} \tag{4.50}$$

$$\frac{\partial\left(g^s\rho^s h^s\right)}{\partial t} = \nabla\cdot\left(g^s k^s\nabla\mathrm{T}\right) + \mathrm{Q}^{s/l} \tag{4.51}$$

Assuming that the contact at the boundary between the liquid and the solid phases is perfect, the heat balance at the liquid/solid interface is zero.

$$\mathrm{Q}^{l/s} + \mathrm{Q}^{s/l} = 0 \tag{4.52}$$

Therefore, the global volume averaged energy conservation in the single multiphase domain writes:

$$\frac{\partial\langle\rho h\rangle}{\partial t} = \nabla\cdot\left(\langle k\rangle\,\nabla\mathrm{T}\right) \tag{4.53}$$

4.3.4 Monolithic formulation of the energy conservation in a multi-domain system

Consider a computational domain Ω composed of N subdomains Ω_i, $i \in 1,\ldots,\mathrm{N}$. The averaged energy conservation equation in each domain Ω_i writes:

$$\frac{\partial\langle\rho h\rangle_{\Omega_i}}{\partial t} = \nabla\cdot\left(\langle k\rangle_{\Omega_i}\nabla\mathrm{T}\right) \tag{4.54}$$

Following the previous work in section 4.2, we can generalise the monolithic formulation of the energy conservation equation for a multi-domain system as follows:

$$\int_\Omega \frac{\partial\widehat{\langle\rho h\rangle}}{\partial t}\mathscr{T}\, d\mathrm{V} + \int_\Omega \widehat{\langle k\rangle}\nabla\mathrm{T}\cdot\nabla\mathscr{T}\, d\mathrm{V} = \int_{\partial\Omega_{\mathrm{Neu}}} q_{\mathrm{B}}\mathscr{T}\, d\mathrm{S} \tag{4.55}$$

where the mixed field of averaged volumetric enthapies can be expressed as:

$$\widehat{\langle \rho h \rangle} = \sum_{i \in 1,\dots,N} \langle \rho h \rangle_{\Omega_i} \mathrm{H}_{\Omega_i} \tag{4.56}$$

and the mixed thermal conductivity including thermal contact resistance is

$$\widehat{\langle k \rangle} = \left(\sum_{1 \leq i \leq N} \frac{\mathrm{H}_{\Omega_i}}{\langle k \rangle_{\Omega_i}} + \sum_{1 \leq i < j \leq N} \delta_{\Gamma_{ij}} \mathrm{R}_{th_{ij}} \right)^{-1} \tag{4.57}$$

The non-linear effect of (4.55) raises up due to the non-linear relationship between T and $\langle \rho h \rangle$, especially with the latent heat during solid-liquid transformation. The numerical resolution of this non-linear equation is based on an energy solver coupled with tabulated thermodynamic properties. The details of this solver and its validation are shown in [97].

4.4 Application to chill cooling and solidification experiment on board the ISS

We only focus hereafter on solidification governed by heat conduction from the droplet to the chill plate without convective heat transport in the bulk liquid metal (no flow is considered). The monolithic formulation of the energy conservation equation in a computational domain Ω containing the metallic sample Ω_M in contact with the chill plate Ω_C together surrounded by Argon gas Ω_A is given by equation (4.55).

Hereafter, the quantities defined in each of the sub-domains Ω_M, Ω_C and Ω_A are indexed by M, C and A respectively. Since the sub-domains Ω_C and Ω_A do not undergo any phase transformation, the exponent φ will be used only for the quantities of the metallic sub-domain to denote the liquid (l) phase and the different solid (s) phases.

Accordingly, the mixed field $\widehat{\langle \rho h \rangle}$ of the averaged volumetric enthalpies $\langle \rho h \rangle_M$, $\langle \rho h \rangle_C$ and $\langle \rho h \rangle_A$ is expressed using the smooth Heaviside functions H_M, H_C and H_A as follows:

$$\widehat{\langle \rho h \rangle} = \langle \rho h \rangle_M \mathrm{H}_M + \langle \rho h \rangle_C \mathrm{H}_C + \langle \rho h \rangle_A \mathrm{H}_A \tag{4.58}$$

Considering a REV, the average volumetric enthalpy of the metal writes:

$$\langle \rho h \rangle_M = \sum_{\varphi \in M} g^{\varphi} \rho_M^{\varphi} h_M^{\varphi} \tag{4.59}$$

The volume fractions g^{φ}, the densities ρ_M^{φ} and the enthalpies h_M^{φ} are tabulated with respect to temperature T for the Fe-0.9wt.%C-0.26wt.%Si alloy as shown in figure 4.16.

As for the chill plate, made only of a solid ceramic phase Si_3N_4, the average volumetric enthalpy is a linear function of the temperature

$$\langle \rho h \rangle_C = \mathrm{C}_{p,C}.\mathrm{T} \tag{4.60}$$

where $\mathrm{C}_{p,C} = 2.303 \times 10^6\ \mathrm{J.K^{-1}}.m^{-3}$.

The same principle applies to the Argon gas enthalpy

$$\langle \rho h \rangle_{\mathrm{A}} = \mathrm{C}_{p,\mathrm{A}}.\mathrm{T} \tag{4.61}$$

with $\mathrm{C}_{p,\mathrm{A}} = 1300\ \mathrm{J.K}^{-1}.m^{-3}$.

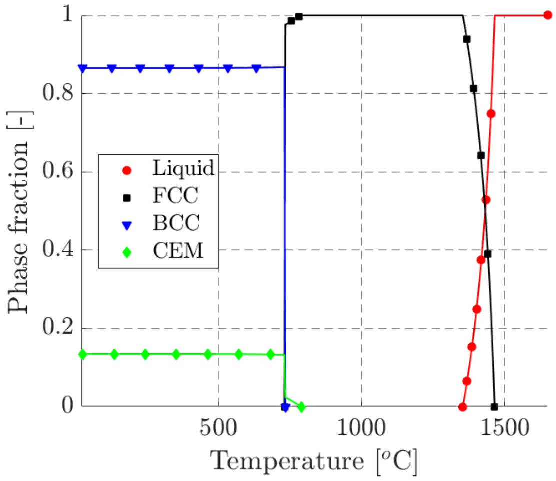

(a) phase volume fractions

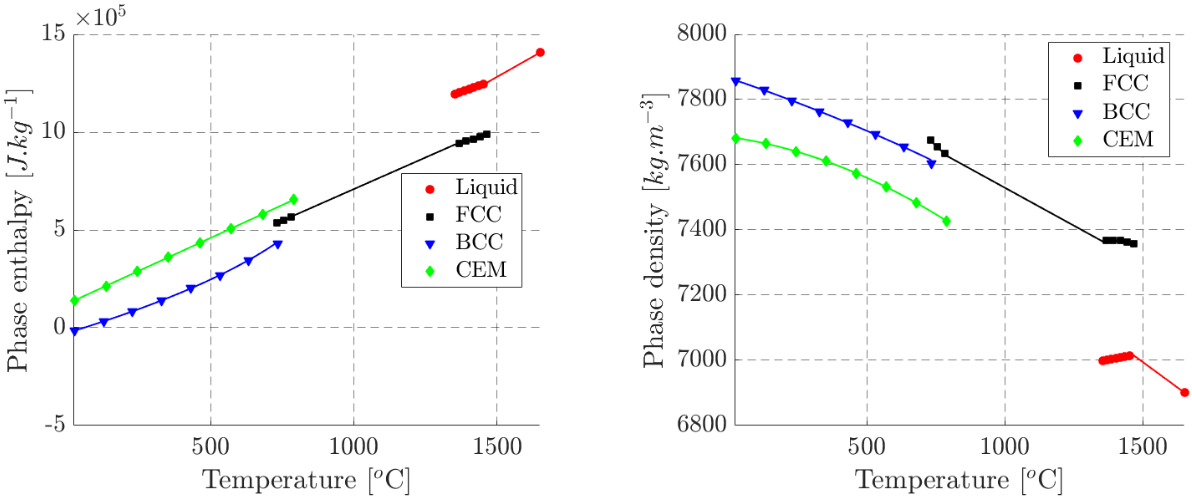

(b) phase intrinsic average enthapies

(c) phase intrinsic average densities

Figure 4.16: Tabulated thermodynamic properties for the Fe-0.9wt.%C-0.26wt.%Si alloy at nominal composition.

The metal-gas interface Γ_{MA} and chill-gas interface Γ_{CA} are considered as perfect. A thermal contact resistance is only applied at the metal-chill interface Γ_{MC}. Therefore, the mixed thermal conductivity in this multi-domain system writes:

$$\widehat{\langle k \rangle} = \left(\frac{\mathrm{H}_{\mathrm{M}}}{\langle k \rangle_{\mathrm{M}}} + \frac{\mathrm{H}_{\mathrm{A}}}{\langle k \rangle_{\mathrm{A}}} + \frac{\mathrm{H}_{\mathrm{C}}}{\langle k \rangle_{\mathrm{C}}} + \delta_{\mathrm{MC}} \mathrm{R}_{th} \right)^{-1} \tag{4.62}$$

where R_{th} is the thermal contact resistance at Γ_{MA} and δ_{MC} is the smooth Dirac function associated to this interface. The average thermal conductivities are constant such as:

$$\langle k \rangle_{\mathrm{M}} = 42\ \mathrm{W}.m^{-1}.\mathrm{K}^{-1}$$

$$\langle k \rangle_{\mathrm{C}} = 50\ \mathrm{W}.m^{-1}.\mathrm{K}^{-1}$$

$$\langle k \rangle_{\mathrm{A}} = 0.01\ \mathrm{W}.m^{-1}.\mathrm{K}^{-1}$$

In this problem, we need two level-set functions to compute the Heaviside and Dirac functions: one level set ϕ_{M} to describe the boundary of the droplet and the second ϕ_{C} for the chill plate boundary. The droplet shape is based on the final shape of the solidified sample on board the ISS shown in Figure 2.16 of chapter 2. It is approximated to an ellipsoid of minor horizontal axis 5.73 mm and major vertical axis 7.65 mm. This ellipsoid is truncated from the top so that the droplet is 7.31 mm high and the plane surface in contact with the chill is a disc 2.2 mm diameter. Note that the final shape of the solidified sample processed on board a zero-g airplane has slightly different dimensions, particularly smaller contact area with the chill as observed in Figure 4.1. The chill plate is a cylinder of 16 mm diameter and 3 mm high as in the ISS experiment. The Heaviside functions H_{M} and H_{C} are determined by formula (4.10) using ϕ_{M} and ϕ_{C} respectively. The gas Heaviside is then $\mathrm{H}_{\mathrm{A}} = 1 - \mathrm{H}_{\mathrm{M}} - \mathrm{H}_{\mathrm{C}}$. The mixing half-thickness ϵ is fixed to 0.18 mm. The Dirac function δ_{MC} is calculated as:

$$\delta_{\mathrm{MC}} = \begin{cases} \delta_{\mathrm{M}} & \text{if } \ \mathrm{H}_{\mathrm{C}} > 0 \\ 0 & \text{if } \ \mathrm{H}_{\mathrm{C}} = 0 \end{cases} \tag{4.63}$$

where δ_{M} is the metal Dirac function defined by equation (3.26) using ϕ_{M}.

The computational domain is a box of a side length of 20 mm in the vertical Z-direction and 28 mm in the X- and Y-directions (Figure 4.17a). The mesh size around the interfaces is 0.06 mm in the direction of the normal to the interface. Inside each domain, the mesh size is 0.2 mm for the metal, 0.3 mm for the chill and 0.6 mm for the gas (Figure 4.17b).

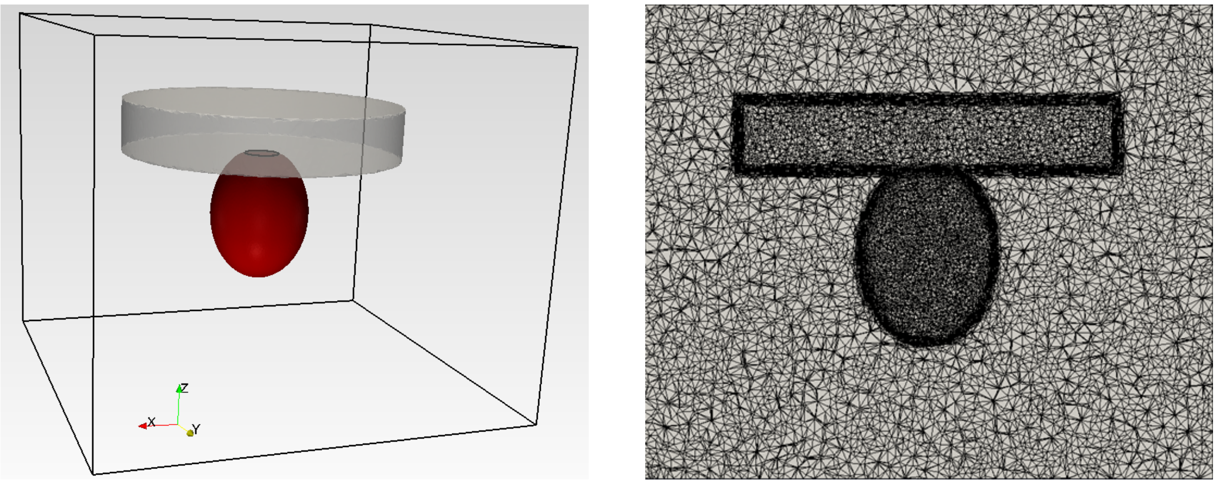

(a) Geometries

(b) Mesh (cross section)

Figure 4.17: The setup of the simulation for chill cooling and solidification of a deformed steel droplet showing (a) the geometries of the droplet and chill plate inside the computational domain and (b) a cross section through the 3D finite element mesh

.

The initial temperature is 1921 K for the metal and the gas and 300 K for the chill plate. The adiabatic condition is considered at the boundaries of the computational domain $q_B = 0$. Several simulations were performed for different values of thermal contact resistance 0, 10^{-5}, 2.10^{-5}, 5.10^{-5} and 10^{-4} (values in $K.W^{-1}.m^2$). The comparison with the experiment is based on the time-evolution of the solidification front position from the chill plate. The experimental curve was obtained from image processing of the video recorded with an embedded high-speed camera in the experimental device on board the ISS as shown in Figure 2.17 in Chapter 2. The solidification front was extracted from the recorded images using the colour contrast between the solid and liquid phases visible on the free surface of the sample. Theoretically, the solidification front is located at the boundary of the solid dendrites with the liquid phase. This interface forms at the liquidus temperature $T_L = 1739$ K. The numerical results with different R_{th} values for $T = T_L$ are shown in figure 4.18a. With a perfect contact ($R_{th} = 0$, i.e. no model for Kapitza resistance), it takes 4 seconds for the liquidus iso-value to reach the bottom of the sample. As it was shown in chapter 2, the front reaches the bottom of the droplet after approximately 8 seconds. When the thermal contact resistance is taken into account in the simulations, the solidification front growth slows down. A value of $R_{th} = 5.10^{-5}$ $K.W^{-1}.m^2$ allows getting closer to the experimental solidification duration. However, the experiment shows that the "contrast-based" front is propagating with a constant speed. The simulation shows a positive acceleration of the growth of the liquidus-based front. Several parameters could be at the origin of the difference: the fluid flow, the deformation of the droplet but also the difference in the criterion for tracking the front. Indeed, the contrast between the liquid and solid phases on the images is only visible when the solid fraction g^s is higher than a certain value. When we choose, as a criterion for front detection, the iso-value $g^s = 10\%$ the time-evolution of the front position becomes slower than the liquidus-based front 4.18b. In this case, the value of $R_{th} = 2.10^{-5}$ $K.W^{-1}.m^2$ gives a good prediction of the experimental behaviour during the first 6 seconds but predicts a shorter solidification duration than observed experimentally.

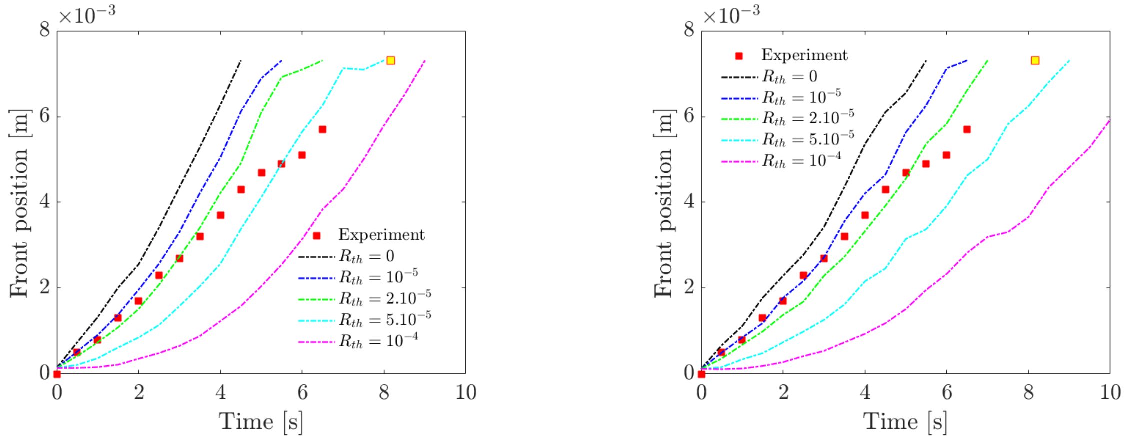

(a) $T = T_L$ (b) $g^s = 10\%$

Figure 4.18: The time-evolutions of the front position for different thermal contact resistance compared to the experiment (the yellow square is extrapolated)

.

4.5 Conclusion

In this chapter, we presented the numerical framework for modelling heat transfer in a multi-domain system involving solidification and thermal contact resistance. In the first part, we proposed a simple and efficient numerical model to account for thermal contact resistance at an arbitrarily-shaped interface while using a monolithic solution with a diffuse interface. The model describes the interface by starting from the level-set method and smoothing the transition from one material to the other by a smoothed Heaviside function, hence defining a diffuse interface. The accuracy and robustness of the model are assessed through benchmarks for both steady and transient diffusion regimes. The results and comparisons with the references show that the model can produce a good prediction of the temperature jump across the interface. The second part of this chapter was dedicated to solidification modelling based on the volume average method and the temperature-based energy solver coupled with thermodynamics tabulations. Finally, the numerical framework was applied to simulate the chill cooling experiments of the steel sample conducted in the context of the CCEMLCC project on board the ISS. These simulations clearly show the influence of the thermal contact resistance on the cooling rate, as well as it gives a first estimation of the order of magnitude of the real resistance value. However, the simulation of solidification by pure conduction in a static drop is far from being sufficient to reproduce what occurs in the experiment, in particular, because of the absence of the convective heat and mass transfers. Simulation of chill cooling and solidification, including convective heat transfer induced by solidification shrinkage and capillary forces present at the metal-gas interface, will be the topic of the next chapter.

Chapter 5

Numerical simulation of chill cooling and solidification of a levitated steel sample in microgravity

Résumé

Ce chapitre est consacré à la modélisation du couplage de l'écoulement fluide et du transfert de chaleur dans le contexte de la solidification et de la ségrégation chimique. Tout d'abord, nous présentons les équations de conservation de l'énergie, de la masse totale, de la quantité de mouvement et de la masse des espèces chimiques d'un système multi-domaines impliquant un alliage métallique multi-composants. Une formulation monolithique permet la résolution d'un seul système d'équations sur un seul maillage eulérien. La description de l'écoulement fluide est enrichie par la prise en compte du retrait de solidification, de la tension de surface et de l'effet Marangoni agissant à l'interface liquide-gaz. Ensuite, nous appliquons le cadre numérique pour simuler le refroidissement et la solidification d'un échantillon d'acier en microgravité. Des simulations numériques préliminaires sont montrées en 2D. Ensuite, une simulation en 3D est présentée. Les résultats numériques sont comparés aux résultats de l'expérience ISS sur l'alliage Fe-0.9wt.%C-0.26wt.%Si.

Contents

5.1 Introduction 110
5.2 Governing equations for conjugate heat transfer including solidification, chemical segregation and capillary forces 110
  5.2.1 Mass conservation 110
  5.2.2 Momentum conservation 112
  5.2.3 Energy conservation equation 117
  5.2.4 Chemical species conservation equation 120
  5.2.5 Modelling of interfaces 123
5.3 Coupling resolution strategy 126
5.4 Application to chill cooling and solidification experiment on board the ISS . . . 128
  5.4.1 Preliminary results and numerical investigations 128
    5.4.1.1 Computational configuration 128
    5.4.1.2 Numerical results and discussion 132
  5.4.2 3D simulation 143
5.5 Conclusion 147

5.1 Introduction

This chapter is dedicated to the modelling of coupling heat transfer and fluid dynamics in the context of solidification and chemical segregation. First, we present the governing equations. Then, we apply the numerical framework to simulate the chill cooling of a steel sample in microgravity. Preliminary numerical tests will be shown in 2D. Then, a 3D simulation will be presented. The numerical results will be compared to the experimental data issued from the ISS on the sample *d1* (Fe-0.9wt.%C-0.26wt.%Si alloy).

5.2 Governing equations for conjugate heat transfer including solidification, chemical segregation and capillary forces

In this section, we start from the governing equations in each subdomain: the metal Ω_M, the chill Ω_C and the surrounding gas Ω_A. Then, we derive the monolithic formulation of the conservation equations that allows prediction of fluid flow coupled with heat transfer including solidification, chemical segregation, thermocapillary forces and shrinkage in an Eulerian framework using a single mesh. Note that in this chapter, we use the same notations defined in the previous chapter.

We showed in chapter 2 through analyses of the ISS experiment that we can assume rigid solid phase. Hence, the conservation equations are built on the assumption that displacement of the solid phase of the metal subdomain $\boldsymbol{u}^s_\mathrm{M}$ is zero. This means that the metal average velocity $\langle \boldsymbol{u} \rangle_\mathrm{M}$ is reduced to its liquid phase averaged velocity $\langle \boldsymbol{u}^l \rangle_\mathrm{M}$ and that heat and mass transfers are purely diffusive in the solid phase.

$$\langle \boldsymbol{u} \rangle_\mathrm{M} = \langle \boldsymbol{u}^l \rangle_\mathrm{M} + \cancel{\langle \boldsymbol{u}^s \rangle_\mathrm{M}} = g^l \boldsymbol{u}^l_\mathrm{M} + g^s \cancel{\boldsymbol{u}^s_\mathrm{M}} \tag{5.1}$$

where $\boldsymbol{u}^l_\mathrm{M}$ is the liquid intrinsic velocity vector.

Hereafter, we give only the final averaged conservation equations in each phase of the metallic subdomain and we refer the reader to the following references [6; 12; 96] for details about the passage from the microscopic to the macroscopic equations.

5.2.1 Mass conservation

In the metal subdomain

The averaged mass conservation equations in the metallic subdomain for the liquid and the solid phases are respectively:

$$\frac{\partial \left(g^l \rho^l_\mathrm{M}\right)}{\partial t} + \nabla \cdot \left(g^l \rho^l_\mathrm{M} \boldsymbol{u}^l_\mathrm{M}\right) = \mathrm{J}^{l/s} \quad \text{in the liquid phase} \tag{5.2}$$

$$\frac{\partial \left(g^s \rho^s_\mathrm{M}\right)}{\partial t} + \nabla \cdot \left(g^s \rho^s_\mathrm{M} \cancel{\boldsymbol{u}^s_\mathrm{M}}\right) = \mathrm{J}^{s/l} \quad \text{in the solid phase} \tag{5.3}$$

where $\mathrm{J}^{l/s}$ and $\mathrm{J}^{s/l}$ represent the mass fluxes at the liquid-solid interface such as:

$$\mathrm{J}^{l/s} = -\frac{1}{\mathrm{V_E}} \int_{\Gamma_{ls}} \rho^l_{\mathrm{M}} \left(\boldsymbol{u}^l_{\mathrm{M}} - \boldsymbol{u}_{\Gamma_{ls}} \right) \cdot \boldsymbol{n}^l d\mathrm{S} \tag{5.4}$$

$$\mathrm{J}^{s/l} = -\frac{1}{\mathrm{V_E}} \int_{\Gamma_{ls}} \rho^s_{\mathrm{M}} \left(\cancel{\boldsymbol{u}^s_{\mathrm{M}}} - \boldsymbol{u}_{\Gamma_{ls}} \right) \cdot \boldsymbol{n}^s d\mathrm{S} \tag{5.5}$$

We recall that $\boldsymbol{u}_{\Gamma_{ls}}$ is the velocity of the liquid-solid interface Γ_{ls}. $\boldsymbol{n}^l$ and $\boldsymbol{n}^s$ are the normal vectors to Γ_{ls} directed outwards to the liquid phase and the solid phase respectively.

Since there is no accumulation or loss of mass at the interface, the mass flux leaving the liquid phase is the same as the flux entering the solid phase through the interface Γ_{ls}. Hence,

$$\mathrm{J}^{l/s} + \mathrm{J}^{s/l} = 0 \tag{5.6}$$

By writing the total average density of the metal as $\langle\rho\rangle_{\mathrm{M}} = g^l \rho^l_{\mathrm{M}} + g^s \rho^s_{\mathrm{M}}$, the averaged mass conservation equation in the metal subdomain writes:

$$\frac{\partial \langle\rho\rangle_{\mathrm{M}}}{\partial t} + \boldsymbol{\nabla} \cdot \left(\rho^l_{\mathrm{M}} \langle \boldsymbol{u}^l \rangle_{\mathrm{M}} \right) = 0 \tag{5.7}$$

We consider that the intrinsic average density of liquid metal is constant $\rho^l_{\mathrm{M}} = \rho^l_{\mathrm{M},0}$. Hence, the gradient of the liquid density $\boldsymbol{\nabla} \rho^l_{\mathrm{M}} = 0$. Accordingly, the mass conservation equation in the metal yields the following relationship:

$$\boldsymbol{\nabla} \cdot \langle \boldsymbol{u}^l \rangle_{\mathrm{M}} = -\frac{1}{\rho^l_{\mathrm{M},0}} \frac{\partial \langle\rho\rangle_{\mathrm{M}}}{\partial t} = \dot{\theta}_{\mathrm{M}} \tag{5.8}$$

This latter relationship expresses the compressibility of the metal due to solidification shrinkage. This term will be present in the following conservation equations which govern the metal subdomain to account for shrinkage.

Note that in this work the compressiblity term $\dot{\theta}_{\mathrm{M}}$ is explicitly discretized in time such as:

$$\dot{\theta}_{\mathrm{M}} = -\frac{1}{\rho^l_{\mathrm{M},0}} \frac{\langle\rho\rangle_{\mathrm{M}} - \langle\rho\rangle^-_{\mathrm{M}}}{\Delta t} \tag{5.9}$$

where $\langle\rho\rangle^-_{\mathrm{M}}$ is the metal density evaluated at the previous time step.

In the surrounding gas subdomain

The density of the surrounding gas in the subdomain Ω_{A}, indexed by a capital A (for Argon), is considered uniform and constant $\langle\rho\rangle_{\mathrm{A}} = \rho_{\mathrm{A}} = \mathrm{C}^{st}$. Therefore, the mass conservation in the gas subdomain is expressed by the following equation:

$$\boldsymbol{\nabla} \cdot \langle \boldsymbol{u} \rangle_{\mathrm{A}} = 0 = \dot{\theta}_{\mathrm{A}} \tag{5.10}$$

In the chill subdomain

The density of the chill plate is considered constant. Thus, the mass conservation in Ω_{C} writes:

$$\boldsymbol{\nabla}\cdot\langle\boldsymbol{u}\rangle_{\mathrm{C}} = 0 = \dot{\theta}_{\mathrm{C}} \tag{5.11}$$

5.2.2 Momentum conservation

In the metal subdomain

The incompressible Navier-Stokes equations, as presented in chapter 3, are not applicable for a solidifying liquid metal. The reasons are: (i) the shrinkage of the solid phase which includes a non-zero-divergence velocity field in the liquid and (ii) the presence of the mushy zone where the liquid flow is impacted by the interaction with the solid dendrites. In this context, we should re-derive the momentum equation which describes the liquid metal flow. For this purpose, we start from the averaged momentum equation for the liquid phase:

$$\frac{\partial\left(g^l_{\mathrm{M}}\rho^l_{\mathrm{M}}\boldsymbol{u}^l_{\mathrm{M}}\right)}{\partial t} + \boldsymbol{\nabla}\cdot\left(g^l\rho^l_{\mathrm{M}}\boldsymbol{u}^l_{\mathrm{M}}\times\boldsymbol{u}^l_{\mathrm{M}}\right) - \boldsymbol{\nabla}\cdot\left(g^l\boldsymbol{\sigma}^l_{\mathrm{M}}\right) = g^l\rho^l_{\mathrm{M}}\boldsymbol{g} + \mathbf{M}^{l/s} \tag{5.12}$$

where $\langle\sigma^l\rangle_{\mathrm{M}} = g^l\sigma^l_{\mathrm{M}}$ is the liquid average stress tensor. For a Newtonian fluid, the stress tensor can be modelled as follows:

$$\langle\sigma^l\rangle_{\mathrm{M}} = 2\mu^l_{\mathrm{M}}\langle\dot{\epsilon}^l\rangle_{\mathrm{M}} + \frac{2}{3}\mu^l_{\mathrm{M}}\dot{\theta}_{\mathrm{M}}\mathbb{I} - \langle p^l\rangle_{\mathrm{M}}\mathbb{I} \tag{5.13}$$

where μ^l_{M} is the dynamic viscosity of the liquid metal and $\langle\dot{\epsilon}^l\rangle_{\mathrm{M}} = \frac{1}{2}\left(\boldsymbol{\nabla}\langle\boldsymbol{u}^l\rangle_{\mathrm{M}} +^{\mathrm{T}}\boldsymbol{\nabla}\langle\boldsymbol{u}^l\rangle_{\mathrm{M}}\right)$ is the strain rate tensor.

The interfacial momentum transfer $\mathbf{M}^{l/s}$ due to phase change at the liquid solid interface can be split into a spherical part $\mathbf{M}^{l/s}_{\mathbb{S}}$ and a deviatoric part $\mathbf{M}^l_d$. The spherical part $\mathbf{M}^{l/s}_{\mathbb{S}} = \bar{p}^l\boldsymbol{\nabla}g^l$ can be interpreted as a buoyant force due to the average interfacial pressure $\overline{p}^l$. This latter can be considered to be equal to the liquid pressure p^l_{M} ($\overline{p}^l \approx p^l_{\mathrm{M}}$). The deviatoric part expresses the dissipative force in the liquid due the contact with the solid crystals. It can be modelled by analogy with Darcy flow in a porous medium such as:

$$\mathbf{M}^{l/s}_d = -\left(g^l\right)^2\mu^l_{\mathrm{M}}\mathbb{K}^{-1}\left(\boldsymbol{u}^l_{\mathrm{M}} - \cancel{\boldsymbol{u}^s_{\mathrm{M}}}\right) \tag{5.14}$$

where $\mathbb{K}$ is the permeability of the mushy zone. We consider in the present work that the permeability is isotropic and we use the model of Carman-Kozeny based on the secondary dendrite arm spacing λ_2 such as:

$$\mathbb{K} = \frac{\lambda_2^2 g^{l3}}{180\left(1-g^l\right)^2} \tag{5.15}$$

Following these considerations, the average momentum equation in the liquid phase becomes:

$$\frac{\partial\left(\rho^l_{\mathrm{M}}\langle\boldsymbol{u}^l\rangle_{\mathrm{M}}\right)}{\partial t}+\nabla\cdot\left(\frac{\rho^l_{\mathrm{M}}}{g^l}\langle\boldsymbol{u}^l\rangle_{\mathrm{M}}\times\langle\boldsymbol{u}^l\rangle_{\mathrm{M}}\right)-\nabla\cdot\left(2\mu^l_{\mathrm{M}}\langle\dot{\boldsymbol{\epsilon}}^l\rangle_{\mathrm{M}}\right)+g^l\nabla p^l_{\mathrm{M}}$$
$$+\frac{2}{3}\mu^l_{\mathrm{M}}\nabla\dot{\theta}_{\mathrm{M}}+g^l\frac{\mu^l_{\mathrm{M}}}{\mathbb{K}}\langle\boldsymbol{u}^l\rangle_{\mathrm{M}}=g^l\rho^l_{\mathrm{M}}\boldsymbol{g}\quad(5.16)$$

We rewrite the first and the second LHS terms considering that the liquid density is constant $\rho^l_{\mathrm{M}}=\rho^l_{\mathrm{M},0}$:

$$\frac{\partial\left(\rho^l_{\mathrm{M}}\langle\boldsymbol{u}^l\rangle_{\mathrm{M}}\right)}{\partial t}+\nabla\cdot\left(\frac{\rho^l_{\mathrm{M}}}{g^l}\langle\boldsymbol{u}^l\rangle_{\mathrm{M}}\times\langle\boldsymbol{u}^l\rangle_{\mathrm{M}}\right)=\rho^l_{\mathrm{M},0}\frac{\partial\langle\boldsymbol{u}^l\rangle_{\mathrm{M}}}{\partial t}+\frac{\rho^l_{\mathrm{M},0}}{g^l}\nabla\langle\boldsymbol{u}^l\rangle_{\mathrm{M}}\cdot\langle\boldsymbol{u}^l\rangle_{\mathrm{M}}+\rho^l_{\mathrm{M},0}\langle\boldsymbol{u}^l\rangle_{\mathrm{M}}\nabla\cdot\boldsymbol{u}^l_{\mathrm{M}}\quad(5.17)$$

We assume that the intrinsic velocity vector of the liquid phase is free-divergence $\nabla\cdot\boldsymbol{u}^l_{\mathrm{M}}=0$. Hence,

$$\nabla\cdot\langle\boldsymbol{u}^l\rangle_{\mathrm{M}}=g^l\cancel{\nabla\cdot\boldsymbol{u}^l_{\mathrm{M}}}+\boldsymbol{u}^l_{\mathrm{M}}\cdot\nabla g^l\quad(5.18)$$

This assumption means that the compressibility condition of the metal (equation (5.8)) derives from the gradient of the liquid volume fraction. This is consistent with the fact that the shrinkage is due to solidification in the mushy zone, and not to the compressibility of the liquid.

Hence, the final average momentum equation in the liquid phase writes:

$$\rho^l_{\mathrm{M},0}\left(\frac{\partial\langle\boldsymbol{u}^l\rangle_{\mathrm{M}}}{\partial t}+\frac{1}{g^l}\nabla\langle\boldsymbol{u}^l\rangle_{\mathrm{M}}\cdot\langle\boldsymbol{u}^l\rangle_{\mathrm{M}}\right)-\nabla\cdot\left(2\mu^l_{\mathrm{M}}\langle\dot{\boldsymbol{\epsilon}}^l\rangle_{\mathrm{M}}\right)+g^l\nabla p^l_{\mathrm{M}}$$
$$+\frac{2}{3}\mu^l_{\mathrm{M}}\nabla\dot{\theta}_{\mathrm{M}}+g^l\frac{\mu^l_{\mathrm{M}}}{\mathbb{K}}\langle\boldsymbol{u}^l\rangle_{\mathrm{M}}=g^l\rho^l_{\mathrm{M},0}\boldsymbol{g}\quad(5.19)$$

One can notice that when $g^l=0$ (fully-solid region), the permeability coefficient $\mathbb{K}$ given by equation (5.15) is zero and $g^l\frac{\mu^l_{\mathrm{M}}}{\mathbb{K}}\to\infty$. This means that Darcy term introduces infinite dissipation forcing the flow velocity to be zero. Therefore, the solution of the equation (5.19) is also valid for the fully-solid region. Consequently, we extend the average momentum conservation equation (5.19) to the whole metallic subdomain by replacing the unknowns $\left(\langle\boldsymbol{u}^l\rangle_{\mathrm{M}}\ ,\ p^l_{\mathrm{M}}\right)$ by $\left(\langle\boldsymbol{u}\rangle_{\mathrm{M}}\ ,\ p_{\mathrm{M}}\right)$ such as:

$$\rho^l_{\mathrm{M},0}\left(\frac{\partial\langle\boldsymbol{u}\rangle_{\mathrm{M}}}{\partial t}+\frac{1}{g^l}\nabla\langle\boldsymbol{u}\rangle_{\mathrm{M}}\cdot\langle\boldsymbol{u}\rangle_{\mathrm{M}}\right)-\nabla\cdot\left(2\mu^l_{\mathrm{M}}\langle\dot{\boldsymbol{\epsilon}}\rangle_{\mathrm{M}}\right)+g^l\nabla p_{\mathrm{M}}$$
$$+\frac{2}{3}\mu^l_{\mathrm{M}}\nabla\dot{\theta}_{\mathrm{M}}+g^l\frac{\mu^l_{\mathrm{M}}}{\mathbb{K}}\langle\boldsymbol{u}\rangle_{\mathrm{M}}=g^l\rho^l_{\mathrm{M},0}\boldsymbol{g}\quad(5.20)$$

In the surrounding gas subdomain

Considering that the flow of the surrounding gas is incompressible, the averaged momentum equation is:

$$\rho_\mathrm{A}\left(\frac{\partial \langle \boldsymbol{u}\rangle_\mathrm{A}}{\partial t} + \boldsymbol{\nabla}\langle \boldsymbol{u}\rangle_\mathrm{A}\cdot\langle \boldsymbol{u}\rangle_\mathrm{A}\right) - \boldsymbol{\nabla}\cdot\left(2\mu_\mathrm{A}\langle\dot{\boldsymbol{\epsilon}}\rangle_\mathrm{A}\right) + \boldsymbol{\nabla} p_\mathrm{A} = \rho_\mathrm{A}\boldsymbol{g} \tag{5.21}$$

In the chill subdomain

The chill plate is considered rigid and at rest. Therefore, $\langle \boldsymbol{u}\rangle_\mathrm{C} = \boldsymbol{0}$. This condition is directly imposed in the solution of Navier-Stokes solver via a Dirichlet condition.

Monolithic weak formulation

To obtain the monolithic formulation that we need to solve with finite element method, we multiply each of the equations (5.20) and (5.21) by a test function and we integer them over the corresponding subdomain. Then we sum the integrated equations, including the appropriate boundary condition at the boundaries separating the subdomains.

So, let us consider a test function $\mathscr{U}$. The weak formulation for the momentum equation in the metal subdomain is:

$$\begin{aligned}&\left(\rho^l_{\mathrm{M},0}\frac{\partial\langle \boldsymbol{u}\rangle_\mathrm{M}}{\partial t} + \frac{\rho^l_{\mathrm{M},0}}{g^l}\boldsymbol{\nabla}\langle \boldsymbol{u}\rangle_\mathrm{M}\cdot\langle \boldsymbol{u}\rangle_\mathrm{M}, \mathscr{U}\right)_{\Omega_\mathrm{M}} + \left(2\mu^l_\mathrm{M}\langle\dot{\boldsymbol{\epsilon}}\rangle_\mathrm{M} : \dot{\boldsymbol{\epsilon}}(\mathscr{U})\right)_{\Omega_\mathrm{M}} - \left(g^l p_\mathrm{M}, \boldsymbol{\nabla}\cdot\mathscr{U}\right)_{\Omega_\mathrm{M}}\\ &\quad - \left(\frac{2}{3}\mu^l_\mathrm{M}\dot{\theta}_\mathrm{M}, \boldsymbol{\nabla}\cdot\mathscr{U}\right)_{\Omega_\mathrm{M}} + \left(g^l\frac{\mu^l_\mathrm{M}}{\mathbb{K}}\langle \boldsymbol{u}\rangle_\mathrm{M}, \mathscr{U}\right)_{\Omega_\mathrm{M}} = \left(g^l\rho^l_{\mathrm{M},0}\boldsymbol{g}, \mathscr{U}\right)_{\Omega_\mathrm{M}} + \left(\langle\boldsymbol{\sigma}\rangle_\mathrm{M}\cdot\boldsymbol{n}_\mathrm{M}, \mathscr{U}\right)_{\partial\Omega_\mathrm{M}}\end{aligned} \tag{5.22}$$

where $\boldsymbol{n}_\mathrm{M}$ is the outward normal vector to the metal boundary $\partial\Omega_\mathrm{M}$.

For the gas subdomain, the weak formulation for the momentum equation writes:

$$\begin{aligned}&\left(\rho_\mathrm{A}\frac{\partial\langle \boldsymbol{u}\rangle_\mathrm{A}}{\partial t} + \rho_\mathrm{A}\boldsymbol{\nabla}\langle \boldsymbol{u}\rangle_\mathrm{A}\cdot\langle \boldsymbol{u}\rangle_\mathrm{A}, \mathscr{U}\right)_{\Omega_\mathrm{A}} + \left(2\mu_\mathrm{A}\langle\dot{\boldsymbol{\epsilon}}\rangle_\mathrm{A} : \dot{\boldsymbol{\epsilon}}(\mathscr{U})\right)_{\Omega_\mathrm{A}} - \left(p_\mathrm{A}, \boldsymbol{\nabla}\cdot\mathscr{U}\right)_{\Omega_\mathrm{A}}\\ &\qquad = \left(\rho_\mathrm{A}\boldsymbol{g}, \mathscr{U}\right)_{\Omega_\mathrm{A}} + \left(\langle\boldsymbol{\sigma}\rangle_\mathrm{A}\cdot\boldsymbol{n}_\mathrm{A}, \mathscr{U}\right)_{\partial\Omega_\mathrm{A}}\end{aligned} \tag{5.23}$$

where $\boldsymbol{n}_\mathrm{A}$ is the outward normal vector to the gas boundary $\partial\Omega_\mathrm{A}$.

In order to reach a unified equation that governs the fluid subdomains Ω_M, Ω_A, we define the global unknowns: $\boldsymbol{u}$ the velocity vector and p the pressure field defined on the entire computational domain Ω as follows:

$$\boldsymbol{u} = \begin{cases}\langle \boldsymbol{u}\rangle_\mathrm{M} & \text{if } \boldsymbol{x}\in\Omega_\mathrm{M}\\ \langle \boldsymbol{u}\rangle_\mathrm{A} & \text{if } \boldsymbol{x}\in\Omega_\mathrm{A}\\ \langle \boldsymbol{u}\rangle_\mathrm{C} = \boldsymbol{0} & \text{if } \boldsymbol{x}\in\Omega_\mathrm{C}\end{cases} \tag{5.24}$$

$$p = \begin{cases} p_{\mathrm{M}} & \text{if } \boldsymbol{x} \in \Omega_{\mathrm{M}} \\ p_{\mathrm{A}} & \text{if } \boldsymbol{x} \in \Omega_{\mathrm{A}} \\ p_{\mathrm{C}} = 0 & \text{if } \boldsymbol{x} \in \Omega_{\mathrm{C}} \end{cases} \tag{5.25}$$

Considering the smooth Heaviside functions $\mathrm{H_M}$, $\mathrm{H_A}$ and $\mathrm{H_C}$ of Ω_{M}, Ω_{A} and Ω_{C} respectively, we introduce the following mixed properties:

- g^{F} the fluid volume fraction:
$$g^{\mathrm{F}} = g^{l}\mathrm{H_M} + \mathrm{H_A} \tag{5.26}$$
- ρ^{F} the fluid density:
$$\rho^{\mathrm{F}} = \rho^{l}_{\mathrm{M},0}\mathrm{H_M} + \rho_{\mathrm{A}}\mathrm{H_A} \tag{5.27}$$
- μ^{F} the fluid dynamic viscosity:
$$\mu^{\mathrm{F}} = \mu^{l}_{\mathrm{M}}\mathrm{H_M} + \mu_{\mathrm{A}}\mathrm{H_A} \tag{5.28}$$
- $\dot{\theta}^{\mathrm{F}}$ the fluid compressiblity condition:
$$\dot{\theta}^{\mathrm{F}} = \dot{\theta}_{\mathrm{M}}\mathrm{H_M} + \dot{\theta}_{\mathrm{A}}\mathrm{H_A} = \dot{\theta}_{\mathrm{M}}\mathrm{H_M} \tag{5.29}$$

Moreover, we extend the definition of the permeability, previously defined for the metallic subdomain, to the rest of the computational domain to use a monolithic Darcy term. The idea is to keep the dissipative Darcy term present in the whole domain but to activate it where it is needed as illustrated in Figure 5.1. The extended permeability $\mathbb{K}^{\mathrm{F}}$ depends on the fluid volume fraction as follows:

$$\mathbb{K}^{\mathrm{F}} = \frac{\lambda_2^2 {g^{\mathrm{F}}}^3}{180\left(1 - g^{\mathrm{F}}\right)^2} \tag{5.30}$$

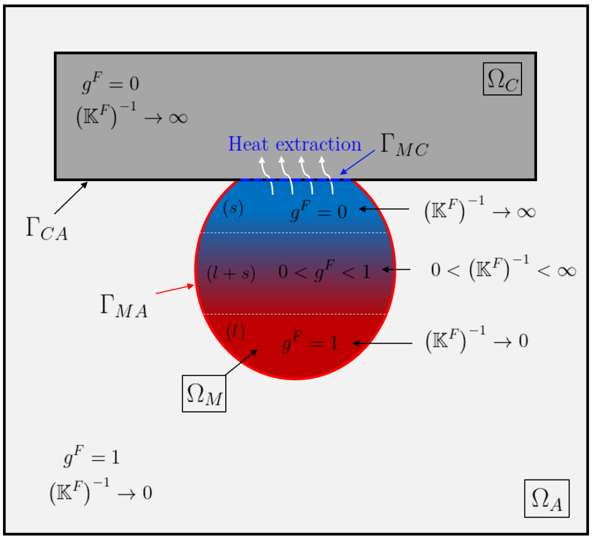

Figure 5.1: Schematic of a multidomain system involving a solidifying metallic subdomain

By summing equations (5.22) and (5.23), we obtain:

$$\begin{aligned}\left(\rho^{\mathrm{F}}\frac{\partial \boldsymbol{u}}{\partial t}+\frac{\rho^{\mathrm{F}}}{g^{\mathrm{F}}}\nabla\boldsymbol{u}\cdot\boldsymbol{u},\mathscr{U}\right)_{\Omega}+\left(2\mu^{\mathrm{F}}\dot{\boldsymbol{\varepsilon}}(\boldsymbol{u}):\dot{\boldsymbol{\varepsilon}}(\mathscr{U})\right)_{\Omega}-\left(p,\nabla\cdot\mathscr{U}\right)_{\Omega}+\left(g^{\mathrm{F}}\frac{\mu^{\mathrm{F}}}{\mathbb{K}^{\mathrm{F}}}\boldsymbol{u},\mathscr{U}\right)_{\Omega}\\ =\left(\frac{2}{3}\mu^{\mathrm{F}}\dot{\theta}^{\mathrm{F}},\nabla\cdot\mathscr{U}\right)_{\Omega}+\left(g^{\mathrm{F}}\rho^{\mathrm{F}}\boldsymbol{g},\mathscr{U}\right)_{\Omega}+\left(\langle\boldsymbol{\sigma}\rangle_{\mathrm{M}}\cdot\boldsymbol{n}_{\mathrm{M}},\mathscr{U}\right)_{\partial\Omega_{\mathrm{M}}}+\left(\langle\boldsymbol{\sigma}\rangle_{\mathrm{A}}\cdot\boldsymbol{n}_{\mathrm{A}},\mathscr{U}\right)_{\partial\Omega_{\mathrm{A}}}\end{aligned}\tag{5.31}$$

The last two surface integrals of the RHS of the equation (5.31) can be split into interfacial terms such as:

$$\begin{aligned}\left(\langle\boldsymbol{\sigma}\rangle_{\mathrm{M}}\cdot\boldsymbol{n}_{\mathrm{M}},\mathscr{U}\right)_{\partial\Omega_{\mathrm{M}}}+\left(\langle\boldsymbol{\sigma}\rangle_{\mathrm{A}}\cdot\boldsymbol{n}_{\mathrm{A}},\mathscr{U}\right)_{\partial\Omega_{\mathrm{A}}}=\left(\left(\langle\boldsymbol{\sigma}^{l}\rangle_{\mathrm{M}}-\langle\boldsymbol{\sigma}\rangle_{\mathrm{A}}\right)\cdot\boldsymbol{n}_{\mathrm{M}},\mathscr{U}\right)_{\Gamma^{l}_{\mathrm{MA}}}+\left(\left(\cancel{\langle\boldsymbol{\sigma}^{s}\rangle_{\mathrm{M}}}-\langle\boldsymbol{\sigma}\rangle_{\mathrm{A}}\right)\cdot\boldsymbol{n}_{\mathrm{M}},\mathscr{U}\right)_{\Gamma^{s}_{\mathrm{MA}}}\\+\left(\langle\boldsymbol{\sigma}^{l}\rangle_{\mathrm{M}}\cdot\boldsymbol{n}_{\mathrm{M}},\mathscr{U}\right)_{\Gamma^{l}_{\mathrm{MC}}}+\cancel{\left(\langle\boldsymbol{\sigma}^{s}\rangle_{\mathrm{M}}\cdot\boldsymbol{n}_{\mathrm{M}},\mathscr{U}\right)_{\Gamma^{s}_{\mathrm{MC}}}}+\left(\langle\boldsymbol{\sigma}\rangle_{\mathrm{A}}\cdot\boldsymbol{n}_{\mathrm{A}},\mathscr{U}\right)_{\Gamma_{\mathrm{AC}}}\end{aligned}\tag{5.32}$$

We neglect the viscous friction force at the chill/gas Γ_{AC} and the solid/gas Γ^{s}_{MC} interfaces. Thus,

$$\left(\langle\boldsymbol{\sigma}\rangle_{\mathrm{A}}\cdot\boldsymbol{n}_{\mathrm{A}},\mathscr{U}\right)_{\Gamma_{\mathrm{AC}}}=\mathbf{0}$$

$$\left(-\langle\boldsymbol{\sigma}\rangle_{\mathrm{A}}\cdot\boldsymbol{n}_{\mathrm{M}},\mathscr{U}\right)_{\Gamma^{s}_{\mathrm{MA}}}=\mathbf{0}$$

The interfacial term $(\langle\boldsymbol{\sigma}^{l}\rangle_{\mathrm{M}}\cdot\boldsymbol{n}_{\mathrm{M}},\mathscr{U})_{\Gamma^{l}_{\mathrm{MC}}}$ at Γ^{l}_{MC} the liquid/chill interface expresses the wetting force between the liquid metal and the chill. Accounting for such capillary force was proposed by [98] in level-set based FE method. In the present work, we consider that the simulations start just after a thin layer of solid metal forms on contact with the chill, thus freezing the interface $\Gamma_{\mathrm{MC}}=\Gamma^{s}_{\mathrm{MC}}$. Consequently, the liquid/chill interface Γ^{l}_{MC} is not present in the simulations. Thus, we omit the interfacial term $(\langle\boldsymbol{\sigma}^{l}\rangle_{\mathrm{M}}\cdot\boldsymbol{n}_{\mathrm{M}},\mathscr{U})_{\Gamma^{l}_{\mathrm{MC}}}$.

Following these considerations, the dynamic boundary condition at the liquid-gas interface Γ^{l}_{MA} writes:

$$\left(\left(\langle\boldsymbol{\sigma}^{l}\rangle_{\mathrm{M}}-\langle\boldsymbol{\sigma}\rangle_{\mathrm{A}}\right)\cdot\boldsymbol{n}_{\mathrm{M}},\mathscr{U}\right)_{\Gamma^{l}_{\mathrm{MA}}}=\left(\boldsymbol{f}_{\mathrm{ST}}+\boldsymbol{f}_{Mar},\mathscr{U}\right)_{\Gamma^{l}_{\mathrm{MA}}}\tag{5.33}$$

where $\boldsymbol{f}_{\mathrm{ST}}$ is the surface tension force vector and $\boldsymbol{f}_{Mar}$ is the Marangoni force vector.

$$\boldsymbol{f}_{\mathrm{ST}}=-\gamma_{lg}\,\kappa_{lg}\,\boldsymbol{n}_{lg}\tag{5.34}$$

$$\boldsymbol{f}_{Mar}=\nabla\gamma_{lg}\cdot\left(\mathbb{I}-\boldsymbol{n}_{lg}\otimes\boldsymbol{n}_{lg}\right)\tag{5.35}$$

γ_{lg} is the surface tension coefficient of the liquid metal. κ_{lg} is the curvature of the liquid/gas interface and $\boldsymbol{n}_{lg}$ is its unit normal vector oriented inwards the metal domain.

As we previously showed in chapter 3, we can transform the surface integral of capillary forces into volume integral using the CSF method via the Dirac function δ_{lg} located at the liquid metal-gas interface Γ^{l}_{MA}.

The final monolithic formulation of Navier-Stokes equations including the mass and the momentum conservation equations becomes therefore as follows:

$$\begin{cases} \left(\rho^{\mathrm{F}}\dfrac{\partial \boldsymbol{u}}{\partial t}+\dfrac{\rho^{\mathrm{F}}}{g^{\mathrm{F}}}\nabla\boldsymbol{u}\cdot\boldsymbol{u},\mathscr{U}\right)_{\Omega}+\left(2\mu^{\mathrm{F}}\dot{\boldsymbol{\epsilon}}(\boldsymbol{u}):\dot{\boldsymbol{\epsilon}}(\mathscr{U})\right)_{\Omega}-\left(g^{\mathrm{F}}p,\nabla\cdot\mathscr{U}\right)_{\Omega}+\left(g^{\mathrm{F}}\dfrac{\mu^{\mathrm{F}}}{\mathbb{K}^{\mathrm{F}}}\boldsymbol{u},\mathscr{U}\right)_{\Omega} \\ =\left(\dfrac{2}{3}\mu^{\mathrm{F}}\dot{\theta}^{\mathrm{F}},\nabla\cdot\mathscr{U}\right)_{\Omega}+\left(g^{\mathrm{F}}\rho^{\mathrm{F}}\boldsymbol{g},\mathscr{U}\right)_{\Omega}+\left(\delta_{lg}\left(\boldsymbol{f}_{\mathrm{ST}}+\boldsymbol{f}_{\mathrm{M}ar}\right),\mathscr{U}\right)_{\Omega} \\ \\ (\nabla\cdot\boldsymbol{u},\mathscr{P})_{\Omega}=\left(\dot{\theta}^{\mathrm{F}},\mathscr{P}\right)_{\Omega} \end{cases} \tag{5.36}$$

5.2.3 Energy conservation equation

In the metal subdomain

The averaged energy conservation equations in each phase of the metallic subdomain write:

$$\frac{\partial\left(g^{l}\rho_{\mathrm{M}}^{l}h_{\mathrm{M}}^{l}\right)}{\partial t}+\nabla\cdot\left(g^{l}\rho_{\mathrm{M}}^{l}h_{\mathrm{M}}^{l}\boldsymbol{u}_{\mathrm{M}}^{l}\right)-\nabla\cdot\left(g^{l}k_{\mathrm{M}}^{l}\nabla\mathrm{T}\right)=\mathrm{Q}^{l/s} \tag{5.37}$$

$$\frac{\partial\left(g^{s}\rho_{\mathrm{M}}^{s}h_{\mathrm{M}}^{s}\right)}{\partial t}+\nabla\cdot\left(g^{s}\rho_{\mathrm{M}}^{s}h_{\mathrm{M}}^{s}\cancel{\boldsymbol{u}_{\mathrm{M}}^{s}}\right)-\nabla\cdot\left(g^{s}k_{\mathrm{M}}^{s}\nabla\mathrm{T}\right)=\mathrm{Q}^{s/l} \tag{5.38}$$

We recall that h_{M}^{φ} and k_{M}^{φ} stand for the intrinsic averaged mass enthalpy and the intrinsic averaged thermal conductivity respectively, with $\varphi \in \{l,s\}$. $\mathrm{Q}^{l/s}$ and $\mathrm{Q}^{s/l}$ are the interfacial heat exchanges at the liquid/solid interface which write as follows:

$$\mathrm{Q}^{l/s}=-\frac{1}{\mathrm{V_E}}\int_{\Gamma_{ls}}\rho^{l}h^{l}\left(\boldsymbol{u}^{l}-\boldsymbol{u}_{\Gamma_{ls}}\right)\cdot\boldsymbol{n}^{l}\,d\mathrm{S}+\frac{1}{\mathrm{V_E}}\int_{\Gamma_{ls}}\boldsymbol{q}^{l}\cdot\boldsymbol{n}^{l}\,d\mathrm{S} \tag{5.39}$$

$$\mathrm{Q}^{s/l}=-\frac{1}{\mathrm{V_E}}\int_{\Gamma_{ls}}\rho^{s}h^{s}\left(\cancel{\boldsymbol{u}^{s}}-\boldsymbol{u}_{\Gamma_{ls}}\right)\cdot\boldsymbol{n}^{s}\,d\mathrm{S}+\frac{1}{\mathrm{V_E}}\int_{\Gamma_{ls}}\boldsymbol{q}^{s}\cdot\boldsymbol{n}^{s}\,d\mathrm{S} \tag{5.40}$$

where $\boldsymbol{q}^{\varphi}=-k^{\varphi}\nabla\mathrm{T}$ is the local heat flux density of the phase $\varphi\in\{l,s\}$.

We assume a perfect contact at the liquid/solid interface Γ_{ls}. Consequently, the heat flux entering the liquid phase at Γ_{ls} is equal to the heat flux leaving the solid phase at the interface. Therefore:

$$\mathrm{Q}^{l/s}+\mathrm{Q}^{s/l}=0 \tag{5.41}$$

Hence the averaged energy conservation equation over the metal subdomain is:

$$\frac{\partial\langle\rho h\rangle_{\mathrm{M}}}{\partial t}+\nabla\cdot\left(g^{l}\rho_{\mathrm{M}}^{l}h_{\mathrm{M}}^{l}\boldsymbol{u}_{\mathrm{M}}^{l}\right)-\nabla\cdot\left(\langle k\rangle_{\mathrm{M}}\nabla\mathrm{T}\right)=0 \tag{5.42}$$

where $\langle k\rangle_{\mathrm{M}}=g^{l}k_{\mathrm{M}}^{l}+g^{s}k_{\mathrm{M}}^{s}$ is the averaged thermal conductivity of the metal.

We can develop the convection term as follows:

$$\nabla\cdot\left(g^{l}\rho_{\mathrm{M}}^{l}h_{\mathrm{M}}^{l}\boldsymbol{u}_{\mathrm{M}}^{l}\right)=\langle\boldsymbol{u}^{l}\rangle_{\mathrm{M}}\cdot\nabla\left(\rho_{\mathrm{M}}^{l}h_{\mathrm{M}}^{l}\right)+\rho_{\mathrm{M}}^{l}h_{\mathrm{M}}^{l}\nabla\cdot\langle\boldsymbol{u}^{l}\rangle_{\mathrm{M}} \tag{5.43}$$

The volume enthalpy of the liquid phase, $\rho^l_{\mathrm{M}} h^l_{\mathrm{M}}$, is not the main unknown of the energy conservation equation. For simplification, we assume that the enthalpy of the liquid is a linear function of temperature. Thus,

$$\rho^l_{\mathrm{M}} h^l_{\mathrm{M}} = \mathrm{C}^l_{p,\mathrm{M}} \mathrm{T} \tag{5.44}$$

where $\mathrm{C}^l_{p,\mathrm{M}}$ is the heat capacity per unit volume in the liquid metal.

Hence, the averaged energy equation over the metal subdomain writes:

$$\frac{\partial \langle \rho h \rangle_{\mathrm{M}}}{\partial t} + \mathrm{C}^l_{p,\mathrm{M}} \langle \boldsymbol{u}^l \rangle_{\mathrm{M}} \cdot \nabla \mathrm{T} - \nabla \cdot (\langle k \rangle_{\mathrm{M}} \nabla \mathrm{T}) = -\rho^l_{\mathrm{M}} h^l_{\mathrm{M}} \dot{\theta}_{\mathrm{M}} \tag{5.45}$$

The term in the RHS of equation (5.45) expresses the heat supplied by the liquid phase in the mushy zone because of solidification shrinkage. It is evaluated at the previous time step.

In the chill subdomain

The heat transfer in the chill plate is governed by heat conduction. The energy conservation equation in the chill subdomain writes:

$$\frac{\partial \langle \rho h \rangle_{\mathrm{C}}}{\partial t} - \nabla \cdot (\langle k \rangle_{\mathrm{C}} \nabla \mathrm{T}) = 0 \tag{5.46}$$

Note that the evolution of the enthalpy in the chill plate made of ceramic is linear with temperature so we can write $\frac{\partial \langle \rho h \rangle_{\mathrm{C}}}{\partial t} = \mathrm{C}_{p,\mathrm{C}} \frac{\partial \mathrm{T}}{\partial t}$. However, we retain the transient term with the enthalpy to conform with the equation set for the metal subdomain. The same remark is valid for the following paragraph dedicated to the gas subdomain.

In the surrounding gas subdomain

The heat transfer in the chill plate is operated by both convection and conduction. The energy conservation equation in the gas subdomain writes:

$$\frac{\partial \langle \rho h \rangle_{\mathrm{A}}}{\partial t} + \nabla \cdot \left(\rho_{\mathrm{A}} h_{\mathrm{A}} \boldsymbol{u}_{\mathrm{A}}\right) - \nabla \cdot (\langle k \rangle_{\mathrm{A}} \nabla \mathrm{T}) = 0 \tag{5.47}$$

Considering that the flow of the gas is incompressible $\nabla \cdot \boldsymbol{u}_{\mathrm{A}} = 0$, the energy conservation equation in the gas subdomain becomes:

$$\frac{\partial \langle \rho h \rangle_{\mathrm{A}}}{\partial t} + \mathrm{C}_{p,\mathrm{A}} \boldsymbol{u}_{\mathrm{A}} \cdot \nabla \mathrm{T} - \nabla \cdot (\langle k \rangle_{\mathrm{A}} \nabla \mathrm{T}) = 0 \tag{5.48}$$

Monolithic weak formulation

In the same way as the momentum equation, we write the weak formulation for each subdomain using a test function $\mathcal{T}$ for the temperature field.

For the metal subdomain, the weak formulation of the energy conservation equation writes:

$$\left(\frac{\partial \langle \rho h\rangle_{\mathrm{M}}}{\partial t},\mathscr{T}\right)_{\Omega_{\mathrm{M}}}+\left(\mathrm{C}^{l}_{p,\mathrm{M}}\,\langle \boldsymbol{u}^{l}\rangle_{\mathrm{M}}\cdot\nabla \mathrm{T},\mathscr{T}\right)_{\Omega_{\mathrm{M}}}+(\langle k\rangle_{\mathrm{M}}\nabla \mathrm{T},\nabla\mathscr{T})_{\Omega_{\mathrm{M}}}$$
$$=(\langle k\rangle_{\mathrm{M}}\nabla \mathrm{T}\cdot \boldsymbol{n}_{\mathrm{M}},\mathscr{T})_{\partial\Omega_{\mathrm{M}}}-\left(\rho^{l}_{\mathrm{M}}h^{l}_{\mathrm{M}}\dot{\theta}_{\mathrm{M}},\mathscr{T}\right)_{\Omega_{\mathrm{M}}} \quad (5.49)$$

For the gas subdomain:

$$\left(\frac{\partial \langle \rho h\rangle_{\mathrm{A}}}{\partial t},\mathscr{T}\right)_{\Omega_{\mathrm{A}}}+\left(\mathrm{C}_{p,\mathrm{A}}\,\langle \boldsymbol{u}\rangle_{\mathrm{A}}\cdot\nabla \mathrm{T},\mathscr{T}\right)_{\Omega_{\mathrm{A}}}+(\langle k\rangle_{\mathrm{A}}\nabla \mathrm{T},\nabla\mathscr{T})_{\Omega_{\mathrm{A}}}=(\langle k\rangle_{\mathrm{A}}\nabla \mathrm{T}\cdot \boldsymbol{n}_{\mathrm{A}},\mathscr{T})_{\partial\Omega_{\mathrm{A}}} \quad (5.50)$$

For the chill plate subdomain:

$$\left(\frac{\partial \langle \rho h\rangle_{\mathrm{C}}}{\partial t},\mathscr{T}\right)_{\Omega_{\mathrm{C}}}+(\langle k\rangle_{\mathrm{C}}\nabla \mathrm{T},\nabla\mathscr{T})_{\Omega_{\mathrm{C}}}=(\langle k\rangle_{\mathrm{C}}\nabla \mathrm{T}\cdot \boldsymbol{n}_{\mathrm{C}},\mathscr{T})_{\partial\Omega_{\mathrm{C}}} \quad (5.51)$$

Following the work in Chapter 4, we sum up the weak formulations of all the subdomains and drop all the interfacial terms of heat exchanges between the subdomains, considering that any contact thermal resistance can be taken into account through the mixing law of the thermal conductivity and the heat capacity.

Consequently, the monolithic weak formulation of energy conservation for the whole computational domain Ω is :

$$\left(\frac{\partial\widehat{\langle\rho h\rangle}}{\partial t}\,,\,\mathscr{T}\right)_{\Omega}+\left(\mathrm{C}^{\mathrm{F}}_{p}\boldsymbol{u}\cdot\nabla \mathrm{T}\,,\,\mathscr{T}\right)_{\Omega}+\left(\widehat{\langle k\rangle}\nabla \mathrm{T}\,,\,\nabla\mathscr{T}\right)_{\Omega}=-\left(\rho^{l}_{\mathrm{M}}h^{l}_{\mathrm{M}}\dot{\theta}^{\mathrm{F}}\,,\,\mathscr{T}\right)_{\Omega} \quad (5.52)$$

where

$$\widehat{\langle\rho h\rangle}=\mathrm{H}_{\mathrm{M}}\,\langle\rho h\rangle_{\mathrm{M}}+\mathrm{H}_{\mathrm{A}}\,\langle\rho h\rangle_{\mathrm{A}}+\mathrm{H}_{\mathrm{C}}\,\langle\rho h\rangle_{\mathrm{C}} \quad (5.53)$$

$$\mathrm{C}^{\mathrm{F}}_{p}=\mathrm{H}_{\mathrm{M}}\mathrm{C}^{l}_{p,\mathrm{M}}+\mathrm{H}_{\mathrm{A}}\mathrm{C}_{p,\mathrm{A}} \quad (5.54)$$

$$\widehat{\langle k\rangle}=\left(\frac{\mathrm{H}_{\mathrm{M}}}{\langle k\rangle_{\mathrm{M}}}+\frac{\mathrm{H}_{\mathrm{C}}}{\langle k\rangle_{\mathrm{C}}}+\frac{\mathrm{H}_{\mathrm{A}}}{\langle k\rangle_{\mathrm{A}}}+\delta_{\mathrm{MC}}\mathrm{R}_{th}\right)^{-1} \quad (5.55)$$

where δ_{MC} is the Dirac function of the metal/chill interface Γ_{MC} and R_{th} is the value of the thermal contact resistance. Note that in this work, the thermal contact resistance only occurs at the metal/chill interface Γ_{MC}.

Any micro-cavities (gap) that may exist between the metal and the chill are probably filled with gas (or vacuum). Therefore, the heat capacity of the gap $\mathrm{C}_{p,\mathrm{G}}$ at the contact surface Γ_{MC} is negligible compared to the mean thermal capacity of the metal and the ceramic $\overline{\mathrm{C}_p}$. According to the model proposed in Chapter 4, only the mixing law of the thermal conductivity is concerned by the consideration of the thermal resistance when $\mathrm{C}_{p,\mathrm{G}} \ll \overline{\mathrm{C}_p}$. Γ_{MA} and Γ_{CA} interfaces involve a full contact with the gas, so the thermal contact is assumed to be perfect at these latter boundaries.

5.2.4 Chemical species conservation equation

In the metal subdomain

For a multi-component alloy, the thermophysical properties depend on the composition of the alloy. Hence, the distribution of the chemical species in the metal can affect the heat transfer, which is coupled with fluid flow. On the other hand, the fluid flow is affecting the distribution of the chemical species in the liquid phase. Therefore it is of significant importance to take into account the mass transfer of the chemical species. Let us index by i a solute of the alloy. The chemical composition in $\% wt$ will denoted w_i. For the sake of simplification, ${w_i}^l_{\mathrm{M}}$ will be denoted ${w_i}^l$.

The averaged species mass conservation equations in each phase are:

$$\frac{\partial\left(g^l\rho^l_{\mathrm{M}}{w_i}^l\right)}{\partial t}+\boldsymbol{\nabla}\cdot\left(g^l\rho^l_{\mathrm{M}}{w_i}^l\boldsymbol{u}^l_{\mathrm{M}}\right)+\boldsymbol{\nabla}\cdot\langle\boldsymbol{j}^l_i\rangle_{\mathrm{M}}={\Phi_i}^{l/s} \tag{5.56}$$

$$\frac{\partial\left(g^s\rho^s_{\mathrm{M}}{w_i}^s\right)}{\partial t}+\boldsymbol{\nabla}\cdot\left(g^s\rho^s_{\mathrm{M}}{w_i}^s\cancel{\boldsymbol{u}^s_{\mathrm{M}}}\right)+\boldsymbol{\nabla}\cdot\cancel{\langle\boldsymbol{j}^s_i\rangle_{\mathrm{M}}}={\Phi_i}^{s/l} \tag{5.57}$$

In the solid phase, we also neglect the diffusion transfer of solutes $\langle\boldsymbol{j}^s_i\rangle_{\mathrm{M}}$, considering that, at the macroscopic scale, the composition of the alloy is more influenced by convection and diffusion in the liquid phase.

As no accumulation of mass occurs at the interface, the mass of the solute i entering the liquid phase ${\Phi_i}^{l/s}$ is the same leaving the solid phase ${\Phi_i}^{s/l}$ at the liquid/solid boundary. Therefore,

$${\Phi_i}^{l/s}+{\Phi_i}^{s/l}=0 \tag{5.58}$$

.

After summing the phase averaged equations we obtain:

$$\frac{\partial\langle\rho w_i\rangle_{\mathrm{M}}}{\partial t}+\boldsymbol{\nabla}\cdot\left(\rho^l_{\mathrm{M}}{w_i}^l\langle\boldsymbol{u}^l\rangle_{\mathrm{M}}\right)+\boldsymbol{\nabla}\cdot\langle\boldsymbol{j}^l_i\rangle_{\mathrm{M}}=0 \tag{5.59}$$

$$\langle\rho\rangle_{\mathrm{M}}\frac{\partial\langle w_i\rangle_{\mathrm{M}}}{\partial t}+\langle w_i\rangle_{\mathrm{M}}\frac{\partial\langle\rho\rangle_{\mathrm{M}}}{\partial t}+\boldsymbol{\nabla}\cdot\left(\rho^l_{\mathrm{M}}{w_i}^l\langle\boldsymbol{u}^l\rangle_{\mathrm{M}}\right)+\boldsymbol{\nabla}\cdot\langle\boldsymbol{j}^l_i\rangle_{\mathrm{M}}=0 \tag{5.60}$$

$$\langle\rho\rangle_{\mathrm{M}}\frac{\partial\langle w_i\rangle_{\mathrm{M}}}{\partial t}+\langle w_i\rangle_{\mathrm{M}}\frac{\partial\langle\rho\rangle_{\mathrm{M}}}{\partial t}+\langle\boldsymbol{u}^l\rangle_{\mathrm{M}}\cdot\boldsymbol{\nabla}\left(\rho^l_{\mathrm{M}}{w_i}^l\right)+\rho^l_{\mathrm{M}}{w_i}^l\dot{\theta}_{\mathrm{M}}+\boldsymbol{\nabla}\cdot\langle\boldsymbol{j}^l_i\rangle_{\mathrm{M}}=0 \tag{5.61}$$

The average mass flux of the solute i in the liquid phase is given by Fick's law:

$$\langle\boldsymbol{j}^l_i\rangle_{\mathrm{M}}=-g^l\mathrm{D}^l_{\mathrm{M}}\nabla\left(\rho^l_{\mathrm{M}}{w_i}^l\right) \tag{5.62}$$

Hence

$$\langle\rho\rangle_{\mathrm{M}}\frac{\partial\langle w_i\rangle_{\mathrm{M}}}{\partial t}+\langle w_i\rangle_{\mathrm{M}}\frac{\partial\langle\rho\rangle_{\mathrm{M}}}{\partial t}+\langle\boldsymbol{u}^l\rangle_{\mathrm{M}}\cdot\boldsymbol{\nabla}\left(\rho^l_{\mathrm{M}}{w_i}^l\right)+\rho^l_{\mathrm{M}}{w_i}^l\dot{\theta}_{\mathrm{M}}-\boldsymbol{\nabla}\cdot\left[g^l\mathrm{D}^l_{\mathrm{M}}\nabla\left(\rho^l_{\mathrm{M}}{w_i}^l\right)\right]=0 \tag{5.63}$$

The mass conservation equation gives:

$$\dot{\theta}_{\mathrm{M}} = -\frac{1}{\rho^l_{\mathrm{M}}}\frac{\partial\langle\rho\rangle_{\mathrm{M}}}{\partial t} \tag{5.64}$$

As we assume that the liquid density $\rho^l_{\mathrm{M}} = \rho^l_{\mathrm{M},0}$ is constant, the chemical species conservation equation becomes:

$$\langle\rho\rangle_{\mathrm{M}}\frac{\partial\langle w_i\rangle_{\mathrm{M}}}{\partial t} + \rho^l_{\mathrm{M},0}\dot{\theta}_{\mathrm{M}}\left(w^l_i - \langle w_i\rangle_{\mathrm{M}}\right) + \rho^l_{\mathrm{M},0}\langle \boldsymbol{u}^l\rangle_{\mathrm{M}}\cdot\boldsymbol{\nabla} {w_i}^l - \boldsymbol{\nabla}\cdot\left(g^l\rho^l_{\mathrm{M},0}\mathrm{D}^l_{\mathrm{M}}\nabla {w_i}^l\right) = 0 \tag{5.65}$$

Now we have two unknown variables: the global averaged composition $\langle w_i\rangle_{\mathrm{M}}$ and the intrinsic averaged liquid composition ${w_i}^l$. We apply Voller-Prakash variable splitting approximation which consists of writing:

$${w_i}^l = \langle w_i\rangle_{\mathrm{M}} - w^*_i \tag{5.66}$$

where

$$w^*_i = \left(\langle w_i\rangle_{\mathrm{M}}\right)^- - \left({w_i}^l\right)^- \tag{5.67}$$

and $(.)^-$ means the value of the variable at the previous time step.

Therefore the species conservation equation writes:

$$\langle\rho\rangle_{\mathrm{M}}\frac{\partial\langle w_i\rangle_{\mathrm{M}}}{\partial t} + \rho^l_{\mathrm{M},0}\langle \boldsymbol{u}^l\rangle_{\mathrm{M}}\cdot\boldsymbol{\nabla}\langle w_i\rangle_{\mathrm{M}} + \boldsymbol{\nabla}\cdot\left(g^l\rho^l_{\mathrm{M},0}\mathrm{D}^l_{\mathrm{M}}\boldsymbol{\nabla}\langle w_i\rangle_{\mathrm{M}}\right) = \rho^l_{\mathrm{M},0}\dot{\theta}_{\mathrm{M}}w^*_i + \rho^l_{\mathrm{M},0}\langle \boldsymbol{u}^l\rangle_{\mathrm{M}}\cdot\boldsymbol{\nabla} w^*_i - \boldsymbol{\nabla}\cdot\left(g^l\rho^l_{\mathrm{M},0}\mathrm{D}^l_{\mathrm{M}}\boldsymbol{\nabla} w^*_i\right) \tag{5.68}$$

In the surrounding media

The transport of the chemical species concerns only the metal subdomain. However, as we adopt an Eulerian monolithic approach for conservation equations, we need to extend the definition of the solute composition to the materials surrounding the metal subdomain, namely the gas and the chill plate subdomains. Intuitively, we can think to cancel the value of the chemical composition of each solute outside the metallic subdomain. However, the gradient of composition in the vicinity of the interface leads to strong artificial fluxes of the species outwards the metallic subdomain. For this reason, we consider that the composition outside the metallic subdomain is equal to the nominal composition $w_{i,0}$ and that the mass density of each solute is equal to that of the liquid metal $\rho^l_{\mathrm{M},0}w_{i,0}$. Then we ensure that during the calculation, this composition remains constant and uniform outside the metallic subdomain to verify the following conservation equations:

$$\rho^l_{\mathrm{M},0}\frac{\partial\langle w_i\rangle_{\mathrm{A}}}{\partial t} = 0 \tag{5.69}$$

$$\rho^l_{\mathrm{M},0}\frac{\partial\langle w_i\rangle_{\mathrm{C}}}{\partial t} = 0 \tag{5.70}$$

Monolithic weak formulation

Let consider $\mathscr{W}$ the test function for the composition field. First, we write the weak formulation of the species conservation equation in the metal.

$$\left(\langle\rho\rangle_\mathrm{M}\frac{\partial\langle w_i\rangle_\mathrm{M}}{\partial t},\mathscr{W}\right)_{\Omega_\mathrm{M}}+\left(\rho^l_{\mathrm{M},0}\langle\boldsymbol{u}^l\rangle_\mathrm{M}\cdot\nabla\langle w_i\rangle_\mathrm{M},\mathscr{W}\right)_{\Omega_\mathrm{M}}-\left(g^l\rho^l_{\mathrm{M},0}\mathrm{D}^l_\mathrm{M}\nabla\langle w_i\rangle_\mathrm{M},\nabla\mathscr{W}\right)_{\Omega_\mathrm{M}}=\left(\rho^l_{\mathrm{M},0}\dot{\theta}_\mathrm{M}w_i^*,\mathscr{W}\right)_{\Omega_\mathrm{M}}$$
$$+\left(\rho^l_{\mathrm{M},0}\langle\boldsymbol{u}^l\rangle_\mathrm{M}\cdot\nabla w_i^*,\mathscr{W}\right)_{\Omega_\mathrm{M}}-\left(g^l\rho^l_{\mathrm{M},0}\mathrm{D}^l_\mathrm{M}\nabla w_i^*,\nabla\mathscr{W}\right)_{\Omega_\mathrm{M}}+\left(g^l\rho^l_{\mathrm{M},0}\mathrm{D}^l_\mathrm{M}\nabla w_i^l\cdot\boldsymbol{n}_\mathrm{M},\mathscr{W}\right)_{\partial\Omega_\mathrm{M}}\quad(5.71)$$

No species mass flux is entering nor leaving the metallic subdomain. Hence:

$$g^l\rho^l_{\mathrm{M},0}\mathrm{D}^l_\mathrm{M}\nabla w_i^l\cdot\boldsymbol{n}_\mathrm{M}=0\quad(5.72)$$

Therefore, the weak formulation of the species conservation equation becomes:

$$\left(\langle\rho\rangle_\mathrm{M}\frac{\partial\langle w_i\rangle_\mathrm{M}}{\partial t},\mathscr{W}\right)_{\Omega_\mathrm{M}}+\left(\rho^l_{\mathrm{M},0}\langle\boldsymbol{u}^l\rangle_\mathrm{M}\cdot\nabla\langle w_i\rangle_\mathrm{M},\mathscr{W}\right)_{\Omega_\mathrm{M}}-\left(g^l\rho^l_{\mathrm{M},0}\mathrm{D}^l_\mathrm{M}\nabla\langle w_i\rangle_\mathrm{M},\nabla\mathscr{W}\right)_{\Omega_\mathrm{M}}=\left(\rho^l_{\mathrm{M},0}\dot{\theta}_\mathrm{M}w_i^*,\mathscr{W}\right)_{\Omega_\mathrm{M}}$$
$$+\left(\rho^l_{\mathrm{M},0}\langle\boldsymbol{u}^l\rangle_\mathrm{M}\cdot\nabla w_i^*,\mathscr{W}\right)_{\Omega_\mathrm{M}}-\left(g^l\rho^l_{\mathrm{M},0}\mathrm{D}^l_\mathrm{M}\nabla w_i^*,\nabla\mathscr{W}\right)_{\Omega_\mathrm{M}}\quad(5.73)$$

The weak formulations of the species conservation equations in the surrounding gas and the chill plate are:

$$\left(\rho^l_{\mathrm{M},0}\frac{\partial\langle w_i\rangle_\mathrm{A}}{\partial t},\mathscr{W}\right)_{\Omega_\mathrm{A}}=0\quad(5.74)$$

$$\left(\rho^l_{\mathrm{M},0}\frac{\partial\langle w_i\rangle_\mathrm{C}}{\partial t},\mathscr{W}\right)_{\Omega_\mathrm{C}}=0\quad(5.75)$$

For an unified resolution of the species conservation equation, we define a global unknown w_i for the composition defined all over the computational domain such as:

$$w_i=\begin{cases}\langle w_i\rangle_\mathrm{M} & \text{if } \boldsymbol{x}\in\Omega_\mathrm{M}\\ \langle w_i\rangle_\mathrm{A} & \text{if } \boldsymbol{x}\in\Omega_\mathrm{A}\\ \langle w_i\rangle_\mathrm{C} & \text{if } \boldsymbol{x}\in\Omega_\mathrm{C}\end{cases}\quad(5.76)$$

The objective is to write the finite element equation that governs w_i over the whole domain. For this purpose, we sum the weak formulations of all the subdomains.

$$\left(\langle\rho\rangle_\mathrm{M}\frac{\partial w_i}{\partial t},\mathscr{W}\right)_{\Omega_\mathrm{M}}+\left(\rho^l_{\mathrm{M},0}\frac{\partial w_i}{\partial t},\mathscr{W}\right)_{\Omega_\mathrm{A}\cup\Omega_\mathrm{C}}+\left(\rho^l_{\mathrm{M},0}\langle\boldsymbol{u}^l\rangle_\mathrm{M}\cdot\nabla w_i,\mathscr{W}\right)_{\Omega_\mathrm{M}}-\left(g^l\rho^l_{\mathrm{M},0}\mathrm{D}^l_\mathrm{M}\nabla w_i,\nabla\mathscr{W}\right)_{\Omega_\mathrm{M}}$$
$$=\left(\rho^l_{\mathrm{M},0}\dot{\theta}_\mathrm{M}w_i^*,\mathscr{W}\right)_{\Omega_\mathrm{M}}+\left(\rho^l_{\mathrm{M},0}\langle\boldsymbol{u}^l\rangle_\mathrm{M}\cdot\nabla w_i^*,\mathscr{W}\right)_{\Omega_\mathrm{M}}-\left(g^l\rho^l_{\mathrm{M},0}\mathrm{D}^l_\mathrm{M}\nabla w_i^*,\nabla\mathscr{W}\right)_{\Omega_\mathrm{M}}\quad(5.77)$$

We can transform the integrals over subdomains into integrals over the whole computational domain using Heaviside functions as follows:

$$\begin{aligned}\left(\widetilde{\rho}_{\mathrm{M}}\frac{\partial w_i}{\partial t},\mathscr{W}\right)_{\Omega}+\left(\rho^{l}_{\mathrm{M},0}\mathrm{H}_{\mathrm{M}}\boldsymbol{u}\cdot\boldsymbol{\nabla}w_i,\mathscr{W}\right)_{\Omega}-\left(g^{l}\mathrm{H}_{\mathrm{M}}\rho^{l}_{\mathrm{M},0}\mathrm{D}^{l}_{\mathrm{M}}\boldsymbol{\nabla}w_i,\boldsymbol{\nabla}\mathscr{W}\right)_{\Omega}\\ =\left(\rho^{l}_{\mathrm{M},0}\dot{\theta}^{\mathrm{F}}w_i^{*},\mathscr{W}\right)_{\Omega}+\left(\rho^{l}_{\mathrm{M},0}\mathrm{H}_{\mathrm{M}}\boldsymbol{u}\cdot\boldsymbol{\nabla}w_i^{*},\mathscr{W}\right)_{\Omega}-\left(g^{l}\mathrm{H}_{\mathrm{M}}\rho^{l}_{\mathrm{M},0}\mathrm{D}^{l}_{\mathrm{M}}\boldsymbol{\nabla}w_i^{*},\boldsymbol{\nabla}\mathscr{W}\right)_{\Omega}\end{aligned}\tag{5.78}$$

where

$$\widetilde{\rho}_{\mathrm{M}}=\langle\rho\rangle_{\mathrm{M}}\mathrm{H}_{\mathrm{M}}+\rho^{l}_{\mathrm{M},0}\left(1-\mathrm{H}_{\mathrm{M}}\right)\tag{5.79}$$

5.2.5 Modelling of interfaces

In the previous conservation equations, we expressed the mixed properties using the Heaviside functions H_{M}, H_{A} and H_{C} as well as the Dirac function δ_{MC} of the metal/chill boundary Γ_{MC} . Moreover, the expression of the capillary forces that act at the liquid-metal/gas interface Γ^{l}_{MA} requires the Dirac function δ_{lg}, the curvature κ_{lg} and the normal vector $\boldsymbol{n}_{lg}$. All these variables depend on the position of the interfaces that we model here in this work by means of the level set method. In this context, we define two level-set functions: ϕ_{M} which describes the boundary $\partial\Omega_{\mathrm{M}}$ of the metal subdomain, and ϕ_{C} which gives the position of the chill plate boundary $\partial\Omega_{\mathrm{C}}$.

$$\phi_{\mathrm{M}}=\begin{cases}d(\boldsymbol{x},\partial\Omega_{\mathrm{M}}) & \text{if } \boldsymbol{x}\in\Omega_{\mathrm{M}}\\ 0 & \text{if } \boldsymbol{x}\in\partial\Omega_{\mathrm{M}}\\ -\,d(\boldsymbol{x},\partial\Omega_{\mathrm{M}}) & \text{if } \boldsymbol{x}\not\in\Omega_{\mathrm{M}}\end{cases}\tag{5.80}$$

$$\phi_{\mathrm{C}}=\begin{cases}d(\boldsymbol{x},\partial\Omega_{\mathrm{C}}) & \text{if } \boldsymbol{x}\in\Omega_{\mathrm{C}}\\ 0 & \text{if } \boldsymbol{x}\in\partial\Omega_{\mathrm{C}}\\ -\,d(\boldsymbol{x},\partial\Omega_{\mathrm{C}}) & \text{if } \boldsymbol{x}\not\in\Omega_{\mathrm{C}}\end{cases}\tag{5.81}$$

From ϕ_{M} and ϕ_{C} we determine smooth Heaviside functions H_{M} and H_{C} for the metal and the chill subdomains respectively:

$$\mathrm{H}_{\mathrm{M}}=\begin{cases}1 & \text{if } \phi_{\mathrm{M}}>\varepsilon\\ \dfrac{1}{2}\left[1+\dfrac{\phi_{\mathrm{M}}}{\varepsilon}+\dfrac{1}{\pi}\sin\left(\dfrac{\pi\phi_{\mathrm{M}}}{\varepsilon}\right)\right] & \text{if } \left|\phi_{\mathrm{M}}\right|\leq\varepsilon\\ 0 & \text{if } \phi_{\mathrm{M}}<-\varepsilon\end{cases}\tag{5.82}$$

$$\mathrm{H_C} = \begin{cases} 1 & \text{if } \phi_\mathrm{C} > \varepsilon \\ \dfrac{1}{2}\left[1 + \dfrac{\phi_\mathrm{C}}{\varepsilon} + \dfrac{1}{\pi}\sin\left(\dfrac{\pi\phi_\mathrm{C}}{\varepsilon}\right)\right] & \text{if } |\phi_\mathrm{C}| \le \varepsilon \\ 0 & \text{if } \phi_\mathrm{C} < -\varepsilon \end{cases} \tag{5.83}$$

Consequently, we deduce the Heaviside of the surrounding gas $\mathrm{H_A}$ such as:

$$\mathrm{H_A} = 1 - \mathrm{H_M} - \mathrm{H_C} \tag{5.84}$$

Note that here we fix a common value of the mixing zone width ε for all the subdomains and that the Heavisides are centred around the boundaries.

From the Heaviside functions we derive two Dirac function δ_M and δ_C such as:

$$\delta_\mathrm{M} = \mathrm{H}'_\mathrm{M} \tag{5.85}$$

$$\delta_\mathrm{C} = \mathrm{H}'_\mathrm{C} \tag{5.86}$$

The metal subdomain Ω_M is in contact with the chill plate Ω_C and the surrounding gas Ω_A. Therefore, the metal boundary $\partial\Omega_\mathrm{M}$ is composed of two interfaces: the metal-chill interface $\Gamma_\mathrm{MC} = \partial\Omega_\mathrm{M} \cup \partial\Omega_\mathrm{C}$ and the metal-gas interface $\Gamma_\mathrm{MA} = \partial\Omega_\mathrm{M} \cup \partial\Omega_\mathrm{A}$.

We recall the definition of the Dirac function δ_MC needed for modelling the thermal contact resistance at the metal/chill interface:

$$\delta_\mathrm{MC} = \begin{cases} \delta_\mathrm{C} & \text{if } \mathrm{H_M} > 0 \\ 0 & \text{if } \mathrm{H_M} = 0 \end{cases} \tag{5.87}$$

In the same way we define the Dirac function δ_MA of the metal/gas interface Γ_MA

$$\delta_\mathrm{MA} = \begin{cases} \delta_\mathrm{M} & \text{if } \mathrm{H_A} > 0 \\ 0 & \text{if } \mathrm{H_A} = 0 \end{cases} \tag{5.88}$$

During the phase transformation of the metal, the metal/gas interface Γ_MA can be composed of a liquid/gas interface Γ^l_MA and a solid/gas interface Γ^s_MA. Therefore, Γ^l_MA where capillary forces are applied, is governed by fluid dynamics as well as phase transformation. However, with the volume averaging method the liquid-solid interface is not explicitly modelled. Hence, we can not clearly separate Γ^l_MA from Γ^s_MA in the mushy zone. In this work, we propose to set a threshold g^l_c for the liquid volume fraction beyond which the metal boundary can be considered predominantly liquid. For this purpose, we define the liquid phase indicator χ_l such as:

$$\chi_l = \begin{cases} 1 & \text{if } g^l \ge g^l_c \\ 0 & \text{if } g^l < g^l_c \end{cases} \tag{5.89}$$

Consequently, the Dirac function δ_{lg}, the normal vector $\boldsymbol{n}_{lg}$ and the curvature κ_{lg} needed for capillary forces modelling, write:

$$\delta_{lg} = \chi_l \; \delta_{\mathrm{MA}} \tag{5.90}$$

$$\boldsymbol{n}_{lg} = \chi_l \; \nabla\phi_{\mathrm{M}} \tag{5.91}$$

$$\kappa_{lg} = \chi_l \; \nabla^2\phi_{\mathrm{M}} \tag{5.92}$$

As we showed in Chapter 3, it is recommended to use a density-scaled Dirac function for surface tension in order to reduce the spurious current around the interface. Accordingly, the scaled Dirac function δ_{lg}^{scaled} is defined by the following equation:

$$\delta_{lg}^{scaled} = 2\,\mathrm{H}_{\mathrm{M}}\;\delta_{lg} \tag{5.93}$$

The motion of the liquid/gas interface is tracked by the resolution of the transport equation of ϕ_{M} such as:

$$\frac{\partial\phi_{\mathrm{M}}}{\partial t} + \boldsymbol{u}\cdot\nabla\phi_{\mathrm{M}} = 0 \tag{5.94}$$

$\boldsymbol{u}$ being the velocity vector resulting from solving the monolithic Navier-Stokes equations, by construction, its value at the solid-metal/gas interface is zero. So the equation ensures the transport of only the liquid part of the boundary $\partial\Omega_{\mathrm{M}}$.

As previously shown, the mass of the object transported with the level set method is not guaranteed to be conserved. So a mass correction method was proposed for constant volume objects. For metals, the difference of densities between the liquid phase and the solid phase makes the volume shrink during solidification. So, a mass correction of a varying volume is required in this context. To correct the mass lost/gained during solidification of the metal subdomain, we use the principle of a redistribution of the mass lost/gained over the metal surface but only at the liquid part Γ_{MA}^{l} such as:

$$\phi_{\mathrm{M}}^{corr} = \phi_{\mathrm{M}} + \chi_l\; c_{\phi} \tag{5.95}$$

where c_{ϕ} is a distance given by:

$$c_{\phi} = \frac{m(t) - m_0}{\int_{\partial\Omega_{\mathrm{M}}} \chi_l\; \langle\rho\rangle_{\mathrm{M}}\, d\mathrm{S}} \tag{5.96}$$

$m(t)$ is the mass of the metal subdomain Ω_{M} at the time t and m_0 is its initial value such as:

$$m(t) = \int_{\Omega} \mathrm{H}_{\mathrm{M}}\,\langle\rho\rangle_{\mathrm{M}}\, d\mathrm{V} \tag{5.97}$$

Finally, as we assume that the chill plate is fixed, the level set function ϕ_{C} is constant over time. No transport equation neither mass correction is applied for it.

5.3 Coupling resolution strategy

In the previous section, we set the system of equations that governs the physics of coupling fluid mechanics with heat transfer in the context of solidification of multi-component alloys. In this section, we present the strategy of solving this coupled multi-physics problem.

The unknowns of this problem are $\boldsymbol{u}$ the velocity vector, p the pressure, T the temperature, w_i the composition of the solute i and the level set function ϕ_{M}. All these variables are coupled with each other. Indeed, the velocity of the fluid influences the transport of energy and chemical species. In addition, energy and chemical species are linked via the microsegregation model. In return, the thermophysical properties of the fluid, conditioned by the temperature and the composition, influence on the velocity field via solidification shrinkage and capillary forces. For each time increment, the calculation starts with the resolution of the conservation of energy and then the transport of chemical species. These resolutions will give direct access to temperature T and chemical composition w_i. Next, the Navier-Stokes equations describing the conservation of mass and momentum are solved. Finally, the new position of the metal/gas interface is determined by solving the transport equation of the level set and its adjustment behind by mass correction method. Thus, for each time increment, the equations are solved only once. This solving scheme, therefore, corresponds to a weak coupling of the equations. Note that the most recent value of the variables will be used during the calculation. The steps of the resolution strategy are given in Figure 5.2.

1. Energy conservation solver

$$\left(\frac{\widehat{\langle\rho h\rangle}}{\Delta t},\mathscr{T}\right)_\Omega+\left(C_p^F\boldsymbol{u}^-\cdot\boldsymbol{\nabla}T,\mathscr{T}\right)_\Omega+\left(\widehat{\langle k\rangle}\boldsymbol{\nabla}T,\boldsymbol{\nabla}\mathscr{T}\right)_\Omega=\left(\frac{\widehat{\langle\rho h\rangle}^-}{\Delta t}-\left(\rho_M^l h_M^l\dot{\theta}^F\right)^-,\mathscr{T}\right)_\Omega$$

After resolution, we obtain $T(t)$

2. Microsegregation model solver

With $T(t)$ and w_i^- as inputs, we obtain from thermodynamic tabulations $g^\varphi(t)$, $h_M^\varphi(t)$, $w_i^\varphi(t)$ where φ denotes the liquid and the different solid phases

3. Chemical species conservation solver

$$\begin{aligned}&\left(\tilde{\rho}_M\frac{w_i}{\Delta t},\mathscr{W}\right)_\Omega+\left(\rho_{M,0}^l H_M\boldsymbol{u}^-\cdot\boldsymbol{\nabla}w_i,\mathscr{W}\right)_\Omega-\left(g^l H_M\rho_{M,0}^l D_M^l\boldsymbol{\nabla}w_i,\boldsymbol{\nabla}\mathscr{W}\right)_\Omega\\&\quad=\left(\tilde{\rho}_M\frac{w_i^-}{\Delta t}+\rho_{M,0}^l\dot{\theta}^F w_i^*,\mathscr{W}\right)_\Omega+\left(\rho_{M,0}^l H_M\boldsymbol{u}\cdot\boldsymbol{\nabla}w_i^*,\mathscr{W}\right)_\Omega-\left(g^l H_M\rho_{M,0}^l D_M^l\boldsymbol{\nabla}w_i^*,\boldsymbol{\nabla}\mathscr{W}\right)_\Omega\end{aligned}$$

After resolution, we obtain $w_i(t)$

4. Navier-Stokes solver

$$\begin{cases}\left(\rho^F\frac{\boldsymbol{u}-\boldsymbol{u}^-}{\Delta t}+\frac{\rho^F}{g^F}\boldsymbol{\nabla}\boldsymbol{u}\cdot\boldsymbol{u},\mathscr{U}\right)_\Omega+\left(2\mu^F\dot{\boldsymbol{\varepsilon}}(\boldsymbol{u}):\dot{\boldsymbol{\varepsilon}}(\mathscr{U})\right)_\Omega-\left(g^F p,\boldsymbol{\nabla}\cdot\mathscr{U}\right)_\Omega+\left(g^F\frac{\mu^F}{\mathbb{K}^F}\boldsymbol{u},\mathscr{U}\right)_\Omega\\ \left(\Delta t\ \gamma_{lg}\ \delta_{lg}\ (\boldsymbol{\nabla}\boldsymbol{u}.\mathbf{P}):\boldsymbol{\nabla}\mathscr{U}\right)_\Omega=\left(\frac{2}{3}\mu^F\dot{\theta}^F,\boldsymbol{\nabla}\cdot\mathscr{U}\right)_\Omega+\left(g^F\rho^F\boldsymbol{g},\mathscr{U}\right)_\Omega+\left(\delta_{lg}\left(\boldsymbol{f}_{ST}+\boldsymbol{f}_{Mar}\right),\mathscr{U}\right)_\Omega\\ \\ (\boldsymbol{\nabla}\cdot\boldsymbol{u},\mathscr{P})_\Omega=\left(\dot{\theta}^F,\mathscr{P}\right)_\Omega\end{cases}$$

After resolution, We obtain $\boldsymbol{u}(t)$ and $p(t)$

5. Level set solver

$$\left(\frac{\phi_M}{\Delta t},\mathscr{F}\right)_\Omega+\left(\boldsymbol{u}\cdot\boldsymbol{\nabla}\phi_M,\mathscr{F}\right)_\Omega=\left(\frac{\phi_M^-}{\Delta t},\mathscr{F}\right)_\Omega$$

We obtain $\phi_M(t)$

6. Mass correction

$$\phi_M^{corr}=\phi_M+\chi_l\ c_\phi$$

We obtain the corrected $\phi_M(t)$

Figure 5.2: The order of the resolution of conservation equations during a time increment

5.4 Application to chill cooling and solidification experiment on board the ISS

We have proposed coupling of fluid mechanics, heat transfer and microsegregation in the context of solidification of multi-component alloys. Now, we will apply this numerical framework to the ISS experiment that we simulate in the previous chapter with only heat conduction. But before reaching a 3D complete simulation, we perform a preliminary study in order to evaluate the influence of some numerical and physical parameters. For this parametric study, we opt for 2D simulations, given their relatively short computation time compared to 3D simulations. A 3D simulation will be presented at the end of this chapter.

5.4.1 Preliminary results and numerical investigations

5.4.1.1 Computational configuration

Geometries and mesh

In the ISS experiment, the chill plate is a cylinder with a radius of 8 mm and a thickness of 3 mm. The initial shape of the metal droplet is estimated from experimental observations 2.15. It is a sphere of 3.14 mm radius truncated at the top so that its total height is 6.08 mm. The surface of contact with the chill is then a disc of 1 mm radius. Let us take the Z-axis as the axis of the symmetry of the problem. We place the Z = 0 plane at the plane of the contact between the chill and the droplet. The 2D simulations are performed in the XZ plane. The 2D computational domain Ω is a rectangular box with a side length of 20 mm in the X direction and 17 mm in the Z direction, as illustrated in Figure 5.3a.

The mesh used in the calculations, as shown in Figure 5.3b, is static, more or less refined in regions of interest. The interfaces where the gradients are the strongest must be fine-meshed. Let us note h_0 the minimum characteristic size of the mesh and fix it at a value of 60 µm. In a 1 mm wide band centred around the boundary of the chill, the mesh size is h_0 in the normal direction and $5h_0$ in the tangential direction. Inside the chill, the mesh is isotropic with a characteristic size of $5h_0$. Since the mesh is static, we have meshed with isotropic elements of a characteristic size of h_0 a region that covers the space where the droplet could elongate. We define this region as part of an ellipse with a major axis of 1 cm and a minor axis of 8 mm.

The half-thickness of the mixture zones ε is fixed to $4h_0$.

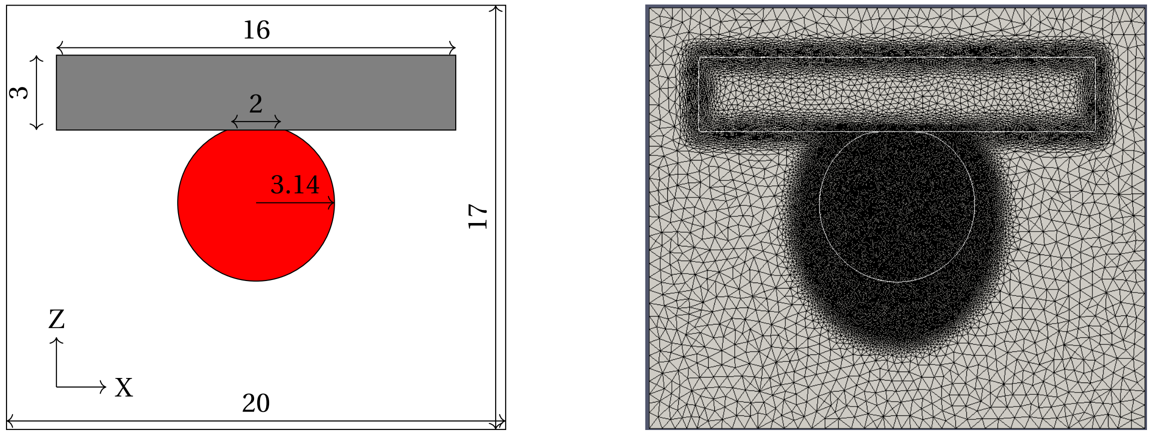

(a) The geometries of the problem (dimensions are given in mm)

(b) 2D mesh

Figure 5.3: The setup of the 2D simulation for chill cooling and solidification of a steel droplet showing: (a) the geometries of the droplet, chill plate and the computational domain, (b) the 2D mesh used for calculations.

.

Initial and boundary conditions

The initial temperature of the metallic droplet is $T_{M,0}$ = 1648 ^{o}C. The surrounded gas is considered at the same initial temperature as the metal. As for the chill plate, its initial temperature is fixed to $T_{C,0}$ = 25 ^{o}C. The system is initially in a steady-state with a zero velocity. The initial composition of the system is the nominal composition of the metallic alloy.

The level set functions ϕ_M and ϕ_C are initialised with the geometrical distance from the initial boundary position of the droplet and the chill respectively.

The boundaries of the computational domain are considered adiabatic. For the Navier-Stokes solver, the pressure and the velocity are free at the boundary. A Dirichlet condition of zero-velocity is imposed in the chill subdomain ($\phi_C \geq 0$).

Physical properties

In the present work, we focus on *d1* sample proceeded on board the ISS and whose composition is given in Chapter 2. This steel will first be approximated by a binary alloy Fe-0.9wt.%C by considering only the Carbon solute. Thus the index i is only $i = 1$. In a later step, we consider a ternary alloy Fe-0.9wt.%C- 0.2wt.%Si which means $i = 1$ corresponds to Carbon solute and $i = 2$ corresponds to Silicon solute.

The energy conservation equation is written with both enthalpy and temperature variables. The relationship between these two variables is not linear for alloys. It is defined by the following relations:

$$\langle \rho h \rangle_M = \sum_{\varphi \in M} g^{\varphi} \rho_M^{\varphi} h_M^{\varphi} \tag{5.98}$$

$$g^{\varphi} = g^{\varphi}\left(T, \langle w_i \rangle_M\right) \tag{5.99}$$

$$\rho_{\mathrm{M}}^{\varphi} = \rho_{\mathrm{M}}^{\varphi}\left(\mathrm{T}, w_i^{\varphi}\right) \tag{5.100}$$

$$h_{\mathrm{M}}^{\varphi} = h_{\mathrm{M}}^{\varphi}\left(\mathrm{T}, w_i^{\varphi}\right) \tag{5.101}$$

$$w_i^{\varphi} = w_i^{\varphi}\left(\mathrm{T}, \langle w_i \rangle_{\mathrm{M}}\right) \tag{5.102}$$

The thermodynamic properties g^{φ}, $\rho_{\mathrm{M}}^{\varphi}$, h_{M}^{φ} and w_i^{φ} are tabulated as a function of temperature and chemical composition. These tables are needed to convert temperature into enthalpy during non-linear iterations of the energy solver. Detailed information on this resolution step can be found in [97]. These same tabulations are also used in the rest of the calculation to compute the volume fractions, densities, enthalpies and compositions of each phase from the resulting temperature of the energy solver.

For the chill plate, made of ceramic $\mathrm{Si_3N_4}$, the enthalpy is linearly linked to the temperature such as $\langle \rho h \rangle_{\mathrm{C}} = \rho_{\mathrm{C}} h_{\mathrm{C}} = \rho_{\mathrm{C}} c_{p,\mathrm{C}} \mathrm{T}$. Therefore, the tabulations for the chill subdomain are built from this latter relation.

By using the monolithic approach for energy conservation, any displacement of the metal/gas interface is energetically converted into a phase change between the gas subdomain on one side and the metal phases on the other. To avoid this purely numerical issue, we use the same tabulated phase enthalpy properties of the liquid metal for the gas subdomain. This assumption applies only to the energy solver.

The physical properties of the materials involved in this problem are given by the table 5.1. The gravity vector is set to zero $\boldsymbol{g} = \mathbf{0}$. The thermal contact resistance R_{th} is, initially, fixed to zero (perfect contact) and, in a further step, calibrated according to the experiment via a parametric study. The threshold g_c^l needed for the definition of the liquid/gas interface where surface tension and Marangoni are applied is fixed to 30%.

Table 5.1: Physical properties of materials

Physical parameter	**Symbol**	**Value**	**Unit**
Metal thermal conductivity	$\langle k \rangle_{\mathrm{M}}$	42	$\mathrm{W.m^{-1}.K^{-1}}$
Liquid heat capacity (per unit volume)	$\mathrm{C}^{l}_{p,\mathrm{M}}$	4.88×10^{6}	$\mathrm{J.K^{-1}.m^{-3}}$
Liquid density (reference value)	$\rho^{l}_{\mathrm{M},0}$	6939	$\mathrm{kg.m^{-3}}$
Solid density (reference value)	$\rho^{s}_{\mathrm{M},0}$	7355	$\mathrm{kg.m^{-3}}$
Liquid dynamic viscosity	μ^{l}_{M}	9.5×10^{-3}	Pa.s
Surface tension of the liquid	γ_0	1.439	$\mathrm{N.m^{-1}}$
Marangoni coefficient	$\frac{\partial \gamma}{\partial \mathrm{T}}$	5.44×10^{-4}	$\mathrm{N.m^{-1}.K^{-1}}$
Secondary dendrite arm spacing	λ_2	90×10^{-6}	m
Solute diffusion in the liquid	$\mathrm{D}^{l}_{\mathrm{M}}$	1.525×10^{-9}	$\mathrm{m^{2}.s^{-1}}$
Gas thermal conductivity	$\langle k \rangle_{\mathrm{A}}$	0.016	$\mathrm{W.m^{-1}.K^{-1}}$
Gas heat capacity (per volume unit)	$\mathrm{C}_{p,\mathrm{A}}$	1300	$\mathrm{J.K^{-1}.m^{-3}}$
Gas density	ρ_{A}	1.6	$\mathrm{kg.m^{-3}}$
Gas dynamic viscosity	μ_{A}	2.26×10^{-5}	Pa.s
Chill thermal conductivity	$\langle k \rangle_{\mathrm{C}}$	50	$\mathrm{W.m^{-1}.K^{-1}}$
Chill heat capacity (per mass unit)	$c_{p,\mathrm{C}}$	700	$\mathrm{J.K^{-1}.kg^{-1}}$
Chill density	ρ_{A}	3290	$\mathrm{kg.m^{-3}}$

Numerical considerations

The semi-implicit formulation of surface tension allows time-step values higher than the limit imposed by the stability condition of an explicit surface tension. Therefore, we set the value of the time-step to approximately 50 times the limit of the stability.

$$\Delta t \approx 50 \times \sqrt{\frac{h_0^3 \left(\rho^{l}_{\mathrm{M},0} + \rho_{\mathrm{A}}\right)}{4\pi\gamma_0}} \tag{5.103}$$

For $h_0 = 60$ µm, we fix the time step to $\Delta t = 5 \times 10^{-4}$ s.

In a preliminary simulation, we encountered a problem of calculation divergence when a small quantity of the liquid metal remains not yet solidified. We attribute this numerical problem to the spurious currents due to capillary forces applied in the small remaining liquid metal surface. Indeed, at the end of the solidification, the temperature gradient becomes weak and consequently Marangoni too. The small volume of the liquid is essentially governed by the solidification shrinkage. When the volume of the liquid phase (g^l = 100%) becomes of the same order of magnitude as a few elements, spurious currents become preponderant and destabilise the movement in the small liquid volume. To avoid this problem, we cancel the capillary forces and allow only the solidification shrinkage when the volume of the liquid phase reaches a percentage of the total volume of the metal set at 3%. The mass correction, on the other hand, is applied even after the disappearance of the fully-liquid metal until the volume of the fully solid metal reaches a limit of 90% of the total volume of the metal.

5.4.1.2 Numerical results and discussion

With the previously defined parameters, a simulation of 7 seconds of solidification time is sufficient to obtain a fully solidified droplet, as shown in Figure 5.4. Indeed, in addition to the two-dimensional effect of the simulation, the contact between the droplet and the cooler is assumed to be perfect. The cooling rate is thus faster than in the experiment. Before proceeding to the configuration of the contact thermal resistance and other possible parameters that would influence the cooling rate, it is interesting first to analyse the behaviour of the droplet predicted by the present simulation. Figure 5.4 represents a sequence of images showing the field of the liquid metal velocity superimposed on the temperature field of the whole system. Note that the gas flow is also taken into account in the simulation, but in this analysis, we only show the liquid flow in the droplet. To display the progress of solidification, the iso-values $g^s = 1\%$ and $g^s = 99\%$ are plotted in red and blue respectively.

The cooling and solidification of the droplet are characterised by two stages: the first stage is marked by a strong temperature gradient. Marangoni currents strongly govern the flow of the liquid phase at this stage. In fact, at the beginning the initial temperatures of the chill and the droplet are very different, creating a strong temperature gradient which triggers and drives heat diffusion in the opposite direction of the gradient (towards the chill, according to Fourier's law). In the metal, this strong heat extraction leads to rapid propagation of the solidification front in the direction of the gradient (downwards). Since the Marangoni coefficient is positive, the Marangoni force applied at the liquid/gas interface is downward. The Marangoni current, therefore, pulls cold liquid at the interface downwards with a velocity of magnitude up to 0.09 m/s. By mass conservation, the hot liquid at the bottom is pushed upwards in the droplet axis. Thus, the solidification front, which is initially convex, flattens out due to the heat supplied at the droplet axis. As the solidification progresses, the gradient dissipates and becomes weaker and weaker. This is illustrated by the increasing distance between the red and blue lines that delimit the mushy zone. As a consequence, the convection by Marangoni is attenuated, giving way to the solidification shrinkage which therefore characterises the second stage. Shrinkage velocities are of a magnitude of the order of 10^{-5} m.s^{-1}, very low compared to the Marangoni velocities.

It can be seen from Figure 5.5b that the final shape of the droplet is slightly elongated in the direction of the temperature gradient. Although this deformation is consistent with the experiment, it is still less pronounced than in the experiment.

Concerning the time-evolution of the front position, as shown in Figure 5.5a, the propagation of the front is much faster than the experiment. This is probably because the contact is not perfect in the experiment. It can also be observed that a simulation with pure conduction provides a prediction of the cooling rate close to the present simulation with the resolution of the fluid flow and segregation. Therefore, the 3D pure conduction calculations, presented in the previous chapter, represent a reliable basis for estimating the thermal resistance value for a complete 3D calculation.

The evolution of the solute composition, shown in Figure 5.6, is very marked by Marangoni convection. Indeed, the Marangoni force at the interface attracts the liquid enriched in solute in the mushy zone towards the interface. Thus, one can notice areas of positive segregation at the interface in the upper part of the droplet and in the vicinity of these areas of positive segregation adjacent areas of negative segregation from which the solute has been subtracted. The solute-enriched liquid is then injected into the completely liquid phase and redistributed through Marangoni induced recirculation currents. Thus, the axis of the droplet fed with the solute is characterised by positive segregation. This redistribution of the solute makes the composition non-homogeneous at the front. This influences the progress of the front, which slows down in areas with positive segregation.

However, the chemical composition on the snapshots shows more positive segregation regions than negative segregation ones. Therefore, it is worth checking whether the mass of the solute is well conserved or not. Figure 5.7 shows the temporal evolution of the total mass of metal and the mass of carbon. Contrary to the total mass, which remains constant over time, it can be seen that the mass of carbon actually increases over time up to 4%. Although this mass gain is small, it is still not negligible. In the following paragraph, we will study the influence of the chemical composition on the shape deformation of the droplet and the cooling rate.

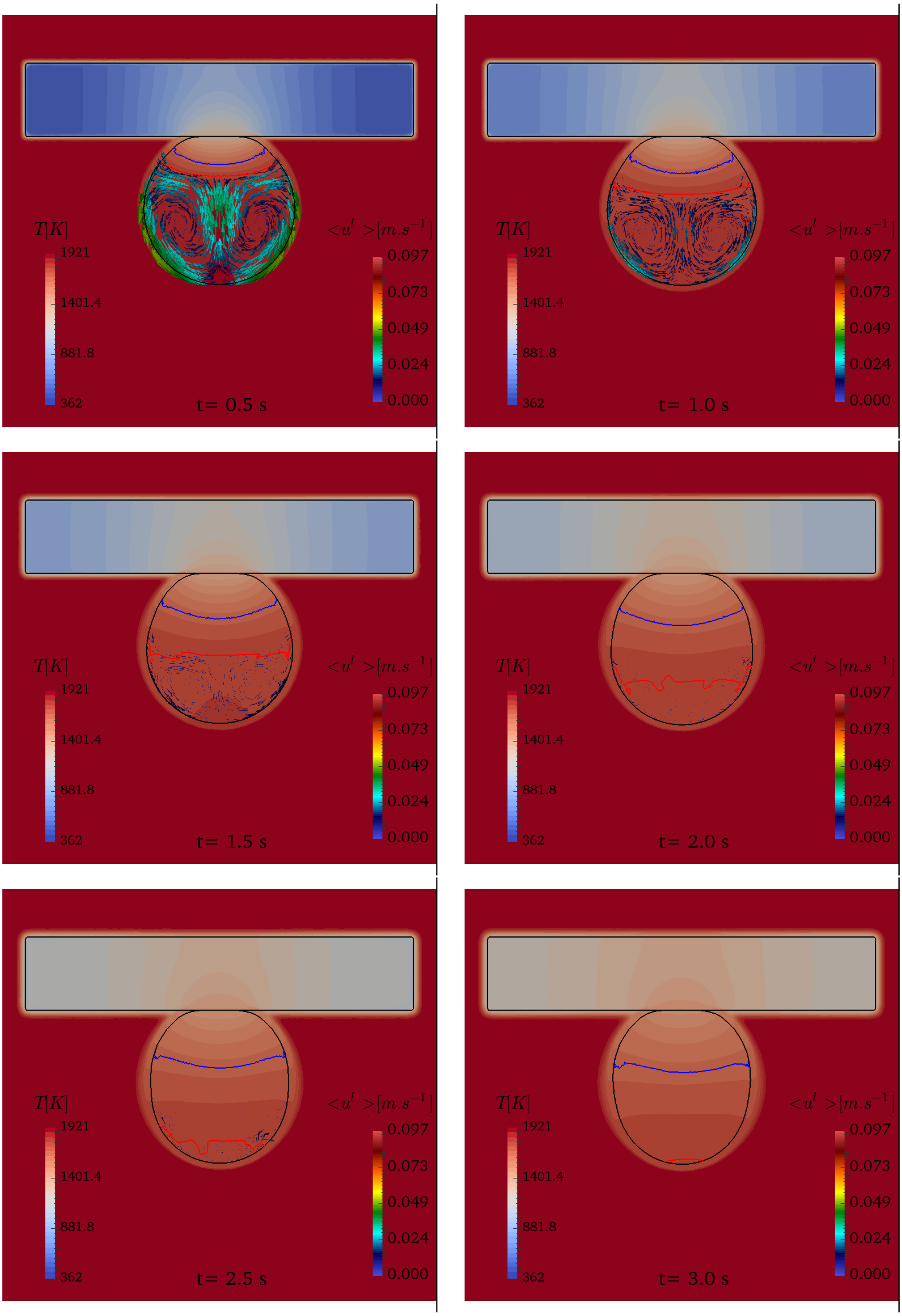

Figure 5.4: Snapshots of the solidifying droplet showing temperature field superimposed to the velocity in the metal at different times.

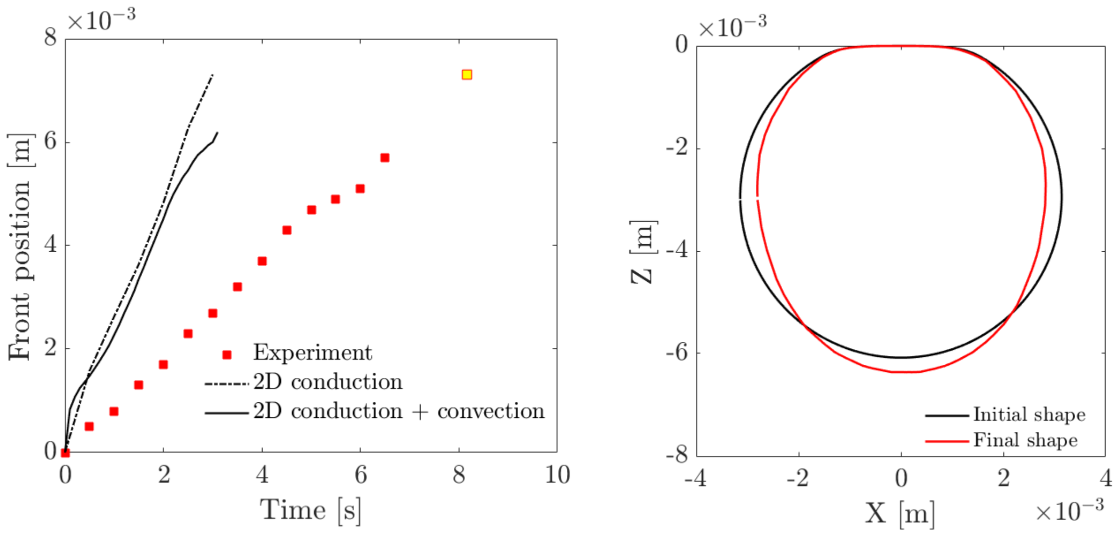

(a)

(b)

Figure 5.5: (a) Temporal signals of the front position for 2D simulation with only heat conduction (dashed black line), 2D simulation with both conduction and convection (black continuous line) and for the experiment on board the ISS (red squares: measured; yellow square: extrapolated). (b) The comparison of the initial shape and the final shape predicted by the 2D simulation showing a slightly-elongated droplet.

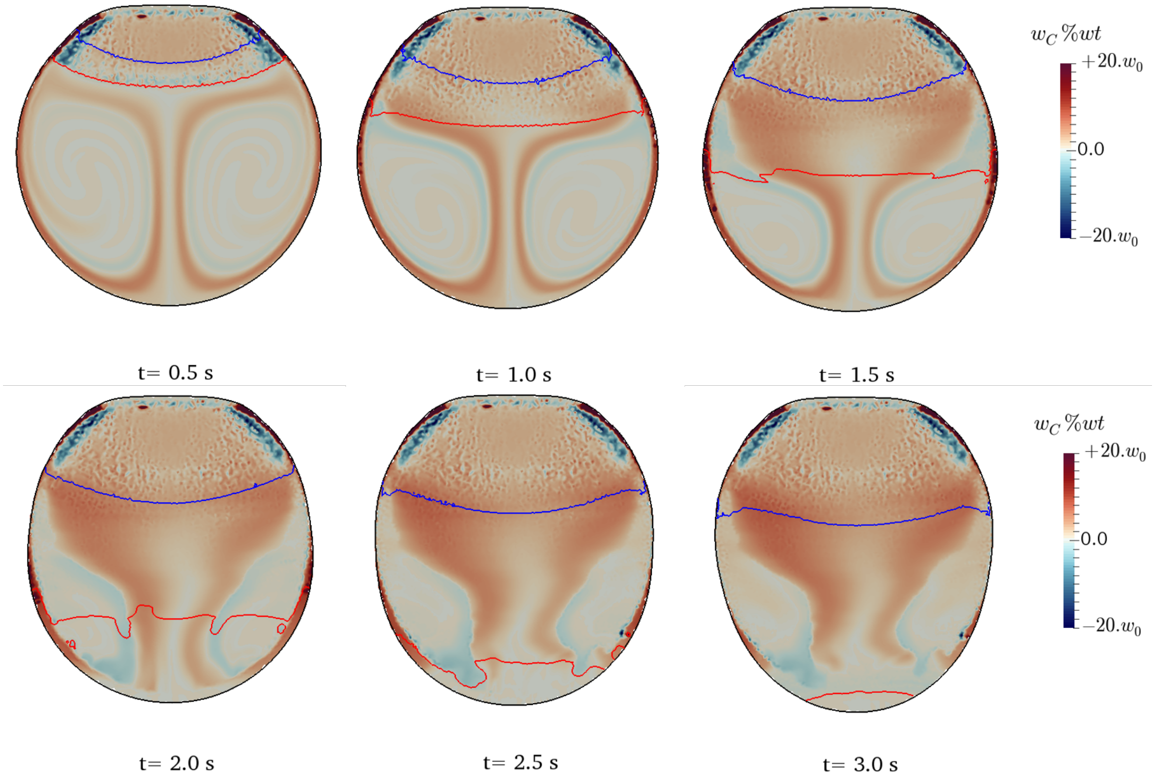

Figure 5.6: Snapshots of the solidifying droplet showing the composition field within the metal domain at different times.

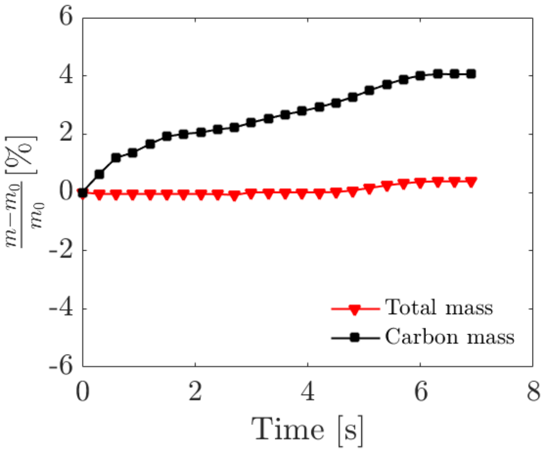

Figure 5.7: Time-evolution of the mass of the droplet and the mass of Carbon

Influence of the chemical composition

In this paragraph, we study the influence of chemical segregation on the behaviour of the droplet during solidification. To do so, we perform a simulation without solving the solute transport equation. It means therefore assuming a uniform and constant composition equal to the nominal composition $w_i = w_{C,0} = 0.9\% wt$. We then consider a case where the alloy is ternary, i.e. Fe-0.9wt.%C-0.26wt.%Si, for which we solve two conservation equations of the chemical species: Carbon and Silicon. Therefore, new thermodynamic tabulations are used specifically for this new approximation of the steel under study.

Figure 5.8 shows the final Carbon and Silicon composition for the ternary alloy. As we transport both compositions with the same convection velocity and diffusion coefficient, the segregation maps for carbon and silicon are similar and reflect the significant influence of the Marangoni currents as already described above for the binary alloy. The difference between these three cases can be seen in the solid fraction field shown in Figure 5.9. Indeed, the phase fractions depend on temperature and chemical composition following a solidification path defined by thermodynamic equilibrium. In cases where segregation has been taken into account, the chemical composition is strongly influenced by convective transport. Regions of positive segregation are created along regions of high liquid velocity, especially at the interface. The solidification front is consequently slowed down in these regions and thus accelerated in regions of negative segregation. This explains, firstly, the irregularities of the front observed for segregated cases, unlike the case of a simulation without segregation where the front is smooth and follows the isotherms. Secondly, as the concentration of solutes is high at the interface for cases with segregation, the liquid/gas surface is greater. This results in higher Marangoni velocities compared to the case without segregation.

The final shape of the solidified droplet is slightly more elongated for cases with segregation, as shown in Figure 5.10. There is a difference of 0.1 mm more than in the case without segregation. As for the position of the solidification front, the temporal evolution is almost the same for all cases with a very slight acceleration of the case without segregation at the end of the solidification. It is important to note here that the position of the front is extracted from the simulations by averaging the positions of the iso-values $g^s = 1\%$. Given the irregularities of the front in the segregated cases, the curves in Figure 5.11 may be different if other criteria for locating the front are chosen, such as the position of the front at the interface with the gas.

Since we do not yet have the chemical segregation analysis of the solidified droplet on board the ISS, we cannot evaluate the segregation predicted by the present simulations, especially since we are facing a numerical problem of mass conservation. But given the comparisons and analyses made here, the differences in final deformation and front propagation are not prominent between the cases with segregation and the case where the chemical species transport equation is not solved. In order not to base the rest of the analysis on a segregation model that should be improved, we will continue the simulations in the following, with a binary alloy assuming that the composition remains constant and uniform.

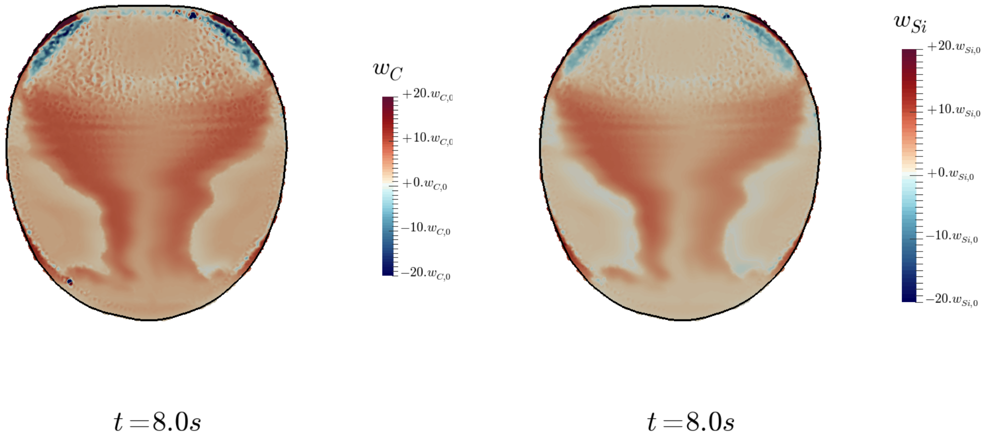

(a) (b)

Figure 5.8: Simulation of solidification of a ternary alloy showing the final composition in (a) Carbon and (b) Silicon.

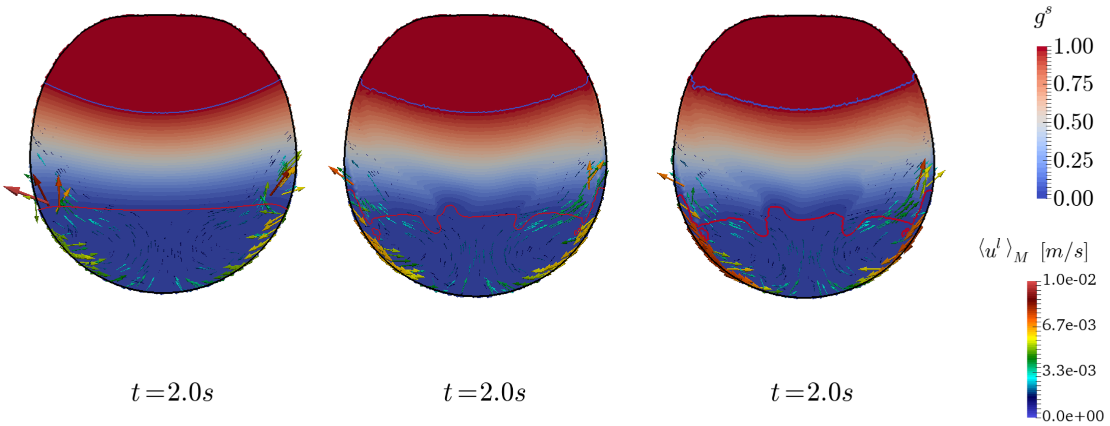

(a) (b) (c)

Figure 5.9: Comparison of the solid fraction field at the time $t = 2s$ for (a) a binary alloy with a constant and uniform Carbon composition, (b) a binary alloy with Carbon transport and (c) a ternary alloy with Carbon and Silicon transport. The red and blue lines mark the position of the iso-values $g^s = 1\%$ and $g^s = 99\%$ respectively

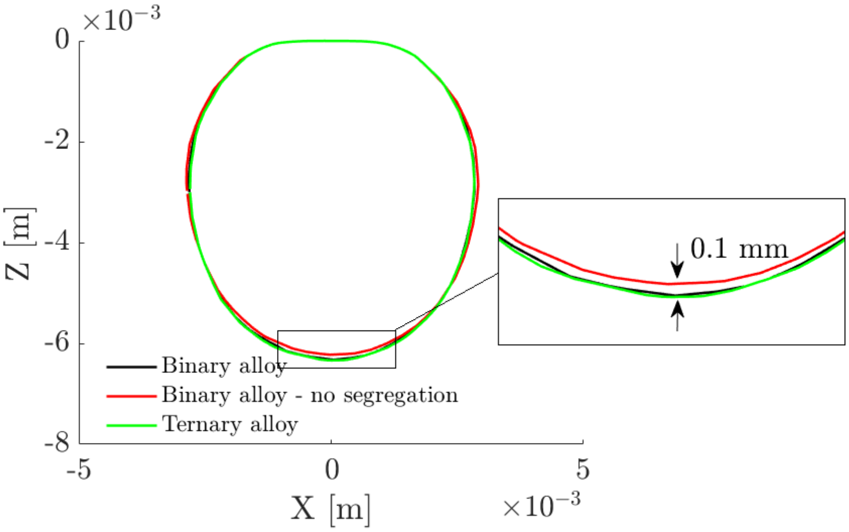

Figure 5.10: Comparison of the final shape of solidified droplet resulting from simulations with a binary alloy Fe-0.9wt.%C, with and without segregation, and a ternary alloy Fe-0.9wt.%C-0.26wt.%Si.

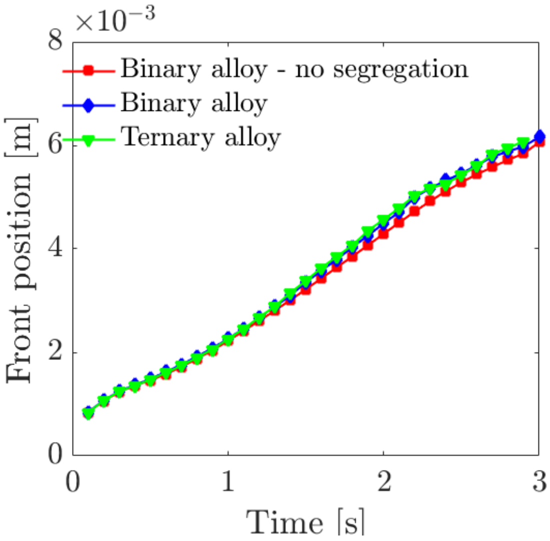

Figure 5.11: Comparison of time-evolution of the position of solidification front for simulations with a binary alloy Fe-0.9wt.%C, with and without segregation, and a ternary alloy Fe-0.9wt.%C-0.26wt.%Si.

Influence of Marangoni coefficient

As reported earlier in Chapter 2, measurement of the surface tension on board the ISS using the oscillation method revealed an increasing linear variation of the surface tension with temperature. The Marangoni coefficient is, therefore, positive. This is in contrast to several liquid metals whose Marangoni coefficient is rather negative [9]. The presence of segregated surface-active elements on the surface of the alloy may be the cause of this positive coefficient. We, therefore, wonder what the behaviour of the droplet would be during solidification if the Marangoni coefficient were negative. To answer this question, we carried out a simulation with a Marangoni coefficient equal to the opposite of the measured one, i.e. $\frac{\partial \gamma}{\partial t}$ = -5.44 . 10^{-4} N.m^{-1}.K^{-1}. The results of the simulation in comparison with the case of a positive coefficient can be discussed based on Figures 5.12 and 5.13. Figure 5.12 shows snapshots of the velocity field of the liquid metal superimposed on the temperature field, for the positive coefficient in the left column and the negative coefficient in the right column. The figure also shows the iso-values of g^s = 1% and g^s = 99%. In the case of decreasing temperature dependence (right), the colder regions correspond to higher surface tension. As a result, the Marangoni force pulls hot liquid from the bottom of the drop towards the solidification front, and by conservation of the mass, the liquid at the front is pushed down along the axis of the drop. In this way, the propagation of the front at the interface is slowed down by the heat brought in from the bottom. It follows that the convexity of the front is emphasised in the case of a negative Marangoni, unlike a positive Marangoni which tends to flatten the front. It can also be seen that the velocity values for a negative Marangoni are lower than those of a case with a positive Marangoni due to the fact that the liquid pulled by the Marangoni force impinges on the mushy zone contrary to the case of a positive Marangoni where the liquid is pushed away from the mushy zone. The difference is also visible in terms of the final deformation shown in Figure 5.13. The drop with a negative Marangoni coefficient shows no elongation compared to the initial shape.

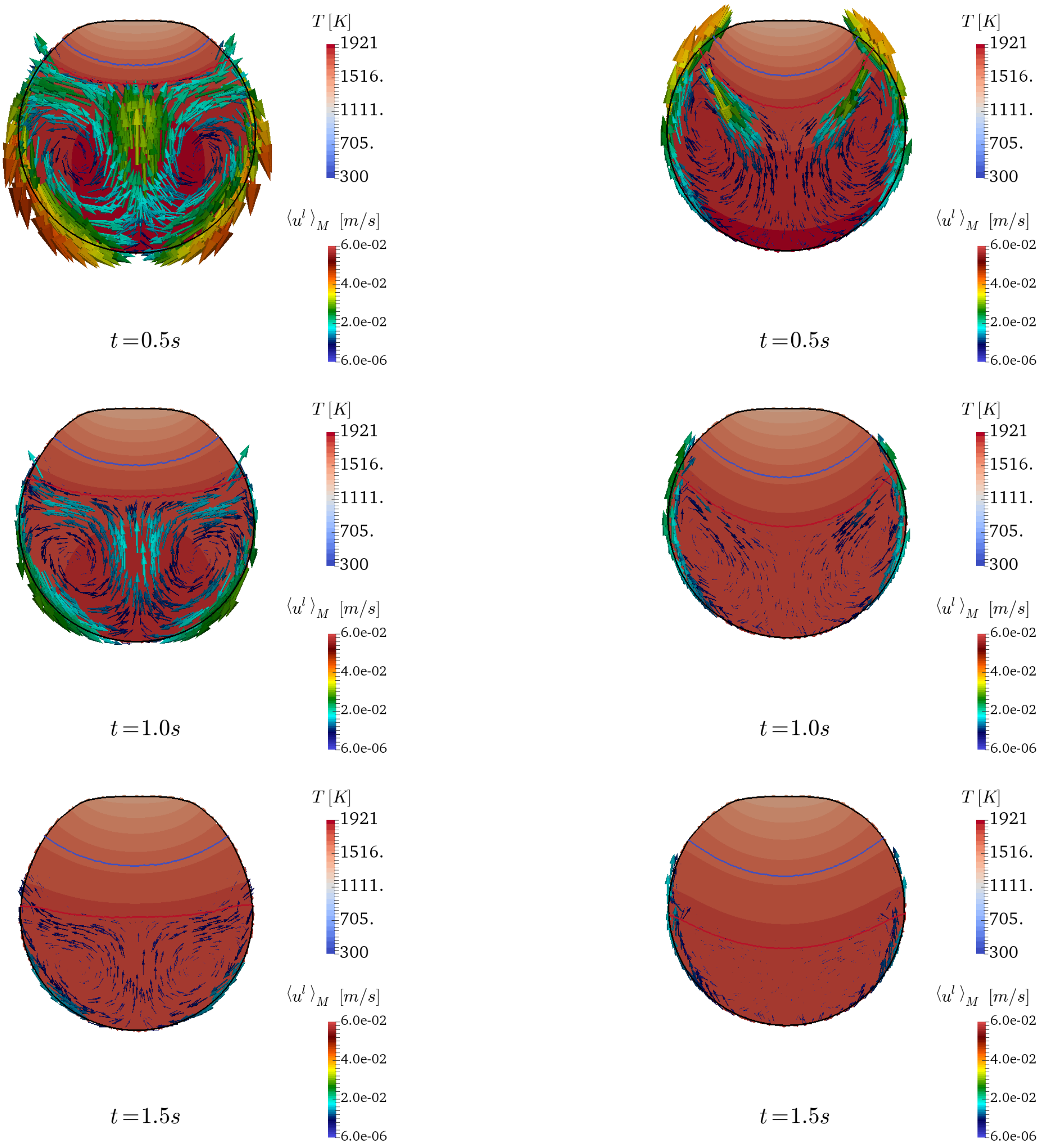

Figure 5.12: Comparison of the flow pattern in the liquid metal for (left) a positive Marangoni and (right) a negative Marangoni. The velocity vectors are superimposed to temperature field at different times. The red and blue lines mark the position of the iso-values $g^s = 1\%$ and $g^s = 99\%$ respectively

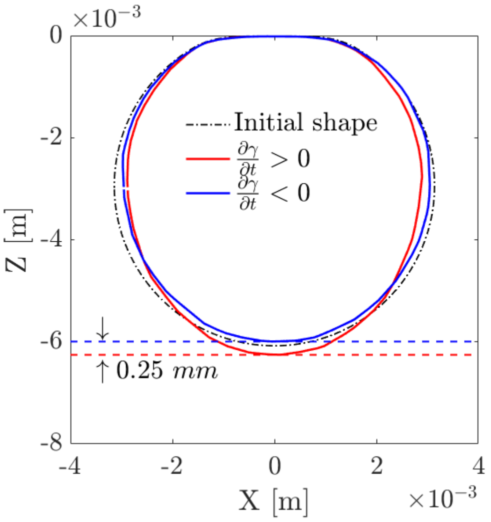

Figure 5.13: Comparison of the final shape predicted by a positive Marangoni coefficient (red) and a negative coefficient (blue). The initial shape is plotted in dashed black line.

Influence of the thermal contact resistance

The cooling rate predicted by the previous simulations is significantly higher than that observed in the experiment. In addition to the two-dimensional nature of the simulations, the contact between the chill and the metal is assumed to be perfect. The objective is now to study the influence of the contact thermal resistance on the cooling rate and the final shape of the droplet. For this purpose, we have carried out a parametric study in 2D pure conduction similar to the one carried out in 3D at the end of the previous chapter. The results of this study are shown in Figure 5.14. This study suggests two interesting values for the thermal resistance $R_{th} = 10^{-4}$ $W^{-1}.m^2.K$ and $R_{th} = 2\ .10^{-4}$ $W^{-1}.m^2.K$. We have therefore carried out two simulations with these values of R_{th}. The temporal evolution of the front position is shown in Figure 5.15a. We notice that the front propagates in two stages: the first stage of acceleration governed by a strong temperature gradient and thus by strong Marangoni convection, and the second stage of deceleration with a weak temperature gradient where the shrinkage at solidification brings heat upwards. During the first acceleration stage, the simulation with the value 10^{-4} $W^{-1}.m^2.K$ follows well the experimental evolution during the first 2.5 seconds. During the second phase, the simulation with the contact thermal resistance value of $2\ .10^{-4}$ $W^{-1}.m^2.K$ follows the experimental evolution. This result leaves the door open to more sophisticated work on the dependence of the contact thermal resistance on other space-time variables, such as contact pressure, temperature, etc. However, in this work, we only consider a constant and uniform value of the thermal resistance. In Figure 5.15b, the final shape of the droplet is displayed for one case with perfect contact and both cases with thermal resistance. It can be seen that the elongation of the droplet becomes greater when cooling is slower.

Figure 5.16 shows the velocity field of the liquid metal superimposed to the solid fraction field of the droplet with a contact resistance equal to $R_{th} = 10^{-4}$ $W^{-1}.m^2.K$. We notice that the velocity

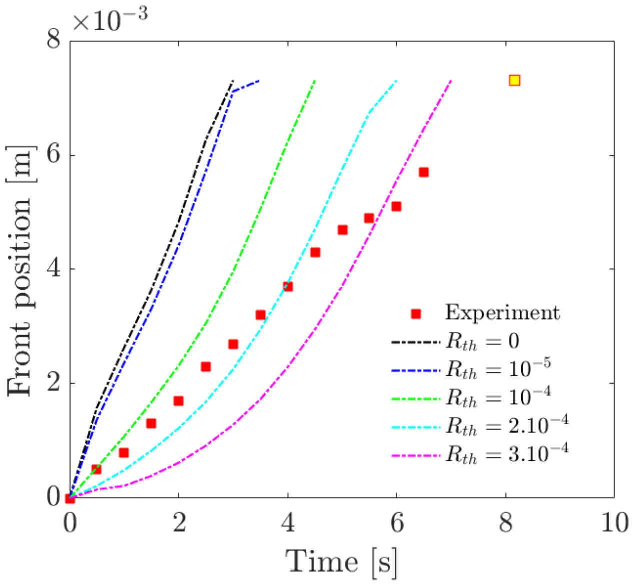

Figure 5.14: Parametric study in 2D pure conduction in which the thermal contact resistance is varying from 0 to 3. 10^{-4} $W^{-1}.m^2.K$. The numerical results are plotted in dashed lines. The measured front position is marked by red squares. The yellow square is the final front position extrapolated form measurements.

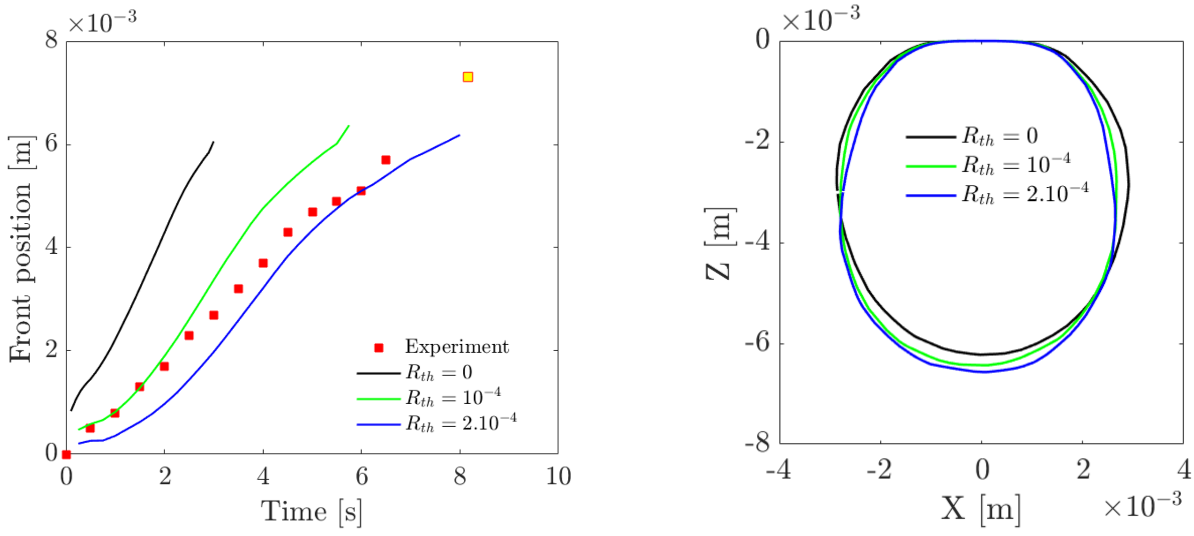

(a)

(b)

Figure 5.15: Comparison of 2D simulations with R_{th}=0 $W^{-1}.m^2.K$, R_{th} = 10^{-4} $W^{-1}.m^2.K$ and R_{th} =2. 10^{-4} $W^{-1}.m^2.K$ for (a) time evolution of the solidification front position and (b) the final droplet shapes

of the liquid reaches, in this case, a maximum value of 0.06 m.s^{-1} less than that reached in a case of perfect contact (Figure 5.4). The thermal resistance, therefore, reduces the temperature gradient by introducing a temperature jump at the interface between the cooler and the metal. During the first 2 seconds, the temperature gradient is high. The mushy zone is narrow. Marangoni currents dominate the behaviour of the liquid. The deformation of the droplet is very slight during this time. As the front moves forward, the gradient decreases, and the mushy zone grows. The deformation of the droplet is more remarkable than before. The deformation can be explained by the double action of Marangoni and solidification shrinkage. The Marangoni force pulls the liquid from the mushy zone near the interface with the gas and injects it downwards into the completely liquid metal. At the same time, the solidification shrinkage attracts the liquid in the mushy zone towards the fully solidified phase.

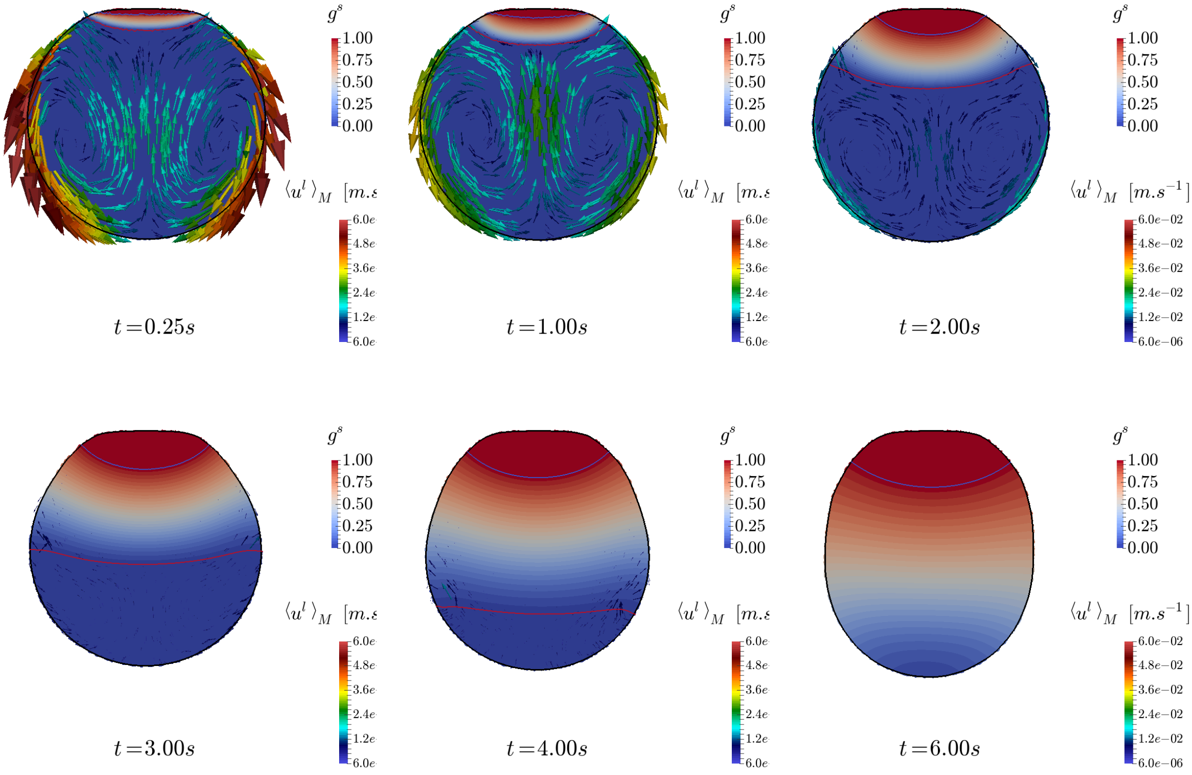
$t = 0.25s$ $t = 1.00s$ $t = 2.00s$

$t = 3.00s$ $t = 4.00s$ $t = 6.00s$

Figure 5.16: Snapshots of the solidifying droplet showing temperature field superimposed to the velocity of the metal at different times. The red and blue lines mark the position of $g^s = 1\%$ and $g^s = 99\%$ respectively

5.4.2 3D simulation

For 3D simulations, we define the calculation domain as a cylinder obtained by revolution symmetry around the Z-axis of the 2D domain. In a similar way to 2D simulations, we consider a fixed mesh with the same characteristic sizes of the 2D mesh, as shown in figure 5.17. The mesh thus generated contains a number of elements equal to 17M, which is requiring very long calculation time. We ran a 3D simulation assuming perfect contact between the drop and the chill. The results of the simulation in the XZ plane are shown in figure 5.18 for different times. Marangoni currents are predominant in the first phase of large temperature gradient which decreases over time. The flow velocity induced by Marangoni reaches a maximal value of 5.2 $\times 10^{-2}$m.s^{-1}. The final shape is shown in figure 5.19b in comparison with the experimental shape. A difference of 0.45 mm less separates the shape predicted by the simulation from that found by the experiment. Nevertheless, the elongation predicted by the 3D simulation is greater than that simulated in 2D. The temporal variation of the front position is given in Figure 5.19a. Note that here the front is defined by the iso-value $g^s = 1\%$ at the interface of the droplet with the gas. Indeed, the front is extracted from the experiment from the processing of the images showing the free surface of the droplet. The growth of the front is more rapid than that observed in the experiment because the contact between the sample and the chill is supposed to be perfect (R$_{th}$ =0 W^{-1}.m^2.K). Another simulation with appropriate thermal contact resistance may bring us closer to reproducing the experimental behaviour, as shown in 2D.

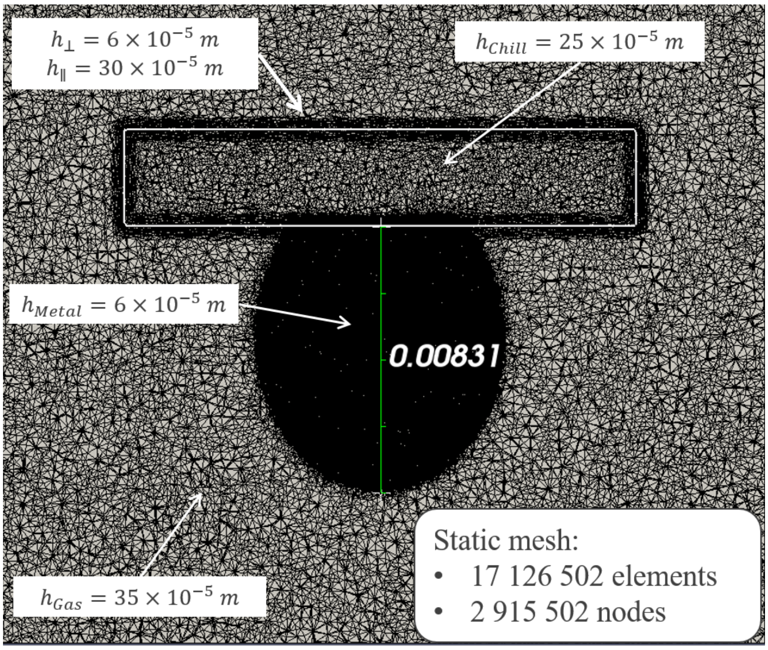

Figure 5.17: The static 3D mesh in a cross section of the computational domain showing the characteristics of the mesh size in each subdomain.

The 3D simulation presented here ran for 50 days on 128 processors. This is due to the very large number of elements contained in the mesh because of the area covering the metal domain, which requires a very small mesh size. Indeed, the number of elements in this area represents more than 85% of the total number of elements. An optimisation of this mesh size is necessary for the following calculations.

In this type of experiment, we are dealing with very high temperature gradients of the order of 1300K, very large density ratio between the metal and the gas of the order of 7000 and a very high surface tension coefficient (compared to that of fluids such as water). Faced with these challenges, we are constrained to use a very high-resolution mesh with the present numerical framework both at the interfaces where the jump in properties is very large and within the metallic domain where Marangoni convection is present with the propagation of the solidification front. We have proposed a semi-implicit formulation that allows to gain up to 50 times in time increments. But the

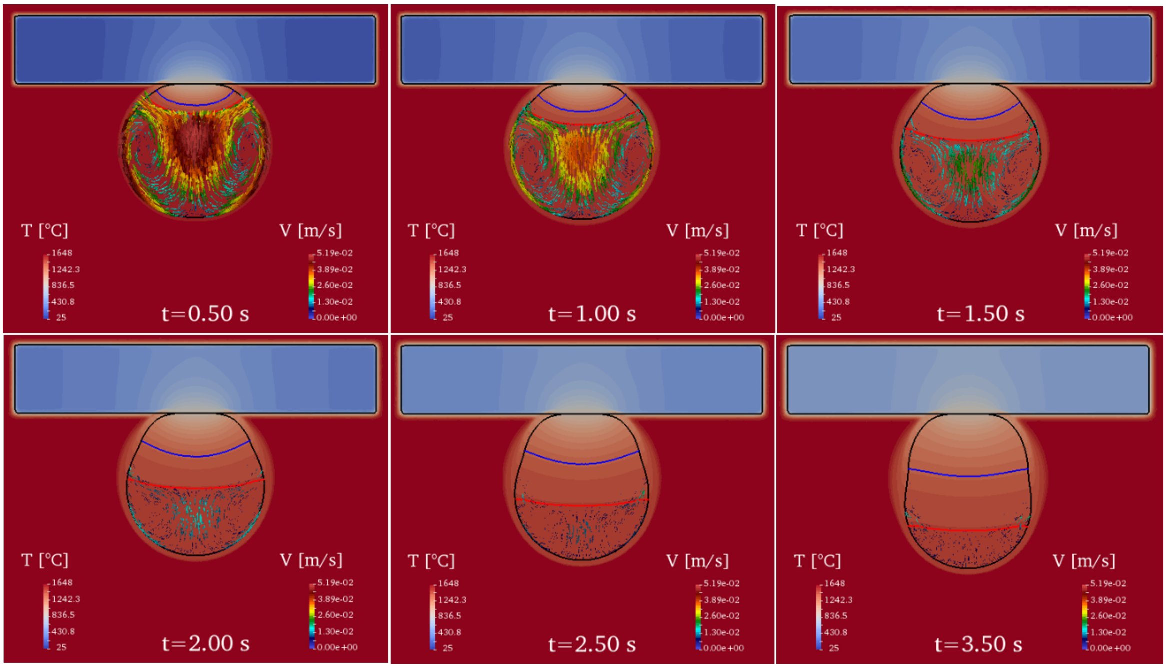

Figure 5.18: Snapshots of the solidifying 3D droplet in perfect contact with the chill. The images show the velocity of the liquid metal and the temperature of the whole domain. The red and the blue lines mark the position of $g^s = 1\%$ and $g^s = 99\%$ respectively.

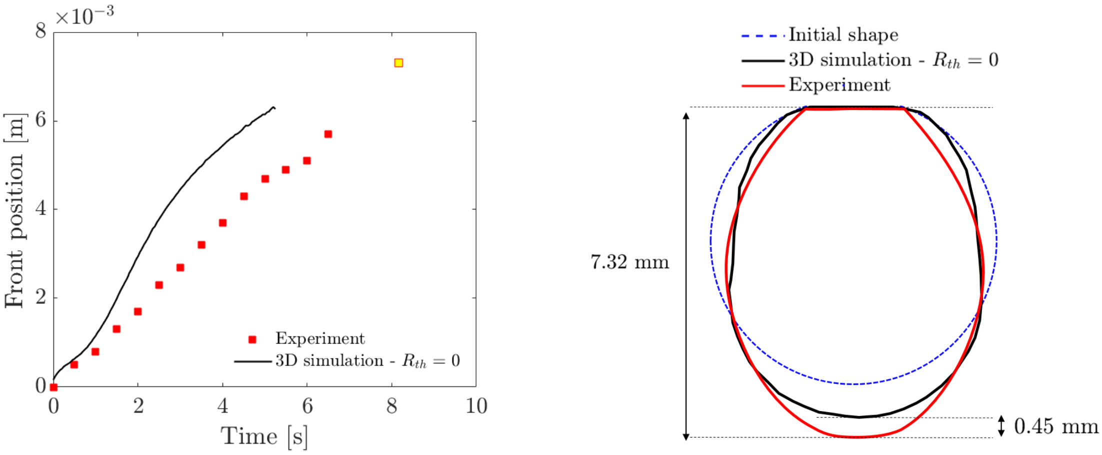

(a)

(b)

Figure 5.19: Comparison of a 3D simulation with perfect contact with the ISS experiment for (a) the time-evolution of the front position (b) the final shape of the solidified droplet.

number of elements required for a mesh that allows both stable calculation and good physics capturing is still very huge and becomes colossal in 3D.

We estimate that an adequate number of elements for a reasonable computation time would be of the order of 2M to 3M elements. To reduce the current 17M element mesh, very sophisticated optimisation work is required. The point to start with is the fact that static mesh makes us refine a region that satisfies a good capture of the physics at all stages of the simulation. This region has been defined by an 8mm major axis ellipsoid to cover the final elongation of the drop. This region has been defined by an 8mm major axis ellipsoid to cover the final elongation of the drop. This region covers more than what is necessary for certain stages of the simulation, especially during the first 2 seconds of the simulation where the shape of the drop is almost spherical. An adaptive meshing method is, therefore, necessary to update the mesh according to the evolution of the droplet shape. We used an adaptation method based on the distance function (level-set) [99]. This method allows the construction of anisotropic mesh elements within a given thickness band around the domain boundaries and isotropic elements outside. This method allowed us to refine the mesh around the chill in the previous simulation (see figure 5.17). Keeping the same mesh around the chill, we tried to build anisotropic mesh around the metal/gas interface with an element size of $2h_0$ in the tangential direction and isotropic mesh inside the metal of size $2h_0$. The resulting mesh is shown in figure 5.20 , and contains 8M elements . Unfortunately, the calculation did not converge. This is because the temperature gradient is parallel to the metal/gas interface, so the mesh should not be coarse in this direction. Marangoni currents are also important inside the droplet and require refinement within the metal domain. We believe that a mesh adaptation based on physical criteria is more suitable in this case. Such a method already exists in CimLib [100]. Its use is not simple and requires configuration work in order to find the best parameters to achieve an optimal mesh capturing at the same time interfaces, fluid dynamics and heat transfer, and allowing a reasonable calculation time.

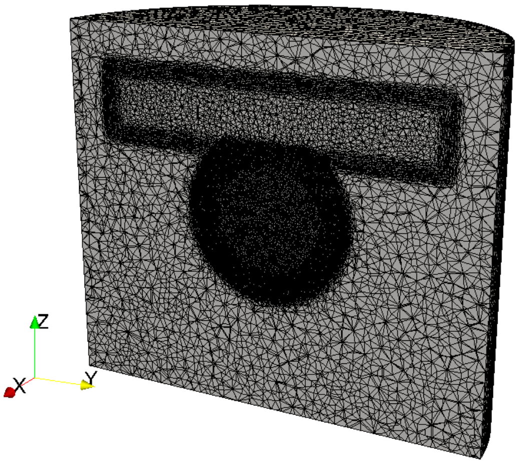

Figure 5.20: A clip of the 3D mesh showing mesh adaptation around the interfaces of the steel droplet and the chill plate. Calculations failed with this mesh.

As mentioned earlier, the 3D simulation predicted that the maximum magnitude of the Marangoni flow is about 5.2×10^{-2}m.s^{-1}. During the EML experiment, the positioner is always active. Hence, it is worth examining the magnitude of the positioner-induced flow and comparing it with the predicted Marangoni flow in order to assess the relevance of taking the electromagnetic field into account in further studies. Xiao et. al. [101] proposed a surrogate model based on parametric numerical experiments of MHD simulations for the ISS-EML facility. Their model enables the estimation of the maximum convective flow velocity due to the positioner as a function of the positioner control voltage $U^P_{ctr} = 7.549$V and the properties of the sample: ρ^l_M, the density, μ^l_M, the viscosity and σ^l_M, the electrical conductivity. As we do not have reliable data about the electrical conductivity of Fe-0.9wt.%C-0.26wt.%Si alloy, we estimate σ^l_M using the Wiedemann–Franz–Lorentz law:

$$\frac{k^l_M}{\sigma^l_M T} = L_0 \tag{5.104}$$

where $L_0 = 2.45 \times 10^{-8}$W.Ω.K^{-1} is Lorentz number. With $T = T_{M,0}$, $k^l_M = \langle k \rangle_M$, the electrical conductivity of Fe-0.9wt.%C-0.26wt.%Si is estimated to $\sigma^l_M = 9.85 \times 10^5 \mathrm{S}.m^{-1}$. Following the work of Xiao et. al. [101], the maximum velocity of the positioner-induced flow for the sample d1 under the operating conditions during the ISS chill cooling experiment is estimated to $u_{max} = 3.9 \times 10^{-2}$m.s^{-1} which is of the same order of magnitude as the Marangoni-induced flow velocity. Therefore, it would be useful to account for the electromagnetic field as a further improvement of the present modelling

5.5 Conclusion

In this chapter, we have presented a general numerical framework for modelling macrosegregation in the presence of thermocapillary convection in a multi-domain context. The proposed numerical framework is based on a so-called "weak coupling" between energy conservation, conservation of chemical species and conservation of momentum and total mass. Energy transfer by diffusion and convection is provided by a thermal solver coupled with thermodynamic tabulations containing the solidification paths for multi-component alloys. The solver is enriched by the thermal contact resistance model developed in chapter 4. The transport of chemical species is achieved by a monolithic solver allowing the resolution of the solute concentration in a multi-domain context. The Navier-Stokes solver allows the resolution of the flow in the presence of capillary forces (surface tension and Marangoni), mushy zone and solidification shrinkage. All this is formulated in an Eulerian monolithic approach using the level set method. The mass correction method proposed in Chapter 3 has been extended for the case of solidification with shrinking volume.

This numerical framework was applied for the simulation of the chill cooling experiment of a steel droplet microgravity. The simulations showed the dominance of Marangoni currents over the liquid flow. They also allowed finding the deformation of the solidifying droplet and its elongation in the direction parallel to the thermal gradient. The same behaviour was observed in the experiment. Through 2D parametric studies, we have shown that by adjusting the value of the thermal resistance we can get closer to the experimental cooling rate. Finally, we showed a 3D simulation assuming perfect contact. The simulation showed the same trend concerning elongation and Marangoni convection. However, the cooling rate is more important than the experiment because the thermal contact is not perfect in the experiment. The 3D simulation, whose results were presented was very time-consuming due to the huge number of elements contained in the mesh. For this reason, unfortunately, we could not perform another calculation with a non-zero thermal resistance in order to compare with the experimental cooling rate.

Chapter 6

Conclusions and Perspectives

This thesis is part of the two ESA projects entitled CCEMLCC and NEQUISOL which use electromagnetic levitation to study the solidification of alloys in microgravity. The common objective of these two projects being to reach a better understanding of containerless solidification, our contribution in these projects focuses on numerical modelling in order to provide a tool for the simulation of the experiments. The work achieved in this thesis deals with aspects related to fluid mechanics and others related to heat transfer. The developments carried out for fluid mechanics bring a contribution to both projects CCEMLCC and NEQUISOL, while the work on the thermal part is oriented towards applications of CCEMLCC project. The coupling is finally applied to the first and unprecedented chill cooling experiment performed on board the ISS. In order to have reference data for the comparison and validation of the simulations, we proposed at the beginning of this manuscript a post-processing of the ISS experiment. We extracted data by image processing from the recordings of the experiment by fast camera.

Fluid Mechanics For the part dealing with fluid mechanics, the main added value of this work is the taking into account of capillary forces that were absent in the previous contributions. This part of the thesis includes two types of contributions: numerical and theoretical.

Concerning the numerical part, the capillary forces are modelled by the CSF (Continuum Surface Force) method which introduces theses forces into Navier-Stokes equations as volume forces. The conversion from surface forces to volume forces is performed by the Dirac function which is calculated from the level-set function. However, we encountered several numerical difficulties related to surface tension and the level-set method.

- Firstly, we noticed that the conservation of mass is not ensured by classical numerical methods and even worse when the value of the surface tension is very high. We therefore proposed a mass correction method first for a constant volume and later for a shrinking volume due to solidification.

- We then tackled the classical problem of spurious currents artificially introduced by the CSF method. We proposed a method of scaling the Dirac function to reduce spurious currents around the interface.

- Numerical diffusion was also one of the numerical problems encountered. On this issue, we proposed a high order temporal discretization in order to reduce discretization errors and consequently numerical diffusion.

- The explicit discretization of surface tension force constrains the stability of the computation by a limit time step beyond which the computation becomes unstable. This limitation can be circumvented by a semi-implicit discretization using an implicit term depending on the fluid velocity. This formulation thus allows to save calculation time, on the other hand its use is associated with an added numerical diffusion.

The present numerical framework dealing with multi-fluid flows with surface tension shows a great capacity to handle high density ratios and very large surface tension values. However, it has some limitations:

- The spurious currents are reduced compared to classical methods, but are not completely eliminated. One way to improve this is to find an alternative method for calculating the interface curvature. Indeed, the curvature as defined in chapter 3 is written as the divergence of the gradient of the level set. The level set field being a P1 (linear) field, its gradient is therefore a P0 field (constant per element) and its divergence is therefore zero. In order not to fall in this case, we build a P1 gradient in each node by interpolation of the P0 gradient from the neighbouring elements. This P1 gradient is then used to calculate a P0 divergence which is then also interpolated to obtain a P1 divergence which finally gives the P1 curvature. This succession of interpolation introduces a loss of information and oscillations in the profile of the curvature.

- In order to use the diffuse interface approach, the thickness of the transition zone must be small compared to a characteristic length of the problem under study. At the same time, a number of elements in the transition zone must be provided, especially to properly describe the Dirac function. This requires the use of a high-resolution mesh around the interface. This can be very time-consuming in 3D. A conservative mesh adaptation method is necessary to update the mesh according to the position of the interface without losing information when transporting fields from one mesh to another.

This thesis also includes a theoretical part proposing an analytical solution of a benchmark inspired from the zero gravity oscillating drop method. This benchmark allows to quantitatively assess the accuracy of numerical methods according to three criteria: mass conservation, oscillation frequency correlated to surface tension and damping rate related to viscosity. For each of these criteria the theory developed provides an analytical solution in both 2D and 3D.

Heat transfer Concerning the part dealing with thermal, we proposed an Eulerian numerical framework to model heat conduction in a multi-domain context. The novelty lies in the development of a model allowing to take into account the thermal contact resistance in the stationary and unsteady regime. The results of the model were confronted with analytical test cases and showed the performance of the model in capturing temperature jumps between two bodies in contact. We then applied the model to simulate the solidification of a steel droplet in contact with a chill. Only conduction was considered in this first application to the CCEMLCC project. The simulations showed that the cooling rate of the metal can be controlled by the value of the thermal resistance. In the simulations of the CCEMLCC experiment, we used the energy solver developed in Saad's thesis [6], which allows coupling with thermodynamic tables containing the solidification paths of a multicomponent alloy. One of the improvements that can be made to this solver is the numerical treatment of thermal shocks when it comes to contact between two bodies at widely separated temperatures. We therefore recommend enriching the solver with a stabilisation method to manage thermal shocks. Such a method has been proposed by [51]. The initial temperature of the chill in this work was fixed at the ambient temperature set to 25°C . Considering the heat radiation to which the chill is exposed during heating and melting of the metallic sample, it can be suspected that the chill, or at least its contact surface, does not remain at ambient temperature. It would be useful to examine the relevance of thermal radiation and its influence on the cooling kinetics in future work. Modelling of thermal radiation with Level-set method in a stabilized FE framework has been proposed by Schmid et. al. [102]. The ability of their model to deal with multi-domain problems has been demonstrated. It would be a promising model for enriching the present work by accounting for thermal radiation.

Segregation We pointed out in chapters 3 and 5 that the total mass of the object described by the level-set function is not guaranteed to be conserved during transport of the interface and we proposed a mass correction method based on a uniform redistribution of the lost/gained mass. For the mass of the chemical species we can first imagine a similar method of global and uniform redistribution of the mass difference of the chemical species. However, it would be more judicious to identify the regions where the resolution of the transport equation leads to mass loss/gain and correct the composition locally so that the mass is globally conserved. Since the resolution of segregation is not the focus of this thesis, we have given little time to this numerical problem and therefore leave the door open for future improvements following this thesis.

Electromagnetic coupling Although the electromagnetic field needed for positioning the sample is much lower in microgravity than in 1g, the flow induced by the positioner during EML testing exists in reduced gravity. As highlighted in chapter 5, the maximum velocity of the positioner-induced flow is estimated to $u_{max} = 3.9 \times 10^{-2}$m.s^{-1} which is of the same order of magnitude as the maximum velocity of Marangoni-induced flow 5.2 $\times 10^{-2}$m.s^{-1}, predicted by the 3D simulation (figure 5.18). It would thus be of great interest to account for the electromagnetic field as a further improvement of the present numerical framework. In this direction, an Electromagnetic-CFD coupling has been already implemented in CEMEF in TherCast® by the PhD work of Luca Marioni [103]. Combining the current modelling of surface tension with Marioni's work will enable simulation of the oscillating droplet in electromagnetic levitation and provide a more realistic comparison with the ISS experiment for measuring surface tension and viscosity. Such comparison has been performed recently by Budenkova et. al. [104].

This work is a step towards a comprehensive modelling of the physics studied in these projects. We are aware that there is still room for further improvement, but we are confident that the proposed numerical framework is compatible with future contributions which may have as an objective the reproduction of the experiment with its smallest details. Before getting there we must first address the improvement of the computational time which has been the major difficulty encountered in this work. Such an improvement would open the way to quantitative comparison with expected experimental characterisations of the droplet when it will be back from the ISS.

Bibliography

[1] C.-A. Gandin, M. Bellet, A. Saad, D. Herlach, T. Volkmann, C. Karrasch, V. Uhlenwinkel, N. Ellendt, N. Cifici, G. Zepon, H. Henein, P. D. Khatibi, J. Valloton, P. Siitonen, F. Costes, M. Antonicelli, M. Bobadilla, and B. Rivaux, "Chill cooling for the electromagnetic levitator in relation with continuous casting of steels (CCEMLCC)," 2014. xii, 4, 18, 82

[2] D. Herlach, C.-A. Gandin, A. Garcia-Escorial, H. Henein, A. Mullis, M. Rettenmayr, G.-U. Grün7, A. Schönecker, and K. Nicholds, "Proposal to esa for a continuation of map project nequisol," 2015. 4

[3] "DLR ElectoMagnetic Levitation." `https://www.dlr.de/mp/DesktopDefault.aspx/tabid-3094/4704_read-6905/gallery-1/gallery_read-Image.22.3298/`. ix, 4

[4] C. Guo, J. Li, H. Yu, Z. Wang, X. Lin, and J. Wang, "Branching-induced grain boundary evolution during directional solidification of columnar dendritic grains," Acta Materialia, vol. 136, pp. 148 – 163, 2017. ix, 8

[5] A. Badillo, D. L. Ceynar, and C. Beckermann, "Growth of equiaxed dendritic crystals settling in an undercooled melt, part 1: Tip kinetics," Journal of Crystal Growth, vol. 309, pp. 197–215, 2007. ix, 8

[6] A. Saad, Numerical Modelling of Macrosegregation Formed During Solidification With Shrinkage Using a Level Set Approach. Theses, Université Paris sciences et lettres, Feb. 2016. ix, 9, 11, 12, 14, 22, 110, 151

[7] D. Herlach, C.-A. Gandin, A. Garcia-Escorial, H. Henein, A. Mullis, M. Rettenmayr, G.-U. Grün, A. Schönecker, and K. Nicholds, "Non-equilibrium solidification, modelling for microstructural engineering of industrial alloys (nequisol)," November 2018. 9

[8] R. W. Hyers, Computer-Aided Experiments in Containerless Processing of Materials, ch. 2, pp. 31–49. John Wiley Sons, Ltd, 2012. 9

[9] I. Egry, E. Ricci, R. Novakovic, and S. Ozawa, "Surface tension of liquid metals and alloys - recent developments," Advances in Colloid and Interface Science, vol. 159, pp. 198–212, 2010. 9, 19, 34, 139

[10] S. Mosbah, Multiple scales modeling of solidification grain structures and segregation in metallic alloys. Theses, École Nationale Supérieure des Mines de Paris, December 2008. 10

[11] S. Mosbah, M. Bellet, and C.-A. Gandin, "Experimental and numerical modeling of segregation in metallic alloys," Metallurgical and Materials Transactions A, vol. 41, pp. 651–669, Mar. 2010. 10

[12] B. Rivaux, Simulation 3D éléments finis des macroségrégations en peau induites par déformations thermomécaniques lors de la solidification d'alliages métalliques. Theses, École Nationale Supérieure des Mines de Paris, July 2011. ix, x, 10, 11, 26, 110

[13] M. Khalloufi, Multiphase flows with phase change and boiling in quenching processes. Theses, Université Paris sciences et lettres, Dec. 2017. 13

[14] Q. Chen, Modélisation numérique thermomécanique de fabrication additive par fusion sélective de lit de poudre par laser : Application aux matériaux céramiques. PhD thesis, 2018. Thèse de doctorat Mécanique numérique et Matériaux Paris Sciences et Lettres (ComUE) 2018. 13

[15] B. Herlach, D. M.and Feuerbacher, "Non-equilibrium solidification of undercooled metallic melts," Advances in Space Research, vol. 11, pp. 255–262, Jan 1991. 13

[16] C.-A. Gandin, M. Bellet, G. Guillemot, E. Hachem, A. Aalilija, S. Zhang, T. Volkmann, C. Kreischer, H. Henein, J. Valloton, B. Rivaux, F. Costes, E. Perchat, H. Combeau, I. Poirtrault, M. Cherif, L. Carroz, J. Demurger, V. Descotes, and L. Collins, "Chill cooling for the electromagnetic levitator in relation with continuous casting of steels (CCEMLCC)," 2020. ix, 19

[17] F. Karmali and M. Shelhamer, "The dynamics of parabolic flight: flight characteristics and passenger percepts," Acta astronautica, vol. 63, pp. 594–602, Sep 2008. 20

[18] "Parabolic flight manoeuvre profile." `http://wsn.spaceflight.esa.int/docs/EUG2LGPr3/EUG2LGPr3-5-ParabolicFlights.pdf`. ix, 21

[19] "ESA zero-g airbus aircraf." `https://www.esa.int/Science_Exploration/Human_and_Robotic_Exploration/Research/Parabolic_flights`. ix, 21

[20] C.-A. Gandin, M. Bellet, A. Saad, A. Aalilija, S. Zhang, T. Volkmann, C. Karrasch, H. Henein, P. D. Khatibi, J. Valloton, M. Bobadilla, B. Rivaux, F. Costes, E. Perchat, H. Combeau, I. Poitrault, J. Demurger, S. Witzke, V. Descotes, and L. Collins, "Project ESA-MAP CCEMLCC – mid-term review," July 2017. x, 24

[21] "NASA sounding rocket flight profile." `https://www.nasa.gov/missions/research/f_sounding.html`. x, 25

[22] "TEXUS-42 sounding rocket." `https://www.esa.int/Science_Exploration/Human_and_Robotic_Exploration/Sounding_rockets_set_for_lift-off`. x, 25

[23] T. Volkmann, N. Johannsen, and D. M. Herlach, "Chill cooling for the electromagnetic levitator in relation with continuous casting of steel," December 2009. x, 26

[24] "Artist's impression of the completed international space station." `https://www.esa.int/ESA_Multimedia/Images/2003/05/Artist_s_impression_of_the_completed_International_Space_Station#.X51GVDnUfnw.link`. x, 27

[25] M. Mohr, "Surface tension and viscosity for sample #20, fec0.9si0.2," June 2019. xi, 33, 34

[26] G. F. Hewitt, "Multiphase flow in the energy industries," Journal of Engineering Thermophysics, vol. 17, pp. 12–23, Mar 2008. 40

[27] A. Aiyejina, D. P. Chakrabarti, A. Pilgrim, and M. K. S. Sastry, "Wax formation in oil pipelines: A critical review," International Journal of Multiphase Flow, vol. 37, pp. 671–694, Sep 2011. 40

[28] R. Visentini, C. Colin, and P. Ruyer, "Experimental investigation of heat transfer in transient boiling," Experimental Thermal and Fluid Science, vol. 55, pp. 95–105, May 2014. 40

[29] J. Dong, K. Inthavong, and J. Tu, Multiphase Flows in Biomedical Applications, pp. 1–24. Singapore: Springer Singapore, 2017. 40

[30] D. Dutykh, C. Acary-Robert, and D. Bresch, "Mathematical modeling of powder-snow avalanche flows," Studies in Applied Mathematics, vol. 127, no. 1, pp. 38–66, 2011. 40

[31] S. Balachandar and A. Prosperetti, Computational Approaches to Multiphase Flow. Fluid Mechanics and its Applications, Netherlands: Springer, 2006. IUTAM Symposium on Computational Approaches to Multiphase Flow, Argonne National Laboratory, October 4-7, 2004. 40

[32] F. H. Harlow and J. E. Welch, "Numerical calculation of time-dependent viscous incompressible flow of fluid with free surface," Physics of Fluids, vol. 8, no. 12, pp. 2182–2189, 1965. 41

[33] B. J. Daly and W. E. Pracht, "Numerical study of density-current surges," Physics of Fluids, vol. 11, pp. 15–30, 1968. 41

[34] C. Hirt and B. Nichols, "Volume of fluid (vof) method for the dynamics of free boundaries," J. Comput. Phys.; (United States), vol. 39:1, pp. 201–225, 1981. 41

[35] S. Osher and J. A. Sethian, "Fronts propagating with curvature-dependent speed: Algorithms based on hamilton-jacobi formulations," Journal of Computational Physics, vol. 79, no. 1, pp. 12 – 49, 1988. 41

[36] M. Shakoor, B. Scholtes, P.-O. Bouchard, and M. Bernacki, "An efficient and parallel level set reinitialization method – application to micromechanics and microstructural evolutions," Applied Mathematical Modelling, vol. 39, no. 23, pp. 7291 – 7302, 2015. 42

[37] C. Bahbah, M. Khalloufi, A. Larcher, Y. Mesri, T. Coupez, R. Valette, and E. Hachem, "Conservative and adaptive level-set method for the simulation of two-fluid flows," Computers and Fluids, vol. 191, p. 104223, 2019. 42

[38] A. Smolianski, Numerical Modeling of Two-Fluid Interfacial Flows. PhD thesis, University of Jyväskylä, 2001. 43

[39] E. Hachem, T. Kloczko, H. Digonnet, and T. Coupez, "Stabilized finite element solution to handle complex heat and fluid flows in industrial furnaces using the immersed volume method," International Journal for Numerical Methods in Fluids, vol. 68, pp. 99–121, 2012. 46, 83

[40] J. U. Brackbill, D. B. Kothe, and C. Zemach, "A continuum method for modeling surface tension," Journal of Computional Physics, vol. 100, pp. 335–354, 1992. 46

[41] K. Yokoi, "A density-scaled continuum surface force model within a balanced force formulation," Journal of Computational Physics, vol. 278, pp. 221–228, 2014. 47

[42] S. Hysing, "A new implicit surface tension implementation for interfacial flows," International Journal for Numerical Methods in Fluids, vol. 51, no. 6, pp. 659–672, 2006. 48, 49

[43] M. Khalloufi, Y. Mesri, R. Valette, and E. Hachem, "High fidelity anisotropic adaptive variational multiscale method for multiphase flows with surface tension," Computer Methods in Applied Mechanics and Engineering, vol. 307, pp. 44–67, 2016. 49

[44] Q. Chen, G. Guillemot, C.-A. Gandin, and M. Bellet, "Three-dimensional finite element thermomechanical modeling of additive manufacturing by selective laser melting for ceramic materials," Additive Manufacturing, vol. 16, pp. 124–137, 2017. 49

[45] G. C. Buscaglia and R. F. Ausas, "Variational formulations for surface tension, capillarity and wetting," Computer Methods in Applied Mechanics and Engineering, vol. 200, no. 45, pp. 3011 – 3025, 2011. 49

[46] D. Forti and L. Dede', "Semi-implicit bdf time discretization of the navier–stokes equations with vms-les modeling in a high performance computing framework," Computers and Fluids, vol. 117, pp. 15. 168–182, 2015. 50

[47] P. Meliga and E. Hachem, "Time-accurate calculation and bifurcation analysis of the incompressible flow over a square cavity using variational multiscale modeling," Journal of Computational Physics, vol. 376, pp. 952–972, 2019. 50

[48] T. Hughes, L. P. Franca, and M. Balestra, "A new finite element formulation for computational fluid dynamics: V. circumventing the babuška-brezzi condition: a stable petrov-galerkin formulation of the stokes problem accommodating equal-order interpolations," Computer Methods in Applied Mechanics and Engineering, vol. 59, pp. 85–99, 1986. 50

[49] D. N. Arnold, F. Brezzi, and M. Fortin, "A stable finite element for the stokes equations," CALCOLO, vol. 21, no. 4, pp. 337–344, 1984. 51

[50] E. Hachem, Stabilized finite element method for heat transfer and turbulent flows inside industrial furnaces. PhD thesis, 2009. Thèse de doctorat Mécanique numérique Paris, ENMP 2009. 51

[51] E. Hachem, B. Rivaux, T. Kloczko, H. Digonnet, and T. Coupez, “Stabilized finite element method for incompressible flows with high reynolds number,” Journal of Computational Physics, vol. 229, pp. 8643–8665, 2010. 51, 52, 151

[52] R. Codina, “Stabilization of incompressibility and convection through orthogonal sub-scales in finite element methods,” Computer Methods in Applied Mechanics and Engineering, vol. 190, pp. 1579–1599, 2000. 52

[53] L. Rayleigh, “On the capillary phenomena of jets,” Proceedings of the Royal Society of London, vol. 29, pp. 71–97, 1879. 53, 54, 55, 60, 61

[54] H. Lamb, “On the oscillations of a viscous spheroid,” London Mathematical Society, vol. 13, pp. 51–66, 1881. 53, 54

[55] H. J. J. Staat, A. van der Bos, M. van den Berg, H. Reinten, H. Wijshoff, M. Versluis, and D. Lohse, “Ultrafast imaging method to measure surface tension and viscosity of inkjet-printed droplets in flight,” Experiments in Fluids, vol. 58:2, 2017. 54

[56] H. Lamb, Hydrodynamics. Cambridge University Press, sixth ed., 1932. 54, 61

[57] R. S. Valentine, N. F. Sather, and W. J. Heideger, “The motion of drops in viscous media,” Chemical Engineering Science, vol. 20, pp. 719–728, 1965. 54

[58] C. Miller and L. Scriven, “The oscillations of a luid droplet immersed in another fluid,” Journal of Fluid Mechanics, vol. 32, pp. 417–435, 1968. 54

[59] A. Prosperetti, “Free oscillations of drops and bubbles : the initial-value problem,” Journal of Fluid Mechanics, vol. 100, pp. 333–347, 1980. 54, 55

[60] A. Prosperetti, “Viscous effects on perturbed spherical flows,” Quarterly of Applied mathematics, vol. 34, pp. 339–352, 1977. 54, 55

[61] J. Tsamopoulos and R. Brown, “Nonlinear oscillations of inviscid drops and bubbles,” Journal of Fluid Mechanics, vol. 127, pp. 519–537, 1983. 54, 55

[62] T. S. Lundgreen and N. N. Mansour, “Oscillations of drops in zero gravity with weak viscous effects,” Journal of Fluid Mechanics, vol. 194, pp. 479–510, 1988. 54

[63] E. Trinh and T. G. Wang, “Large-amplitude free and driven drop-shape oscillations: experimental observations,” Journal of Fluid Mechanics, vol. 122, pp. 315–338, 1982. 54

[64] G. B. Foote, “A numerical method for studying liquid drop behavior: simple oscillation,” Journal of Computational Physics, vol. 11, pp. 507–530, 1973. 54

[65] X. Xiao, R. W. Hyers, R. K. Wunderlich, H.-J. Fecht, and D. M. Matson, “Deformation induced frequency shifts of oscillating droplets during molten metal surface tension measurement,” Applied Physics Letters, vol. 113(1), p. 011903, 2018. 54, 55

[66] D. L. Cummings and D. A. Blackburn, “Oscillations of magnetically levitated aspherical droplets,” Journal of Fluid Mechanics, vol. 224, pp. 395–416, 1991. 54

[67] A. Bratz and I. Egry, “Surface oscillations of electromagnetically levitated viscous metal droplets,” Journal of Fluid Mechanics, vol. 298, pp. 341–359, 1995. 54

[68] I. Egry, E. Ricci, R. Novakovic, and S. Ozawa, “Surface tension of liquid metals and alloys - recent developments,” Advances in Colloid and Interface Science, vol. 159, pp. 198–212, 2010. 54

[69] R. K. Wunderlich and M. Mohr, “Non-linear effects in the oscillating drop method for viscosity measurements,” High Tempertures- High Pressures, vol. 48, pp. 253–277, 2019. 55

[70] D. Joseph, “Potential flow of viscous fluids: Historical notes,” International Journal of Multiphase Flow, vol. 32, pp. 285–310, 2006. 59

[71] C. Bahbah, M. Khalloufi, A. Larcher, Y. Mesri, T. Coupez, R. Valette, and E. Hachem, “Conservative and adaptive level-set method for the simulation of two-fluid flows,” Computers & Fluids, vol. 191, p. 104223, Sep 2019. 77

[72] P. Kapitza, “E10 - the study of heat transfer in helium ii - j. phys. u.s.s.r. 4, 181 (1941),” in Helium 4 (Z. Galasiewicz, ed.), pp. 114 – 153, Pergamon, 1974. 82

[73] E. Swartz and R. O. Pohl, “Thermal boundary resistance,” Reviews of Modern Physics, vol. 61, pp. 605–668, 1989. 83

[74] A. Hamasaiid, M. Dargusch, T. Loulou, and G. Dour, “A predictive model for the thermal contact resistance at liquid-solid interfaces: Analytical developments and validation,” International Journal of Thermal Sciences, vol. 50, pp. 1445–1459, 2011. 83

[75] H. Prajapati, D. Ravoori, R. Woods, and A. Jain, “Measurement of anisotropic thermal conductivity and inter-layer thermal contact resistance in polymer fused deposition modeling (fdm),” Additive Manufacturing, vol. 21, pp. 84 – 90, 2018. 83

[76] M. Grujicic, C. Zhao, and E. Dusel, “The effect of thermal contact resistance on heat management in the electronic packaging,” Applied Surface Science, vol. 246, pp. 290 – 302, 2005. 83

[77] T. Chen, D. Chen, B. Sencer, and L. Shao, “Molecular dynamics simulations of grain boundary thermal resistance in uo2,” Journal of Nuclear Materials, vol. 452, pp. 364 – 369, 2014. 83

[78] L. Steg and H. Lew, “Chapter 32 - hypersonic ablation,” in The High Temperature Aspects of Hypersonic Flow (W. Nelson, ed.), vol. 68, pp. 629 – 680, Elsevier, 1964. 83

[79] D. Baker and D. Assanis, "A methodology for coupled thermodynamic and heat transfer analysis of a diesel engine," Applied Mathematical Modelling, vol. 18, pp. 590 – 601, 1994. 83

[80] C. P. Hallam and W. D. Griffiths, "A model of the interfacial heat-transfer coefficient for the aluminum gravity die-casting process," Metallurgical and Materials Transactions B, vol. 35, p. 721–733, 2004. 83

[81] A. Bendada, A. Derdouri, M. Lamontagne, and Y. Simard, "Analysis of thermal contact resistance between polymer and mold in injection molding," Applied Thermal Engineering, vol. 24, pp. 2029 – 2040, 2004. 83

[82] K. Pericleous, K. Chan, and M. Cross, "Free surface flow and heat transfer in cavities: The sea algorithm," Numerical Heat Transfer, Part B: Fundamentals, vol. 27, pp. 487–507, 1995. 83

[83] G. Storr and M. Behnia, "Comparisons between experiment and numerical simulation using a free surface technique of free-falling liquid jets," Experimental Thermal and Fluid Science, vol. 22, pp. 79 – 91, 2000.

[84] R. Fedkiw, T. Aslam, B. Merriman, and S. Osher, "A non-oscillatory eulerian approach to interfaces in multimaterial flows (the ghost fluid method)," Journal of Computational Physics, vol. 152, pp. 457 – 492, 1999.

[85] J. Principe and R. Codina, "A numerical approximation of the thermal coupling of fluids and solids," International Journal for Numerical Methods in Fluids, vol. 59, pp. 1181 – 1201, 2009. 83

[86] D. Hasselman and L. Johnson, "Effective thermal conductivity of composites with interfacial thermal barrier resistance," Journal of Composite Materials, vol. 21, pp. 508–515, 1987. 83

[87] A. Jain and K. K. Tamma, "Parabolic heat conduction specialized applications involving imperfect contact surfaces: Local discontinuous galerkin finite element method—part 2," Journal of Thermal Stresses, vol. 33:4, pp. 344–355, 2010. 83

[88] J. Yvonnet, Q.-C. He, Q.-Z. Zhu, and J.-F. Shao, "A general and efficient computational procedure for modelling the kapitza thermal resistance based on xfem," Computational Materials Science, vol. 5, pp. 1220–1224, 2011. 83, 85

[89] J. Liu, S. Gu, E. Monteiro, and Q. He, "A versatile interface model for thermal conduction phenomena and its numerical implementation by xfem," Computational Mechanics, vol. 4, p. 825–843, 2014. 83

[90] S. Torquato and M. Rintoul, "Effect of the interface on the properties of composite media," Physical Review Letter, vol. 75, pp. 4067–4070, 1995. 83

[91] R. Lipton and B. Vernescu, “Composites with imperfect interface,” Proceedings of the Royal Society of London A, vol. 452, 1945.

[92] C.-W. Nan and R. Birringer, “Effective thermal conductivity of particulate composites with interfacial thermal resistance,” Journal of Applied Physics, vol. 81, pp. 6692–6699, 1997.

[93] H. L. Duan and B. Karihaloo, “Effective thermal conductivities of heterogeneous media containing multiple imperfectly bonded inclusions,” Physical Review B, vol. 75, p. 064206, 2007. 83

[94] S. Patankar, Numerical heat transfer and fluid flow. Series on Computational Methods in Mechanics and Thermal Science, Hemisphere Publishing Corporation (CRC Press, Taylor & Francis Group), 1980. 86

[95] S. Ganesan and D. R. Poirier, “Conservation of mass and momentum for the flow of interdendritic liquid during solidification,” Metallurgical Transactions B, vol. 21, p. 173, Feb 1990. 99

[96] C. Ni, J.and Beckermann, “A volume-averaged two-phase model for transport phenomena during solidification,” Metallurgical Transactions B, vol. 22, p. 349, Jun 1991. 99, 110

[97] A. Saad, C.-A. Gandin, and M. Bellet, “Temperature-based energy solver coupled with tabulated thermodynamic properties - application to the prediction of macrosegregation in multicomponent alloys,” Computational Materials Science, vol. 99, pp. 221–231, 2015. 101, 130

[98] B. Julien, Y. Liu, and N. Moulin, “Finite element setting for fluid flow simulations with natural enforcement of the triple junction equilibrium,” Computers Fluids, vol. 171, pp. 103–121, 07 2018. 116

[99] H. Resk, L. Delannay, M. Bernacki, T. Coupez, and R. Logé, “Adaptive mesh refinement and automatic remeshing in crystal plasticity finite element simulations,” Modelling and Simulation in Materials Science and Engineering, vol. 17, p. 075012, aug 2009. 146

[100] T. Coupez, “Metric construction by length distribution tensor and edge based error for anisotropic adaptive meshing,” Journal of Computational Physics, vol. 230, no. 7, pp. 2391 – 2405, 2011. 146

[101] X. Xiao, R. W. Hyers, and D. M. Matson, “Surrogate model for convective flow inside electromagnetically levitated molten droplet using magnetohydrodynamic simulation and feature analysis,” International Journal of Heat and Mass Transfer, vol. 136, pp. 531–542, Jun 2019. 147

[102] Q. Schmid, Y. Mesri, E. Hachem, and R. Codina, “Stabilized mixed finite element method for the m 1 radiation model,” Computer Methods in Applied Mechanics and Engineering, vol. 335, pp. 69 – 90, June 2018. 151

[103] L. Marioni, Computational Modelling and Electromagnetic-CFD Coupling inCasting Processes. Theses, Université Paris sciences et lettres, November 2017. 151

[104] O. Budenkova, A. Gagnoud, and Y. Delannoy, “Numerical simulations of turbulent flow in an electromagnetically levitated metallic droplet using k-ω SST and reynolds stress models,” Magnetohydrodynamics, vol. 56, no. 2, p. 81–91, 2020. 151

RÉSUMÉ

L'étude de la solidification en microgravité permet aux chercheurs de dissocier les phénomènes indépendants de la gravité de ceux qui en dépendent. L'objectif est de parvenir à une meilleure compréhension de la solidification permettant à l'industrie métallurgique d'atteindre les propriétés recherchées pour les produits métalliques et d'éviter les défauts qui apparaissent lors de leur élaboration. C'est dans ce contexte que les projets NEQUISOL et CCEMLCC de l'Agence spatiale européenne sont définis. Dans le cadre de ces deux projets, nous proposons une modélisation numérique pour simuler les expériences de solidification d'échantillons métalliques en lévitation électromagnétique dans la Station Spatiale Internationale. Notre outil numérique est basé sur la résolution par éléments finis des équations de conservation de l'énergie, de la masse totale, de la quantité de mouvement et de la masse des espèces chimiques d'un système multidomaine impliquant un alliage métallique multicomposant. Une formulation monolithique permet la résolution d'un seul système d'équations sur un seul maillage eulérien. Une formulation éléments finis VMS stabilisée est proposée pour résoudre les équations de Navier-Stokes. La modélisation est enrichie par la prise en compte du retrait de solidification, de la tension de surface et de l'effet Marangoni agissant à l'interface liquide-gaz. Un modèle de résistance thermique de contact est développé et validé, permettant de prendre en compte les imperfections de contact thermique entre les différents matériaux. La méthode Level Set est utilisée pour modéliser les interfaces entre les sous-domaines. L'interface liquide-solide dans le sous-domaine métallique est implicitement représentée par la méthode de la moyenne volumique. Dans un premier temps, nous proposons des simulations d'expériences de mesure de la tension de surface et de la viscosité des métaux liquides en utilisant la technique de la goutte oscillante en microgravité. Ce benchmark offre une comparaison quantitative entre les résultats numériques et une solution analytique que nous avons dérivée en 2D et 3D. Une fois que nous avons validé notre modélisation numérique de la dynamique de l'interface liquide-gaz, nous effectuons des simulations de solidification d'une gouttelette d'acier et la comparons aux données de la première et unique expérience réalisée dans la Station Spatiale Internationale dans le cadre du projet CCEMLCC.

MOTS CLÉS

Simulation numérique; Éléments Finis; Level Set; Tension de Surface; Marangoni; Résistance thermique de contact; Goutte oscillante; Solidification; Microgravité

ABSTRACT

The study of solidification in microgravity allows researchers to dissociate gravity-independent phenomena from gravity-dependent ones. The objective is to reach a better understanding of solidification allowing the metallurgical industry to meet the expected properties of their metal products and to avoid the defects that appear during their elaboration. In this context, the NEQUISOL and CCEMLCC projects of the European Space Agency are taking place. As part of these two projects, we propose a numerical framework to simulate the solidification experiments of metallic samples in electromagnetic levitation in the International Space Station. Our numerical tool is based on the finite element resolution of the conservation equations of energy, total mass, momentum and mass of the chemical species of a multi-domain system involving a multicomponent metal alloy. A monolithic formulation allows the resolution of one set of equations on a single Eulerian mesh. A stabilised VMS Finite Elements formulation is proposed to solve the Navier-Stokes equations. The modelling is enriched by taking into account solidification shrinkage, surface tension and the Marangoni effect acting at the liquid-gas interface. A contact thermal resistance model is developed and validated enabling the consideration of thermal contact imperfections between the different materials. The Level Set method is used to model the interfaces between the sub-domains. The liquid-solid interface within the metal sub-domain is implicitly represented by the volume average methodology. In a first step, we propose simulations of measurement experiments of surface tension and viscosity of liquid metals using the oscillating drop technique in microgravity. This benchmark offers a quantitative comparison between the numerical results and an analytical solution that we derived in both 2D and 3D. Once we have validated our numerical modelling of the dynamics of the liquid-gas interface, we perform simulations of the solidification of a steel droplet and compare it with data from the first and unique experiment performed on board the International Space Station in the framework of the CCEMLCC project.

KEYWORDS

Numerical simulation; Finite Element; Level Set; Surface tension; Marangoni; Thermal contact resistance; Oscillating drop; Solidification; Microgravity